A Multiscale Method for Simulating Fracture in Polycrystalline Metals

Erik Saether

Dissertation submitted to the Faculty of the
Virginia Polytechnic Institute and State University
in partial fulfillment of the requirements for the degree of

Doctor of Philosophy
in
Engineering Mechanics

Surot Thangjitham, Chair
Richard Barnwell
Norman E Dowling
John C Duke
David Y Gao
Edward H Glaessgen

Keywords: Multiscale Analysis, Finite Element Method, Molecular Dynamics, Cohesive Zone Models, Decohesion Finite Elements, Polycrystalline Metals.

Copyright 2008, Erik Saether. No copyright is asserted in the United States under Title 17, U.S. Code. The U.S. Government has a royalty-free license to exercise all rights under the copyright clamed herein for Governmental Purposes. All other rights are reserved by the copyright owner.

April 18, 2008
Blacksburg, Virginia

A Multiscale Method for Simulating Fracture in Polycrystalline Metals

Erik Saether

Abstract

The emerging field of nanomechanics is providing a new focus in the study of the mechanics of materials, particularly in simulating fundamental atomic mechanisms involved in the initiation and evolution of damage. Simulating fundamental material processes using *first principles* in physics strongly motivates the formulation of computational multiscale methods to link macroscopic failure to the underlying atomic processes from which all material behavior originates.

A combined concurrent and sequential multiscale methodology is developed to analyze fracture mechanisms across length scales. Unique characterizations of grain boundary fracture mechanisms in an aluminum material system are performed at the atomic level using molecular dynamics simulation and are mapped into cohesive zone models for continuum modeling within a finite element framework. Fracture along grain boundaries typically exhibit a dependence of crack tip processes (i.e. void nucleation in brittle cleavage or dislocation emission in ductile blunting) on the direction of propagation due to slip plane orientation in adjacent grains. A new method of concurrently coupling molecular dynamics and finite element analysis frameworks is formulated to minimize the overall computational requirements in simulating atomistically large material regions. A sequential multiscale approach is advanced to model microscale polycrystal domains in which atomistically-based cohesive zone parameters are incorporated into special directional decohesion finite elements that automatically apply appropriate ductile or brittle cohesive properties depending on the direction of crack propagation. The developed multiscale analysis methodology is illustrated through a parametric study of grain boundary fracture in three-dimensional aluminum microstructures.

Acknowledgments

First, I wish to express my sincere gratitude and respect to my advisor, Professor S. Thangjitham, for his guidance and motivation during the course of my doctoral research. I am particularly grateful for the many discussions we have had regarding my ongoing research into nanomechanics and multiscale methods at NASA Langley Research Center (LaRC) from which my dissertation topic has developed. My sincere appreciation is also extended to my other committee members at Virginia Tech, Dr. R. Barnwell, Dr. N.E. Dowling, Dr. J.C. Duke, and Dr. D.Y. Gao for helpful feedback and general support for my research.

I am indebted to Dr. E.H. Glaessgen at NASA LaRC who is also a member of my committee and who leads the team of which I am a member in the area of computational damage science. He has contributed to the overall technical research and his efforts have been instrumental for integrating my work on multiscale methods within overall technical goals at NASA. In addition, he has provided significant editorial oversight in the development of this dissertation. Heartfelt appreciation is given to my other colleagues with whom I directly interact and whose collaboration has been vital towards accomplishing the goals of the current research. Dr. V. Yamakov has provided important collaboration in the areas of molecular dynamic simulation and the physics of solids, and Ms. D. Phillips has been indispensable for her diligence and insight into evaluating developed software and generating simulation models. Both have contributed greatly to my research in developing multiscale simulations methods.

Outline of the dissertation and technical advancements

The first two chapters of this dissertation serve to present essential background information to put into perspective the development and technical advancements of the overall multiscale analysis methodology presented in following chapters. Chapter 1 contains a basic introduction to concurrent and sequential multiscale analysis methods. The aim of this chapter is to present the capabilities and limitations of current multiscale methods. Chapter 2 discusses molecular dynamics simulation. This chapter begins with an overview of MD analysis methods and contains brief descriptions of various MD techniques that are used and referenced in the present work. Following this, a detailed discussion is presented of a MD analysis of fracture along a selected grain boundary configuration demonstrating directional growth characteristics. This discussion details various modeling considerations that have been neglected in other published work.

Chapter 3 begins with a discussion of the computational constraints on MD system size and the resulting impact of boundary proximity on simulation results. To limit the computational requirements on imposing far-field boundary conditions in MD simulations, a new approach to concurrent multiscale methods involving MD-FEM coupling is developed and described in detail in this chapter. This approach presents certain features that are unavailable in similar multiscale methods developed to date that pertain to interface coupling and finite temperature applications. The developed concurrent multiscale method is denoted as the embedded statistical coupling method (ESCM).

Chapter 4 presents an extensive discussion of cohesive zone models (CZM) that includes empirical macroscopic models and quantitative models based on atomistic processes, mode mixity, and the mathematical representation of CZM constitutive laws. A novel method for the extraction of CZM parameters from MD simulation is detailed. This method improves upon other treatments by introducing a systematic statistical approach to determining atomistic traction-displacement relationships. Selected theoretical issues in the calculation of CZMs such as successfully partitioning elastic and

inelastic contributions to the cohesive zone energy are discussed. In addition, a new casting of these constitutive relationships into a piece-wise linear representation that avoids specific functional forms that may constrain the representation of these constitutive laws is presented. The subsequent use of atomistically-derived CZM parameters within nonlinear decohesion finite element formulations constitutes a sequential multiscale approach for simulating fracture at higher length scales.

Chapter 5 contains the development of novel 1-D and 2-D 'directional' decohesion finite elements that incorporate criteria to selectively apply appropriate CZMs depending on the direction of crack propagation and surrounding grain orientation, and incorporate mode mixity in a general manner. A discussion of computational and theoretical demands for determining CZMs permitting a complete characterization of the orientation space of grain boundaries and determination of the effect of defects is presented including a discussion of the current state-of-the-art in developing a 'bottom-up' description and simulation of material failure processes.

Chapter 6 presents several illustrations of the developed methodology. A recent enhancement to the ESCM approach is presented where decohesion finite elements and a nonlinear solution procedure is included in the FEM analysis and permits the nearly seamless propagation of a crack from the continuum domain into the MD region. Sequential multiscale analysis at larger length scales is illustrated by using selected 1-D, 2-D, and 3-D problems wherein parametrically varied CZM relationships are applied to qualitatively assess the sensitivity of CZM parameters on simulated intergranular crack growth behavior in polycrystalline metallic microstructures.

Finally, Chapter 7 presents a discussion of the contribution and significance of the current research and suggests future directions in research that will need to be examined to fully develop a multiscale strategy for linking atomic-scale processes with macroscopic material failure.

Table of Contents

1. Overview of Multiscale Analysis Methods 1

1.1 Introduction 1

1.2 Multiscale modeling 2

1.2.1 Concurrent multiscale methods 3

1.2.1.1 The Macroscopic, Atomistic, Ab initio Dynamics method 5

1.2.1.2 The Finite Element-Atomistic method 6

1.2.1.3 The Coarse Grained Molecular Dynamics method 7

1.2.1.4 The Quasicontinuum method 7

1.2.1.5 The Bridging Domain method 9

1.2.1.6 The Coupled Atomistic/Discrete Dislocation method 10

1.2.1.7 The Equivalent Continuum model 12

1.2.2 Sequential multiscale methods 13

1.3 The current research into developing a multiscale analysis methodology 13

2. Molecular Dynamics Simulation 17

2.1 Introduction 17

2.2 Selected topics in molecular dynamics simulation 17

2.2.1 Atomic interactions 17

2.2.2 Statistical mechanics 21

2.2.3 Periodic boundary conditions 23

2.2.4 Atomistic and continuum strain and stress measures 25

2.2.5 Phonon damping 31

2.2.6 Molecular dynamics analysis of polycrystalline metals 34

2.2.7 Grain boundary description in polycrystalline metals 35

2.3 Molecular dynamics simulation of fracture 37
2.3.1 Introduction 37
2.3.2 The molecular dynamics model 38
2.3.3 The continuum model 44
2.3.4 Intergranular fracture along grain boundaries 46
2.3.4.1 The mechanisms of crack propagation along the Σ99 grain boundary by MD simulation 46
2.3.4.2 Rice and Tadmor-Hai criteria for twinning vs. cleavage at the crack tip 48
2.3.4.3 Plastic contribution to the stress field near the crack: MD – FEM comparison 50
2.4 Concluding remarks for Chapter 2 54

3. Coupling Molecular Dynamics and Finite Element Analyses 56

3.1 Introduction 56
3.2 The ESCM model 59
3.2.1 MD and FEM model components 60
3.2.2 MD/FE interface 61
3.2.3 Surface MD region 62
3.2.4 Phonon damping 64
3.2.5 MD-FEM coupling 66
3.3 Numerical verification of the ESCM 71
3.3.1 The simulation models 71
3.3.1.1 The MD model 72
3.3.1.2 The FEM model 73
3.3.2 Numerical test results and analyses 74
3.3.2.1 Verification of the surface tension and the Surface MD Region stiffness compensation 74
3.3.2.2 Simulation of the dynamics of the coupled MD-FEM system 78

3.3.2.3 Test for stress-strain continuity over the MD and the FEM regions: elastically deformed plate with a circular hole 80

3.3.2.4 Example of an edge crack simulation along a grain boundary in aluminum 84

3.4 Concluding remarks for Chapter 3.....86

3.A Appendix: ESCM model construction 88

3.B Appendix: Calculation of compensating forces 92

4. Cohesive Zone Modeling of Material Failure 98

4.1 Introduction.....98

4.2 General features of cohesive zone models.....100

4.3 Atomistic-based cohesive zone models 107

4.3.1 Determination of atomistic traction-displacement laws using cohesive zone volume elements.....111

4.3.2 CZM models for interfacial sliding.....120

4.4 Generalized representation of cohesive zone models 125

4.5 Remarks on the general characterization of GB CZM parameters 129

4.6 Concluding remarks for Chapter 4.....132

4.A Appendix: Formulation of a general representation for mixed-mode cohesive zone models 134

5. Decohesion Finite Element Formulations 141

5.1 Introduction.....141

5.2 Directional decohesion element formulation.....146

5.3 Concluding remarks for Chapter 5.....153

6. Illustration of the Developed Multiscale Methodology 155

6.1 Introduction.....155

6.2 Enhancement to the ESCM concurrent multiscale approach.....155

6.2.1 Crack propagation through a continuum-atomistic interface.....156

6.3 Simulation of intergranular failure in aluminum polycrystals.....160

6.3.1 Analysis of Mode I fracture in a 2-D bicrystal 161

6.3.2 Analysis of mixed-mode fracture in a 2-D polycrystal.....171

6.3.3 Analysis of general mixed-mode fracture in 3-D polycrystal models 174

6.4 Concluding remarks for Chapter 6.....180

7. Summary and Significance of the Current Research..... 182

References..... 186

List of Figures

1.1. General schematic of coupled atomistic/continuum regions 3

1.2. Hierarchy of models over length scales 4

1.3. Structure of MAAD coupling 5

1.4. FEAt model of a crack tip in an fcc crystal 6

1.5. Depiction of CG and MD regions in the CGMD approach 7

1.6. Repatoms used to define individual atoms and local continuum regions in the QC method 8

1.7. Application of bridging domain coupling method in 2D 9

1.8. Close-up of dislocation detection and near interface 10

1.9. Decomposition of coupled MD-FEM domain using linear superposition 11

1.10. Depiction of ECM and MD region in the MLPG approach to MD-FEM coupling 12

1.11. Multiscale analysis with cohesive zone models 14

2.1. 1^{st}, 2^{nd}, and 3^{rd} neighbors in [111] atomic projection of fcc aluminum crystal 20

2.2. Periodic boundary conditions. The center box (shaded) is shown along with its first periodic images (white) 23

2.3. Explode view of a carbon nanotube bundle cross-section 25

2.4. PBC-unit cell showing outside periodic image nanotubes in the (2,3)-plane and image atoms in the (1,2)-plane 25

2.5. Computational box for molecular dynamics simulations 27

2.6. Stress component definitions 28

2.7. Local atomic velocity superposition within MD domain partitions 32

2.8. a) Atomic positions in two adjacent grains separated by a {130}/<001> 37^{o}-tilt boundary. b) Superposed lattices showing coincident lattice sites marked as half-filled symbols indicating $\Sigma = 5$ 36

2.9. Grain boundary energy as a function of misorientation angle 36

2.10. Molecular-dynamics system before crack initiation representing the simulation set-up 38

2.11. Atomistic snapshot giving the crystallography and structure of the GB interface 39

2.12. The mesh of the finite element model with a built-in lenticular crack 45

2.13. MD snapshots of cracks which have propagated under four different initial hydrostatic stresses: σ = 3.5 (a), 3.75 (b), 4.0 (c) and 4.25 GPa (d) 47

2.14. Stress contours from the FEM model (a-c) and the corresponding atomistic stress maps (d-f) 52

2.15. Stress contours from the FEM model (a-c) and the corresponding stress maps (d-f) 53

3.1. Model topology used in the ESCM approach 59

3.2. Structure of the MD/FE interface 61

3.3. Forces within the Interface and Surface MD Regions. R_I are FEM reaction forces, f_s are the resultant surface region forces, and f_c are applied compensating forces 64

3.4. Flowchart summarizing the coupled analysis procedure 70

3.5. Model geometry of the test MD-FEM coupled system 71

3.6. Dependence of the pressure p_s caused by the surface tension of a circular MD domain of radius d_{MD} simulated with free surface boundary conditions. The slope is proportional to the surface energy per unit area γ 75

3.7. Evolution of the internal pressure of a circular MD system with and without surface tension compensation 76

3.8. Evolution of the longitudinal tensile σ_{xx} and transverse σ_{yy} stress components 77

3.9. Dynamic response of the coupled MD-FEM system under far-field homogeneous tensile strain ε_{xx} applied either instantaneously (black) or in five consecutive increments (gray) 79

3.10. Simulation of an open hole specimen. Comparison of the stress field for σ_{xx}, σ_{yy}, and σ_{xy} stress components of the coupled MD-FEM system (a, c, e) with a full three-dimensional anisotropic continuum FEM solution (b, d, f) 81

3.11. Stress profiles in the open hole specimen for σ_{xx} and σ_{yy} along (a) the x-axis and (b) the y-axis scanned through the center of the hole. The symbols represent the ESCM simulation data, while the full lines represent fully continuum FEM results For reference, the surface tension induced pressure p_s is also shown 83

3.12. ESCM simulation of an edge crack propagating along a <110>/Σ99 symmetric tilt grain boundary in Al at 2% far-field uniaxial strain 85

3.A1. Generation of MD model by equilibrating within a larger rectangular MD model under PBCs 89

3.A2. Flowchart summarizing the MD-FEM model construction 91

4.1. Fundamental fracture modes in solids 98

4.2. Bilinear cohesive zone model 101

4.3. Depiction of intrinsic and extrinsic CZMs.....104

4.4. Exploded view of a 3-D grain microstructure.....104

4.5. Interpolation of CZM components.....106

4.6. Atomic structure of Al-Si interface.....108

4.7. Atomistic derivation of a stress-strain relation during debonding of an Al-Si interface. The four snapshots above and below the plot show structural changes of the interface at different stages of debonding at the atomic level 109

4.8. Atomistic stress-strain relations for Al-Si, Al-Al, and Si-Si interfaces.....109

4.9. Schematic diagram of the slicing of the system volume in the MD simulation and defining the representative regions for extracting the parameters for the cohesive-zone interface elements in a continuum simulation.....112

4.10. Stress and opening profiles extracted along the crack growing for 123 ps in a system prestressed at 4.25 GPa hydrostatic load. The corresponding snapshot of the crack is shown at the bottom 114

4.11. Surface stress vs. crack opening curves $\sigma^s_{yy}(\lambda)$ characterizing the propagation of the cleavage tip in the $+x$ direction (a) and in the $-x$ direction (b) for three preloads.....117

4.12. Traction-displacement relationship $\sigma^s_{yy}(\lambda)$ and the corresponding work of separation $\Gamma(\lambda)$ for the case of 4.25 GPa prestress compared for the brittle ($+x$) and the twinning ($-x$) tip 118

4.13. Comparison between the brittle CZM derived using pure MD and coupled MD-FEM models 119

4.14. ESCM model under pure shear loading.....121

4.15. Initial configuration of GB subjected to shearing forces to induce sliding in the [7 7 10] direction.....122

4.16. Migration of GB and resulting lattice defects due to applied shear.....123

4.17. Resulting MD-derived CZM for Mode II sliding in the [7 7 10] direction 123

4.18. Final configuration of GB under Mode II sliding in the [1 1 0] direction.....124

4.19. MD-derived CZM for pure Mode II sliding in the [1 1 0] direction.....124

4.20. Hypothetical CZMs associated with fundamental fracture modes 125

4.21. Tabular description of a general piece-wise linear CZM shape 126

4.22. Stiffness definitions in an effective interpolated piece-wise linear mixed-mode CZM curve.....127

4.23. Coupling of Mode II sliding CZM with Mode I fracture.....128

4.24. Grain boundary energy as a function of misorientation angle.....131

5.1. Embedding decohesion elements along GBs to study microstructural fracture 142

5.2. Decohesion element cohesive surfaces 143

5.3. Direction-dependant crack growth behavior incorporated into decohesion finite element formulations 147

5.4. Geometric configuration of a crack with an intersecting slip plane 148

5.5. Relative opening displacements for Mode I and Mode II fracture in a 6-node quadratic decohesion element 151

5.6. Estimated direction of GB opening and sliding in mixed-mode fracture 152

6.1. Configuration of the simulation model for edge-crack propagation along a grain boundary in aluminum 156

6.2. CZVE elements along the crack path inside the inner MD region within the ESCM 157

6.3. Snapshots of the ESCM model configurations simulating an edge crack propagating along a GB in a bicrystal of aluminum with CZM elements along the GB interface 159

6.4. Stress map of σ_{yy} corresponding to the snapshots given in Figure 6.3 160

6.5. Possible bilinear traction-displacement relationships 161

6.6. Edge cracked tension models for Mode I opening 165

6.7. Assumed process zone in CZM representation 165

6.8. Cohesive zone models used in two series of parametric studies 166

6.9. Relative crack length vs. percent edge strain for CZM Series A 169

6.10. Relative crack length vs. percent edge strain for CZM Series B 170

6.11. Process zone vs. $1/\tau_{mx}$ for Series B and Process zone vs. G for Series A 171

6.12. Random microstructural model 171

6.13. Process of dominant microcrack formation in a polycrystal model using cohesive zone models 172

6.14. Parametric study of Mode I global stress/strain response in a polycrystal with brittle vs ductile GBs 174

6.15. Assumed symmetric tilt angles for GBs 175

6.16. Simulation of a triple junction showing different opening behavior with different assumed GB tilt angles using directional decohesion elements 176

6.17. Model of a 3-D 25-grain microstructure 177

6.18. Failure sequence in the 3-D polycrystal model 179

6.19. Stress-Strain curves for the 3-D polycrystal model 180

List of Tables

4.1. Various cohesive zone models and their parameters 102

6.1. CZM parameters used to simulate different relative elastic and plastic behavior at the crack tip in a bicrystal. Fracture toughness is a function of the increase in plasticity 167

6.2. CZM parameters defining brittle Mode I behavior at the 2-D crack tip 172

6.3 CZM parameters used to simulate different proportions of elastic and plastic Mode I opening behavior at the 2-D crack tip 173

6.4. CZM parameters defining GB properties in the triple junction model 176

6.5. CZM parameters used to simulate different relative elastic and plastic Mode I opening behavior at the 3-D crack tip 178

List of Abbreviations

BDM	: Bridging domain method
BVP	: Boundary value problem
CADD	: Coupled atomistic/discrete dislocation method
CGMD	: Coarse grained molecular dynamics method
CNA	: Common neighbor analysis
CZM	: Cohesive zone model
CZVE	: Cohesive zone volume element
DC	: Direct coupling
DFT	: Density functional theory
EAM	: Embedded atom method
ECM	Equivalent continuum model
ESCM	: Embedded statistical coupling method
FE	: Finite element
FEAt	: Finite element-atomistic method
FEM	: Finite element method
GB	: Grain boundary
IVC	: Interface volume cell
MAAD	: Macroscopic, atomistic, ab initio dynamics method
MD	: Molecular dynamics
MS	: Molecular statics
PBC	: Periodic boundary condition
QC	: Quasicontinuum method
SC	: Statistical coupling
SVC	: Surface volume cell
TB	: Tight binding

Chapter 1

Overview of Multiscale Analysis Methods

1.1 Introduction

Classical fracture mechanics is based on a continuum description of material domains and fracture behavior described in terms of empirical parameters (K_{IC}, J-R curves, CTOA, etc.). In contrast, the emerging field of nanomechanics is providing a new focus in the study of the mechanics of materials, particularly that of simulating fundamental atomic mechanisms involved in the initiation and evolution of damage and provides a more complete understanding of the physics of fracture. In metals, these atomic-scale processes include those leading to the creation of traction-free surfaces (e.g., atomic bond breakage) and permanent deformation (e.g., dislocations, twins, stacking faults). Multiscale analyses attempt to bridge length scales by providing different physics-based models that can appropriately represent damage mechanisms at each scale. At the nanoscale, either quantum mechanics (i.e., ab-initio, tight-binding (TB) or density-functional theory (DFT)) methods or classical molecular dynamics (MD) or molecular statics (MS) methods are used to simulate fundamental material processes using *first principles* in physics and provide an understanding of deformation and fracture processes at the atomistic level. These predictions of material behavior at nanometer length scales promise the development of physics-based 'bottom-up' multiscale analyses that can aid in understanding the evolution of failure mechanisms across length scales. However, modeling atomistic processes quickly becomes computationally intractable as the system size increases. With current computer technology, the computational demands of modeling suitable domain sizes (on the order of hundreds of atoms for quantum mechanics-based methods, and potentially billions of atoms for classical mechanics-based methods) and integrating the governing equations of state over sufficiently long time intervals, quickly reaches an upper bound for practical analyses. In contrast, continuum mechanics methods such as the finite element method (FEM) provide an

economical numerical representation of material behavior at length scales in which continuum assumptions apply. This strongly motivates the development of analytical multiscale methods to link macroscopic failure to the underlying atomic processes from which all material behavior originates.

1.2 Multiscale modeling

Multiscale analysis is a class of systematic methodologies that have been developed to relate material behavior over a range of length scales. Multiscale analyses attempt to bridge length scales by providing different physics-based models that can most appropriately represent damage mechanisms at each scale. In this approach, models that best simulate the relevant physics at lower length scales are united with models at larger length scales through information transfer involving averaging, homogenization, or superposition schemes. The ultimate success of this approach is dependent on the accuracy of data linkage and the intrinsic fidelity of the physical models used.

Multiscale methods may be generally classified as either sequential or concurrent [1-3]. Sequential modeling typically involves some form of averaging of physical parameters that can serve as initial conditions or provide calibrated material constants to another model which is analyzed separately. A desirable aspect of sequential methods is the uncoupling of length and time scales between independent material models. Concurrent multiscale analysis involves the simultaneous solution of strongly linked material models. A general schematic of the coupled atomic and continuum regions is depicted in Figure 1.1. In general, there exists a domain representing material at the atomic level and a domain that is simulated using a continuum representation such as FEM. An intermediate region involves an interface between these two different computational procedures and typically includes an overlap region of “pad” atoms/nodes in which different coupling schemes are used. Sequential methods are typically used for heterogeneous materials for which different constitutive laws are required at different length scales. The total material deformation, stress, and strain fields are decomposed into the sum of a coarse macro-component and a fine micro-component. The fine and

coarse fields are determined through separate analyses and are coupled via the summation used to obtain the solution for the total field [4-8]. A desirable aspect of sequential methods is the uncoupling of length and time scales between independent material models. The averaging or homogenization of information across length scales that is inherent to sequential multiscale methods is depicted in Figure 1.2 where a notional

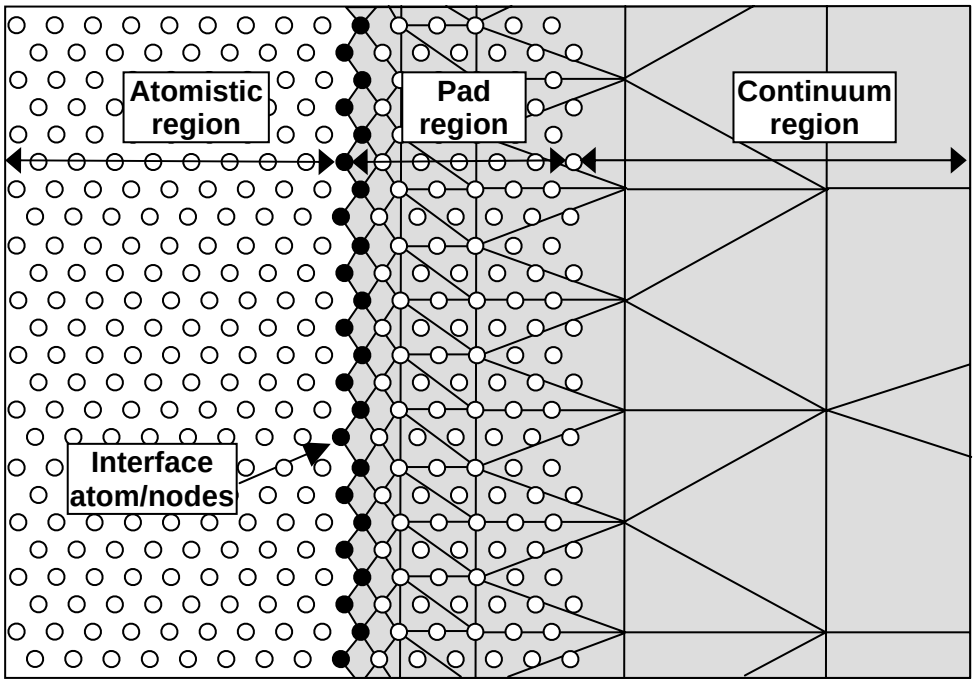

Figure 1.1. General schematic of coupled atomistic/continuum regions.

coupling is shown across domains representing characteristic features at the sub-atomic through structural scales.

1.2.1 Concurrent multiscale methods

Many concurrent multiscale methods have been developed over the past number of years. The common approach of the concurrent methods is to identify a small region of the simulated system where the representation of material is performed at the atomic level. This atomistic region is embedded into a larger surrounding region where the material is represented at the continuum level. In developing analytical approaches using

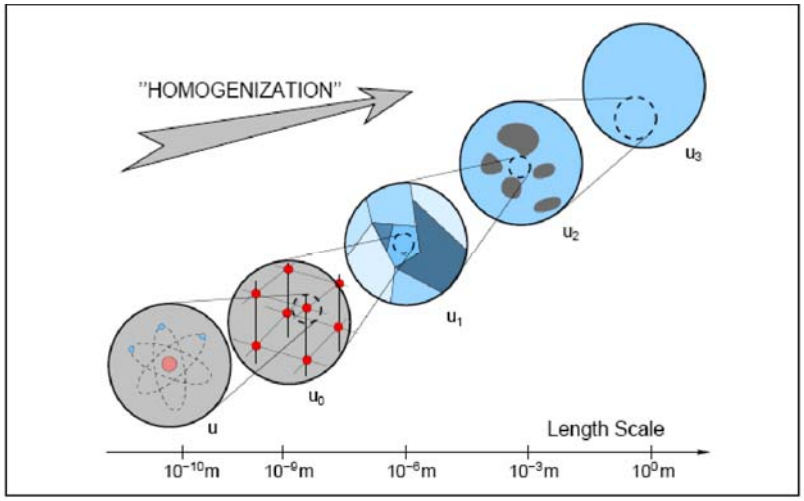

Figure 1.2. Hierarchy of models over length scales (From Oden et al. [9]).

this simulation paradigm, a primary concern has been the seamless coupling of forces and displacements between the different models at the interface between the two regions. The inherent mismatch between computational frameworks – atomistic (such as molecular-dynamics or molecular-statics) and continuum (such as finite element or finite difference) methods – and the differing representation of material properties, can lead to various numerical and theoretical difficulties. These difficulties will be highlighted in the discussion that follows.

In order to achieve a successful coupling, the usual approach is to refine the continuum representation (the FEM mesh or the finite difference grid) down to the atomic scale by superposing each node over an atom at the interface region. A general schematic of concurrently coupled atomic and continuum regions is depicted in Figure 1.1. In general, there exists a domain representing material at the atomic level and a domain that is simulated using a continuum representation. An intermediate region involves an interface between these two different computational procedures that typically includes an overlap region of “pad” atoms/nodes in which different coupling schemes are used. In this way, the atomistic degrees of freedom – position and momentum of each atom – are identified directly with the continuum degrees of freedom – nodal displacements and their derivatives. Several extensive reviews of concurrent methods have been presented in the literature [1,2,9]. While numerous variations on basic procedures for coupling atomistic

and continuum domains exist, only a handful have been well-developed and have gained a measure of widespread use. A brief review of these methods, representing the current state-of-the-art, follows.

1.2.1.1 The Macroscopic, Atomistic, Ab initio Dynamics method

The Macroscopic, Atomistic, Ab initio Dynamics (MAAD) procedure was developed by Broughton et al. [10], Abraham et al. [11-14], and Shen et al. [15,16] to simulate fracture by combining ab initio quantum analysis, molecular dynamics, and finite element continuum models. The ab initio analyses utilizes tight binding (TB) procedures to predict bond breakage at the crack tip, molecular dynamics (MD) based on empirical force potentials to model the crack wake and surrounding atomic lattice, and a finite element (FE) model to simulate the far-field material. A total Hamiltonian describes the dynamics of the system by combining Hamiltonians of the three separate regions and their interfaces. In this approach, the FEM nodes correspond in a one-to-one manner with the interface atoms of the MD region. Figure 1.3 shows the basic division of the overall simulation into regions governed by different computational methods.

Two significant issues have been raised regarding the MAAD approach. One is that the timestep used to integrate the governing equations in each of the three domains is

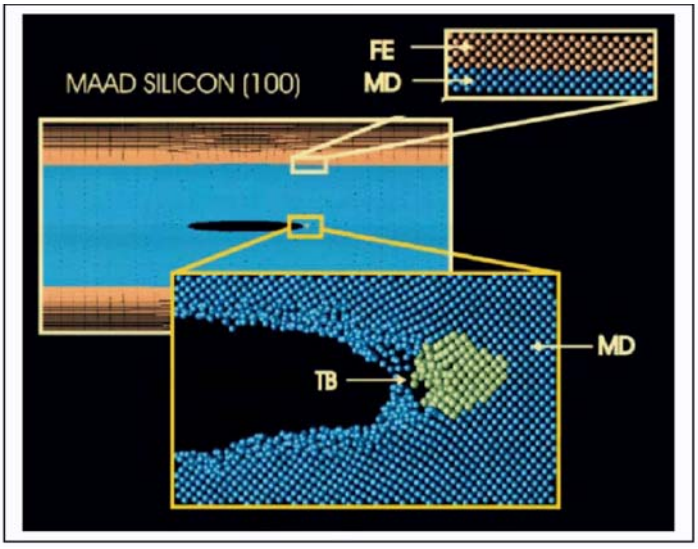

Figure 1.3. Structure of MAAD coupling. (From Buehler [17]).

equal to the smallest step required in any of them, causing a large increase in computational cost. Another issue regards the lack of damping that may be needed to remove spurious reflections at the interfaces between the three regions.

1.2.1.2 The Finite Element-Atomistic method

The Finite Element-Atomistic (FEAt) method developed by Kohlhoff et al. [18], Gumbsch and Beltz [19], and Gumbsch [20] is a methodology similar to MAAD that links atomistic representation to a continuum finite element field. Both FEAt and MAAD utilize a domain of "pad" atoms in the "handshaking" region of the MD-FEM interface in which individual atoms are directly linked to finite element nodes. These regions are shown in Figure 1.4. An interesting feature of FEAt is that non-local elasticity theory [21] is used in the pad (overlapping) region to describe the continuum representing the finite range of atomistic forces and can be considered as a continuation of the lattice. These approaches have been successfully applied to the problem of crack propagation but the direct atom to node linkage at the MD-FEM interface gives rise to undesirable phonon reflection.

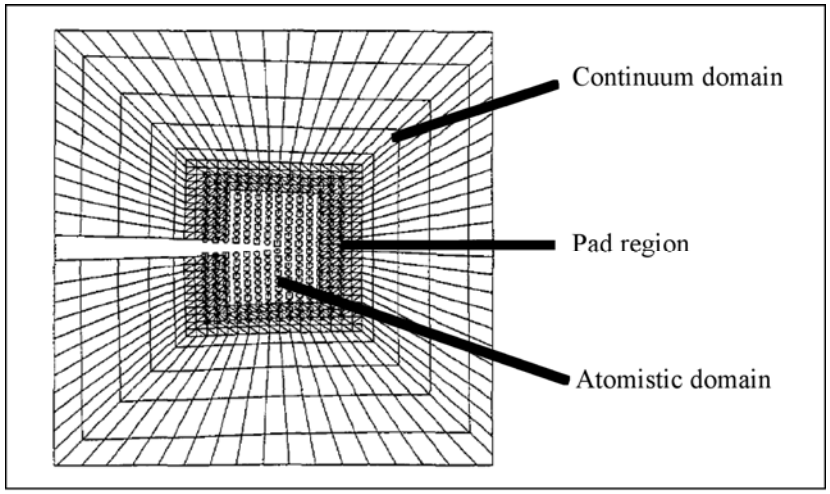

Figure 1.4. FEAt model of a crack tip in an fcc crystal. (From Gumbsh and Beltz [19]).

1.2.1.3 The Coarse Grained Molecular Dynamics method

A generalized formulation of conventional FEM utilizes FEM nodes superposed over the entire material domain to develop another computational scheme for atomistic-continuum coupling called Coarse Grained Molecular Dynamics (CGMD) developed by Rudd and Broughton [22,23]. In this approach, a refined region is defined in which atoms and nodes correspond in a one-to-one fashion and is denoted as the molecular dynamics region in Figure 1.5. Outside this domain, the finite element mesh is coarsened with individual nodes associated with many atoms. It is this coarse-grained (CG) finite element region that reduces the computational cost of representing the entire material domain. Thus, the MD region is solved using the integrated equations of motion for each atom, while the kinematics of the nodal degrees of freedom in the CG region are obtained using the equations of continuum FEM. A benefit of the CGMD method is that the interface between the MD and CG regions reduces spurious elastic wave scattering compared to other MD-FEM coupling methods. The refined MD and finite element CG regions are shown in Figure 1.5.

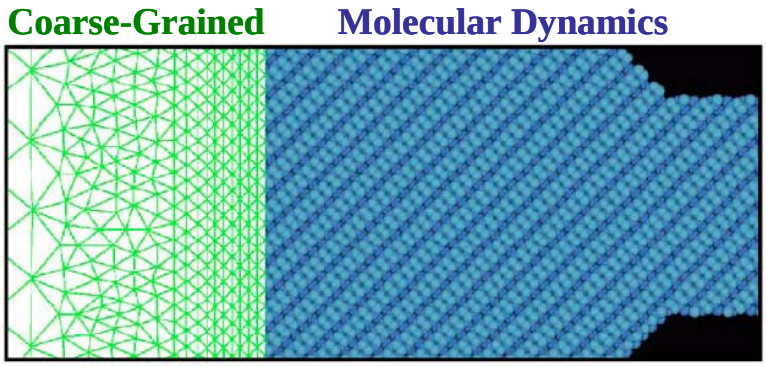

Figure 1.5. Depiction of CG and MD regions in the CGMD approach. (From Rudd and Broughton [23]).

1.2.1.4 The Quasicontinuum method

The Quasicontinuum (QC) method was originally formulated by Tadmor et al. [24] to provide a direct coupling of an atomistic region to a continuum domain. Additional

developments to the method are presented by Knap and Ortiz [25], Miller and Tadmor [26], and Sansoz et al. [27]. The QC method is based on a fully atomistic description of the material domain using the introduction of "representative atoms" or "repatoms". The repatoms have a dual role in defining either "nonlocal" individual atoms that are subjected to a force environment of neighboring atoms or "local" atoms that function similarly to continuum finite element nodes. Calculation of deformation gradients over local atomistic domains are performed and, if small, causes the application of the Cauchy-Born rule [28] to be performed in which kinematic constraints similar to finite element shape functions are enforced on clusters of atoms that are considered as a local continuum. The partitioning of the QC region into local continuum regions and MD domains is shown in Figure 1.6. Based on the Cauchy-Born rule, which assumes that, for small strains in a local domain, atoms in this domain follow the overall strain in the material, continuum regions utilize FEM shape functions over the domain, and material properties are obtained by a summation of the empirical potential function of the contained atoms. Remeshing is constantly performed to update the model to resolve atomic scale detail where needed and to redefine continuum atomic subdomains where deformation gradients are small and can be grouped to minimize computational cost. The method is commonly applied to 2D problems and, because of the direct one-to-one relation between repatoms, was originally restricted to zero Kelvin temperature states.

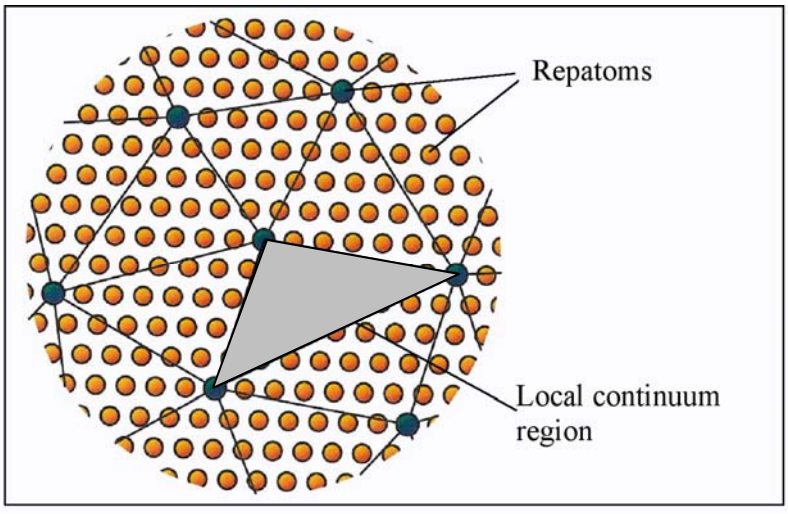

Figure 1.6. Repatoms used to define individual atoms and local continuum regions in the QC method. (From Knap and Ortiz [25]).

A finite temperature QC method has subsequently been developed [26,29]. The method offers a direct transition between atomistic and continuum fields and can effectively follow the evolution of atomistic mechanisms such as dislocation nucleation and crack propagation. However, special treatments are required to remove spurious "ghost forces" at the interface, to ameliorate exaggerated free-surface effects, and to account for finite temperature states. The QC method offers a general modeling technique and has been applied to simulate nanoindentation, fracture, dislocation motion, and interaction of grain boundaries.

1.2.1.5 The Bridging Domain method

Another representative concurrent coupling approach is the bridging domain method of Belytschko et al. [29] and Xiao et al. [30], and is based on an overlay approach in which MD and FEM representations are superposed in an interface region. This method relaxes the strict atom-node spatial correspondence required in many other methods by allowing interpolation of FEM nodal degrees of freedom to be associated with atomic displacements in the bridging domain. The bridging domain with molecular model – continuum model overlap is shown in Figure 1.7. The method explicitly develops coupled energy Hamiltonians for the atomistic and continuum regions and enforces compatibility in the bridging domain using Lagrange multipliers. Dynamic behavior is simulated through an explicit algorithm that includes a multiple time-step scheme. This approach also avoids spurious wave reflection at the MD/FEM interface without introducing damping or filtering procedures.

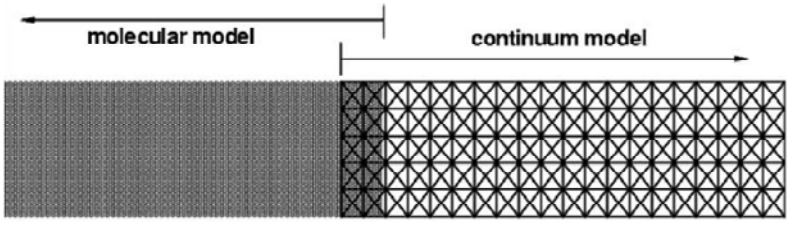

Figure 1.7. Application of bridging domain coupling method in 2D. (From Xiao and Belytschko [30]).

1.2.1.6 The Coupled Atomistic/Discrete Dislocation method

The Coupled Atomistic/Discrete Dislocation (CADD) method developed by Shilkrot et al. [31,32], Curtin and Miller [33], Shilkrot et al. [34], and Shiari et al. [35] is specifically designed for problems in which dislocation formation and interaction are the physical mechanisms of interest and persist over long distances. The coupling at the interface is similar to the MAAD and FEAt methods in that it uses a pad region in which "handshaking" between atomic and continuum degrees of freedom occur. CADD is formulated to identify the type of dislocation approaching the MD/FEM interface from the atomic domain and then pass the dislocation into a surrounding linear elastic continuum. Passing the dislocation involves adding both a dislocation to the continuum and a negative image of the dislocation into the atomistic domain to eliminate the original dislocation. A detection band is created near the MD-FEM interface to determine the type of dislocation entering the continuum (eg., an edge or screw dislocation). This detection scheme is shown in Figure 1.8 where, for 2D dislocations, active slip planes are separated by relative angles of $\pi/3$.

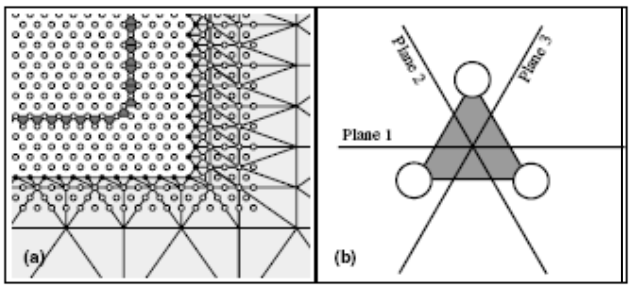

Figure 1.8. Close-up of dislocation detection and near interface.
(From Shilkrot et al. [34]).

The continuum is assumed linear elastic such that a superposition can be made to decompose the continuum into an infinite domain that contains the long-range singular dislocation stress fields represented by dislocation dynamics methods and a finite domain region that contains smooth displacement fields represented by FEM. The decomposition of the coupled MD-FEM domain in CAAD is shown in Figure 1.9 with (1) depicting the infinite continuum region, (2) showing the bounded region defined by finite elements,

and (3) illustrating the purely atomistic region. The infinite continuum domain represents the dislocations as superposed analytic solutions.

This method directly addresses the representation of discrete dislocation plasticity in a continuum field using established dislocation dynamics (DD) methods [36]. Because

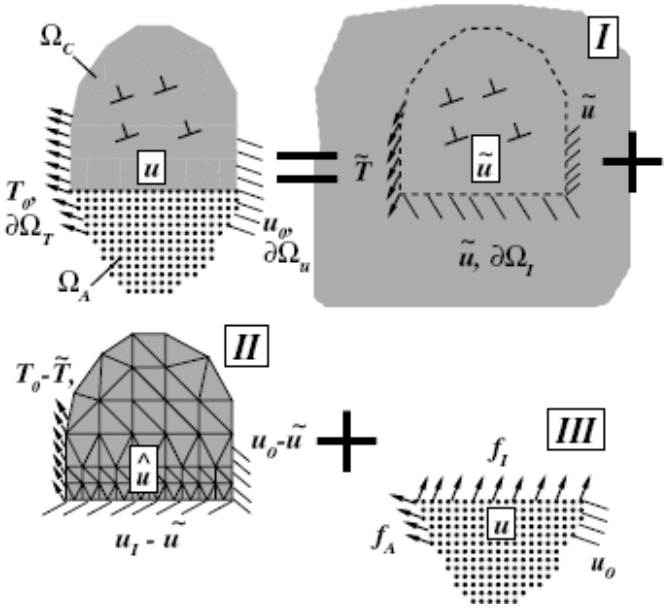

Figure 1.9. Decomposition of coupled MD-FEM domain using linear superposition. (From Shilkrot et al. [34]).

the dislocations are represented analytically, a computationally demanding full atomic simulation is not required, yielding a significant improvement in modeling efficiency. The transition between the atomic and continuum finite element domains utilizes a one-to-one node-atom linking that directly ties the interface atoms to the nodes in the continuum. An extension of the atomic region into the continuum is assumed in which pad atoms are superposed with continuum elements and are connected to nodal displacements. These atoms minimize the effect of the free surface on the interface atoms but contribute a modeling error by introducing nonphysical stiffness along the interface. CADD is currently restricted to simulating dislocations in two dimensions.

1.2.1.7 The Equivalent Continuum Model

A combined MD and Equivalent Continuum Model (ECM) method has been developed by Shen and Atluri [16], which is similar to the Quasi-continuum methods, but uses the meshless local Petrov-Galerkin (MLPG) representation to link the MD and ECM regions. In general, meshless methods are developed to overcome some of the disadvantages of the finite element method, such as the need to interpolate discontinuous secondary variables across interelement boundaries and the need for remeshing in large deformation problems. The Cauchy-Born hypothesis is applied in the ECM region for determining the elastic properties of the continuum from the atomistic description of the system. The ECM and MD regions are depicted in Figure 1.10.

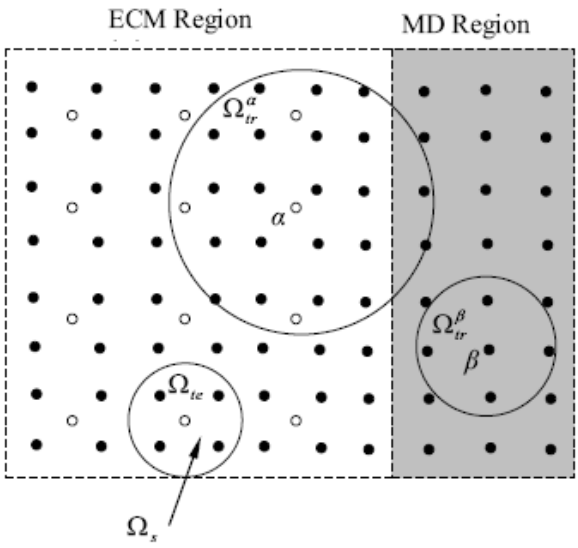

Figure 1.10. Depiction of ECM and MD region in the MLPG approach to MD-FEM coupling. (From Shen and Atluri [16]).

As shown in Figure 1.10, in the MD region, the solid points represent atoms, while in the ECM region, the solid points represent atoms and the open points represent nodes used in the MLPG method. Thus, in the ECM region, atoms and nodes do not have to be coincident. The ECM method has been demonstrated in one-dimensional chain models and in the two-dimensional analysis of graphene sheets.

1.2.2 Sequential multiscale methods

Sequential – or "hierarchical" - methods are typically used for heterogeneous materials for which different constitutive laws are required at different length scales. Some approaches treat the total material deformation and stress and strain fields decomposed into the sum of a coarse macro-component and a fine micro-component. The fine and coarse fields are determined through separate analyses and are coupled via the summation used to obtain the solution for the total field [4-6,8,37]. Another approach, which is utilized in the present work, utilizes the concept of cohesive zone models (CZM) using averaged representations of atomistic deformation processes at lower dimensional scales to simulate material behavior at larger length scales.

The notional flow of sequential coupling that utilizes CZMs to carry information of microscopic failure mechanisms to predict damage progression at larger length scales is depicted in Figure 1.11. Hitherto, the properties of the CZM have been determined empirically or heuristically and mixed mode fracture has been limited to empirical relationships that have been applied at all length scales. In Figure 1.11, CZMs provide the critical transition between inherently atomistic and inherently continuum representations. Because of their importance and pervasive use in sequential multiscale analysis, the sequential coupling methodology presented in the current research will focus on CZM-based methods.

1.3 The current research into developing a multiscale analysis methodology

The methodology developed in the current research utilizes a combined concurrent and sequential approach towards performing multiscale analysis. A new concurrent approach is developed to link an embedded MD region with a surrounding FEM domain that functions to provide the proper elastic response under far-field applied boundary conditions. The results using the MD analysis are then cast into CZMs that are subsequently used in a sequential multiscale analysis of metallic polycrystals.

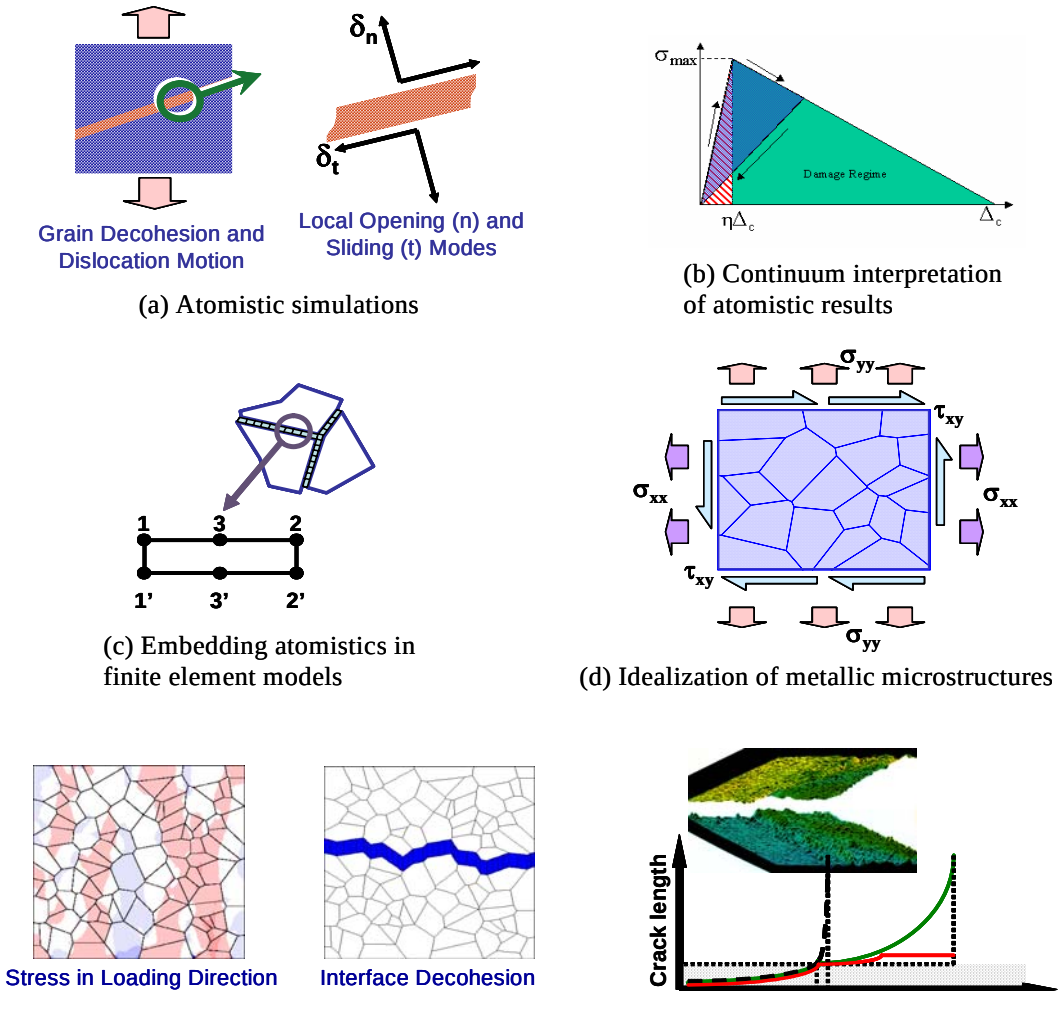

Figure 1.11. Multiscale analysis with cohesive zone models.

Atomistic simulation using MD is used to characterize damage processes in aluminum polycrystals. These damage mechanisms include the physical processes that govern dislocation formation and interaction that, in turn, lead to intergranular crack initiation and propagation in metallic microstructures. In the present research, intergranular fracture along grain boundaries (GBs) is emphasized. Determination of characteristic CZMs are made for Mode I fracture and Mode II sliding. These CZMs represent material behavior in the form of traction-displacement relationships based on ensemble averages obtained from MD analyses. An additional aspect of fracture along GBs involves slip planes in the

adjacent grains that may be activated in dislocation emission depending on crystallographic orientation. This orientation-dependent activation has the effect of causing intergranular fracture to exhibit either a ductile or brittle propagation behavior. For meaningful simulation of GB fracture at larger length scales, this effect must be considered.

A concurrent multiscale procedure is used to reduce the kinematic degrees of freedom required to represent the entire material domain. In the region of fracture nucleation and propagation, a complete atomistic MD representation is used. In regions removed from the nonlinear processes, where the material exhibits small deformation gradients, a continuum finite element method (FEM) representation is used. To achieve this linkage between simulation approaches, a unique statistical MD-FEM coupling procedure is developed. This methodology improves on current coupling approaches by eliminating the requirement that the finite element discretization be scaled down to atomic dimensions at the atomic-continuum interface. Using a statistics-based coupling scheme, atomic displacement averages over volume domains are linked with finite element degrees of freedom along the interface thus allowing an immediate scale-up of domain lengths and a further reduction in kinematic unknowns to describe the behavior of the complete material domain.

A sequential multiscale modeling strategy is subsequently developed in which the results of atomistic MD simulation of physical behavior at the nanoscale are mapped into CZMs for continuum FEM representation of metallic polycrystals. Once the traction-displacement relationships from MD are known, they can be used to define specialized ‘decohesion’ elements that can be placed along all possible fracture interfaces in a finite element mesh. Finite element simulations can then be used to study the failure properties of the material at larger scales. The methodology is very generic and can be used for any interface that is subjected to fracture provided that the atomistic simulation captures all relevant mechanisms. A new formulation of a directional decohesion finite element is made to incorporate different directional growth characteristics depending on the surrounding crystallographic orientation and crack opening direction induced by far-field

loading. In addition, arbitrary shape of individual CZMs is allowed by replacing fixed functional forms with generically defined tabular entries. It is anticipated that this research will make a significant contribution to the development of multiscale analysis methods for polycrystalline materials. The overall scheme of the developed multiscale analysis methodology is depicted in Figure 1.11.

Chapter 2

Molecular Dynamics Simulation

2.1 Introduction

The field of molecular dynamics has developed into a sophisticated analysis methodology for simulating atomic-scale processes of different material types (see Haile [38] and Allen and Tildesley [39]). Methods of MD provide a means of simulating those processes involved in material failure such as void nucleation and dislocation formation and interaction that form the foundation of a 'bottom-up' multiscale analysis methodology.

Section 2.2 will provide an overview of MD methods as background. Section 2.3 will discuss an MD study of an intergranular crack that demonstrates a directional dependence on how the crack propagates, namely in a brittle or ductile manner. This chapter ends with a discussion of limitations in using a purely MD representation which motivated the development of a new concurrent coupling method that is fully described in Chapter 3.

2.2 Selected topics in molecular dynamics simulation

The purpose of this section is to provide a background for references to various specific MD methods utilized in the simulation of atomic scale fracture as will be discussed beginning in Section 2.3.

2.2.1 Atomic interactions

Molecular dynamics simulations represent the behavior of individual atoms as point masses that influence neighboring atoms through calculated force fields. The level of atomic description varies tremendously. The most refined description utilizes quantum theory that can be applied using well known physical constants such as the velocity of light, values for the masses and charges of nuclear particles, and differential relationships

to directly calculate molecular properties and geometries. This formalism is referred to as ab initio (from first principles) quantum mechanics. The computational demands of this representation are high, and only small sets of atoms can be simulated. For larger atomic aggregates, empirical and semi-empirical potential functions have been developed to approximate atomic force fields. These potential functions can approximately account for quantum interactions between electron shells and represent physical properties of the atoms being simulated, such as elastic constants and lattice parameters, through fitting parameters [40]. Depending on the atomic system being studied, pair or many-body potentials have been developed to provide the correct interaction behavior while minimizing computational expense. This approach to MD replaces quantum mechanics with classical Newtonian mechanics to predict the trajectories of individual atoms. Newton's Second Law is expressed as

$$\boldsymbol{F}_{\mathrm{i}} = m_{\mathrm{i}}\,\boldsymbol{a}_{\mathrm{i}} \tag{2.1}$$

for each atom, i, in a system constituted by N atoms. Here, m_{i} is the atomic mass, $\boldsymbol{a}_{\mathrm{i}}$ is the acceleration vector, and $\boldsymbol{F}_i$ is the resultant force acting on the i^{th} atom due to the interactions with other neighboring atoms. The force can also be expressed as the gradient of the potential energy, V, as

$$\boldsymbol{F}_{\mathrm{i}} = -\nabla V \tag{2.2}$$

The simulation is performed by numerically integrating the equations of motion over small time steps (usually 10^{-15} sec or 1 fs). Various integration rules can be applied to compute the velocities of the atoms from the forces and atom locations. For example, a simple and popular integration scheme is the Velocity Verlet algorithm developed by Swope et al. [41] is given by

$$\begin{aligned} \boldsymbol{r}_{\mathrm{i}}(t+\Delta t) &= \boldsymbol{r}_{\mathrm{i}}(t) + \boldsymbol{v}_{\mathrm{i}}(t)\Delta t + \frac{1}{2}\boldsymbol{a}_{\mathrm{i}}(t)\Delta t^2 \\ \boldsymbol{v}_{\mathrm{i}}(t+\Delta t) &= \boldsymbol{v}_{\mathrm{i}}(t) + \frac{1}{2}\left[\boldsymbol{a}_{\mathrm{i}}(t) + \boldsymbol{a}_{\mathrm{i}}(t+\Delta t)\right]\Delta t \end{aligned} \tag{2.3}$$

where the algorithm yields new positions, $\boldsymbol{r}_i(t+\Delta t)$, and velocities, $\boldsymbol{v}_i(t+\Delta t)$, using known values at time t and the current acceleration calculated from the force potential as $\boldsymbol{a}_i(t+\Delta t) = -\nabla V[\boldsymbol{r}_i(t+\Delta t)]/m_i$.

These values then provide the trajectories, or time dependent locations, for each atom. In the context of molecular dynamics, Newton's Second Law may be expressed as

$$m_i \frac{d\boldsymbol{v}_i}{d\tau} = \sum_j F_2(\boldsymbol{r}_i, \boldsymbol{r}_j) + \sum_j \sum_k F_3(\boldsymbol{r}_i, \boldsymbol{r}_j, \boldsymbol{r}_k) + \cdots \tag{2.4}$$

and

$$\frac{d\boldsymbol{r}_i}{d\tau} = \boldsymbol{v}_i \tag{2.5}$$

where m_i is the mass of atom i, $\boldsymbol{r}_i$ and $\boldsymbol{v}_i$ are the position and velocity vectors associated with the i^{th} atom, respectively, τ is the time, and F_2 and F_3 are pair and three-body force interactions of atoms surrounding the i^{th} atom, respectively.

Pair potentials are the simplest way to model the interaction of two atoms. Among the best known is the Lennard-Jones potential [42] for non-bonding interactions given by

$$\Phi = 4\varepsilon\left[\left(\frac{\sigma}{r_{ij}}\right)^{12} - \left(\frac{\sigma}{r_{ij}}\right)^{6}\right] \tag{2.6}$$

where ε is the depth of the energy well, σ is the van der Waals radius, and r_{ij} is the separation distance between the i^{th} and j^{th} atoms in a pair. The r_{ij}^{-6} term represents the attractive contribution to the van der Waals forces between neutral atoms. The other component of the van der Waals interactions mimics the Coulomb interaction of the nuclei and the Pauli repulsion between overlapping electron clouds and is modeled by the short-ranged r_{ij}^{-12} term.

For metals, simple pair potentials are inadequate to describe the distributed electronic environment of each atom. Figure 2.1 depicts the neighborhood of an atom in fcc aluminum. For any atom, the outer shell of electrons is loosely held and becomes delocalized within the surrounding neighborhood of atoms and thus forms a 'gas' of electrons spread throughout the entire lattice. To better represent force interactions within metallically bonded lattices, a potential containing an additional 'embedding' term known as the Embedded Atom Model (EAM) has been developed by Daw and Baskes [43] (see also Daw et al. [44]). The form of EAM contains two contributions to the potential energy, E, of the whole system made up by N particles. The potential may be expressed as

$$E = \sum_i G_i\left(\sum_{j\neq i}\rho_j^a\left(r_{ij}\right)\right) + \frac{1}{2}\sum_{i,j\,(j\neq i)}U_{ij}\left(r_{ij}\right) \tag{2.7}$$

where G_i is the embedding energy as a function of the local electron density, ρ_j^a is the spherically average local electron density, U_{ij} is an atom-pair interaction term, and r_{ij} is the distance between atoms i and j. EAM has proven to be an accurate representation of the atomic force environment for atoms in a metallic lattice.

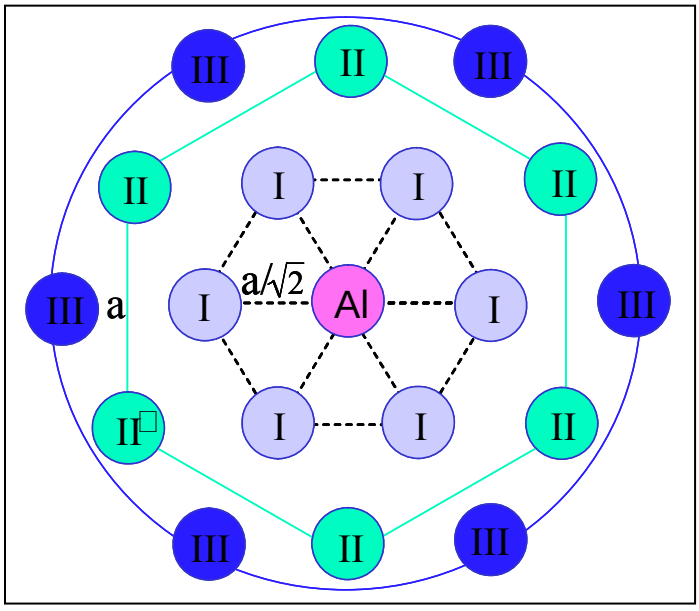

Figure 2.1. 1st, 2nd, and 3rd neighbors in [111] atomic projection of fcc aluminum crystal.

2.2.2 Statistical mechanics

In a molecular dynamics simulation, macroscopic properties of a system may be obtained through microscopic simulations, such as for example, to examine the energetics and mechanisms of conformational change. The connection between microscopic simulations and macroscopic properties is made via statistical mechanics that provides the rigorous mathematical expressions that relate macroscopic properties to the distribution and motion of the atoms and molecules of an N-body system. Molecular dynamics simulations provide the means to solve the equations of motion of the particles to study both thermodynamic properties and/or time dependent (kinetic) phenomena.

Statistical mechanics represents macroscopic systems from a molecular point of view [45]. The goal is to understand and to predict macroscopic phenomena from the properties of individual molecules making up the system. In order to connect the macroscopic system to the microscopic system, time independent statistical averages are often introduced.

The thermodynamic state of a system is usually defined by a small set of parameters, for example, the temperature, T, the pressure, P, and the number of particles, N. Other thermodynamic properties may be derived from the equations of state and other fundamental thermodynamic equations. The mechanical or microscopic state of a system is defined by the atomic positions, q, and momenta, p; these can also be considered as coordinates in a multidimensional space called phase space. For a system of N particles, this space has $6N$ dimensions. A single point in phase space, denoted by G, describes the state of the system. An ensemble is a collection of points in phase space satisfying the conditions of a particular thermodynamic state. A molecular dynamics simulation generates a sequence of points in phase space as a function of time; these points belong to the same ensemble, and they correspond to the different configurations of the system and their respective momenta. An ensemble is a collection of all possible systems that have different microscopic states but have an identical macroscopic or thermodynamic state.

Different ensembles exist with characteristics that should match the physical process being modeled:

- Microcanonical ensemble (*NVE*): The thermodynamic state characterized by a fixed number of atoms, *N*, a fixed volume, *V*, and a fixed energy, *E*. This corresponds to an isolated system.
- Canonical Ensemble (*NVT*): This is a collection of all systems whose thermodynamic state is characterized by a fixed number of atoms, *N*, a fixed volume, *V*, and a fixed temperature, *T*.
- Isobaric-Isothermal Ensemble (*NPT*): This ensemble is characterized by a fixed number of atoms, *N*, a fixed pressure, *P*, and a fixed temperature, *T*.
- Grand Canonical Ensemble (*mVT*): The thermodynamic state for this ensemble is characterized by a fixed chemical potential, *m*, a fixed volume, *V*, and a fixed temperature, *T*.

For example, an experiment is usually made on a macroscopic sample that contains an extremely large number of atoms or molecules sampling an enormous number of conformations. In statistical mechanics, averages corresponding to experimental observables are defined in terms of ensemble averages. An ensemble average is taken over a large number of replicas of the system considered simultaneously. The ensemble average is given by

$$\langle A \rangle_{ensemble} = \frac{\iint A(p^n, q^n)\rho(p^n, q^n)dp^n dq^n}{\iint \rho(p^n, q^n)dp^n dq^n} \tag{2.8}$$

where $A(p^n, q^n)$ is the observable of interest in the n^{th} system state and is expressed as a function of the momenta, p, and the separation distances, q, of the system. $\rho(p^n,q^n)$ is the distribution of the observable and is individually integrated in the numerator of Equation (2.8) as a normalizing factor. The integrations are performed over all possible variations

of q and p. Examples of properties that can be calculated as ensemble averages include elastic properties, temperature, pressure, and density.

2.2.3 Periodic boundary conditions

MD analyses are typically performed using a triclinic computational box that contains the atomic system. The atoms that lie within the cut-off radius of their atomic force potential from the box surface will experience different degrees of surface effects that in many cases are undesirable. To simulate an infinite system in which all atoms experience the same force field environment, periodic boundary conditions (PBCs) are imposed. Periodic boundaries are imposed by assuming that the computational box is surrounded by an infinite number of identical systems, as shown in Figure 2.2. In the figure, the circle around atom 1 has a radius equal to half of the shaded box side dimension while the box encompasses the nearest periodic image of each of the other atoms. In the course of the simulation, the atoms in each of the boxes move in the same way. Hence, if an atom leaves the simulation box at one side, an identical atom enters the box at the other.

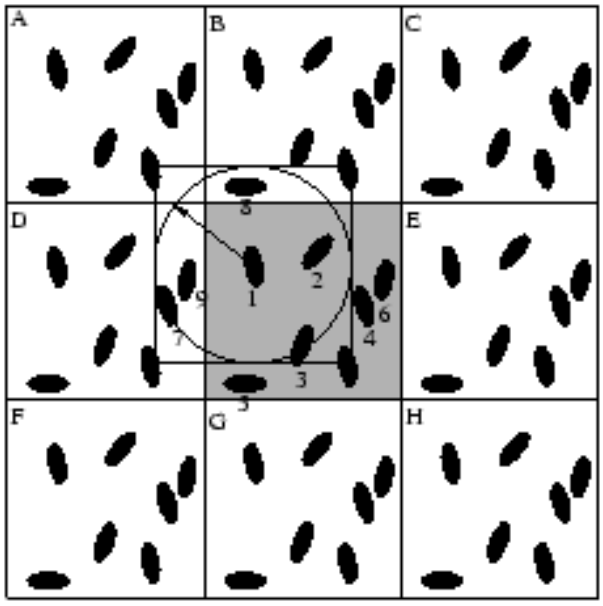

Figure 2.2 Periodic boundary conditions. The center box (shaded) is shown along with its first periodic images (white).

Periodic boundary conditions are usually used in conjunction with the minimum image convention for short-ranged forces. Here we only consider interactions between each atom and the closest periodic image of its neighbors. Short-ranged forces are often truncated to increase computational efficiency. For consistency with the minimum image convention, this cut-off distance must be less than or equal to half the box length.

Periodic boundary conditions can sometimes have an effect on the system under consideration. This is especially pronounced for small system sizes and for properties with a large long-range contribution, such as light scattering factors. They also inhibit long wavelength fluctuations that are important near phase transitions. However, they have little effect on equilibrium properties. The most commonly shaped simulation cell is cubic or triclinic. It is also possible to use cells of other shapes, such as the rhombic dodecahedron or the truncated octahedron. For studying surfaces, it is common to retain periodicity in two dimensions, while discarding it in the direction perpendicular to the surface.

For example, the transverse mechanical properties of a carbon nanotube bundle were obtained by Saether et al. [46] and Saether [47] utilizing periodic conditions to simulate an infinite unit cell system. Figure 2.3 shows an exploded view of an idealized nanotube bundle. Two views of the 3-D unit cell are depicted in Figure 2.4. Each nanotube interacted with other nearest-neighbor nanotubes through nonbonding forces as expressed by the Lennard-Jones potential, which is indicated by arrows in Figure 2.4a.

More complex boundary conditions have been developed to couple discrete atomistic domains with continuum finite element representations. This coupling of computational domains can be performed to extend the complete material domain with only the region of interest modeled down to the atomic level with far-field boundary conditions effectively represented. This minimizes the computational cost of performing large-scale simulations.

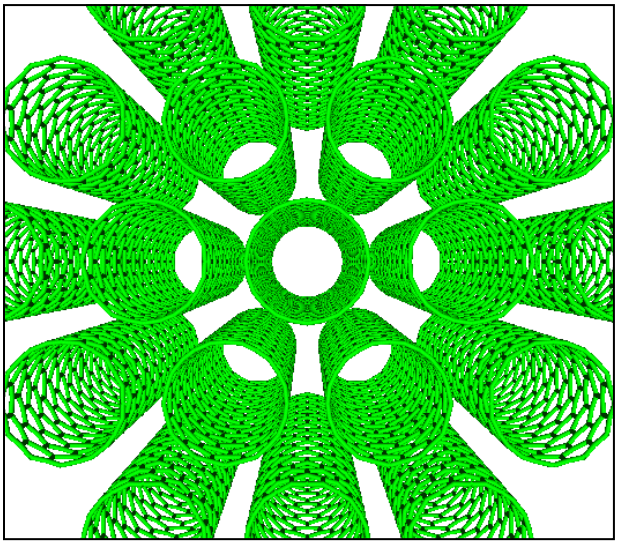

Figure 2.3. Explode view of a carbon nanotube bundle cross-section. (From Saether et al. [46]).

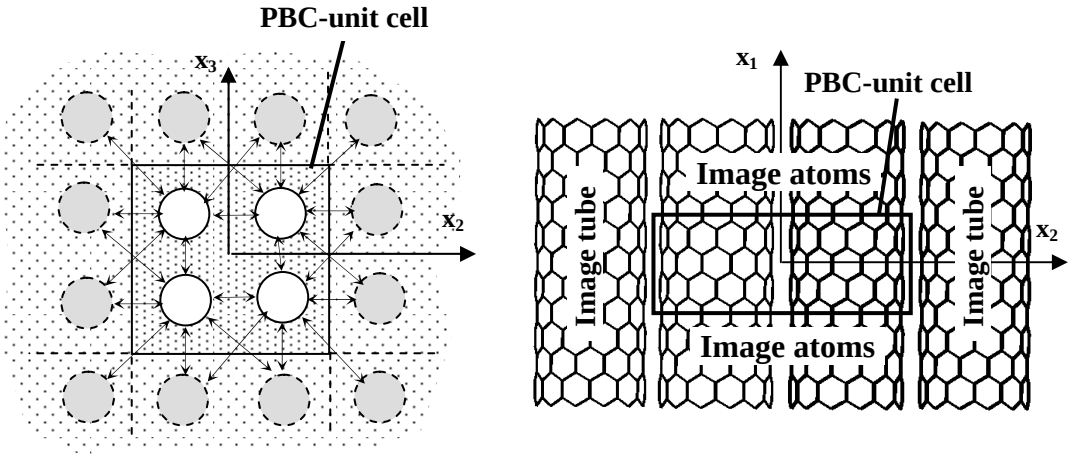

a) (2,3)-plane section b) (1,2)-plane section

Figure 2.4. PBC-unit cell showing outside periodic image nanotubes in the (2,3)-plane and image atoms in the (1,2)-plane. (From Saether et al. [46]).

2.2.4 Atomistic and continuum strain and stress measures

Atomic motion is only constrained by the energy barriers caused by force-field interactions with surrounding atoms and the presence of fixed boundaries. Atomic motion

is characterized by discrete trajectories that are modified by force interactions over spatial distances. A continuum domain, however, assumes a connected field of infinitesimal material particles that exhibit deformation fields that are continuous for a simply-connected domain. For various motions of atomic aggregates, those resulting in permanent lattice rearrangements such as in dislocation formation, continuum representations must resort to Eulerian fluid descriptions that become plastic flow representations to approximate the deformation state. Strain states may be described, however, using either the current or reference state.

The motion of material particles in a continuum gives rise to deformations that are described by a displacement vector $\boldsymbol{u}(x_i)$ and the associated deformation gradient given by

$$\boldsymbol{F} = \boldsymbol{u}\nabla \tag{2.9}$$

The Jacobian is given by the third invariant of the deformation gradient tensor as

$$\boldsymbol{J} = \det(\boldsymbol{F}) \tag{2.10}$$

In a continuum, the mapping function between deformation states can be applied to a reference position vector anywhere within the domain, and maps it to some new value in the continuous deformed configuration. For a material particle assemblage, the position vectors can only take on discrete values corresponding to particle positions for both the reference and deformed configurations.

Strain definitions are purely geometrical descriptions and pose little difficulty in mapping between discrete and continuous fields. Analogous strain measures may be infinitesimal or finite and may be defined in a Lagrangian sense with respect to a reference initial configuration or in an Eulerian manner with respect to a current deformed state.

Strain states are imposed on the system through application of a procedure originally developed by Parrinello and Rahman [48]. The computational volume, depicted in Figure 2.5, is defined by three vectors, $\vec{a}$, $\vec{b}$, and $\vec{c}$. The geometry of the box is specified by

$$[h] = [\vec{a}\ \vec{b}\ \vec{c}] \tag{2.11}$$

For convenience, the matrix $\boldsymbol{G}$ is defined as:

$$[G] = [h]^{T}[h] \tag{2.12}$$

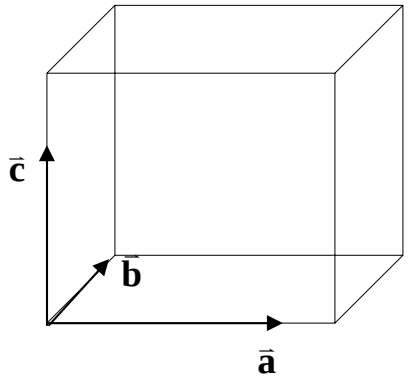

Figure 2.5. Computational box for molecular dynamics simulations.

If $\boldsymbol{h_o}$ is the initial geometry of the computational box, strains may be imposed to the system by relating altered box dimensions, $\boldsymbol{h}$, to components of the Green-Lagrange strain tensor as

$$\begin{aligned} \varepsilon_{\lambda\mu} &= \frac{1}{2}\left(\frac{\partial u_\lambda}{\partial x_\mu} + \frac{\partial u_\mu}{\partial x_\lambda} + \sum \frac{\partial u_\nu}{\partial x_\mu}\frac{\partial u_\nu}{\partial x_\lambda} \right) \\ &= \frac{1}{2}\left([h_o]^{-T}[G][h_o]^{-1} - \mathrm{I} \right) \end{aligned} \tag{2.13}$$

Strain components written explicitly in terms of the geometry are given by

$$\varepsilon_{ii} = \frac{\left(h_{ii} - h_{o,ii}\right)}{h_{o,ii}}$$
$$\varepsilon_{\substack{ij \\ i \neq j}} = \frac{1}{2}\left(\frac{h_{ij}}{h_{o,jj}} + \frac{h_{ji}}{h_{o,ii}}\right) \tag{2.14}$$

The concept of stress is generally a much more difficult quantity to define in atomistic systems and to compare with continuum stress definitions. Stress measures combine both force and deformation states using assumed reference configurations. This can lead to disparities when mapping between atomic and continuum fields. In continuum mechanics, the Cauchy stress tensor completely characterizes the internal forces acting in a deformed solid. The physical significance of the components of the stress tensor is illustrated in Figure 2.6. σ_{ij} represents the i^{th} component of traction acting on a plane with normal in the e_j direction. The Cauchy stress is the most physically meaningful measure of internal force distribution. This stress measure represents force per unit area of the deformed solid and is commonly referred to as the 'true stress' [49-51]. Consequently, to define these stress components one must know not only what the deformed solid looks like, but also what it looked like before deformation. Several alternative stress measures have been defined for small deformations that define forces as acting on the undeformed solid. These alternative stress definitions are briefly described.

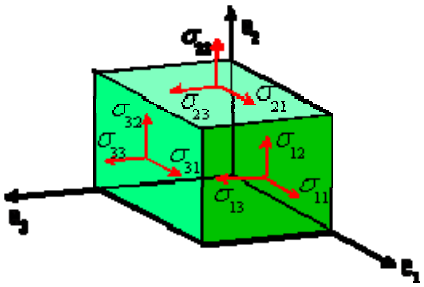

Figure 2.6. Stress component definitions.

The Kirchhoff stress has no physical significance and is related to Cauchy stresses as

$$\boldsymbol{\tau} = \boldsymbol{J}\,\boldsymbol{\sigma} \tag{2.15}$$

The nominal or First Piola-Kirchhoff stress can be regarded as the internal force per unit undeformed area acting within a solid and is given by

$$\boldsymbol{\tau} = \boldsymbol{J}\,\boldsymbol{F}^{-1}\boldsymbol{\sigma} \tag{2.16}$$

The material or Second Piola-Kirchhoff stress can also be visualized as force per unit undeformed area, except that the forces are regarded as acting on the undeformed solid rather than on the deformed solid. This stress measure is given by

$$\boldsymbol{\tau} = \boldsymbol{J}\,\boldsymbol{F}^{-1}\boldsymbol{\sigma}\,\boldsymbol{F}^{-T} \tag{2.17}$$

These different stress measures have different physical interpretations. The Cauchy stress is the most precise physical measure of internal force distribution – it is the force per unit area acting inside the deformed solid. The other stress measures are best described as generalized forces within a Lagrangean mechanics framework, which are work-conjugate to particular strain measures. This implies that the stress measure multiplied by the time derivative of the strain measure yields the rate of work done by the forces. The Cauchy and Kirchhoff stress definitions are not conjugate to any convenient strain measure. This is the primary reason for the use of the First (nominal) and Second (material) Piola-Kirchhoff stress measures. The nominal stress is conjugate to the deformation gradient and the material stress is conjugate to the Lagrange strain tensor.

Just as there exist different continuum stress definitions, the derivation of stress measures for an atomic ensemble have also led to different definitions. The virial theorem developed by Clausius [52] and Maxwell [53,54] to determine the stress field applied to the surface of a fixed volume containing interacting particles first defined the definition of atomic ensemble stresses. The virial theorem has been incorrectly applied to obtain point-wise local stresses. In order to correct for this misuse, various definitions of stress have been developed that satisfy the equation for the balance of linear momentum in a dynamic continuum. These approaches have led to many variants and have led to an on-going controversy over the validity of such measures [55,56].

Defining the force interaction between atoms using a pair potential yields

$$\vec{f}^{\,\alpha\beta} = -\frac{\partial V}{\partial r^{\alpha\beta}} \frac{\vec{r}^{\,\alpha\beta}}{r^{\alpha\beta}} \tag{2.18}$$

where V is the interatomic pair potential from which the force $\vec{f}^{\,\alpha\beta}$ on atom α is due to the influence of neighboring atom β. A stress measure derived by Basinski, Duesber, and Taylor (BDT stress) [57] is based on the assumption that the bulk stress tensor can be used to define the stress in a small volume Ω^{α} even in an inhomogeneously deformed atomic assemblage. The BDT stress tensor is given by

$$\sigma_{ij}^{\alpha} = \frac{1}{\Omega^{\alpha}} \left[\frac{1}{2} m^{\alpha} v_i^{\alpha} \, v_j^{\alpha} - \frac{1}{2} \sum_{\beta} \frac{\partial V}{\partial r^{\alpha\beta}} \frac{r_i^{\alpha\beta} \, r_j^{\alpha\beta}}{\left| \vec{r}^{\,\alpha\beta} \right|} \right] \tag{2.19}$$

where m^{α} and v^{α} are the mass and velocity of atom α, respectively, and $\vec{r}^{\,\alpha\beta} = \vec{r}^{\,\alpha} - \vec{r}^{\,\beta}$. It can be noted that the first term corresponds to kinetic energy – and hence to the temperature state – and the second term to the potential energy of the system. Another stress measure due to Cheung and Yip (CY stress) [58] is based on a simple force-area concept in which the momentum flux and force are computed across a planar area normal to the x_j coordinate. The resulting stress definition is given by

$$\sigma_{ij}^{\alpha} = \frac{1}{A} \left[\frac{1}{2} \sum_{\alpha} \frac{m^{\alpha} v_i^{\alpha}}{\Delta t} - \frac{1}{2} \sum_{\alpha} \sum_{\beta} \frac{\partial V}{\partial r^{\alpha\beta}} \frac{r_i^{\alpha\beta} \, r_j^{\alpha\beta}}{\left| \vec{r}^{\,\alpha\beta} \right|} \right] \tag{2.20}$$

where A is an associated area and Δt is a time step measure. A difficulty with the BDT and CY stress definitions is that they are both inconsistent with the conservation of linear momentum. To correct this deficiency, Cormier, Rickman, and Delph derived an additional stress measure based on ensemble averages (CRD stress) [59] given by

$$\sigma_{ij}^{avg}\left(\vec{\boldsymbol{r}}\right)=\frac{1}{\Omega^{'}}\left[\sum_{\alpha}\frac{p_i^{\alpha}\,p_j^{\alpha}}{m}\Lambda^{\alpha}\left(\vec{\boldsymbol{r}}\right)-\frac{1}{2}\sum_{\alpha\neq\beta}\frac{\partial V}{\partial r^{\alpha\beta}}\frac{r_i^{\alpha\beta}\,r_j^{\alpha\beta}}{\left|\vec{\boldsymbol{r}}^{\,\alpha\beta}\right|}l^{\alpha\beta}\left(\vec{\boldsymbol{r}}\right)\right] \tag{2.21}$$

where $\Omega^{'}$ is the selected spherical volume about the point $\vec{\boldsymbol{r}}$, and $\Lambda^{\alpha}\left(\vec{\boldsymbol{r}}\right)$ is unity if particle α lies with the averaging volume and is zero otherwise. In addition, $0\le l^{\alpha\beta}\le 1$ is the fraction of the α - β bond length.

As shown by Zimmerman et al. [56], the virial stress definition and other definitions discussed above converge rapidly to a Cauchy stress as the size of the atomic subdomain over which stress is calculated is increased.

2.2.5 Phonon damping

In a crystal lattice, a phonon is a quantized mode of vibration. This corresponds to a stress wave in a continuum solid. Applied loads and propagating defects such as cracks can generate phonons that can reflect off outer boundaries, return to the location where they were generated and cause an undesirable self-interaction. Therefore, these disturbances need to be damped out in order to equilibrate the atomic system. Both local and global schemes have been addressed in the literature. Local damping schemes have been developed that introduce a heat bath or viscous damping that is applied nonselectively to all atomic velocity components equally that tends to drive the local system temperature towards zero Kelvin [60]. Another, more global approach, utilizes a computationally intensive digital filtering method based on fast Fourier transforms to separate out specific frequency responses [61].

The present work develops a new approach to phonon damping that utilizes a simple filter based on averaging velocity components within local domain partitions is developed that preserves the MD thermal state while removing correlated or group velocities associated with undesirable phonons. This damping scheme is further discussed

in Chapter 3. These phonon disturbances can be generated by the application of external loads that disrupt the entire atomic domain or produced by deformation processes in the interior atomic domain that propagate out to the MD/FEM interface and are reflected back to the interior that result in an interference with the atomistic processes that originally generated the phonons.

The basis for this approach is the recognition that general atomic motion is composed of a superposition of velocities due to random thermal vibration and group velocities associated with phonons. Thus, the velocity of each atom may be decomposed into thermal and group components:

$$\vec{\boldsymbol{v}}_i = \vec{\boldsymbol{v}}_i^{\,thermal} + \vec{\boldsymbol{v}}_i^{\,group} \tag{2.22}$$

Using a general partitioning of the MD field into subdomains, the superposition of atomic velocity modes can be represented as shown in Figure 2.7.

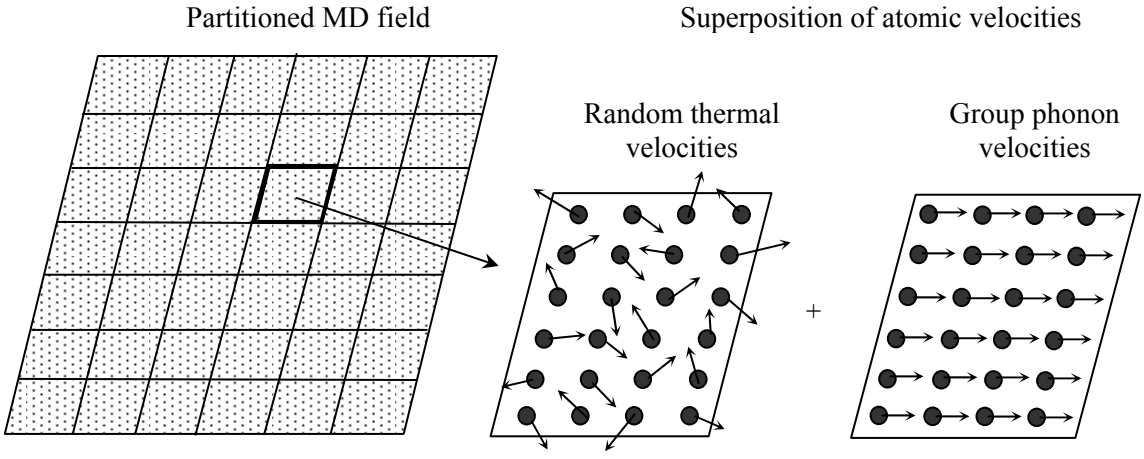

Figure 2.7. Local atomic velocity superposition within MD domain partitions.

Because thermal vibrations are random, the thermal velocity field of an aggregate of atoms is directionally isotropic, and the average atomic velocity fluctuates about zero. The magnitude of this fluctuation is related to the number of atoms in the local domain partition, N, and the statistical average may be expressed as:

$$< \vec{\boldsymbol{v}}^{\,thermal} > = \frac{1}{N} \sum_{i=1}^{N} \vec{\boldsymbol{v}}_i^{\,thermal} \rightarrow \vec{0} \quad as \quad N \rightarrow \infty \tag{2.23}$$

Thus, the average velocity vector within each MD domain partition is obtained in the limit as

$$< \vec{\boldsymbol{v}} > = \vec{0} + < \vec{\boldsymbol{v}}^{\,group} > = \vec{\boldsymbol{V}}^{\,group} \tag{2.24}$$

which, for a finite number of atoms, approximately eliminates the thermal velocity component and uncovers the resultant group velocity, $\vec{\boldsymbol{V}}^{\,group}$, of the phonon traversing the local partition. The size of the local partition is variable but must be less than the wavelength of the phonon to be damped; partitions greater than the smallest phonon wavelength will cause an error in the determination of the local group velocity and invalidate any damping procedure. Assuming an adequate partition size, a simple estimation of the group acceleration vector, $\vec{\boldsymbol{\alpha}}^{\,group}$, can be estimated over the current time step, Δt, as:

$$\vec{\boldsymbol{\alpha}}_i^{\,group} = \frac{\Delta \vec{\boldsymbol{V}}^{\,group}}{\Delta t} \tag{2.25}$$

A damping factor, ξ, can be introduced to modify the magnitude of the group acceleration vector that is used as a corrective term in the integration of the equations of motion to remove the phonon group velocity. The increment in atomic trajectory for the i^{th} atom in the local partition at the current time step can be obtained using a modified acceleration given by:

$$\vec{\alpha}_i = \frac{\vec{f}_i}{m_i} - \xi \vec{\alpha}_i^{group} \tag{2.26}$$

The modified acceleration effectively damps the phonon component of velocity when applied over a number of time steps. The advantages of this damping procedure are the simplicity of implementation and the avoidance of effecting thermal components of atomic velocities. Therefore, this approach effectively damps phonon disturbances while preserving system temperatures by not effecting atomic thermal vibrations. This approach is demonstrated in the MD-FEM coupled methodology presented in Chapter 3.

2.2.6 Molecular dynamics analysis of polycrystalline metals

A primary focus in the MD simulation of metals is the analysis of the formation, evolution, and damage mechanisms of polycrystalline microstructure. Deformation mechanisms involve processes of void nucleation and coalescence in intergranular and transgranular fracture and the simulation of a myriad of dislocation processes that evolve due to applied far-field loads. Understanding such failure mechanisms in materials is crucial to the development of new materials with high strength and toughness.

Metallic bonding, as in face centered cubic (fcc) metals, consists of delocalized electrons that are shared between all atoms in the lattice. Thus, simple atom-pair potentials cannot be used to account for all of the mutual interactions between the electron clouds surrounding the atoms. Modifications, such as cluster potentials, pair functionals, and cluster functionals, have been made to pair potentials to develop general classes of interatomic potentials. As discussed in Section 2.2.1, the embedded-atom method (EAM), which uses a pair functional, has been successful in simulating the atomic bonding in fcc metals and the form of this potential has been shown in Equation (2.7). Great care is needed in the development of energy potentials, and further work is needed to develop accurate potential energy functions for specific types of atomic

interactions. Once developed, the interatomic potentials can be used in MD simulations of deformation and fracture.

2.2.7 Grain boundary description in polycrystalline metals

The present work focuses on the intergranular fracture of grain boundaries. This selection was made because of the variety of associated failure mechanisms associate with GB failure compared to transgranular failure along slip planes. Grain boundaries may be described by the crystallographic misorientation between the adjacent crystal structure of the grains, which is described by the sigma angle Σ [62]. The sigma angle is calculated as the reciprocal ratio of coincident lattice sites (CLS) to total lattice sites (TLS) or $\Sigma = TLS/CLS$. This ratio is a measure of the relative departure from two adjacent crystals having the same orientation, or $\Sigma = 1$. Figure 2.8a shows a symmetric tilt boundary between two grains. When superposed as in Figure 2.8b, it can be seen that one in five of the atomic positions are coincident. Therefore, the sigma measure for this grain boundary is 5.

This leads to a general characterization of GBs which consist of high, low, and intermediate energies associate with the relative crystallographic orientations along the GB interfaces. For an aluminum bicrystal, GB energies are depicted in Figure 2.9 [63]. For a misorientation angle directly related to the crystallographic directions of the joined grains (as opposed to the alternative Σ angle representation), the distribution of the grain boundary energy is clearly evident. Although the possible characterization of GB energy for a small number of energy levels sufficient to provide adequate interpolation for any intermediate grain boundary energy or misorientation is intriguing, as will be discussed in Section 4.6, accurate means for reducing the computational requirements to describe the behavior of GBs in the full configurational space remains illusive.

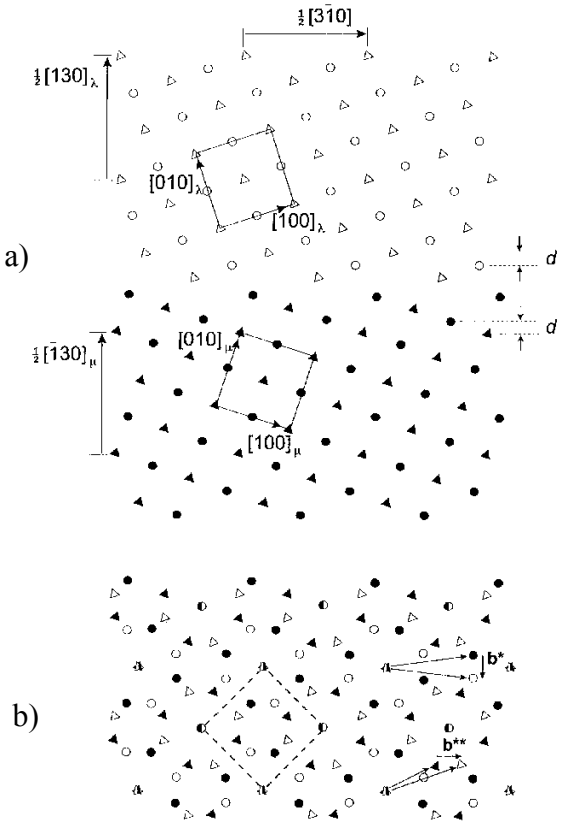

Figure 2.8. a) Atomic positions in two adjacent grains separated by a {130}/<001> 37°-tilt boundary. b) Superposed lattices showing coincident lattice sites marked as half-filled symbols indicating Σ = 5. (From Hull and Bacon [62]).

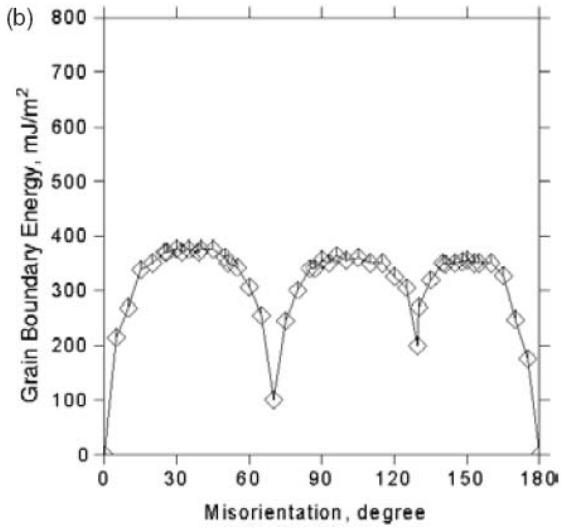

Figure 2.9. Grain boundary energy as a function of misorientation angle. (From Lee and Choi [63]).

2.3 Molecular dynamics simulation of fracture

2.3.1 Introduction

This section presents simulations focused on characterizing intergranular fracture in fcc aluminum for application to multiscale analysis. A molecular dynamics model for crack propagation under steady-state conditions is developed to analyze intergranular fracture along a common flat Σ99 [1 1 0] symmetric tilt grain boundary in aluminum.

The system was subjected to a hydrostatic tensile load in order to avoid shear stresses away from the crack that could induce undesired dislocation formation, and subjected to low temperature (100 K). The simulation reveals asymmetric crack propagation in the two opposite directions along the grain boundary. In one direction, the crack propagates in a brittle manner by cleavage with very little or no dislocation emission, and in the other direction, the propagation is ductile through the mechanism of deformation twinning. This behavior is consistent with the Rice criterion [64] for cleavage vs. dislocation blunting transition at the crack tip. The preference for twinning to dislocation slip is in agreement with the predictions of the Tadmor and Hai criterion [65]. A comparison with finite element calculations shows that while the stress field around the brittle crack tip follows the expected elastic solution for the given boundary conditions of the model, the stress field around the twinning crack tip has a strong plastic contribution. The following sections present details of the simulation relevant to the overall topic of multiscale analysis; a complete presentation of the analysis is contained in Yamakov, Saether, Phillips, and Glaessgen [66,67].

The MD model used for the simulation is discussed in Section 2.3.2, and a description of an elastic finite element simulation used for comparison is detailed in Section 2.3.3. Details of GB crack propagation are contained in Section 2.3.4. A concluding section presents an assessment of the overall simulation results.

2.3.2 The molecular dynamics model

The MD simulation is focused on steady-state crack propagation and is modeling using the configuration shown in Figure 2.10. With periodic boundary conditions in all directions, the model represents an aluminum multilayer system of alternating sets of thick and thin crystalline layers separated by four flat GBs. The two broad layers, marked as “Crystal I” and “Crystal II”, form a bicrystalline system with a flat GB in the middle,

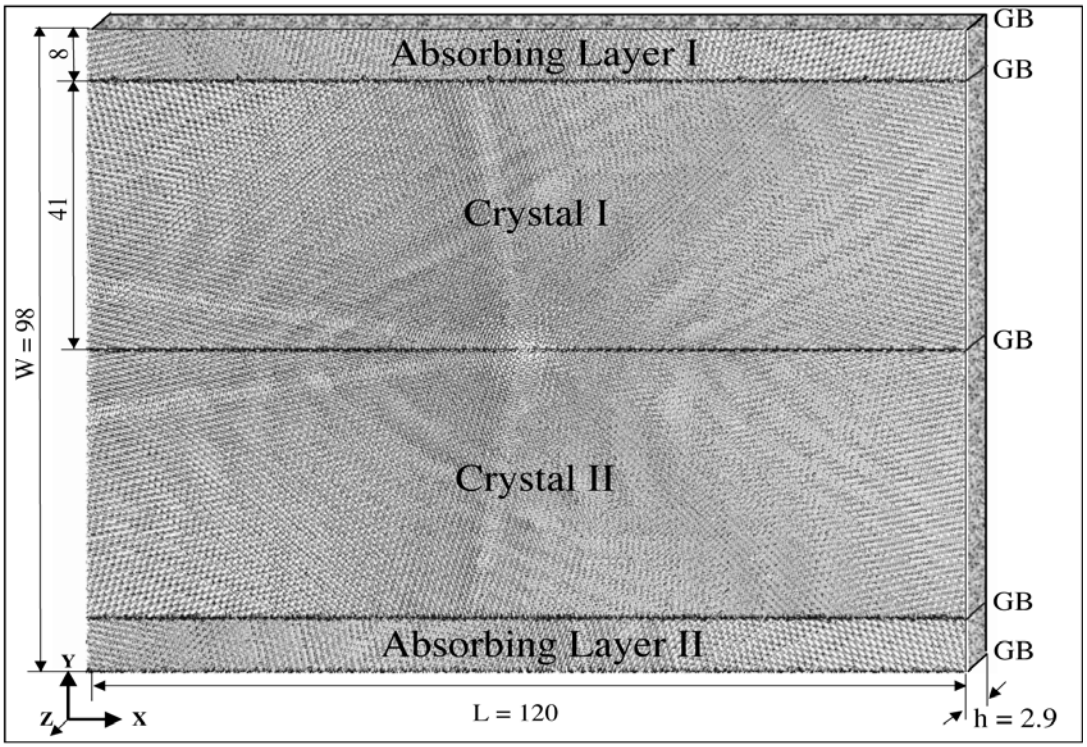

Figure 2.10. Molecular-dynamics system before crack initiation representing the simulation set-up.

through which the crack propagates. In Figure 2.10, size dimensions are in nm. Grain boundaries (GB) are shown as parallel lines of dark atoms separating the crystalline phases of Crystal I, Crystal II, and Absorbing Layers I and II as indicated. The crystallographic orientations of Crystal I and Crystal II are presented in Figure 2.11. Common neighbor analysis (CNA) as developed by Honeycutt and Andersen [68], and Clarke and Jonsson [69], is used to identify atoms in different crystallographic states: fcc (small dots), hcp (triangles), and non-crystalline atoms (large dots). Atoms with more

than 1/3 of their nearest neighbors missing are identified as surface atoms (squares), indicating existing vacancies in the GB. The length scale is in units of the lattice constant of Al, a_o = 0.405 nm.

In the imposed coordinate system of the model, the orientation of Crystal I is: (x:[7 $\bar{7}$ $\bar{1}$0]; y:[5 $\bar{5}$ 7]; z: [1 1 0]), and the orientation of Crystal II is: (x:[7 $\bar{7}$ $\bar{1}$0]; y:[$\bar{5}$ 5 $\bar{7}$]; z: [1 1 0]) (see Figure 2.11). In this way, Crystal II is a mirror image of Crystal I relative to the crystallographic plane {5 5 7}, which

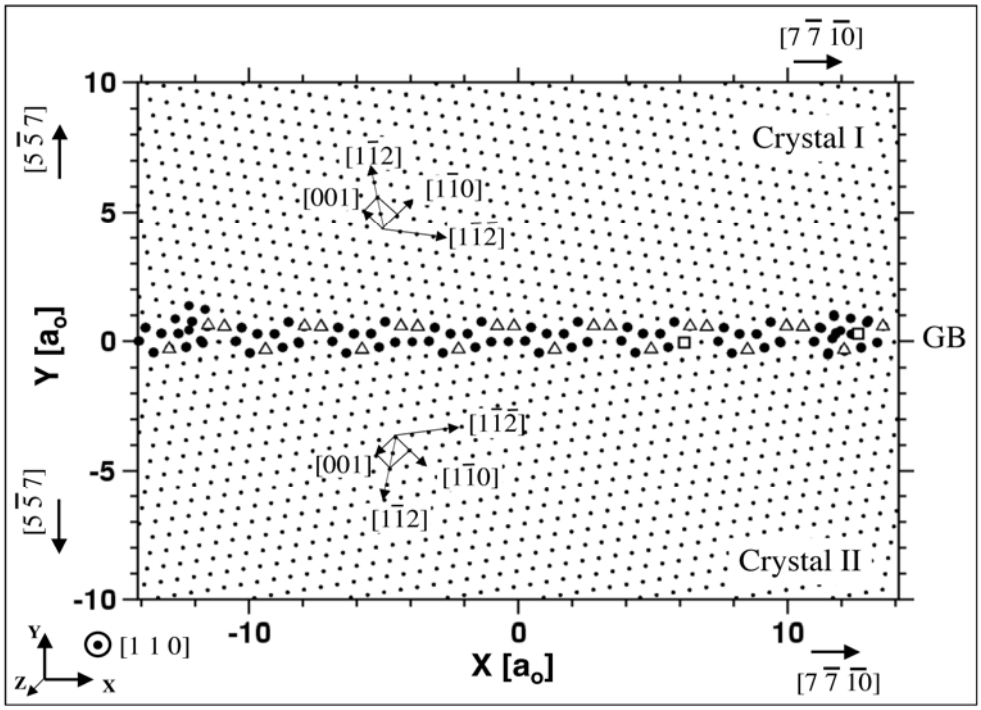

Figure 2.11. Atomistic snapshot giving the crystallography and structure of the GB interface.

becomes the plane of the GB between them. The GB thus formed is a <1 1 0> ∑99 symmetric tilt GB, for which the atomic structure in Al is known from the literature (Dahmen et al. [70]). This is a high-angle grain boundary (tilt angle of 89.42^o) with a large excess (i.e., above the perfect crystal) energy, γ_{GB} = 0.60 ± 0.05 J/m^2, estimated here for a relaxed structure at T = 100 K. The high excess GB energy facilitates its

decohesion [71]. The surface energy of the GB plane, γ_s, at 100 K is estimated in this work at $\gamma_s = 0.952 \pm 0.010$ J/m^2 and is in good agreement with experimental data for the Al surface energy.

The two smaller layers, Absorbing Layer I and Absorbing Layer II, on both sides of the bicrystalline system (Figure 2.10) have the same crystallographic orientations as Crystal II and Crystal I, respectively. Consequently, the GBs formed by these layers are of the same crystallographic type as the GB between Crystal I and Crystal II. The purpose of these layers in the simulation is to serve as shock-wave absorbers [60], where a damping friction coefficient is applied to the atoms to absorb the phonon waves generated from the crack tips. In addition, the GBs between these layers and Crystal I and II act as absorbers for the dislocations that may be emitted and spread out from the crack tip during propagation. In this way, the negative effect of the periodic boundary conditions in the *y*-direction creating periodic images of all crack-tip disturbances and influencing the crack propagation is suppressed.

Of particular importance for the simulation of fracture and dislocation plasticity is the close fit of the potential to the experimentally measured surface and stacking-fault energies. Potential-dependent parameters that will be used in this study are the relaxed stable stacking-fault energy, $\gamma_{sf} = 0.146$ J/m^2, the unstable stacking-fault energy, $\gamma_{us} = 0.168$ J/m^2 - as defined in Mishin et al. [72] - and the unstable twinning energy, $\gamma_{ut} = 0.210 \pm 0.010$ J/m^2 estimated according to the method described in Tadmor and Hai [65].

The system thickness, *h*, in the *z*-direction equals only 10(2 2 0) crystallographic planes (accounting for the symmetry of the fcc lattice), or $h = 10\sqrt{2}/2a_o \approx 2.9$ nm. This thickness is more than four times larger than the range of the interatomic potential, $r_c = 1.55a_o = 0.628$ nm, which prevents interference of the atoms with their periodic images and preserves the local three-dimensional (3D) physics in the system. The small thickness in the *z*-direction allows the system size in the *x*- and *y*- directions to extend up to 21<7 7 10>$a_o \approx 120$ nm, and 24<5 5 7>$a_o \approx 97$ nm, respectively (see Figures 2.10 and 2.11),

while limiting the number of simulated atoms to 1,994,000, thus allowing the simulation to be carried out on a modest Beowulf cluster.

The choice of the [1 1 0] crystallographic orientation of the smallest system dimension *z* is not random [73]. The [1 1 0] direction is the common axis of the $(\bar{1}\ 1\ 1)$ and $(1\ \bar{1}\ 1)$ planes, which are glide planes for the most common slip dislocations (i.e., 1/2<110> dislocations) in fcc metals. It has been shown in Yamakov et al. [74] that all of the six slip systems available on these two planes can operate unobstructed by the small system size in this direction. Moreover, a number of complex dislocation interactions and events are still possible between these six slip systems, as in a full 3D space [75,74]. As the dislocation activity is expected to be very important in this simulation, the choice of the [1 1 0] direction as a columnar axis for this quasi-two dimensional set-up ensures the best resemblance to a full 3D environment. The main constraint is that the dislocation lines of all possible dislocations have to be straight lines parallel to the columnar direction. A comparison between this quasi-2D and a full 3D environment in a nanocrystalline model shows that some grain size effects, related to the curvature of the dislocation loops presented in 3D, are suppressed [177]. Specifically, as the stress needed to expand a dislocation loop is inversely proportional to the loop radius and is limited by the very small grain size of the polycrystalline metal, there is a substantial grain size dependence of the yield stress. This geometrical dependence is absent in a quasi-2D model, because the small thickness of the system constrains the dislocation lines to be straight and parallel to each other, preventing the formation of dislocation loops. The lack of curvature of the dislocation lines, as well as of the crack front, should be regarded as a simplification in this model. In the case where the grain size is large enough not to be a governing parameter, the presence of curvature usually helps the defect nucleation process, such as dislocations and microvoids, at or around the crack tip. While it is expected that neglecting the effects of curvature would not *qualitatively* change the fracture mechanism, it may affect the process *quantitatively* in terms of decreased peak stress and work of debonding.

The simulation temperature of T = 100 K is low enough to suppress GB and surface diffusion processes and to facilitate brittle fracture in aluminum. The temperature is kept constant by using the Nose-Hoover thermostat (see Nose [74]).

The system is constructed using four blocks of perfect crystals (each one for Crystal I, Crystal II, Absorbing Layer I, and Absorbing Layer II in Figure 2.10), which are thermally equilibrated at 100 K at zero constant pressure. The constant pressure equilibration is achieved by using the Parrinello-Rahman constant-stress simulation [48]. After the thermal equilibration at zero pressure, the system is loaded hydrostatically in tension, i.e.,

$$\sigma_{xx} = \sigma_{yy} = \sigma_{zz} = \sigma \tag{2.27}$$

and is dynamically equilibrated at this constant stress. After establishing equilibrium between the strain in the system and the applied external stress, the system size in all three dimensions is fixed under the constant strain condition.

The transition from a constant stress to a constant strain simulation transforms the volume fluctuations, always present in a finite system under thermodynamic equilibrium, into stress fluctuations. Thus, further equilibration at constant strain is necessary to smooth out these fluctuations. The simulation then proceeds under NVP canonical ensemble conditions subjected to this constant strain – constant temperature condition. Although the simulations are carried out under constant strain, for convenience in presentation, the various analyses will reference the value of prestress that corresponds to a particular value of prestrain.

To ensure crack nucleation and growth at the nanometer scale, the prestress was varied between 3.5 and 4.25 GPa. If the system were *uniaxially* strained, these very high prestress values would have caused strong plasticity effects not related to the crack, such as spontaneous dislocation nucleation from the GBs [75]. Applying triaxial hydrostatic stress eliminates these undesirable plasticity effects.

The crack in the system is nucleated by screening (shielding) the atomic interactions between atoms at both sides of the GB plane between Crystal I and Crystal II along a region of length l_o. As the crack grows and the crack opening becomes large enough to prevent interaction of atoms on the adjacent crack faces along the screened region, the previously screened atomic interactions are restored and the crack continues to evolve on its own. The crack starts growing if l_o is larger than the critical Griffith length L_g defined when the energy spent to create the upper and lower crack surface $2\gamma_s$ minus the energy gained by destroying the GB γ_{GB} is equal to the released strain energy $-dU/dl$, per length l,

$$2\gamma_s - \gamma_{GB} = -dU/dl \tag{2.28}$$

An estimate of L_g is made by calculating dU/dl as a function of σ and l. This calculation is performed by using an anisotropic elastic finite element model of the elastic equivalent of the MD system, as will be discussed later. For the values of prestress applied in this study, σ = 3.5, 3.75, 4.0, and 4.25 GPa, the obtained Griffith lengths are L_g = 6.08, 5.32, 4.71, and 4.21 nm, respectively. The initial crack length is set equal to the crystallographic period in the x-direction, l_o = <7 7 10>a_o = 5.7 nm, to reflect the existing periodicity of the equilibrated GB structure [70] induced by the lattice of the two joined crystals. This value of l_o is larger than L_g for most of the prestresses, except for σ = 3.5 GPa, ensuring the initiation of crack growth for these prestresses. Crack growth also occurs for σ = 3.5 GPa (L_g = 6.08 mn), because the use of a many-body potential causes, all the atoms within the interaction range of the screened atoms to be affected by the screening, effectively increasing the initial crack length.

The identification of various structural defects including dislocations, twins, stacking faults, etc. appearing around the growing crack is important for understanding the mechanism of deformation. A procedure for atom identification based on the atom's coordination number and on the common-neighbor-analysis (CNA) technique [68,69] is used. The technique makes it possible to identify atoms in fcc and hcp states. Layers of hcp atoms in a fcc lattice are formed at stacking faults and twin boundaries [77] and can be used very successfully for visualizing the ongoing dislocation processes in fcc crystals

[78]. Atoms that are not identified in a fcc or hcp state are considered to be in a non-crystalline state and indicate the presence of GBs or dislocation cores. In addition, atoms that have lost more than 1/3 of their neighbors inside the interaction range of the potential are considered surface atoms. On average, 1 nm^2 of a flat {5 5 7} surface contains 16 surface atoms. The crack free surface is estimated by counting the number of surface atoms, and when divided by 2*h* (see Figure 2.10; the prefactor 2 accounts for the two crack surfaces), conveniently gives an effective crack length *l*. Under this convention, the thermalized structure of a $\langle 110 \rangle \Sigma 99$ symmetric tilt GB, shown in Figure 2.11, appears as quasi-periodic, with a regular pattern of hcp atoms immersed in a disordered layer with the presence of a few distributed vacancies, identified by the appearance of a few isolated surface atoms inside the GB region. Classifying atoms in this way presents a unique possibility to distinguish and quantify the various atomic processes occurring at the crack tip.

2.3.3 The continuum model

The continuum model is constructed using finite element methods to determine the energy of an equivalent linear elastic system and to determine the critical Griffith crack length to gage the onset of crack propagation. The FE configuration, with dimensions scaled to reproduce the proportions of the MD system, is presented in Figure 2.12. The relative crack length, *l/L*, varied from 0.05 to 0.91, corresponding to the absolute crack length from 6 to 110 nm in the MD system, shown in Figure 2.10. Generalized plane strain in the *z*-direction is used to emulate the hydrostatic loading conditions in the MD system, shown in Figure 2.10.

The FEM calculations are anisotropic linear-elastic, carried out under displacement control in the *x*- and *y*-directions, and use generalized plane strain to reproduce the hydrostatic triaxial stress in the MD simulation.

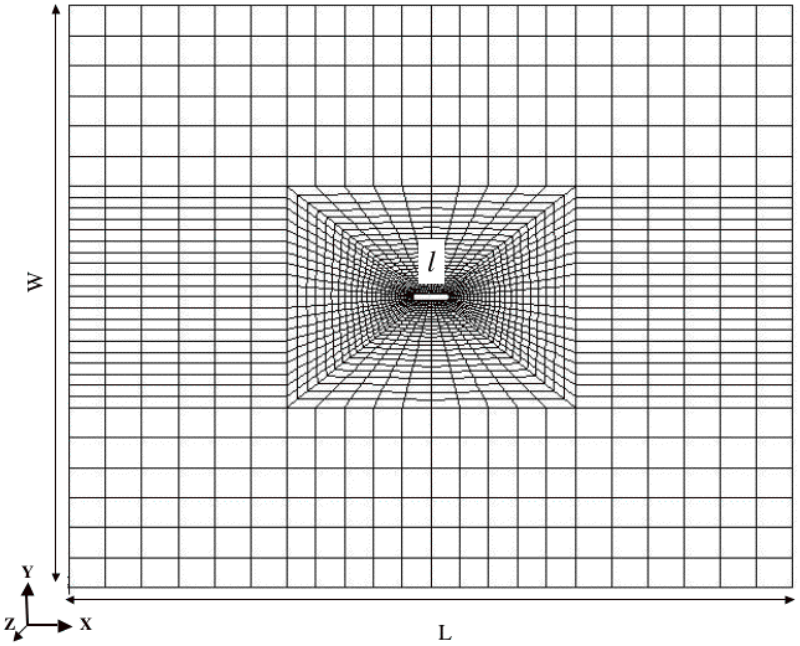

Figure 2.12. The mesh of the finite element model with a built-in lenticular crack.

The use of periodic boundary conditions in the constant strain MD simulation, described previously, constrains the problem in the same manner as the generalized plane strain condition in continuum mechanics. The commercial software package ABAQUS [79] is used. The model contains a combination of six-node triangular elements and eight-node quadrilateral elements that support generalized plane strain. The anisotropic elastic constants are obtained from the MD interatomic potential and transformed according to the crystallographic orientations of the atomic microstructure. Higher order terms in the elastic constants are not included as they are not available from the published data for this potential [72] and are not easy to calculate. This limits the FE simulation to be linear elastic.

The FEM model contains a built-in lenticular slit, which simulates the MD approximation to a crack of varying relative length, $0.05 < l/L < 0.91$, and is used to study the evolution of the system at different stages of the crack growth. To avoid stress singularities, the edges of the slit have a finite, but very small, initial radius $\lambda = 0.008L$,

which, when scaled to the MD dimensions, corresponds to an initial crack opening of approximately 1 nm, i.e., slightly larger than the range of the interatomic MD potential. Two significant differences between the FEM and MD models have to be outlined here. First, the FE calculations are static and linear-elastic. No dynamic or nonlinear effects are incorporated, and the results are relevant for static "cracks" under small strain when the nonlinear effects can be neglected. Second, there is no elastic equivalent of the GBs in the FEM system. It is assumed that the difference between the elastic response of the GBs and the interior of the grains does not significantly alter the crack behavior because of the relatively small volume ratio of the GB in the system. Thus, the FEM simulations used here aid in understanding the MD results by distinguishing between plastic and elastic processes in the MD simulation.

2.3.4 Intergranular fracture along grain boundaries

The following subsections discuss specifics of fracture mechanisms, directional characteristics of crack propagation, predictive criteria, and elastic-plastic processes at the crack tip.

2.3.4.1 The mechanisms of crack propagation along the Σ99 grain boundary by MD simulation

During simulation as described in Section 2.3.2, the GB opens after 8 ps of screening of the atomic interactions in a region of 5.7 nm length along the middle of the GB between Crystal I and Crystal II (Figure 2.10), and a crack starts to grow in both directions along the GB interface. Figure 2.13 shows MD snapshots of cracks that have grown in the MD system shown in Figure 2.10 for four different initial hydrostatic prestresses: σ = 3.5, 3.75, 4.0, and 4.25 GPa. CNA is used to identify atoms in different crystallographic states: fcc (in gray), hcp (in red), and non-crystalline atoms (in blue). Atoms with more than 1/3 of their nearest neighbors missing are identified as surface atoms (in green). Thus, a number of different formations are indicated in the figure as follows: ① - GB interface; ② - twin boundary; ③ - core of a partial or twinning dislocation; ④ - nanovoid at the crack tip; ⑤ - slip dislocation; ⑥ - GB dislocation; and ⑦ - secondary slip.

In all cases, the crack growth is not symmetric in the +*x* and -*x* directions (as defined in Figure 2.10) along the GB (① in Figure 2.13). The growth in the -*x* direction has produced two twin patterns (② in Figure 2.13) by emitting a series of twinning dislocations (③ in Figure 2.13) [77], and is almost symmetric about the grain boundary of the two adjacent crystals. The crack propagation in this direction is greatly reduced, when compared to the propagation in the +*x* direction, with energy expended through ductile blunting at the crack tip. The growth in the +*x* direction proceeds through a continuous process of void formation (④ in Figure 2.13). Because the crack tip emits very few dislocations (③ and ⑤ in Figure 2.13), crack propagation in the +*x* direction proceeds much faster than in the –*x* direction, and does so in an almost brittle fashion. After being emitted, some of the dislocations glide away from the crack tip and are absorbed by the next GB layer to form GB dislocations (⑥ in Figure 2.13). Secondary slip (⑦ in Figure

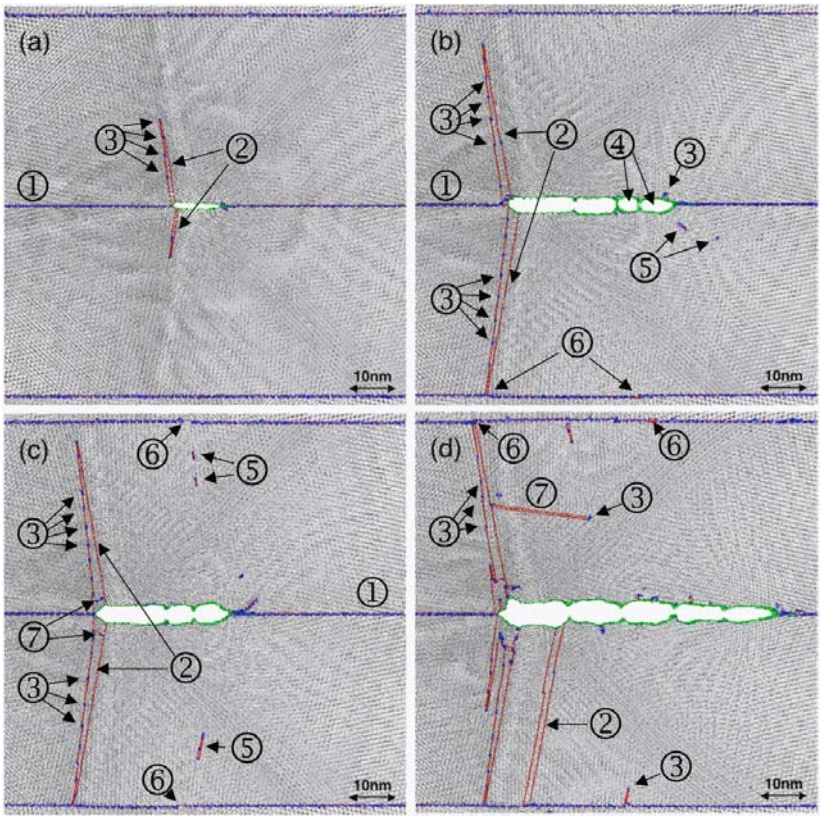

Figure 2.13. MD snapshots of cracks which have propagated under four different initial hydrostatic stresses: σ = 3.5 (a), 3.75 (b), 4.0 (c) and 4.25 GPa (d).

2.13) on a slip plane along the $[1\ \bar{1}\ \bar{2}]$ direction (see Figure 2.11) may also accommodate deformation non-parallel to the primary slip plane along the $[1\ \bar{1}\ 2]$ direction, where twinning ③ and primary slip dislocations ⑤ propagate.

A detailed description of all of the atomistic processes, accompanying the crack growth and governing the decohesion of the GB interface can be found in Yamakov, Saether, Phillips, and Glaessgen [66].

2.3.4.2 Rice and Tadmor-Hai criteria for twinning vs. cleavage at the crack tip

The ability of GBs in fcc metals to produce asymmetric crack growth was first found in an MD simulation of intergranular fracture in Cu by Cleri et al. [80]. In their work, a crack propagated in the interface plane of the symmetric tilt (221)/(221) grain boundary. The crack advanced by brittle fracture along the $[1\ \ 1\ \ \bar{4}]$ direction and was blunted by dislocation emission along the opposite $[\bar{1}\ \ \bar{1}\ \ 4]$ direction. The difference in behavior at the two crack tips was attributed to the orientation of the slip planes relative to the GB. A slip plane inclined at angle θ to the GB makes the angle θ to the propagation direction of one crack tip, and the angle π-θ with the propagation direction of the opposing tip. Thus, for certain GBs, the Rice criterion [64] for dislocation nucleation versus cleavage might be satisfied for the crack tip at angle θ, but not for the crack tip at an angle π-θ, leading to asymmetric crack propagation.

The crack grows primarily in the direction of the π-θ tip since the brittle propagation takes much less energy. Note that, for transgranular fracture, every direction in the fcc lattice has inverse symmetry, so such asymmetry in crack propagation is not expected to appear.

In the crystallographic model, presented in Figure 2.11, the propagation direction $[\bar{7}\ \ 7\ \ 10]$ along the GB plane makes an angle $\theta = 79.98^{o}$ with the twinning direction

$[1\ \bar{1}\ 2]$ in both crystals, giving $\cos\theta = 1/\sqrt{33}$. The Rice criterion for dislocation emission for the two propagation directions with $+\cos\theta$ (-*x* direction) and $\cos(\pi - \theta) = -\cos\theta$ (+*x* direction) can be written as

$$\frac{\gamma_{us}}{2\gamma_s - \gamma_{GB}} - \frac{(1 \pm \cos\theta)\sin^2\theta}{8} \quad \begin{cases} > 0 \text{ for brittle fracture} \\ < 0 \text{ for ductile fracture} \end{cases} \tag{2.29}$$

where the dislocations at the crack tip are edge twinning dislocations (shown as ③ in Figure 2.13) with their Burgers vector coinciding with the twinning direction and lying in the (1 1 0) plane of the model. Using the values for γ_{us}, γ_s, and γ_{GB} given in Section 2.3.2, the left side of Equation (2.29) equals 0.127±0.01. The right side of Equation (2.29) is determined to be 0.142 and 0.100 for the -*x* and +*x* propagation directions, respectively. Thus, the Rice criterion predicts that the crack tip should propagate in a ductile manner in the -*x* direction, and in a brittle manner in the +*x* direction, in agreement with the behavior seen in Figure 2.13.

While the Rice criterion explains the ductile-brittle asymmetry of the crack found in the simulations (Figure 2.13), an additional consideration is needed to explain the preference for twinning rather than the emission of slip dislocations in the -*x* direction. Tadmor and Hai [63] have recently derived a Pierels based criterion for the onset of deformation twinning at a crack tip in fcc metals by comparing the energies for nucleating a twinning or slip dislocation. This criterion introduces a so-called unstable twinning energy γ_{ut}, which, by analogy with the unstable stacking-fault energy γ_{us}, gives the energetic barrier that must be exceeded to form a twin from an existing stacking-fault. The criterion is given by the parameter *T* as

$$T = \lambda\sqrt{\frac{\gamma_{us}}{\gamma_{ut}}} = \begin{cases} < 1 & \text{slip dislocation} \\ > 1 & \text{deformation twin} \end{cases} \tag{2.30}$$

where λ is a factor that is dependent on both the γ_{sf} / γ_{us} ratio and the orientation of the slip system of the twinning dislocations with respect to the crack plane. For the twinning tip in this simulation, λ = 1.51 (as applied from Tadmor and Hai [65]), and $\sqrt{\frac{\gamma_{us}}{\gamma_{ut}}} = 0.9$, which results in T = 1.36. This suggests that twinning, rather than slip dislocation emission, will be the preferred deformation mechanism.

The brittle-ductile analysis based on the Rice criterion is for static or sufficiently slow crack growth. The criterion does not account for dynamic effects occurring at the crack tip propagating in the +*x* direction (Yamakov, Saether, Phillips, and Glaessgen [66]). Crack propagation is expected to be brittle throughout. Nevertheless, apart from these dynamic effects, there is good agreement between the simulation results and the two conditions expressed through Equations (2.29) and (2.30). This allows the prediction of the type of decohesion by knowing the crystallographic orientations of the grains and a few material parameters, such as the surface, GB, stacking-fault, and twinning energies.

2.3.4.3 Plastic contribution to the stress field near the crack: MD - FEM comparison

The plastic processes at the crack tips, including twinning and dislocation emission, have a pronounced effect on the stress distribution near the growing crack. This effect is best revealed by a comparison between the stress distributions obtained from the MD and the linear elastic FEM simulations for the models presented in Figures 2.10 and 2.12. While the MD simulation considers the material structure at the atomic level and intrinsically incorporates all the plastic processes together with the elastic response of the bicrystal, the FEM model assumes an elastically equivalent system and gives only the elastic solution. Another aspect of the FE simulation is that it gives a static solution when the system is in *elastic* equilibrium. By contrast, the MD simulation describes a continuously evolving system with all dynamic effects present. To avoid the implications of the dynamic effects in the comparison between FEM and MD results, the

corresponding MD stress distribution is calculated after the atomistic system reaches *elasto-plastic* equilibrium and the crack stops growing. The dynamic solution for the elastic stress as a function of the crack velocity in a steady-state analytical model [81] is given by Ching [82]. Ching's solution is not studied here because extracting the non-equilibrium dynamic stress from MD is not a trivial task and goes beyond the scope of this work.

The virial theorem, which is the basis for calculating the local virial stress (Equation (2.19)), provides the oldest and most frequently used expression for relating forces and motion within an atomic system to a continuum stress. The virial stress is defined through the local momentum flux carried by the particles in a small volume element (see Lutsko [83]), rather than as a force acting over a small surface element, i.e., the definition of the Cauchy stress used in continuum mechanics. Because the Cauchy stress assumes continuous structure of matter, the two definitions increasingly diverge at the atomic scale. However, in the limit of time and volume averages at equilibrium, the virial stress coincides with the Cauchy stress (see Zimmerman et al. [49,56]).

The comparison between the stress distributions obtained from the FE and MD simulations for two cases of cracks are given in Figures 2.14 and 2.15 in the form of two-dimensional (x-y) stress-maps of the system created for each of the three stress components acting in the (x-y) plane: σ_{xx}, σ_{yy}, and σ_{xy}. Figure 2.14 presents the case of the small prestress of 3.5 GPa, which produces a 10 nm crack at equilibrium in the MD simulation (seen in Figure 2.13(a)). The size of the crack is sufficiently small compared to the system size, and the elastic stress field calculated by the FEM simulation (Figures 2.14(a-c)) does not experience edge effects from the boundary conditions and thus resembles an infinite plate. The stress distribution for the brittle crack tip (the circled area in Figs. 2.14(d-f)) obtained by the MD simulation shows very good quantitative similarity to the FEM result. This similarity suggests that the crack propagation in the MD system in the $+x$ direction is indeed brittle with essentially no plasticity. However, for the twinning tip, there is a significant difference between the MD and FEM results. The FEM stress distribution is symmetric for the two crack tips, as they are elastically equivalent in

the FEM model (Figures 2.14(a-c)). In contrast, twinning occurs in the MD system at the tip propagating in the -*x* direction and significantly alters the stress field.

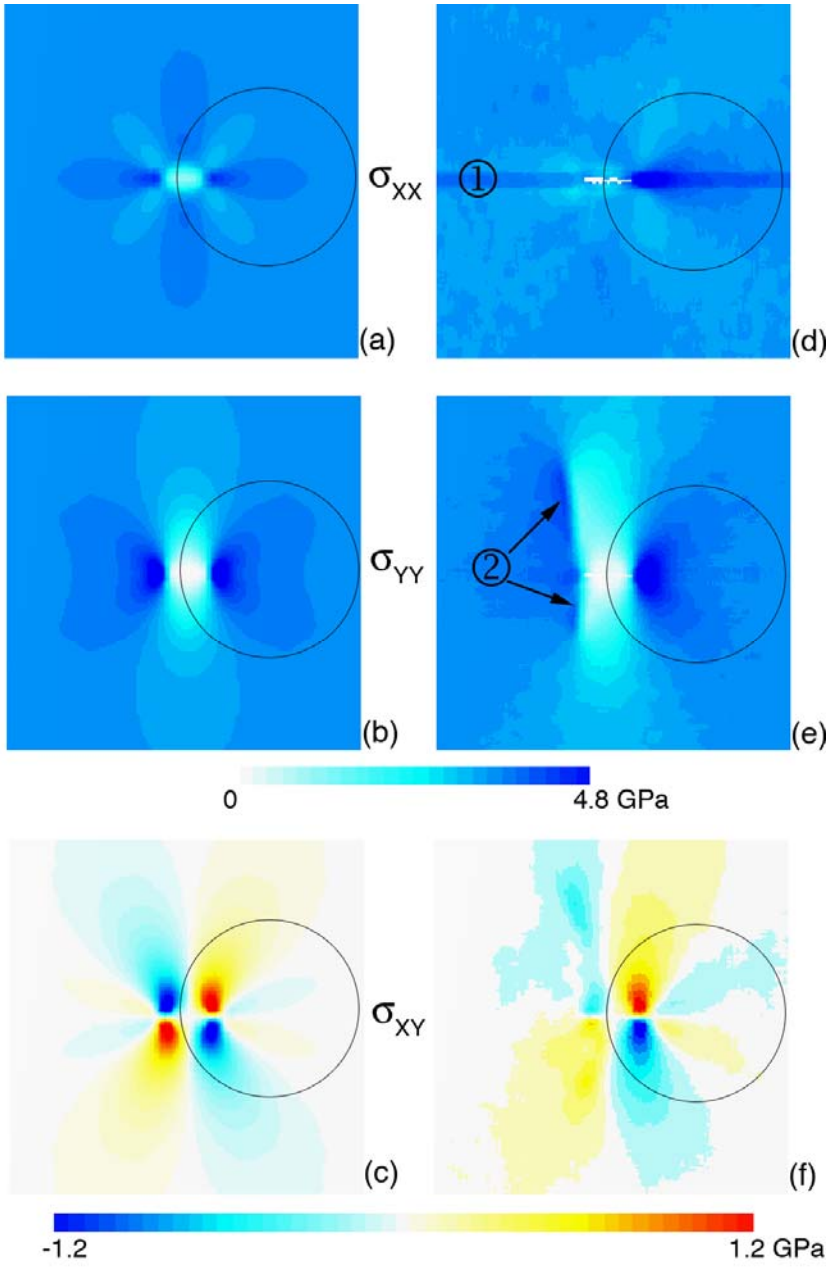

Figure 2.14. Stress contours from the FEM model (a-c) and the corresponding atomistic stress maps (d-f).

The σ_{xx} and σ_{xy} stress components are largely relieved, while the σ_{yy} stress is distributed along the twin boundaries (② in Figure 2.14(e)) and relieved at the crack tip. This reduction in local stress state explains the very slow crack propagation in the -*x* direction of the MD model.

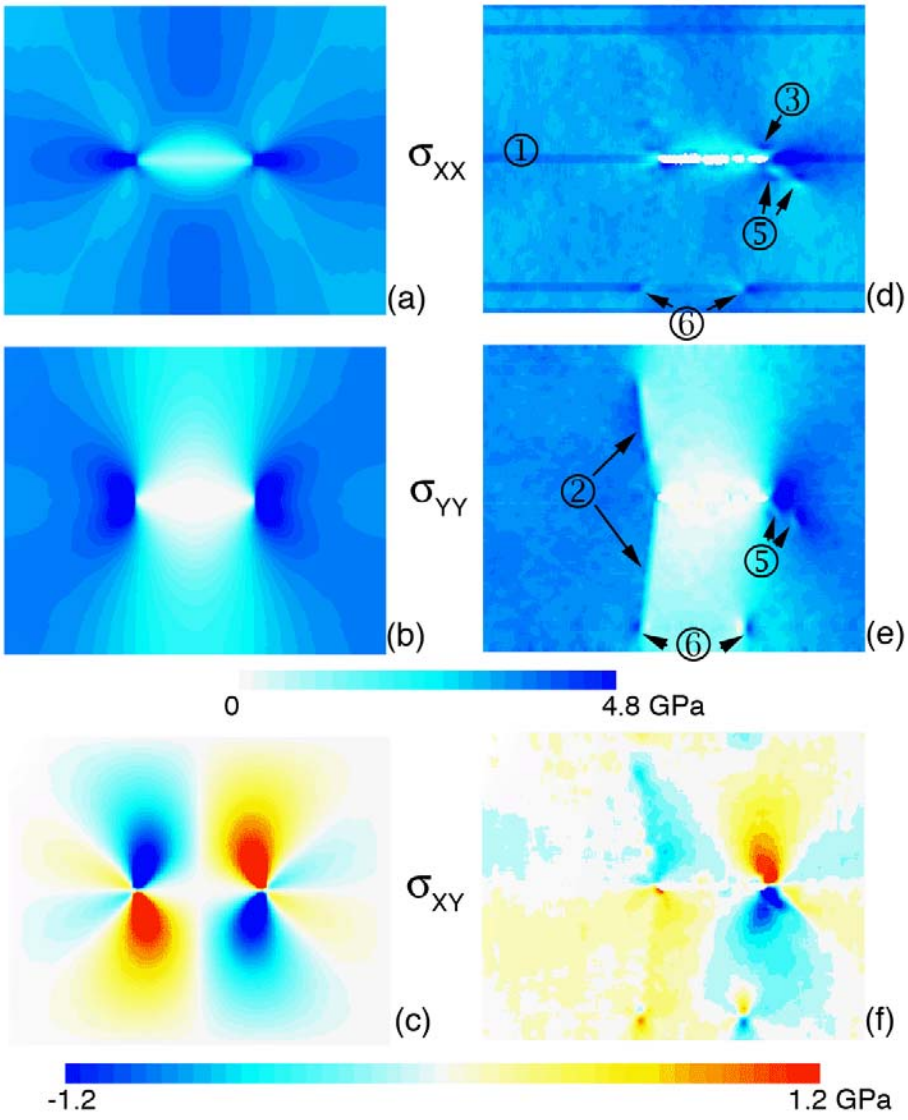

Figure 2.15. Stress contours from the FEM model (a-c) and the corresponding stress maps (d-f).

The GB layer, present in the MD model, but not in the FEM model, increases the σ_{xx} and suggests a stiffer GB layer. This stiffening effect should be taken with caution as the

virial stress calculation in the MD simulation (Equation (2.19)), as discussed previously, may give erroneous results when computed over small disordered atomic domains containing structural defects (e.g., GBs and surfaces, dislocation cores, etc. [49]). It has been suggested that the highly constrained thermodynamic state of GBs in multilayer systems may appear stiffer than the crystal lattice in certain directions [84]. At a larger prestress of 3.75 GPa, the crack in the MD model reached almost 40 nm in length. The stress fields, presented in Figure 2.15 (corresponding to the MD snapshot in Figure 2.13(b)), are strongly affected by the system boundaries at $y = \pm W/2$, as compared with the stress fields in Figure 2.14. In the MD case (see Figs. 2.15(d-f) related to the snapshot in Figure 2.13(b)), the stress field away from the crack tips is similar to the corresponding FEM stress field, while the near-tip stress distribution is strongly affected by the plastic mechanisms at the crack tips. The contribution to the stress from the developed twinning on the $-x$ side of the crack (② in Figs. 2.13(b) and 2.15(e)) and the few dislocations remaining in equilibrium with the crack tip on the $+x$ side (⑤ in Figs. 2.15(d-f)) can be easily identified. Both processes effectively relieve the stress around the crack tips as compared to the FEM elastic solution (Figs. 2.15(a-c)) and lead the MD system into elasto-plastic equilibrium.

2.4 Concluding remarks for Chapter 2

A model has been developed to study the process of debonding of a high-energy ∑99 GB in Al through crack propagation under hydrostatic loading conditions. The work reveals the atomic mechanisms in the damage zone near the crack tips during intergranular fracture. Here, the crack propagation has been shown to proceed in a different manner in the two opposite directions along the GB interface. While in one direction the crack progresses in a brittle manner, the propagation in the opposite direction is of a ductile type, characterized by the presence of plastic mechanisms including twinning at the crack tip. The difference in the mechanism is due to the inclination of the slip planes to the GB interface making different angles with respect to the two opposite propagation directions.

The brittle vs. ductile propagation simulated in both directions along the GB interface is found to agree well with the predicting criteria of Rice and Tadmor-Hai. This good compliance with the two criteria can lead to the generation of atomistically-based CZMs for larger-scale finite element simulations by knowing the crystallographic orientations of the grains in the microstructure and a few material parameters. The parameters, including surface, GB, stacking-fault, and twinning energy, are readily available experimentally. Others, such as the unstable stacking-fault energy and the unstable twinning energy, need more precise estimates and may require the use of first-principal calculations.

In general, the MD simulation of intergranular fracture exhibited an essential computational constraint that affected the results of the simulation. This deficiency is directly attributable to the system size limitations in performing a purely atomistic simulation. The model used was composed of ~2 million atoms to represent the atomistic region to study Mode I crack propagation as described in Section 2.3. This model was unable to model a domain large enough to accurately simulate far-field boundary conditions in order to eliminate finite geometry effects. Therefore, the development of a new concurrent multiscale procedure involving MD-FEM coupling has been developed and is fully discussed in Chapter 3.

Chapter 3

Coupling Molecular Dynamics and Finite Element Analyses

3.1 Introduction

The concept of bridging length scales by concurrently coupling atomistic and continuum computational paradigms is particularly attractive as a highly efficient means of reducing the computational cost of simulations in cases that require modeling of relatively large material domains to capture the complete deformation field, but where atomic and subatomic refinement is needed only in very localized regions. Such computational issues arise in modeling crack nucleation and propagation, and in modeling dislocation formation and interaction. By using coupled models the size limitations of the atomistic simulation can be minimized by embedding an inner atomistic region where complex dynamic processes and large deformation gradients exist within an outer domain where the deformation gradients are small so that a continuum representation of the material becomes appropriate.

Section 1.1 presented an overview of various methods that have been developed to address different problems involving the atomistic modeling of large material domains. The most challenging problem in developing these coupled methods is the formulation of a seamless computational connection along an interface between different material representations. A common feature of many of these approaches for coupling atomistic and continuum representations is the refinement of the finite element mesh to atomic length scales to link the kinematics of finite element nodes and discrete atoms along their common interface. In this chapter, approaches that relate atoms and finite element nodes in a one-to-one manner, or through a form of interpolation, will be referred to as *direct* coupling (DC) approaches.

While DC approaches are straightforward, the fundamental difficulty in their development lies in the inherent differences between the atomistic and continuum computational models. The physical state of the atomistic region is described through nonlocal interatomic forces between discrete atoms of given position and momentum, while the physical state of the continuum region is described through continuous stress-strain fields that reflect local statistical averages of atomic interactions at larger length and time scales. In general, the formal connection between continuum and discrete quantities can only be achieved through an adequate statistical averaging over scales where the discreteness of the atomic structure can be approximated as a continuum. A consequence of some DC interfacing strategies in their initial formulation, such as QC, required that the analysis be performed quasistatically at 0 K. Further details of direct coupling methods may be found in the original publications and in several general review papers by Park and Liu [2], Li and E [85], and Miller and Tadmor [26].

An alternative approach to the DC approaches is developed in this chapter to construct a coupled MD-FEM system. The approach is based on solving a coupled boundary value problem (BVP) at the MD/FE Interface for a MD region embedded within a FEM domain. The method uses statistical averaging over both time and volume in atomistic subdomains at the MD-FE Interface to determine nodal displacement boundary conditions for the continuum FEM. These enforced displacements, in turn, generate interface reaction forces that are applied as constant traction boundary conditions [117] between updates of the FEM solution to the atoms within the localized MD subdomains. Thus, the present approach may be described as a local-nonlocal BVP because it relates *local* continuum nodal quantities with *nonlocal* statistical averages of atomistic quantities over selected atomic subdomains. An iterative procedure between the MD statistical displacements and the FEM reaction forces ensures continuity at the interface. In this way, the problem of redefining continuum variables at the atomic scale is avoided, and the developed interface approach links different time and length scales between the MD region and FEM domain. Typically, one finite element at the interface encompasses a region of several hundred to several thousand atoms. A lower bound for the number of atoms associated with each finite element node is determined by the

requirement of obtaining a minimally fluctuating average of atomic displacements and the magnitude of generated gradients in the MD region bordering the FEM domain. With an effective average at this scale, the discreteness of the atomic structure is homogenized enough so that the FEM domain responds to the atomistic region as an extension of the continuum. At the same time, between the FEM solution updates, the traction boundary conditions are constant and applied to the MD region to ensure that the elastic field from the FEM domain is correctly transferred to the atomistic region. With the emphasis of using statistical averages to couple the two computational schemes, the developed approach is identified as a *statistical* coupling (SC) approach. Based on the SC approach, the developed MD-FEM coupling method is referred to as the embedded statistical coupling method (ESCM). ESCM provides an enhanced coupling methodology that is inherently applicable to three-dimensional domains, avoids discretization of the continuum model to atomic scale resolution, permits arbitrary temperatures to be applied, and treats in a rigorous manner the compensation of surface effects in the MD system. Complete details of the ESCM are presented in the current chapter and in Saether, Yamakov, and Glaessgen [85-87].

This chapter will detail the ESCM approach for coupling MD and FEM computational domains for the case of systems that reach thermodynamic equilibrium or evolve quasistatically. While there is no principle difficulty in implementing this approach for non-equilibrium systems, it is beneficial to first consider the case of equilibrium simulations to illustrate initial applications of this methodology.

The remainder of this chapter is organized as follows. Section 3.2 describes the structure of the coupled MD-FEM model. This includes discussions of the MD and FEM material representations, the coupling interface, and the iterative MD-FEM coupling methodology. Section 3.3 presents several validation studies to substantiate the accuracy of the developed methodology. Finally, Section 3.4 presents concluding remarks on the overall effectiveness of the ESCM.

3.2 The ESCM model

The ESCM approach is developed to reduce computational costs incurred while simulating "large" volumes of material by virtually embedding an inner atomistic MD system within a surrounding continuum FEM domain. In principal, the shape of the atomistic region may be arbitrary as shown in Figure 3.1, however, for simplicity, the special case of a circular region is assumed in the present work. Similarly, although any constitutive behavior may be assumed for the FEM domain, the present study considers a linear elastic continuum.

The structure of the ESCM model consists of four regions: 1) an Inner MD Region; 2) an Interface MD Region wherein MD and finite elements are superimposed; 3) a Surface MD Region that does not interact with the finite element nodes but is used to compensate for atomic free edge effects; and 4) a FEM domain in which standard finite element equations apply. These four regions are depicted in Figure 3.2.

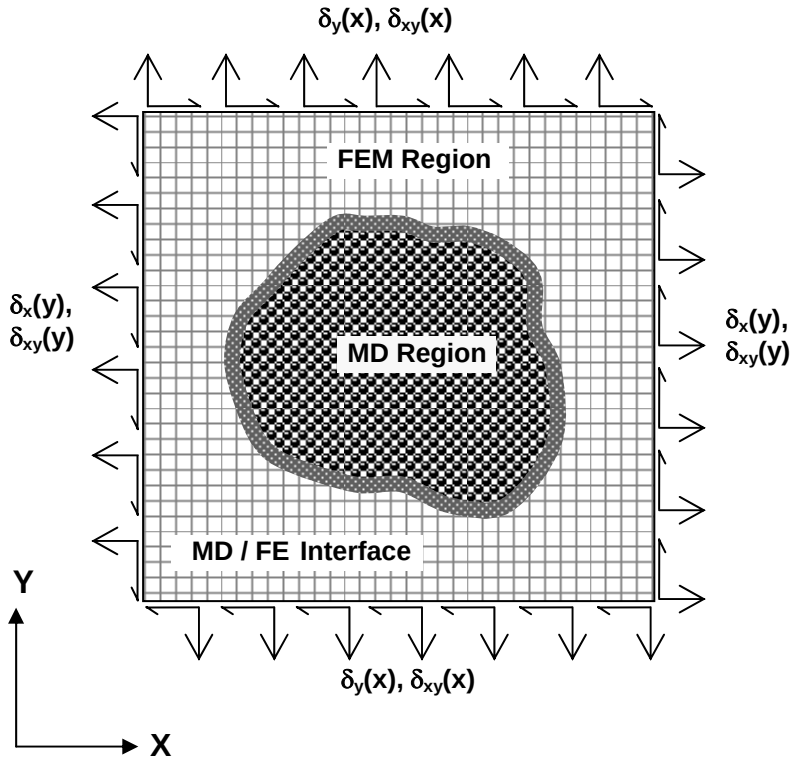

Figure 3.1. Model topology used in the ESCM approach.

Complete details of the ESCM procedure will be presented by discussing general aspects of the MD and FEM computational systems, followed by specific details of the MD/FE Interface, the Surface MD Region and the MD-FEM coupling procedure.

3.2.1 MD and FEM model components

The Inner MD Region is used to model material phenomena at the atomistic level. This Inner MD Region should be large enough to ensure a statistically smooth transition from a continuum to an atomistic representation while modeling any of the types of processes (e.g., dislocation formation, void nucleation, or crack propagation) that are required by the simulation. Together, the Inner, Interface, and Surface MD Regions constitute the complete MD system.

It is important to emphasize that the partitioning of the MD system into different regions is not a physical separation of the system. An atom assigned to a particular location freely interacts with atoms in its interaction neighborhood that may reside in a different region. Thus, the overall simulation is performed using any conventional MD technique without any imposition of direct kinematic constraints. The only difference between the three MD regions is that, while the atoms in the Inner MD Region are subject only to their interatomic forces, the Interface and Surface MD Regions serve the added purpose of facilitating the application of external forces involved in the ESCM procedure.

The addition of a FEM domain permits a large reduction in the computational cost of the performed simulations by replacing the atomistic representation with a continuum model in those parts of the system where the deformation gradients are small and atomic-level resolution is not necessary. The current application uses the FEM domain to simulate an extended material model such that the elastic deformation and load transfer due to applied far-field boundary conditions are accurately transferred to the Inner MD Region. The continuum field is currently assumed to be static with linear elastic material properties but other applications of ESCM might require the incorporation of nonlinear

material behavior, such as plasticity or general dynamic response, where nonlinear processes generated in the Inner MD Region could be propagated into the continuum.

3.2.2 MD/FE Interface

The main role of the MD/FE Interface is to provide a computational linkage between the MD region and FEM domain. The atoms that surround a given finite element node at the interface are partitioned to form a cell in the Interface MD Region, called an interface volume cell (IVC), as shown in Figure 3.2. A similar partitioning is also applied to the Surface MD Region, forming surface volume cells (SVCs). The IVCs compute averaged MD displacements at their mass center that are then prescribed as displacement boundary conditions to the associated interface finite element nodes. The IVCs need not coincide in size or shape with the finite element to which the finite element node belongs. In the model described in this paper, the IVCs are formed through a Voronoi-type construction [88] by selecting those atoms with a common closest finite element node.

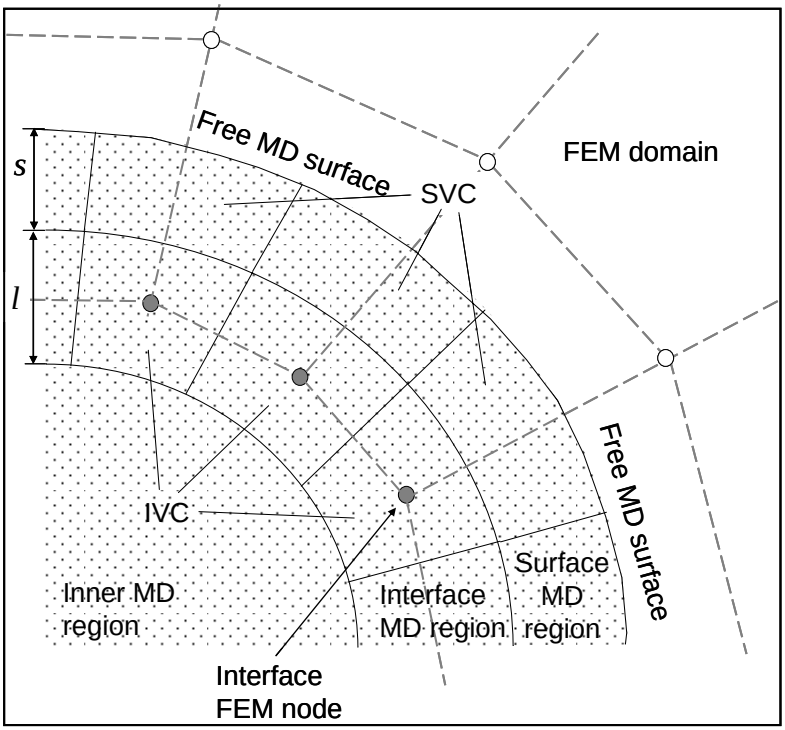

Figure 3.2. Structure of the MD/FE interface.

During the coupled MD-FEM simulation, a spatial average within each k^{th} IVC is performed to yield the center of mass displacement, $\vec{\delta}_{CM,k}$, which is further averaged over a certain period of M MD time steps to yield the statistical displacement vector, $\vec{\delta}_{I,k}$

$$\vec{\delta}_{I,k} = \left\langle \vec{\delta}_{CM,k} \right\rangle_t = \frac{1}{M} \sum_{j=1}^{M} \left(\vec{r}_{CM,k}(t_j) - \vec{r}_{CM,k}(0) \right). \tag{3.1}$$

In the above expression, $\vec{r}_{CM}(t_j) = \frac{1}{N_k} \sum_{i=1}^{N_k} \vec{r}_i(t_j)$ is the center of mass of the IVC containing N_k atoms at positions $\vec{r}_i$ at time t_j of the j^{th} MD step. The mass center displacement, $\vec{\delta}_{CM,k}$, in Equation (3.1) is calculated relative to the initial zero-displacement position of the k^{th} IVC, $\vec{r}_{CM,k}(0)$. The determination of this initial position is discussed in Appendix 3.A. In turn, the IVCs distribute reaction forces from the interface finite element nodes as external forces applied to the corresponding atoms within the IVC.

3.2.3 Surface MD Region

In order for the MD domain to deform freely in response to applied reaction forces, it is modeled using free surface boundary conditions. However, the existence of a free surface introduces several undesirable effects in the MD system. First, it creates surface tension forces that must be removed to avoid distorting the MD response. Second, because atoms that should lie within the cutoff radius of the free surface-atom's potential are missing, the coordination number of the surface atoms is reduced so they are less strongly bonded to the surrounding atomic field than those within the interior. Under sufficiently large reaction forces, these atoms may be separated from the surface layer causing a surface degradation within the MD domain. To mitigate these free surface effects and to stabilize the atoms in the Interface MD Region, a Surface MD Region is introduced as shown in Figure 3.2.

While the Surface MD Region eliminates the free surface effects within the Inner MD Region, it also introduces an undesirable fictitious stiffness that elastically constrains the deformation of the Inner MD Region. The separate effects of surface tension and the fictitious stiffness cannot be computed independently. However, their combined effect may be defined as a resultant force, $\vec{f}_s$, which acts at the boundary between the Surface MD Region and the Interface MD Region, and is given by the sum of two components expressed as

$$\vec{f}_s = \vec{\xi} + \vec{\tau}\,. \tag{3.2}$$

In Equation (3.2), $\vec{\xi}$ is the elastic reaction of the Surface MD Region under deformation and $\vec{\tau}$ is the force that results from the surface tension. Both forces are shown in Figure 3.3.

A way to mitigate both the surface tension and the elastic response of the Surface MD Region is to estimate and compensate for the force $\vec{f}_s$. In the ideal case, when $\vec{f}_s$ is fully compensated, the Surface MD Region acts as if it possesses zero stiffness and experiences no surface tension, thereby mitigating spurious influences on the Inner MD Region. Subdividing the Surface MD region into a number of SVCs helps to follow the variations of $\vec{f}_s$ along the perimeter of the Interface MD Region. For convenience, the partitioning of SVCs can be made to follow the IVC partitioning of the Interface MD Region. The resultant force is then calculated individually for each SVC. To compensate for $\vec{f}_s$, a counterforce, $\vec{f}_c$, is computed along the IVC/SVC interface and then distributed over the atoms of each SVC in a similar manner as the nodal reaction forces are applied to the IVCs of the Interface MD Region. The calculation of the counterforce, $\vec{f}_c$, is presented in Appendix 3.B.

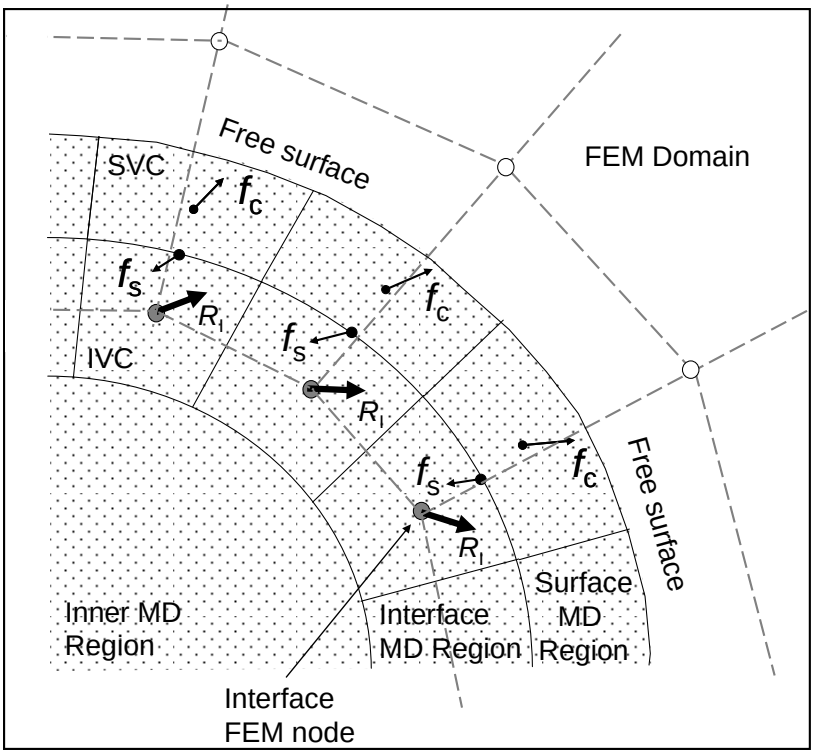

Figure 3.3**.** Forces within the Interface and Surface MD Regions. R_I are FEM reaction forces, f_s are the resultant surface region forces, and f_c are applied compensating forces.

3.2.4 Phonon damping

Both the IVCs and SVCs serve the additional role of providing a dissipative damping mechanism for phonons propagating into the interface. Potential sources of phonon generation are the application of the FEM reaction forces to the IVCs and the resonant elastic oscillations in the dynamic MD region. Phonons can also be generated from within the Inner MD Region as a result of simulated atomistic processes. In the current application of ESCM, these oscillations must be damped in order to achieve equilibrium with the static FEM domain. A number of different damping schemes have been addressed in the literature. Holian and Ravelo [89], and more recently, Schäfer et al. [90], found that applying linearly increasing viscous damping to the atoms in a region

surrounding the center of the MD system can effectively absorb the intense phonon waves coming from a propagating crack. In this scheme, a friction force, $\vec{\eta}$, is given by

$$\vec{\eta} = -\chi \vec{\mathbf{v}} \tag{3.3}$$

and is applied to the atoms of the damped region in proportion to the atom's velocity, $\vec{\mathrm{v}}$, and an appropriately chosen viscous coefficient χ [90,91]. The method is efficient and simple to implement. Its drawback is that it erroneously decreases the local temperature in the damping region resulting in undesirable strain gradients because of thermal contraction.

To avoid disturbing the thermal field, the damping used in the present method is based on a modified form of Equation (3.3), where, instead of being proportional to each individual atom's velocity, $\vec{\eta}$ is set proportional to the group velocity of the mass center of a certain volume of *N* atoms. The frictional force, $\vec{\eta}$, and the group velocity of the mass center, $\vec{v}_{cm}$, are given by

$$\vec{\eta} = -\chi \vec{\mathbf{v}}_{cm}; \quad \vec{\mathbf{v}}_{cm} = \frac{1}{N} \sum_{i=1}^{N} \vec{\mathbf{v}}_i \tag{3.4}$$

By controlling the size of this damping region, one can damp phonons of wavelengths larger than the volume size while leaving the shorter wavelengths associated with random thermal fluctuations unaffected because their contribution to the group velocity averages to zero. Phonons introduced by the finite element mesh cannot have wavelengths smaller than the distance between the interface finite element nodes. Thus, it is convenient to choose both the Interface and Surface MD Regions as the volumes in which damping is applied.

To ensure gradual stepwise increase of the viscous coefficient, χ, from zero to χ_{max}, the Interface and the Surface MD Regions are additionally subdivided into *K* layers of

atoms parallel to the interface line. The layer thickness is equal to the range of the applied interatomic potential (0.65 nm). In each layer, χ increases by a fixed amount $\Delta\chi$ starting from $\Delta\chi$ for the innermost layer, which neighbors the Inner MD region, to $K\Delta\chi = \chi_{max}$ for the outermost layer, at the edge of the MD domain. The damping volumes used for calculating the group velocity in Equation (3.4) are the cross-sections of the layers with the IVCs and SVCs.

A discussion of criteria for the selection of the value of the viscous coefficient, χ, can be found in Schäfer et al. [90]. In those instances where viscous wave damping is not adequate (e.g., collisional dynamics), the more precise non-reflective boundary condition techniques discussed in Moseler et al. [91], Cai et al. [92], and Park et al. [93] may be implemented.

3.2.5 MD-FEM coupling

The MD-FEM coupling in the ESCM is achieved through an iterative equilibration scheme between the MD region and the FEM domain. In this scheme, iterations begin with displacements at the MD/FE Interface that are calculated as statistical averages over the atomic positions within each IVC and averaged over the time of the MD run. These average displacements are then imposed as displacement boundary conditions, $\{\vec{\delta}_I\}$, on the FEM domain. The resulting FEM BVP is then solved to recover new interface reaction forces, $\{\vec{R}_I\}$, resulting from the applied interface displacements and any imposed far-field loading. The new interface reaction forces, $\{\vec{R}_I\}$, are then distributed to the atoms in the IVCs, thus defining new constant traction boundary conditions on the MD system. This MD-FEM iteration cycle repeats until a stable equilibrium of both displacements and forces between the atomistic and continuum material fields is established at the interface. The governing equations of motion for the MD system and FEM domain and the numerical coupling procedure are presented next.

The stiffness of the material in the FEM domain is described through a partitioning of the global stiffness matrix into a set of stiffness submatrices, $[K_{\alpha\beta}]$, with $\alpha,\beta = V, F, I$ indicating: V as variables within the interior of the FEM domain; F as far-field variables, and I as interface variables. Using these definitions, the static continuum equations of state at the n^{th} FEM update at time t_n are given by

$$\begin{bmatrix} [K_{VV}] & [K_{VF}] & [K_{VI}] \\ [K_{FV}] & [K_{FF}] & [K_{FI}] \\ [K_{IV}] & [K_{IF}] & [K_{II}] \end{bmatrix} \begin{Bmatrix} \{\delta_V(t_n)\} \\ \{\delta_F(t_n)\} \\ \{\delta_I(t_n)\} \end{Bmatrix} = \begin{Bmatrix} \{R_V(t_n)\} \\ \{R_F(t_n)\} \\ \{R_I(t_n)\} \end{Bmatrix} \tag{3.5}$$

To ensure that the FEM domain has the same elastic properties as the MD system, the stiffness terms in the $[K_{\alpha\beta}]$ submatrices are calculated from the anisotropic elastic constants derived from the MD interatomic potential [72] at the same temperature as the MD simulation. The finite element model is subjected to two types of displacement boundary conditions: (i) the far-field displacements $\{\delta_F\}$, which define the load over the entire coupled MD-FEM system; and (ii), the interface displacements $\{\delta_I\} = (\vec{\delta}_I^{\,1}, \vec{\delta}_I^{\,2}, .. \ \vec{\delta}_I^{\,k}, ..)$, which represent the deformation response of the MD system at the 1^{st}, 2^{nd}, ... , and k^{th} IVC.

The solution for the unknown displacements in the interior of the FEM domain, $\{\delta_V\}$, is given by

$$\{\delta_V(t_n)\} = [K_{VV}]^{-1}(\{R_V(t_n)\} - [K_{VF}]\{\delta_F(t_n)\} - [K_{VI}]\{\delta_I(t_n)\}) \tag{3.6}$$

which allows the calculation of the interface reaction forces, $\{R_I(t_n)\} = (\vec{R}_I^{\,1}, \vec{R}_I^{\,2}, .. \ \vec{R}_I^{\,k}, ..)$ of the 1^{st}, 2^{nd}, ... , and k^{th} IVC to be obtained from

$$\{R_I(t_n)\} = [K_{IV}]\{\delta_V(t_n)\} + [K_{IF}]\{\delta_F(t_n)\} + [K_{II}]\{\delta_I(t_n)\} \tag{3.7a}$$

together with the far-field forces of constraint

$$\{R_F(t_n)\}=[K_{FV}]\{\delta_V(t_n)\}+[K_{FF}]\{\delta_F(t_n)\}+[K_{FI}]\{\delta_I(t_n)\} \tag{3.7b}$$

The dynamics of an atom i of mass $\mu^{(i)}$ at position $r^{(i)}$ in the embedded MD regions is described by Newton's equations of motion

$$\begin{aligned} &m_i\,\ddot{\vec{r}}_i = \vec{f}_i; && i \in \text{Inner MD Region} \\ &m_i\,\ddot{\vec{r}}_i = \vec{f}_i + \vec{R}_I^k / N_I^k - \chi\,\vec{\mathbf{v}}_{cm}^k; && i \in (IVC)_k \text{ Interface MD Region} \\ &m_i\,\ddot{\vec{r}}_i = \vec{f}_i + \vec{f}_c^{\,k} / N_S^k - \chi\,\vec{\mathbf{v}}_{cm}^k; && i \in (\text{SVC})_k \text{ Surface MD } R\text{egion} \end{aligned} \tag{3.8}$$

The atoms in the Inner MD Region experience only the atomic force $\vec{f}_i = \sum_j \vec{f}^{\,(i,j)}$ resulting from their j^{th} neighbors. The term, $\vec{f}^{\,(i,j)}$, is expressed by Equation (3.B4) as shown in Appendix 3.B. The atoms in the interface region, assigned to a given k^{th} IVC, are subjected to the additional external force, $\vec{R}_I^k$ (Equation (3.7a)), which is distributed over the number of contained atoms, N_I^k. The atoms in the Surface MD Region belonging to a given k^{th} SVC experience the additional counterforce, $\vec{f}_c^{\,k}$, which is distributed over the N_S^k atoms contained in their volume. In order to maintain the continuity of forces between adjacent cells, the force distribution is interpolated with a linear (or higher order) interpolation between atomic positions as a function of each atom's distance from the mass center of its associated cell. In the present study, a simple linear interpolation was applied. For the equations governing the Interface and the Surface MD Regions in Equation (3.8), the viscous friction force, $\chi\,\vec{\mathbf{v}}_{cm}^k$, defined in Equation (3.3), is applied uniformly to the atoms contained within the IVCs and SVCs.

During the MD integration of Equation (3.8) for a period $\Delta t_{\text{M}} = M\Delta t$, where M is the number of time steps and Δt is the duration of the time step, the new average displacements $\{\delta_I(t_{n+1})\}$ are computed from Equation (3.1). The new atomistic

displacements for the next FEM update at time $t_{n+1} = t_n + \Delta t_M$ are reapplied in Equations (3.6) and (3.7a) to calculate the next iterative update of the recovered forces, $\{R_I(t_{n+1})\}$. During the same time interval, the compensation forces $\{f_c(t)\}$ are also evolving through Equation (3.B15) (in Appendix 3.B). The period Δt_M is selected by a determination of the convergence rate to a stable equilibrium state between the MD region and the FE domain. The algorithm for the entire coupled simulation is summarized in Figure 3.4.

Convergence of the interface forces $\{R_I\}$ and displacements $\{\delta_I\}$ can be achieved only if the MD system can reach a force balance with the surrounding FEM system. Once equilibrium is attained, the motion of the IVC mass centers is zero, or

$$\dot{\vec{r}}_{CM}^{\,k} = \vec{v}_{CM}^{\,k} = 0\,, \tag{3.9a}$$

and the change of the total momentum, Δp_k, of any k^{th} IVC due to the FEM reaction force for the period of the MD simulation of M time steps is also zero, or

$$\Delta \vec{p}_k = \sum_{n=1}^{M} \sum_{i=1}^{N_I^k} m_i \, \ddot{\vec{r}}_i(t_n) \Delta t = 0\,. \tag{3.9b}$$

Performing the same double summation on the second equation in Equation (3.8) results in

$$\frac{1}{M} \sum_{m=1}^{M} \sum_{i=1}^{N_I^k} \vec{f}_i(t_m) = \left\langle \sum_{i=1}^{N_I^k} \vec{f}_i \right\rangle_t = -\vec{R}_I^k \tag{3.10}$$

which states that, at equilibrium and in accordance with Newton's 3rd law, the FEM reaction force becomes equal and opposite to the average MD atomic force in the corresponding k^{th} IVC. Equation (3.10) thus expresses the establishment of static force equilibrium between the MD system and the FEM domain.

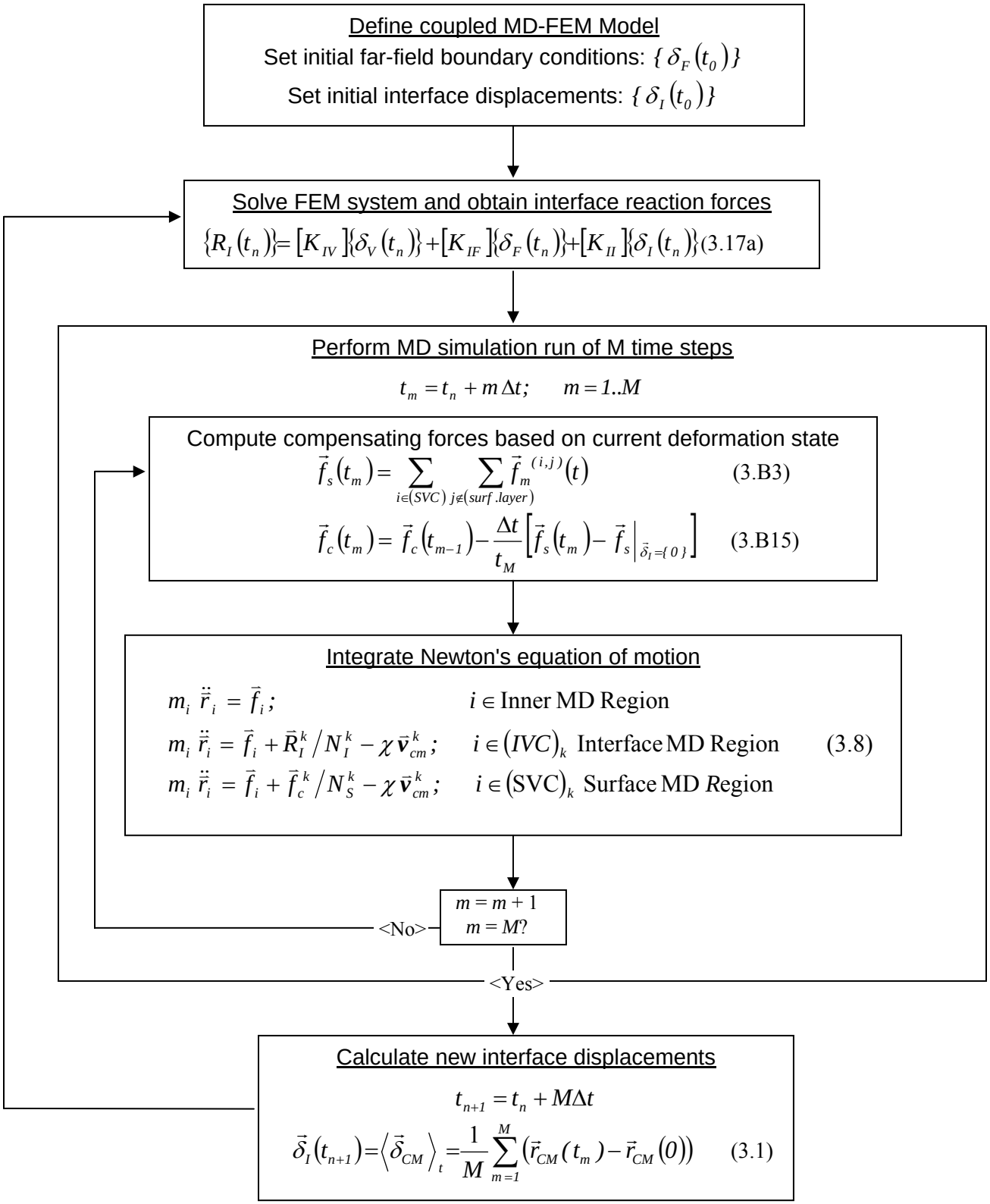

Figure 3.4. Flowchart summarizing the coupled analysis procedure.

3.3 Numerical Verification of the ESCM

3.3.1 The simulation models

Four test cases are considered to investigate the behavior of ESCM. First, the effectiveness of the application of compensation forces for the mitigation of surface tension effects is examined. Second, the dynamic behavior of the MD system is explored by varying the rate and sequence of applied external loads. Third, the stress-strain continuity between the MD region and the FEM domain is assessed through comparison with an exact solution of an elastically deformed plate with a circular hole. Fourth, a simulation of the propagation of an edge crack through the FEM domain into the MD system is performed to determine the suitability of ESCM for solving problems related to crack growth.

The model geometry used in all of the verification studies is shown in Figure 3.5. This model consists of a circular Inner MD Region of diameter, d_{MD}, that is embedded in a larger exterior square FEM domain of elastic material with a side dimension of $d_{FE} = 20d_{MD}$. A general discussion of issues related to model construction in applying ESCM is presented in Appendix 3.A, while the specifics of the MD and FEM models will be discussed next.

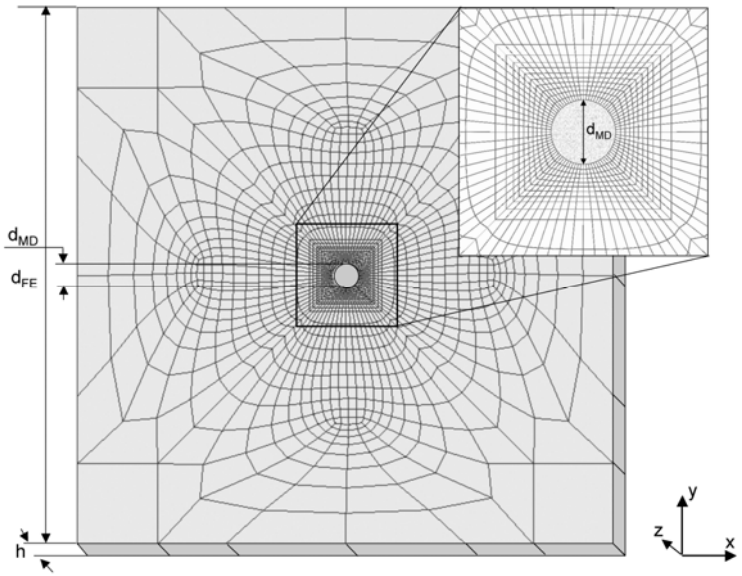

Figure 3.5. Model geometry of the test MD-FEM coupled system.

3.3.1.1 The MD model

The material for the simulation models was chosen to be a perfect crystal of aluminum. The atomic properties of aluminum were represented by the embedded atom model (EAM) potential of Mishin et al. [72], which was fitted to give the correct zero-temperature lattice constant, a_o = 0.405 nm, elastic constants, cohesive energy, vacancy formation energy, etc. For accurate coupling, material properties of the FEM model are obtained directly from the EAM interatomic potential.

The first three test simulations, presented in Sections 3.3.2.1 to 3.3.2.3, use a common MD system which will be described here. The forth test is performed on a bicrystal MD model which will be described in Section 3.3.2.4. For the first three tests, the MD domain is constructed as a circular disk of monocrystalline aluminum with its main crystallographic axes [1 0 0], [0 1 0], and [0 0 1] oriented along the *x*-, *y*-, and *z*-directions, respectively. The MD system is simulated with periodic boundary conditions along the *z*-direction and with free surface boundary conditions along its perimeter. These boundary conditions allow the MD domain to deform in an unconstrained manner in the *x*-*y* plane under the external reaction forces from the FEM domain while maintaining constant zero pressure along the *z*-direction using the Parrinello-Rahman constant-pressure simulation technique [48]. Constant temperature is maintained by applying the Nose-Hoover thermostat [76] in the Inner MD region only. A new application of the Nose-Hoover thermostat is used that involves decomposing the MD region into local regions and applying the thermostat independently to better damp out 'hot spot' that can develop in highly defected areas such as around crack tips. The thickness of the plate along the *z*-axis is equal to $h = 5a_o \approx 2.0$ nm (Figure 3.5). Though very thin, the MD system mechanically behaves as an infinitely thick plate due to the applied periodic boundary conditions along the *z*-direction. The tests were performed at near zero temperature (T = 10 K) to minimize the thermal noise and at room temperature (T = 300 K) to demonstrate ESCM for more practically relevant situations in which thermal effects are important. For the models used in the present work, effective viscous wave damping in the Interface and the Surface MD regions was achieved by setting χ_{max} = 3 eVps/nm^2.

For this χ and a damping layer with a width of 0.65 nm, the effective average temperature in the damping volumes decreased by only 10% compared to the bulk temperature.

Four different models were prepared with the diameter of the circular MD system varying from 22 nm to 164 nm. Reference positions of the IVC mass centers, $\vec{r}_{CM}(0)$, were determined using methods outlined in Appendix 3.A. The width of the Surface MD Region, defined at the free surface of the MD system, was fixed at 2 nm.

3.3.1.2 The FEM model

The elastic continuum region was modeled using 8-node hybrid-stress hexahedral finite elements that have a reduced sensitivity to mesh distortion compared to standard displacement-based elements and allow explicit stiffness coefficients to be analytically derived thereby minimizing their computational requirements [94,95]. The elastic constants in the material constitutive matrix were derived from the interatomic potential for pure aluminum at T = 10 K. The values were averaged for uniaxial stresses from 100 to 500 MPa, accounting for the non-linear material properties, as: C_{11} = 112.7 GPa, C_{12} = 59.4 Gpa, and C_{44} = 30.6 GPa. These values differ by only 3% from the static, zero Kelvin elastic constants reported for this potential in Mishin et al. [72].

The continuum finite element model contains an open inner region of diameter d_{MD}, within which the atomistic domain is embedded. Along its perimeter, 80 nodes at $z = +h/2$ and 80 nodes at $z = -h/2$ were placed to form 160 FEM interface nodes to communicate with the embedded MD system.

The dimensions of the finite element mesh, d_{FE} , d_{MD} and h as shown in Figure 3.5 were initially defined through the proportions of $d_{FE} : d_{MD} : h = 20 : 1 : 1$. Then, a direct scaling of the finite element nodal coordinates was performed such that the dimensions d_{MD} and h matched the dimensions of the MD system. Finally, a second scaling of the FEM system was performed to preserve the outer dimension ratio $d_{FE} : d_{MD} = 20 : 1$.

3.3.2 Numerical test results and analyses

The four test cases selected to interrogate the essential features of the ESCM are presented in the following sections. Discussions assessing results and details of the analyses are included to thoroughly investigate the verification simulations.

3.3.2.1 Verification of the surface tension and the Surface MD Region stiffness compensation

The purpose of this simulation is to estimate the magnitude of the surface forces and their effect on coupling the two computational domains, as well as the efficiency of the compensation procedure to mitigate surface tension effects and the spurious constraint of the Surface MD Region stiffness. The simulation is performed for the case of a homogeneous perfect crystal of aluminum. Because the effect of the surface tension is expected to be relatively weak, the temperature of the simulations was kept at $T = 10$ K to minimize the thermal noise and to increase the sensitivity of the force and pressure measurements.

The pressure inside the system due to surface tension is defined as the radial component of the stress tensor, $p_s = \sigma_{rr}$, averaged over an isolated MD system with free surface boundary conditions in the *x*- and *y*-directions, and periodic, zero pressure boundary conditions applied in the *z*-direction. The definition of virial stress [59] inside the MD system was used. The surface pressure increases from 10 to 80 MPa, with d_{MD} decreasing from 164 to 22 nm as presented in Figure 3.6. The expected dependence of p_s on surface tension, γ, ($p_s = 2\gamma / d_{MD}$) for a cylindrical nanoparticle examined in Yamakov, Saether, Phillips, and Glaessgen [67] is well reproduced. The surface tension, estimated from the slope of a linear fit to the results in Figure 6 as $\gamma = 0.9$ J/m^2, is found to be in the range of the calculated surface energies for the interatomic potential used (γ_s = 0.87, 0.943, and 1.006 J/m^2 for (111), (100), and (110) surfaces, respectively. While the

values for p_s (< 0.1 GPa) are relatively small for a MD simulation (where typical loads are of the order of 1 GPa), particularly for small MD systems, its contribution should not be neglected.

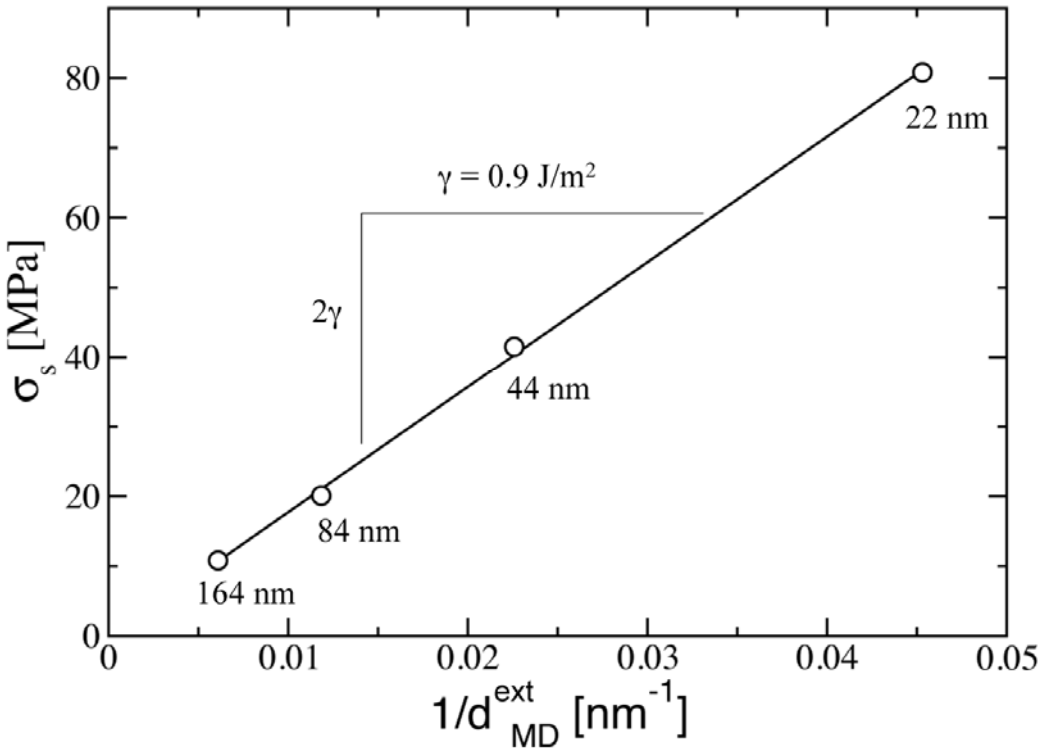

Figure 3.6. Dependence of the pressure p_s caused by the surface tension of a circular MD domain of radius d_{MD} simulated with free surface boundary conditions. The slope is proportional to the surface energy per unit area γ.

The effect of applying a counterforce to compensate for the surface tension is shown in Figure 3.7 for the case of d_{MD} = 44 nm. When no surface compensation force is applied, the internal pressure, p_s, gradually increases from zero due to the evolving effect of surface tension forces and approaches the value of p_s = 41.5 MPa. In contrast, repeating the same simulation with the compensation force applied, quickly reduces p_s to near zero. The short initial increase in the value of p_s observed during the first 10 ps is a result of the iteration procedure (Equation (3.B15)) for adjusting the counterforce, f_c,

having not yet reached convergence and the compensation being not yet complete. The compensation becomes complete approximately 20 ps after the beginning of the simulation.

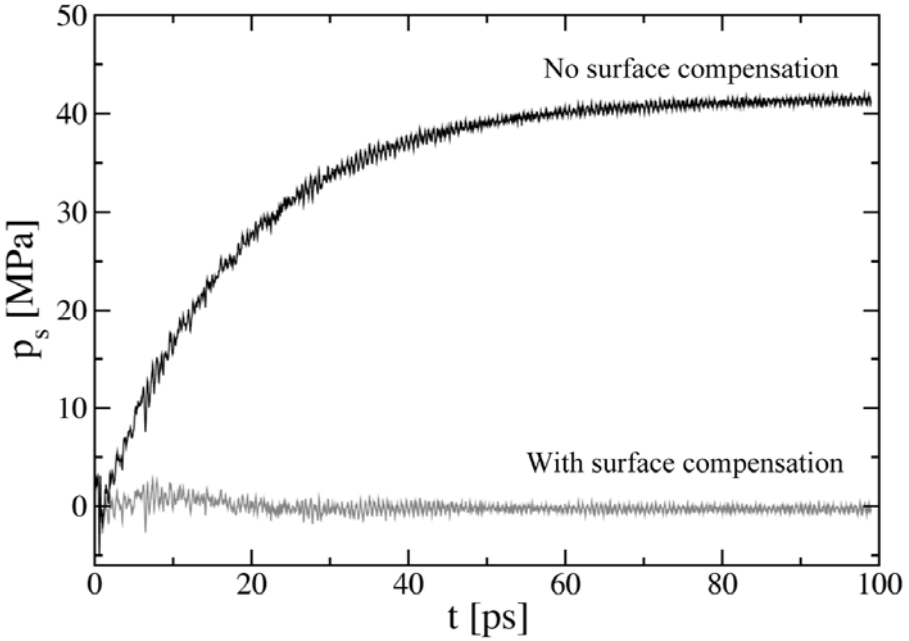

Figure 3.7. Evolution of the internal pressure of a circular MD system with and without surface tension compensation.

Under deformation, the stiffness of the Surface MD Region creates an elastic reaction force that adds to the surface tension. As explained in Section 3.2.3, the iteration procedure for f_c was developed to compensate for both effects. Figure 3.8 shows the combined effect of surface tension and the elastic stiffness of the Surface MD Region on the equilibrium stress state of the Inner MD Region for four different MD system sizes ranging from d_{MD} = 22 to 164 nm at 0.5% far-field strain. As the dynamic response of the MD system strongly depends on its size, to make the simulations comparable, the time t is rescaled by an estimated relaxation time, t_o, for each system size. The relaxation time is defined in the standard way as the period required for an exponential variable to decrease

by 1/e (0.386) of its initial value. In Figure 3.8, the exponential variable is the deviation of the current stress, $\sigma_{xx}(t)$, at time, t, from its equilibrium value, σ_∞, established at t/t_o = 5 with no counterforce, $\vec{f}_c(t)$

$$\sigma_\infty - \sigma_{xx}(t) = e^{-t/t_o} \quad . \tag{3.11}$$

The relaxation time, t_o, increases with increasing size and mass of the MD region. For d_{MD} = 22, 44, 84, and 164 nm (containing 47 600, 190 300, 693 400, and 2 641 000 atoms, respectively), a curve fit to Equation (11) gave t_o = 5.1, 19.5, 61, and 200 ps, respectively.

Initially (t/t_o < 5), no counterforce was applied in the Surface MD Region, and σ_{xx} equilibrated to a lower level compared to the far-field stress, σ_o, of a homogeneously

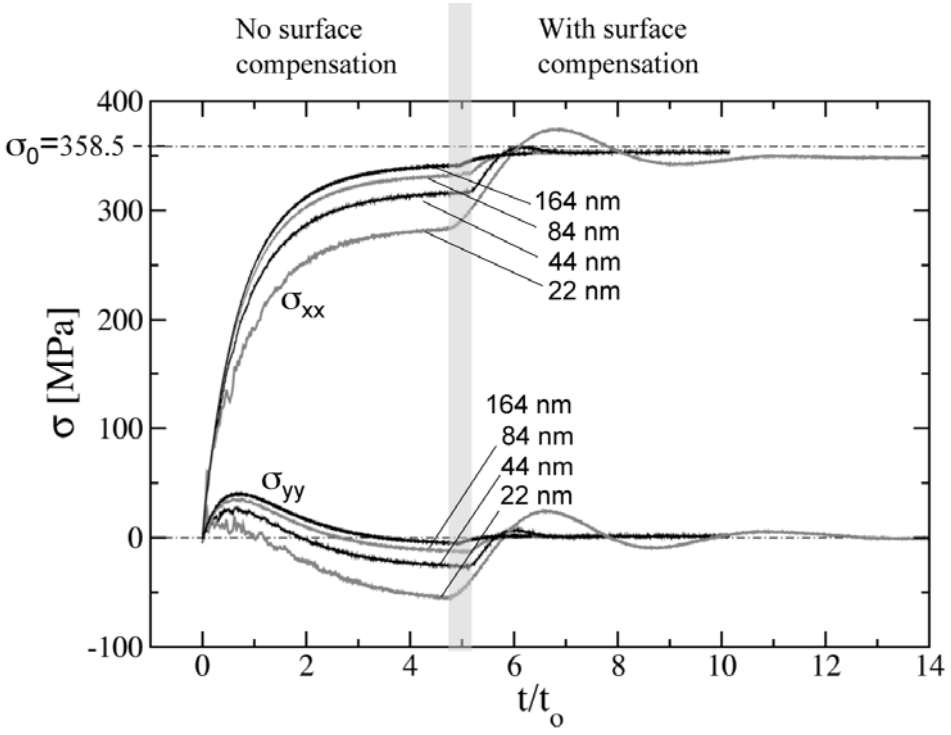

Figure 3.8. Evolution of the longitudinal tensile σ_{xx} and transverse σ_{yy} stress components.

strained plate. The stress due to the Poisson contraction of the unconstrained boundaries ($y = \pm d_{FE}/2$), σ_{yy}, also deviated from the expected zero level. The reason for these deviations is the combined effect of surface tension and the elastic stiffness of the Surface MD Region. The deviations of both σ_{xx} and σ_{yy} decrease proportionally to the increase of d_{MD}, as expected because of the decreasing surface-to-volume ratio. When the counterforce is applied ($t/t_{\mathrm{o}} > 5$), the effect of the spurious forces in the Surface MD Region for all of the tested MD systems of d_{MD} from 22 to 164 nm is almost entirely negated.

3.3.2.2 Simulation of the dynamics of the coupled MD-FEM system

The dynamic behavior of the coupled MD-FEM system in the simplest case of a uniformly loaded homogeneous aluminum plate is depicted in Figure 3.9. The figure presents the stress response of the Inner MD Region to the applied far-field strain. The system is the same as that used for the results in Figure 3.7, with d_{MD} = 44 nm. In this numerical test, the prescribed strain of ε_{xx} = 0.5% was reached in two ways: first, by an instantaneously applied far-field strain of 0.5% at the outer-boundaries of the FEM Domain, and second, by five consecutive increments of 0.1% each. In both cases, the length of the MD iteration run was $\Delta t_{\mathrm{M}} = M\Delta t$ = 1 ps with M = 500 and Δt = 2 fs.

The tensile component of the stress in the MD system, σ_{xx}, converges to nearly the same value for both cases shown in Figure 3.9 and is very close to the far-field stress of the FEM Domain, σ_o ($\sigma_{xx} \rightarrow$ 354 MPa and σ_o = 358.5 MPa). Similarly, σ_{yy} quickly relaxes to zero after a temporary jump in response corresponding to each increase in the applied far-field strain. The test shows that the state of equilibrium, wherein the MD system is in force balance with the FEM Domain, is obtained with little dependence on step size for monotonic loading up to 0.5% strain.

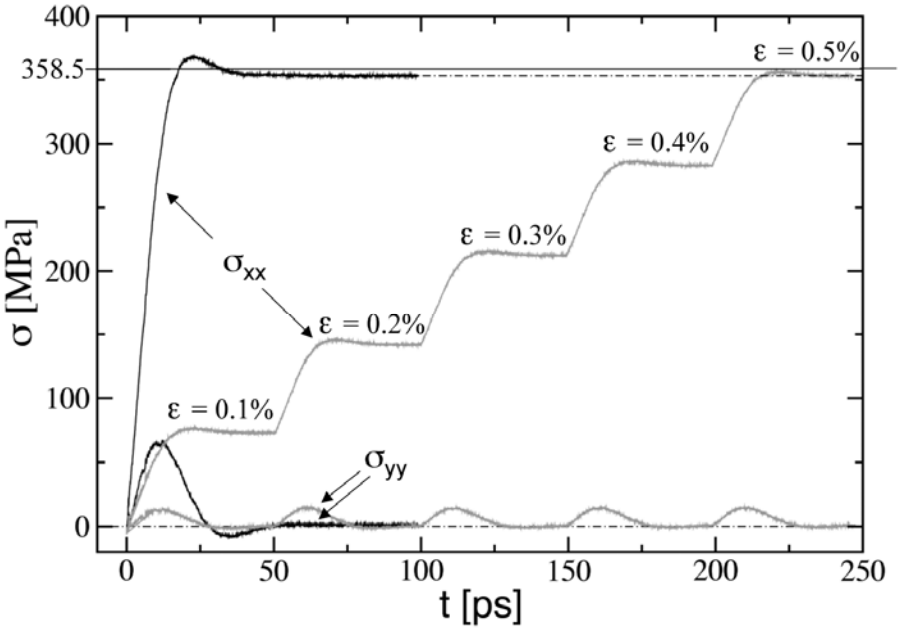

Figure 3.9. Dynamic response of the coupled MD-FEM system under far-field homogeneous tensile strain ε_{xx} applied either instantaneously (black) or in five consecutive increments (gray).

After each strain increment of 0.1%, the MD system reached equilibrium with the FEM domain within approximately 25 ps, which is consistent with the estimate for t_o = 19.5 ps in Figure 3.7 for d_{MD} = 44 nm. This time was approximately the same as for the instantaneous jump to 0.5%. The relatively large response time observed in Figures 3.8 and 3.9 indicates that using a static finite element model (Equation (3.5)) for the continuum part of the system is not suitable for simulating processes in the MD system that are evolving faster than t_o.

3.3.2.3 Test for stress-strain continuity over the MD and the FEM regions: elastically deformed plate with a circular hole

To assess the capability of the ESCM for generating compatible stress-strain fields in the elastic continuum domain and the MD atomistic region, the classic example of a plate with a circular hole subjected to uniaxial loading was used. In addition to having an exact elasticity solution for the slightly anisotropic material properties used [96,97], this model is particularly convenient for two reasons. First, it provides large stress variations (from zero to $2.82\sigma_o$) around the hole, which can be used to test the continuity of the stress field at the MD/FE interface in the case of large stress gradients. Secondly, keeping the peak stress, $2.82\sigma_o$, well below the theoretical elastic limit of the material (recently estimated for the applied interatomic potential to be between 3 and 5 GPa [98] prevents the occurrence of any plastic mechanisms in the MD region, which is not addressed in the present study, and a static elastic equilibrium can be achieved everywhere in the system.

For comparison, an equivalent fully continuum three dimensional anisotropic FE model was also simulated with a hole of radius 20 nm. This model was generated within a square FE mesh of dimension 1.6 μm by 1.6 μm and having the same elastic properties as the FE part of the coupled MD-FEM model.

In both models, the square plate was deformed at 0.5% uniaxial strain along the *x*-direction through fixed displacement-controlled boundary conditions imposed on the outer sides of the FEM system 800 nm away from the hole in the MD domain. At this strain, the far-field stress, estimated in Figure 3.9, is σ_o = 358.5 MPa.

Starting from an undeformed MD region, the coupled MD-FEM iterative simulation was performed on the coupled system until equilibrium was established between the MD domain and the FEM domain whereby $\{\delta_I\}$ and $\{R_I\}$ converged to constant values. The stress field for σ_{xx}, σ_{yy}, and σ_{xy} stress components of the coupled MD-FEM system was calculated and compared with the fully continuum FEM solution that was obtained using the ABAQUS software package [79]. This comparison is shown in Figure 3.10.

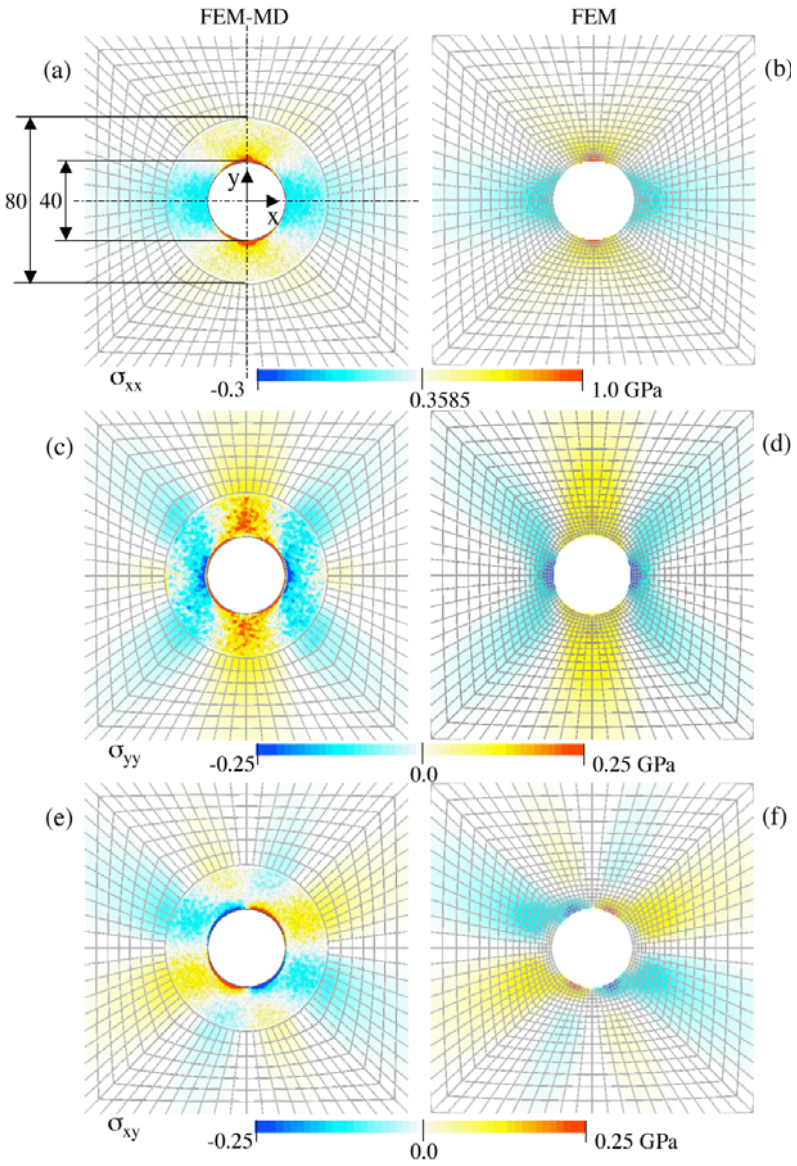

Figure 3.10. Simulation of an open hole specimen. Comparison of the stress field for σ_{xx}, σ_{yy}, and σ_{xy} stress components of the coupled MD-FEM system (a, c, e) with a full three-dimensional anisotropic continuum FEM solution (b, d, f).

The stress profiles for σ_{xx} and σ_{yy} taken along sections coincident with the *x*- and *y*-axes passing through the center of the hole as shown in Figure 3.10(a) are presented in Figures 3.11(a) and 3.11(b), respectively. The continuity of the stress profiles is well preserved at the MD/FE interface apart from fluctuations that result from chaotic atomic

thermal vibrations. Additionally, the stress profiles of the coupled model closely follow the stress profiles of the fully continuum FEM analysis of the equivalent model. The largest discrepancy is observed at the edges of the circular hole, where the MD stress is systematically higher than the continuum solution. This can be explained by accounting for the surface tension effects at the hole surface present in the atomistic domain. From the previous analysis (Figure 3.3) it was found that the normal pressure of a free surface with a curvature radius of 40 nm is p_s = 45 MPa. This value agrees well with the normal component of the stress estimated from the MD simulation (σ_{xx} along the *x*-profile in Figure 3.11(a), and σ_{yy} along the *y*-profile in Figure 3.11(b)) at the edge of the hole, where the corresponding FEM solution approaches zero.

The largest discrepancy is seen for the tangential component of the stress (σ_{yy} along the *x*-profile in Figure 3.11(a) and σ_{xx} along the *y*-profile in Figure 3.11(b)) in the MD system, which deviates substantially from the continuum prediction when approaching the surface of the hole. As shown in Figure 3.11(b), the continuum solution closely approaches the theoretical value of $2.82\sigma_o$ that is calculated for the slightly anisotropic material used. One reason for this discrepancy may be the definition of virial stress, which gives poor convergence and erroneous estimates near free surfaces (Zimmerman et al. [49]). But more likely it is that the continuum model does not correctly account for the nature of the surface tension, which results from the occurrence of missing bonds between the atoms at the free surface.

3.3.2.4 Example of an edge crack simulation along a grain boundary in aluminum

An important application of the ESCM technique described in this paper is the simulation of atomistic processes related to damage. A typical example is the tip of an edge crack, where the idealized elastic stress field decreases as $1/\sqrt{r}$ and extends to a distance *r* from the tip. The crack tip stress field is much larger than a MD system can computationally simulate. A coupled MD-FEM model for this example is presented in

Figure 3.12, where the MD system is used to atomistically simulate the plastic zone at the crack tip, and the FEM domain is used to provide the continuum elastic boundary conditions of a far-field tensile strain of ε_{yy} = 2% applied along the *y*-direction. To investigate the applicability of ESCM at higher temperatures, the simulation was carried out at room temperature (T = 300 K).

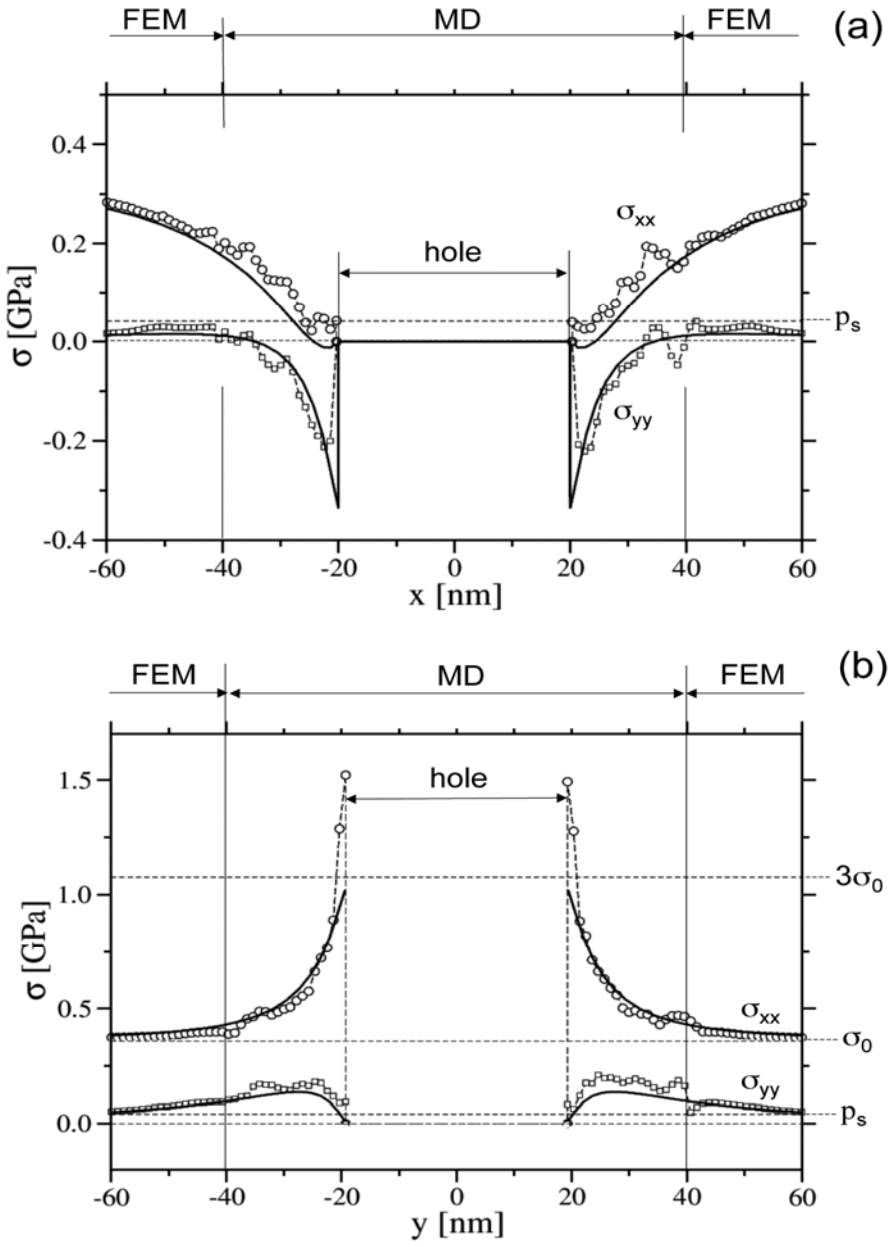

Figure 3.11. Stress profiles in the open hole specimen for σ_{xx} and σ_{yy} along (a) the *x*-axis and (b) the *y*-axis scanned through the center of the hole. The symbols represent the ESCM simulation data, while the full lines represent fully continuum FEM results. For reference, the surface tension induced pressure p_s is also shown.

The dimensions of the system are: h = 2.9 nm, d_{MD} = 45 nm, and d_{FE} = 900 nm. The MD system represents a bi-crystal with a high-angle grain boundary formed between the two crystals along which the edge crack propagates. In the selected coordinate system of the model, the orientation of one of the crystals is: (x:[$7\ \bar{7}\ \bar{1}0$]; y:[$5\ \bar{5}\ 7$]; z: [$1\ 1\ 0$]), and the orientation of the other crystal is: (x:[$7\ \bar{7}\ \bar{1}0$]; y:[$\bar{5}\ 5\ \bar{7}$]; z: [$1\ 1\ 0$]). In this way, both crystals are mirror images of each other relative to the crystallographic plane {$5\ 5\ 7$}, which becomes the plane of the grain boundary (GB) between them. The GB thus formed is a <1 1 0> $\sum$99 symmetric tilt GB. Crack propagation along this GB at a cryogenic temperature of T = 100 K has been discussed in Chapter 2

In the stresses discussed in Chapter 2, it was found that, while in one direction the crack becomes blunted by deformation twinning, in the opposite direction it propagates in a brittle-like manner with very little dislocation emission. The latter direction has been chosen as the propagation direction for the edge crack of the simulation in Figure 3.12. The simulation using the ESCM approach performed at room temperature showed higher dislocation plasticity than at T = 100 K [67,43,99]. The remaining problem is how to transfer this plasticity to the FEM continuum. Some work related to this issue has been started independently by Shilkrot et al. [31,32], Curtin et al. [33], and Qu et al. [100], where the CADD coupling methodology has been developed to follow and transmit dislocations between the atomistic and continuum regions. However, that methodology is not employed here.

What is essential in the example shown in Figure 3.12 is that the ESCM approach preserves the continuity of the stress – strain field at the MD-FE Interface even for a dynamic problem such as crack propagation simulated at room temperature. The depicted profile shows the continuity of stresses across the boundary when the crack speed is slow compared to the elastic response time of the system. In the example shown in Figure 3.10, the crack propagation speed was approximately 100 m/s or on the order of 1/30 the speed of sound.

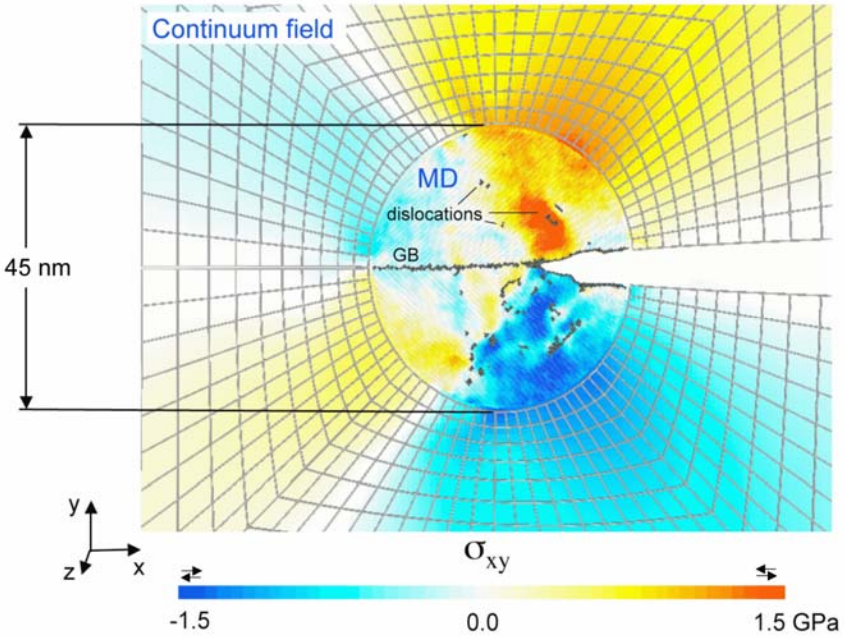

Figure 3.12. ESCM simulation of an edge crack propagating along a <110>/Σ99 symmetric tilt grain boundary in Al at 2% far-field uniaxial strain.

3.4. Concluding remarks for Chapter 3

A new statistical approach to couple MD with FEM simulations, denoted the embedded statistical coupling method (ESCM), has been developed. The approach is based on solving the boundary value problem through an iterative procedure for both MD and FEM systems at their common interface. The two systems are simulated independently, and they communicate only through their boundary conditions. The FEM system is loaded along the MD/FE Interface by nodal displacement boundary conditions that are obtained as statistical averages of the atomic positions in the MD system at the mass centers of representative interface volume cells (IVCs) associated with each finite element node along the interface. The MD system, in turn, is simulated under periodically updated constant traction boundary conditions that are obtained from the FEM system as reaction forces to the MD displacements at the interface. This iterative approach allows

the continuity at the MD/FE interface to be achieved at different length and time scales inherent to both systems without the need of redefining continuum quantities at the atomic scale and atomic quantities at the continuum scale, thus avoiding this theoretically controversial concept.

Using static FEM calculations for the continuum part of the system, the ESCM shows excellent convergence for systems simulated under static elastic equilibrium and preserves stress continuity at the MD/FE Interface for systems exhibiting relatively slow dynamics governed by the MD simulation of the atomistic part of the system. Additional study needs to be performed to check if the implementation of a dynamic FEM simulation can improve the dynamics of the system away from equilibrium.

Compared to the widely used direct coupling methods, ESCM does not discretize the MD/FE Interface to atomistic scales but uses a statistical mapping of atomistic behavior to a continuum FEM representation. ESCM presents a simple and flexible technique in providing elastic boundary conditions for an MD model and eliminates some of the finite-size artifacts inherent to a purely atomistic simulation. Because of the statistical connection between the MD and the FEM systems, there is no limitation on the temperature of the atomistic system as long as the thermal corrections to the elastic properties of the continuum system are considered.

In general, the method is relatively easy to implement. Although a specialized standalone FEM code was developed to generate results in the present work, any conventional FEM code, including commercial packages, can be used to solve the FEM part of the model. In addition, only small modifications to an otherwise conventional MD code are necessary to apply the constant tractions to the MD system. Other modifications to the MD code would include the incorporation of the developed phonon damping procedure plus the addition of a local Nose-Hoover thermostat to effectively thermalize regions that exhibit local ‘hot spots’ such as at crack tips.

The verification simulations performed in this study demonstrated the effectiveness of the ESCM to couple atomistic and continuum modeling into a unified multiscale simulation. Several idealized test cases were analyzed to interrogate the behavior of the ESCM. First, the effectiveness of using the Surface MD Region to provide means to emulate infinite boundary conditions for the MD system was verified. Second, the dynamic behavior of the coupled MD-FEM system was explored demonstrating convergence to the same equilibrium state while varying the rate and sequence of applied loads. Third, the stress-strain continuity between the MD region and the FEM domain was validated using the model of an elastically deformed plate with a circular hole. Finally, simulating the slow propagation of an edge crack was performed to demonstrate the overall representational capability of the coupled MD-FEM model in a system evolving quasi-statically.

APPENDIX 3.A

ESCM Model Construction

In the ESCM approach, the statistical basis for numerically coupling the different computational frameworks provides a much less restrictive set of interfacing requirements compared to DC methods and, thus, allows a greater independence in the construction of the associated MD and FEM models. This aspect of ESCM, however, results in additional preparatory work in constructing the coupled model, primarily involving the preparation of the initial state of the MD region.

The construction procedure starts with the definition of the shape and size of the MD region and FEM domain. The dimensions of the MD system are defined by the dimensions of the combined Inner, Interface, and Surface MD Regions. The dimensions of the FEM domain are selected such that the outer boundary defines the desired overall material domain and the inner boundary coincides with the IVC mass centers along the MD/FE Interface. The finite element mesh conveniently provides a regular distribution of node locations to be used in a Voronoi construction of the IVCs along the MD/FE Interface. Appropriate interpolation methods (e.g. linear interpolation employing finite element shape functions) must be used to accurately map quantities (e.g. interface displacements) between the IVC mass centers and the corresponding finite element nodes.

It is additionally important in the construction of the ESCM model that the reference states of the MD and FEM systems coincide as closely as possible. For a static FEM domain, the displacements are zero when the applied forces are zero. For a MD region, displacements are statistical quantities that can include some statistical error in their estimate that needs to be minimized.

Preparatory simulations of the MD region involve thermalization, equilibration, and the determination of external compensating forces. The calculation of these compensating forces are discussed in Appendix 3.B and are required to maintain the initial atomic reference states that are necessary for this domain to exhibit the response of an infinite

system influenced only by external forces when coupled to the FEM computational domain. To perform the preparatory simulations, an initial MD model of rectangular shape is chosen that is large enough such that the geometry of the desired MD region (which in the present work is a circular disc) is contained as a subset. This subset can subsequently be extracted by removing the atoms outside the desired MD region boundaries (see Figure 3.A1).

To accurately define the zero-displacement reference state of the MD region, the system is thermally equilibrated at zero stress and simulated as an NPT (constant number of atoms, constant pressure, and constant temperature) ensemble under periodic boundary conditions (PBC) in all three dimensions. PBCs are necessary during this step to avoid the presence of a free surface because the surface tension would produce a pressure, p_s, on the surface, resulting in erroneous zero-displacement positions for the IVC mass centers.

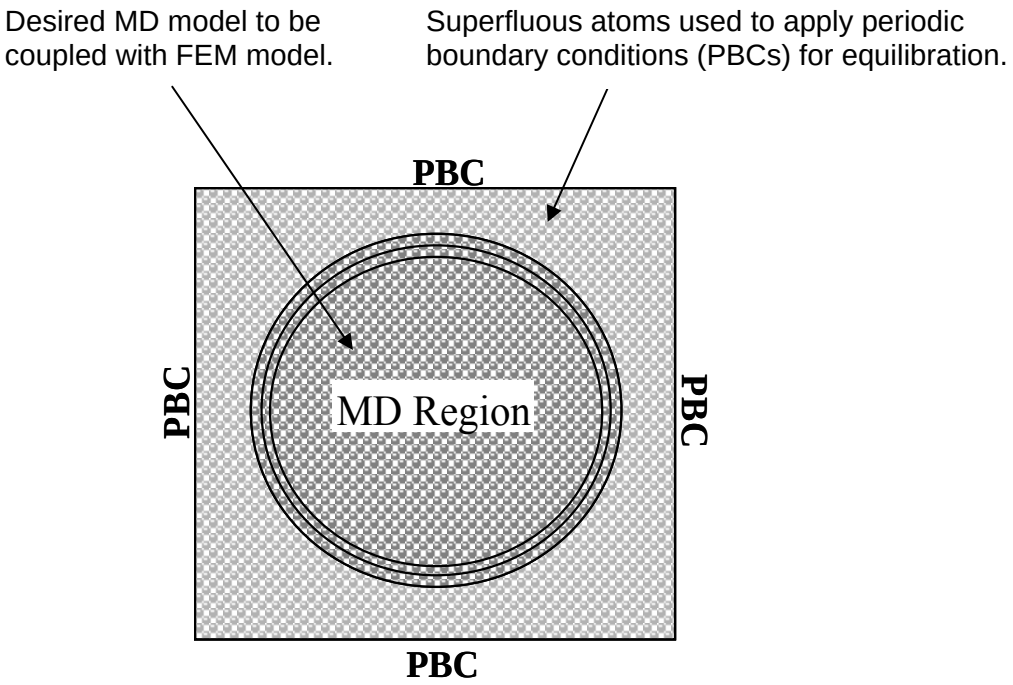

Figure 3.A1**.** Generation of MD model by equilibrating within a larger rectangular MD model under PBCs.

After achieving equilibrium, an additional MD simulation under PBCs at zero pressure and constant temperature is carried out to obtain the statistical time average of the mass centers. Larger IVCs and longer initialization times result in smaller statistical errors in the reference state because the statistical error of the estimated averages depends on the number of atoms, N, per IVC and the time, t, of the simulation as $1/\sqrt{N t}$. Therefore, the simulation should be carried out long enough such that any systematic error is reduced to a level having negligible influence on the coupled simulation.

Two additional issues must be addressed in the model generation. First, the width of the Surface MD Region will generally not fully contain the domain of atoms having equilibrium states disrupted due to free surface effects. Therefore, an additional simulation will be required to obtain the forces, $\vec{f}_s\big|_{\vec{\delta}_I=\{0\}}$, in the reference state as explained in Appendix 3.B (Equation (3.B15)). Second, the elastic anisotropy of the FEM domain is a function of the crystallographic orientation of the atomistic microstructure and should be derived from the interatomic potential used in the MD system under the equivalent thermal and mechanical loading conditions to avoid mismatch of elastic properties at the interface.

The operations discussed in this appendix complete the model construction. This model, together with applied far field boundary conditions, is used to start the first MD – FEM iteration of the coupled simulation.

A summary of the individual steps involved in developing the complete ESCM model is presented in Figure 3.A2.

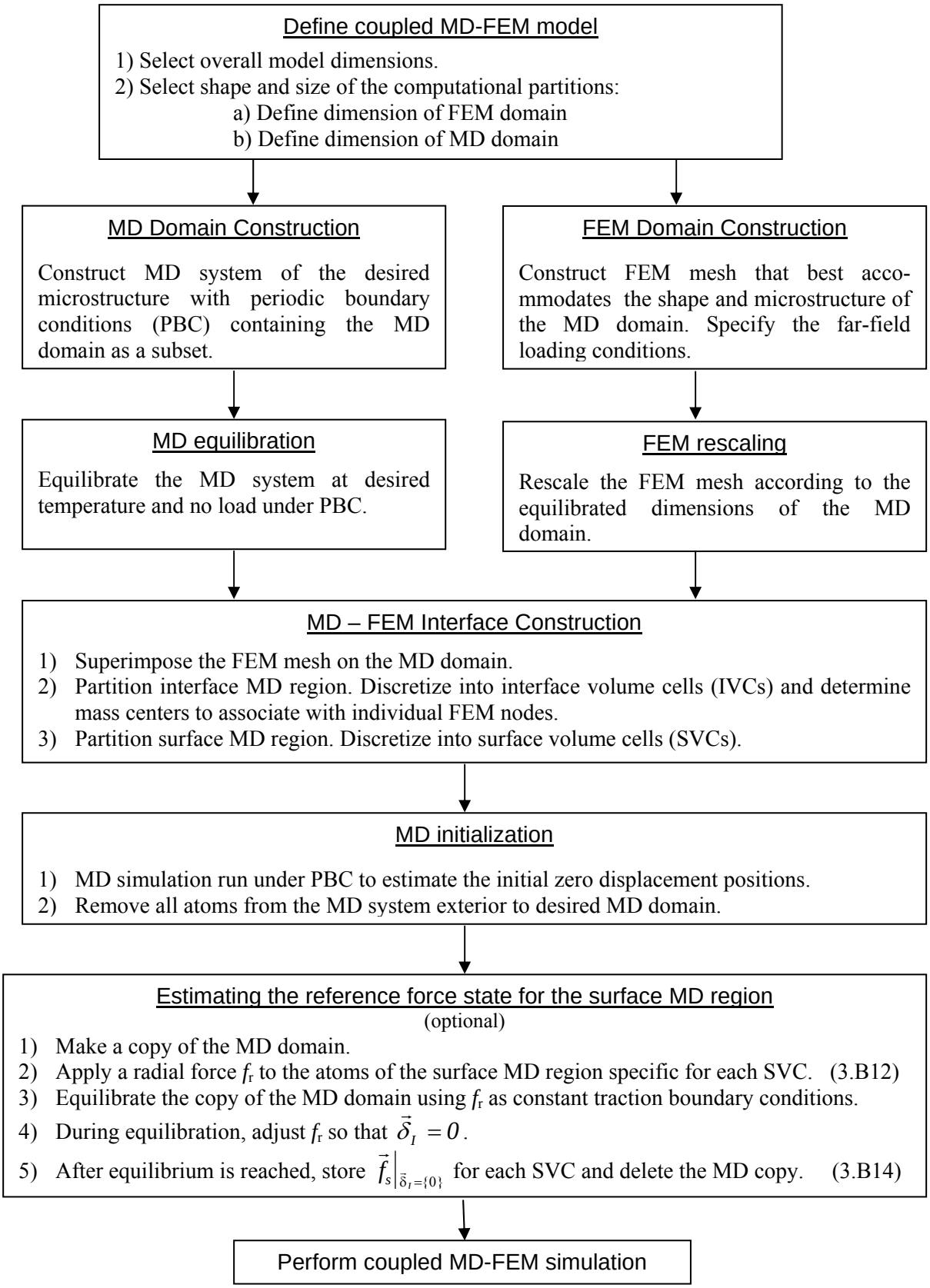

Figure 3.A2. Flowchart summarizing the MD-FEM model construction.

APPENDIX 3.B

Calculation of Compensating Forces

As discussed in Section 3.2.3, there are two spurious forces created within the MD system in the ESCM approach that have to be eliminated. One is the surface tension force, $\vec{\tau}$, created by the applied free surface boundary conditions at the perimeter of the MD system. The other is the elastic reaction force, $\vec{\xi}$, of the Surface MD Region created by its stiffness as the MD system deforms. The method to neutralize both of these forces is based on applying an external counterforce to the atoms within the Surface MD Region

$$\vec{f}_c = -\left(\vec{\xi} + \vec{\tau}\right) \tag{3.B1}$$

The counterforce is specifically determined for each SVC and is uniformly distributed over the atoms of the SVC so that the total sum of forces in the SVC is zero

$$\vec{f}_c + \vec{\xi} + \vec{\tau} = 0 \tag{3.B2}$$

Because $\vec{\xi}$ and $\vec{\tau}$ cannot be estimated directly during the simulation, the expression of the counterforce given in (Equation (3.B1)) cannot be used to directly determine $\vec{f}_c$. What can be determined in the MD simulation, however, is the net spurious force, $\vec{f}_s$, that is generated in the surface MD Region and imposed on the remainder of the MD system. As illustrated in Figure 3.3, the surface region force, $\vec{f}_s$, for a given SVC is defined as the force between the SVC and the Interface MD Region. It is calculated individually for each SVC of the Surface MD Region as a sum over the pair forces between atoms (*i*) of the SVC and all of their interaction neighbors (*j*) lying outside the surface region

$$\vec{f}_s(t) = \sum_{i \in (SVC)} \sum_{j \notin (surf.layer)} \vec{f}^{(i,j)}(t) \tag{3.B3}$$

The pair force between atoms (i) and (j) for an EAM potential [Mishin et al., 1999] can be expressed as

$$\vec{f}^{(i,j)}(t) = -\left[\frac{\partial \phi^{(i)}(t)}{\partial r^{(i,j)}} + \frac{\partial \phi^{(j)}(t)}{\partial r^{(i,j)}}\right]\frac{\vec{r}^{(i,j)}}{r^{(i,j)}} \tag{3.B4}$$

where $\phi^{(i)}(t)$ is the potential energy of atom (i) at time t, and $\vec{r}^{(i,j)} = \vec{r}^{(i)} - \vec{r}^{(j)}$ with $r^{(i,j)} = \left|\vec{r}^{(i,j)}\right|$.

To ensure that the equilibrium condition for a perfect crystal lattice is satisfied at zero pressure and $T =$ 0 K, the following condition must be met

$$\vec{f}_s(0)\Big|_{P=0,T=0} = \{0\} \tag{3.B5}$$

A requirement on the division of the Surface MD Region is that each SVC must occupy a whole number of lattice unit cells. The reason for this requirement is because any resultant force at the atomic scale is a sum of attractive and repulsive forces between interacting atoms. The equilibrium condition is satisfied only for the special case of a complete, periodic, lattice unit cell. Conversely, equilibrium is not satisfied for individual atoms or for arbitrarily defined groups of atoms.

During simulation with evolving deformations and with the presence of a free surface, $\vec{f}_s$ is equal to (after averaging the thermal fluctuations, inherent in each atomistically calculated force) the sum of $\vec{\xi}$ and that part of $\vec{\tau}$, indicated as $\vec{\tau}_s$, which is contained in the Surface MD Region only

$$\vec{f}_s = \vec{\xi} + \vec{\tau}_s \tag{3.B6}$$

In the above equation, an assumption is made that a very thin surface region of a few nanometers thickness may not contain all the surface tension effects, so that the total surface tension force is decomposed into two components

$$\vec{\tau} = \vec{\tau}_s + \vec{\tau}_I \tag{3.B7}$$

where $\vec{\tau}_s$ is the component that is contained in the surface region, and $\vec{\tau}_I$ is the component that is contained in the remaining inner part of the MD system. Only $\vec{\tau}_s$ would give contribution to $\vec{f}_s$ in Equation (3.B6).

When the counterforce, $\vec{f}_c$, is applied, $\vec{f}_s$ now equals

$$\vec{f}_s = \vec{\xi} + \vec{\tau}_s + \vec{f}_c \tag{3.B8}$$

Using the definition for $\vec{f}_c$ expressed by Equation (3.B1) for full compensation yields

$$\vec{f}_s = \vec{\xi} + \vec{\tau}_s - \left(\vec{\xi} + \vec{\tau}\right) = -\vec{\tau}_I \tag{3.B9}$$

Equation (3.B9) gives the criteria for full compensation of the spurious forces as $\vec{f}_s = -\vec{\tau}_I$. The counterforce, $\vec{f}_c$, can now be defined as the force which is needed to maintain $\vec{f}_s(t) = -\vec{\tau}_I$. This definition has the desirable feature of not requiring that $\vec{\xi}$ and $\vec{\tau}$ be determined explicitly. An iterative procedure is used to maintain $\vec{f}_s(t) = -\vec{\tau}_I$ by correcting $\vec{f}_c(t)$ within each SVC by the negative of the difference between $\vec{f}_s(t)$ and $-\vec{\tau}_I$ at any given time *t*, as

$$\vec{f}_c(t + \Delta t) = \vec{f}_c(t) - \frac{\Delta t}{t_M}\left[\vec{f}_s(t) + \vec{\tau}_I\right]; \quad \vec{f}_c(0) = \{0\} \tag{3.B10}$$

Here, Δt is the MD time step, and $t_M >> \Delta t$ is an adjustable inertial time parameter that controls the sensitivity of the counterforce to fast atomic fluctuations of the surface region force (a suitable choice was found to be $t_M = 1000\Delta t$).

In order to perform the iteration in Equation (3.B10), the surface force component, $\vec{\tau}_I$, has to be determined. If the Surface MD Region is thick enough, $\vec{\tau}_I$ is a small fraction of $\vec{\tau}$, and a good simplifying assumption is to set $\vec{\tau}_I = 0$, which reduces Equation (3.B10) to

$$\vec{f}_c(t+\Delta t) = \vec{f}_c(t) - \frac{\Delta t}{t_M}\vec{f}_s(t); \quad \vec{f}_c(0) = \{0\} \tag{3.B11}$$

Otherwise, when $\vec{\tau}_I$ is considered non-negligible, the following method can be used for its estimation and is based on two considerations. First, when the MD system is not deformed, the elastic surface region reaction force is zero, or $\vec{\xi} = 0$. Second, the assumption is made that the deformation does not change the surface tension, which is appropriate if changes in the surface curvature and the surface energy due to deformation are negligible.

A non-deformed state is defined when the estimated displacements, $\vec{\delta}_I$, are zero. Here, it is recalled that $\vec{\delta}_I$ was defined in Equation (3.B1) relative to $\vec{r}_{CM}(0)$ for a defect free system equilibrated under fully 3D periodic boundary conditions with no free surface. To make $\vec{\delta}_I = 0$, an external radial force per unit area given by

$$\vec{f}_r = -\vec{\tau} = -\frac{\gamma}{r} \tag{3.B12}$$

is uniformly applied to the atoms of the surface region having a free surface with surface tension, γ, and radius of curvature, r. Equation (3.B12) is the Young-Laplace's equation for the internal pressure of a cylindrical particle of radius r due to its surface tension.

Even though the Young-Laplace's equation is strictly applicable to liquids, it has been shown that it also provides a reasonable approximation for very small metallic domains (Huang et al. [99]).

Under the conditions that $\vec{\delta}_I = 0$ and $\vec{\xi} = 0$, only $\vec{\tau}_s$ and $\vec{f}_r$ would contribute to $\vec{f}_s$, which can be presented as

$$\vec{f}_s = \vec{\tau}_s + \vec{f}_r = \vec{\tau}_s - \vec{\tau} = -\vec{\tau}_I \tag{3.B13}$$

Expressed in another way, recalling Equation (3.B3), $\vec{\tau}_I$ is defined as:

$$\vec{\tau}_I = -\vec{f}_s\Big|_{\vec{\delta}_I=\{0\}} = -\sum_{i\in(SVC)}\sum_{j\notin(surf.layer)}\vec{f}^{(i,j)}\Big|_{\vec{\delta}_I=\{0\}} \tag{3.B14}$$

Equation (3.B14) allows $\vec{\tau}_I$ to be calculated through the atomistic forces in an equilibrated MD system when $\vec{\delta}_I = 0$. To avoid uncertainties from random thermal fluctuations in the atomistic calculation of $\vec{f}_s\big|_{\vec{\delta}_I=\{0\}}$, a suitable time averaging at equilibrium can be used in Equation (3.B14).

After substituting Equation (3.B14) in Equation (3.B10), the iteration procedure for calculating the counterforce becomes

$$\vec{f}_c(t+\Delta t) = \vec{f}_c(t) - \frac{\Delta t}{t_M}\left[\vec{f}_s(t) - \vec{f}_s\Big|_{\vec{\delta}_I=\{0\}}\right]; \quad \vec{f}_c(0) = \{0\} \tag{3.B15}$$

The iteration in Equation (3.B15) is performed separately for each SVC to obtain and update $\vec{f}_c(t)$ at every MD time step to counteract both $\vec{\xi}$ and $\vec{\tau}$ at the same time during the coupled simulation by maintaining $\vec{f}_s(t) \approx \vec{f}_s\big|_{\vec{\delta}_I=\{0\}}$. Introducing the initial force state $\vec{f}_s\big|_{\vec{\delta}_I=\{0\}}$ as a reference state in Equation (3.B15) allows the use of a very thin Surface MD

Region (1 to 2 nm has been used in the present study), so that its stiffness could be small and the compensating force, $\vec{f}_c(t)$, would be a small perturbation to the interatomic forces. For a thicker Surface MD Region, $\vec{\tau}_I \to 0$, and the simplified iteration (Equation (3.B11)) can be used instead.

Chapter 4

Cohesive Zone Modeling of Material Failure

4.1 Introduction

Cohesive zone models (CZMs) were originally developed by Dugdale [101] and Barenblatt [102] to represent complicated nonlinear fracture processes in ductile and quasi-brittle materials. In addition, CZMs were found suitable to describe adhesion and frictional-slip along an interface [103,104]. These models are frequently used in conjunction with the finite element method (FEM) to study fracture at macroscopic length scales in a wide variety of materials. The resulting element formulation is referred to herein as a 'decohesion' finite element and several enhanced formulations of this type of element is presented in Chapter 5.

The classical CZM approach is formulated as a constitutive relationship to represent separation in various fracture modes of two initially coincident surfaces. The relative displacements associated with the creation of new fracture surface for the three fundamental fracture modes are depicted in Figure 4.1.

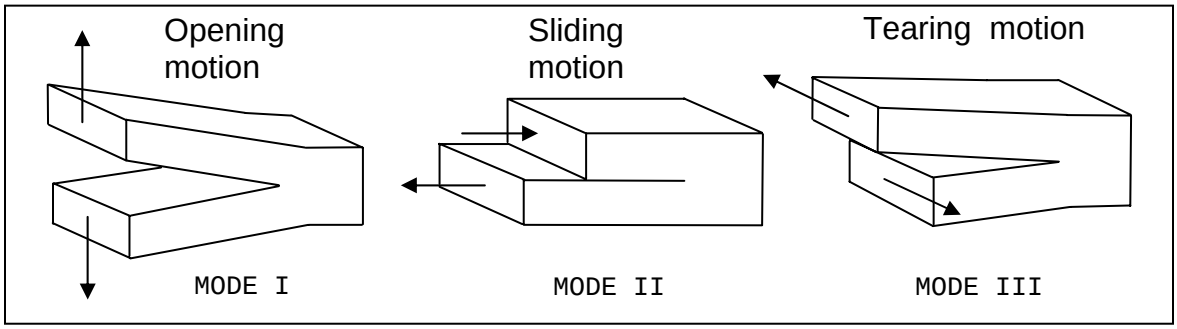

Figure 4.1. Fundamental fracture modes in solids.

While cohesive zone models are a useful method to simulate material failure, because the parameters that are typically used to define them are taken from bulk material properties [105-116,162,118,119], they do not adequately describe the actual physics of microstructural failure and fracture modes. A general description of extracting CZM

parameters from continuum analyses using an inverse approach is given by Hong and Kim [120]. There are significant differences in the simulation of material failure depending on the length scale considered. For microstructurally long cracks, failure can be represented by the three fundamental fracture modes involving Mode I opening, Mode II sliding, and Mode III tearing (Figure 4.1). Details of specific nanoscale failure mechanisms can be neglected and the overall material behavior can be homogenized into a process zone at the crack tip that simply varies in extent and is typically represented as a plastic zone in advance of a crack tip. This process zone can be characterized through mechanical testing and then used to define parameters of the CZM.

Macroscale values of strength and toughness that are typically input to CZMs represent the aggregate response of thousands or millions of grains, grain boundaries, and defects within the specimens from which they were obtained. For analysis at microscale length scales, these average values cannot represent the unique response of a particular interface at which a local fracture event might occur. If the microscale predictions are to become quantitative, determination of grain boundary and defect properties is required. A means of making this connection is to use the results of MD simulation to develop the constitutive relations of CZMs based directly on atomistic simulation of fundamental damage mechanisms. This yields more accurate failure properties that will eventually lead to predictions of the failure properties of a large class of materials and microstructures, even when experimental data is not available. This approach constitutes the basis for a sequential multiscale methodology for simulating damage.

However, it should be noted that the simplicity of macroscopic fracture mode definitions based solely on relative displacements cannot capture the full range of nanoscopic material processes involved with failure at atomic length scales. These processes include grain boundary migration, sliding, and interaction with surrounding defects under applied normal and shearing loads. Thus, at the nanoscale, current CZM formulations may require additional development to represent the full range of material failure mechanisms leading to separation of cohesive surfaces.

The following sections present various aspects of CZM formulations. Section 4.2 discusses the general aspects of contemporary CZM methods that include mixed-mode formulations utilizing empirical CZM parameters for application at various length scales. Section 4.3 presents current approaches for deriving CZMs from atomistic simulation including a newly developed methodology for nanoscale and microscale applications. Section 4.4 discusses a generalized representation of CZM constitutive laws. Finally, Section 4.5 discusses computational issues in generating a comprehensive characterization of CZMs for the range of GB orientations for general polycrystalline material analysis.

4.2 General features of cohesive zone models

Cohesive zones are considered a superposition of separable top and bottom surfaces that deform in response to applied surface tractions. Cohesive zone models generally represent the constitutive behavior of the cohesive surface in the form of a traction-displacement relationship where relative displacements represent the discontinuity – or "jump" - of a displacement component across the top and bottom surfaces.

Central to the CZM approach is the requirement that the area under the CZM traction-displacement curve represents the work of separation required to open a crack - the fracture toughness - and is given by Tvergaard and Hutchinson [105] as

$$G_c = \int_0^{\Delta^f} \tau \, d\Delta \tag{4.1}$$

where G_c is the work of separation, τ is the surface traction, Δ is a general form of the displacement, and Δ^f is the critical displacement at which complete separation has occurred and the tractions are zero.

Figure 4.2 shows a common bilinear traction-displacement law that depicts characteristic regions common to all CZMs. These features comprise an initial linear

region ($\Delta < \Delta^o$) in which loading and displacements may be assumed reversible or irreversible, a maximum traction at which damage onset occurs ($\Delta = \Delta^o$), and a softening region ($\Delta^o \le \Delta < \Delta^f$) that represents material degradation until a final displacement is reached at which the material exhibits complete failure ($\Delta = \Delta^f$).

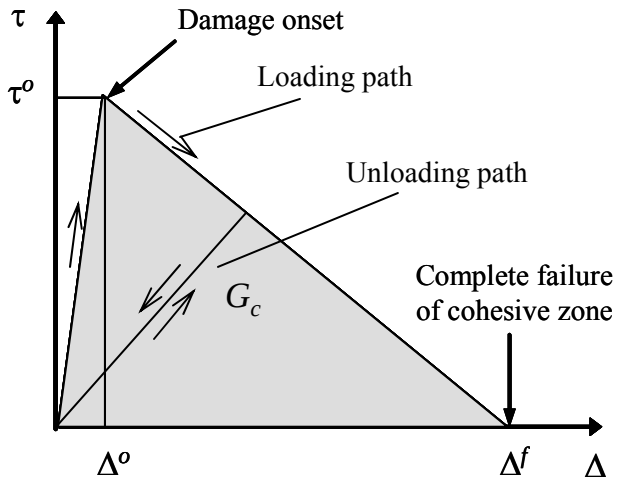

Figure 4.2. Bilinear cohesive zone model.

If a potential function $\phi = \phi(\Delta)$ representing the free energy of decohesion exists, the traction-displacement relationships $\tau(\Delta)$ corresponding to different fracture modes can be obtained by differentiation of the potential with respect to a particular displacement component. The existence of an energy potential yields the work of separation as independent of the loading history. The particular form of the traction-displacement relation is generally selected for analytical convenience whereas the energy of decohesion, G_c, is often of primary concern. However, various CZM formulations have been presented in the literature with an additional emphasis on the importance of the shape of the constitutive relation to better represent material response [121-123,172].

The most commonly assumed forms of the traction-displacement law have been expressed as exponential, bilinear, and trapezoidal functions. Some attempts have been made to determine the most appropriate shape based on fundamental bonding characteristics in metals [124,125]. Other work has been presented that attempt specifically demonstrate the importance of the shape of traction-displacement laws in numerical predictions [126]. This continues to remain a debatable topic in CZM formulations. A general review of various forms of CZMs is presented in Chandra et al. [123]. Table 4.1 shows a range of various CZM functions that have been presented in the literature and embedded into CZM elements. The table illustrates the basic form of the CZMs, their key parameters, and important features.

Table 4.1. Various cohesive zone models and their parameters. (From Chandra et al. [123]).

Author (year)	Proposed model	Model parameters	Problem solved	Model constants	Comments
Barenblatt (1959, 1962)	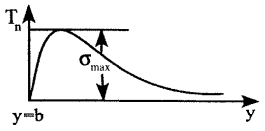	$K = \int_0^{d+d'} \frac{G_1(t)\,dt}{\sqrt{t}}$ $= \sqrt{\frac{\pi E T_t}{1-\nu^2}}$ (ductile) $= \sqrt{\frac{\pi E T_0}{1-\nu^2}}$ (brittle) $T = T_0 + T_1$ T_0 is work of separation for brittle materials T_1 is work of plastic deformation	Perfectly brittle materials		The first to propose the cohesive zone concept
Dugdale (1960)	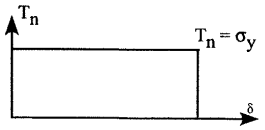	$\frac{s}{a} = 2\sin^2\left(\frac{\pi}{4}\frac{T}{\sigma_y}\right)$ For small value of T/σ_y $\frac{s}{l} = 1.23\left(\frac{T}{\sigma_y}\right)^2$	Yielding of thin ideal elastic–plastic steel sheets containing slits	Plastic zone ranges from 0.042 to 0.448 (in.)	Cohesive stress equated to yield stress of material
Needleman (1987)	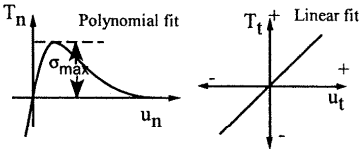	ϕ_{sep} is work of separation δ are normalizing parameters σ_{max} is cohesive strength	Particle-matrix decohesion	$\delta = 10^{-9}$ to 10^{-8} m cohesive energy 1–10 J/m^2 σ_{max} = 1000–1400 MPa σ_y = 350–450 MPa	Phenomenological model; predicts normal separation
Rice and Wang (1989)	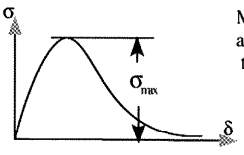 Model based on atomic fit of the type $(1+x)e^{-x}$	E_0 is initial Young's modulus h is normalizing parameter σ_{max} is maximum stress α is constant $\left(\frac{E_0 h}{\alpha^2} = 2\gamma\right)$	Solute segregation		Ascending part is equated to E_0 considers normal separation and ignores shear separation
Needleman (1990a)	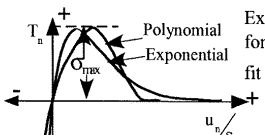 Exponential fit for T_n. Linear fit for T_t	ϕ_{sep} is work of separation δ are normalizing parameters σ_{max} is cohesive strength	Particle-matrix decohesion	$\delta = 10^{-9}$ to 10^{-8} m	Predicts normal separation

Table 4.1 (*continued)*

Author (year)	Proposed model	Model parameters	Problem solved	Model constants	Comments
Needleman (1990b)	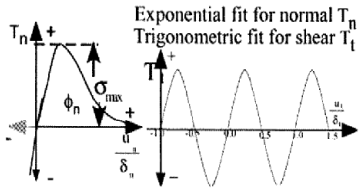	ϕ_n, ϕ_t are work of normal and shear separation δ_n, δ_t are critical displacements σ_{max} is cohesive strength	Decohesion of interface under hydrostatic tension	$\delta_n = \delta_t =$ 2×10^{-10} to 2×10^{-9} m $J_{IC}/\phi_n =$ 0.57–2.59 $\sigma_{max}/\sigma_0 = 2, 3$	Periodic shear traction to model Pieriels shear stress due to slip
Tvergaard (1990)	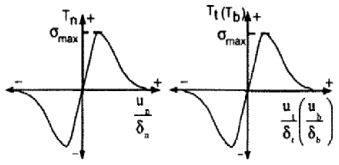	δ_n, δ_t are critical displacements σ_{max} is cohesive strength	Interfaces of whisker reinforced metal matrix composites	$\delta_n = \delta_t =$ 1×10^{-9} m $E = 60$ GPa (Young's mod) $\sigma_y/E = 0.005$ $\sigma_{max}/\sigma_y = 5$–9	Quadratic model
Tvergaard and Hutchinson (1992)	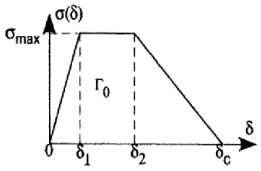	Γ_0 is work of separation δ_c is critical displacement σ_{max} is peak normal traction /interface strength δ_1, δ_2 are factors governing shape	Crack growth in elasto-plastic material, peeling of adhesive joints	$\Gamma_{ss}/\Gamma_0 = 0$–10 ($\Gamma_{ss} =$ Pl wk.), $\delta_n^c/\delta_t^c = 1$ $\sigma_{max}/\sigma_y = 0$–14 δ_1, $\delta_2 = 0.15, 0.5$ $\sigma_y/E = 1/300$	Claims shape of separation law are relatively unimportant
Xu and Needleman (1993)	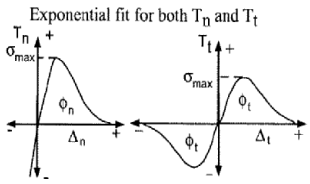	ϕ_n is work of normal separation ϕ_t is work of shear separation δ_n, δ_t are critical displacements σ_{max} is cohesive strength	Particle-matrix decohesion	$\delta_n = \delta_t =$ 2×10^{-10} to 2×10^{-9} m	Predicts shear and normal separation

In fracture studies at the micromechanical level, decohesion elements can be placed between the continuum finite elements that discretize the grain interior to predict transgranular fracture or placed between the continuum finite elements on either side of a grain boundary to predict intergranular fracture. Recent work presented by Zhang et al. [127] uses the designation "intrinsic" and "extrinsic" CZMs to refer to the presence or absence, respectively, of an initial linear elastic segment in the CZM curve. This linear region seen in intrinsic CZMs can have the disadvantage of introducing an artificial compliance to the model and is avoided by using an "extrinsic" formulation. This artificial compliance is of particular importance when the location of fracture is unknown and decohesion elements are placed between every continuum element in the model. To avoid this artificial compliance, intrinsic CZMs may be placed selectively in specific locations when the crack path is predetermined. Alternatively, extrinsic CZMs can be

placed globally or adaptively inserted only where local stresses exceed a maximum traction, thus avoiding any constraint on crack path location. A depiction of intrinsic and extrinsic CZMs for a bilinear law is presented in Figure 4.3.

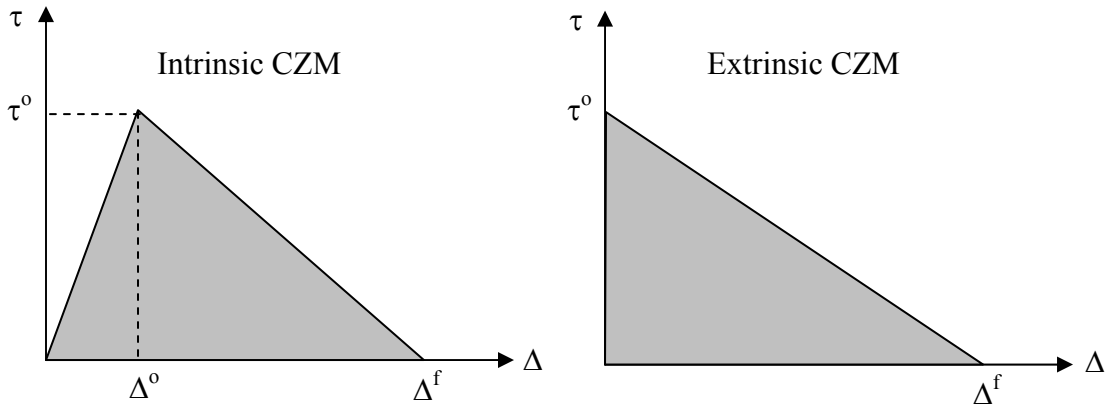

Figure 4.3. Depiction of intrinsic and extrinsic CZMs.

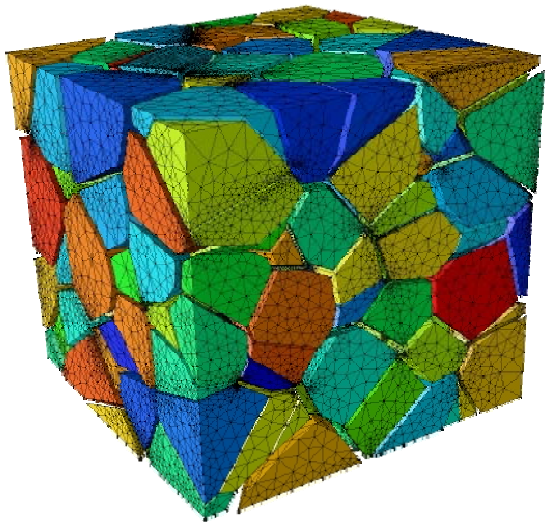

Figure 4.4. Exploded view of a 3-D grain microstructure.

Modeling material failure with CZMs has advanced to a level of maturity such that large-scale simulations of fracture in polycrystals can be performed such as depicted in Figure 4.4. However, significant research will be required to fully quantify CZMs at the atomic level for various material systems and GB characteristics. Many analyses have been reported using CZMs to simulate small material regions such as metallic microstructures but still employ empirical parameters and assume a homogenized material. Recently, Zavattieri et al. [128] studied the fracture of alumina-ceramic microstructures subjected to multi-axial dynamic loading. A bilinear traction-displacement relationship was parameterized using empirical data, such as the macroscopic fracture toughness K_{IC}. Zavattieri and Espinosa [129] used a modification of the same model to study interface effects of an aluminum specimen in contact with steel plates. Wei and Anand [130] have used a modified CZM model to study intergranular fracture in nanocrystalline Ni. In their FEM model, the CZM-based decohesion element approximated both reversible and irreversible sliding-separation deformations at the grain boundaries prior to failure. The parameterization of the model was, again, performed by using available macroscopic experimental data for stress-strain curves of nanocrystalline Ni in tension with an average grain size of 15-40 nm and having a comparatively large number of grains. Iesulauro et al. [114,115] have applied the CZM technique to simulate fatigue crack initiation in aluminum polycrystals.

Physics-based approaches for calculating GB energy commonly utilize MD methods [63,131]. An important issue on the validity of MD simulations is the large applied strain-rates that can yield incorrect results. Large strain-rates are a consequence of the computational demands of MD simulation; there is a practical computational limit based on atomic domain size and simulation time. With practical simulation times on the order of picoseconds (10^{-12} sec), high applied strain rates are required that can produce discrepancies between simulation results and experiment [130].

Under combined loading, CZMs representing material response for individual normal or tangential loading are coupled using a selection of combined measures of displacement, tractions, and energy. An illustrative mixed-mode CZM approach follows a formulation presented by Turon et al. [132] in which a bilinear traction-displacement law is assumed for both normal and tangential fracture modes, and a single effective traction-displacement relationship is interpolated from pure-mode CZMs based on mode mixity. The resulting interpolated CZM relates a combined effective traction to an effective combined displacement jump. In Turon et al. [132], the effective CZM is used to determine an internal state variable that describes the general degree of damage and is subsequently used to modify the stiffness of the cohesive zone. This effective CZM assumes macroscopic material behavior and is coupled using phenomenological constitutive relations.

The interpolation of CZM components is depicted in Figure 4.5. Relative displacement jumps between the upper and lower nodes, $\delta = \delta^{top} - \delta^{bot}$, corresponding to

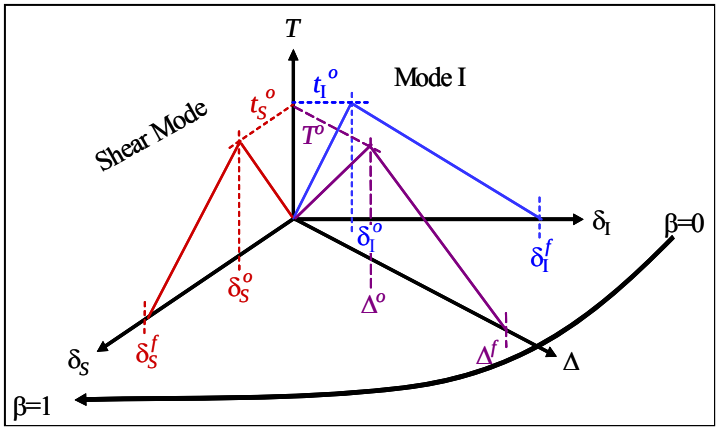

Figure 4.5. Interpolation of CZM components.

the maximum traction indicate the onset of damage, and final failure of the cohesive zone is assumed after the relative displacement jump yields a zero traction. The numbering of coordinates is assumed in a local element coordinate system which is used to define the various relative fracture modes as

$$\begin{Bmatrix} \delta_1 \\ \delta_2 \\ \delta_3 \end{Bmatrix} = \begin{Bmatrix} \delta_1^{top} - \delta_1^{bot} \\ \delta_2^{top} - \delta_2^{bot} \\ \delta_3^{top} - \delta_3^{bot} \end{Bmatrix} \begin{matrix} : \text{ModeI opening} \\ : \text{Mode II sliding} \\ : \text{Mode III tearing} \end{matrix} \tag{4.3}$$

The displacements corresponding to the initial onset of failure and final failure in the interpolated CZM curve are denoted by Δ^o and Δ^f, respectively.

4.3 Atomistic-based cohesive zone models

The simulation of matter using MD accounts for the atomistic processes that is the basis for the behavior of materials. Thus, the ultimate representation of fracture begins at nanometer dimensional scales at which the formation, propagation, and interaction of fundamental damage mechanisms dictate local deformation and fracture. These mechanisms include dislocation formation and interaction, interstitial void formation, precipitate aggregates, and atomic motion such as Coble creep. Ultimately, small-scale damage evolution leads to macroscopic failure modes such as distributed plastic yielding and the development of large cracks exhibiting Mode I, II, and III opening behavior. Of importance to the current research, MD-based CZMs represent the statistics of atomistic failure processes thereby forming the basis of a sequential multiscale analysis approach.

The first serious attempt to extract relevant parameters for CZM decohesion laws from atomistic (molecular-dynamics or molecular-static) simulations was made by Gall et al. [134]. Here, an atomistic model of an aluminum-silicon interface (Figure 4.6) was used to study interface debonding. The interatomic potential used was a modified embedded atom method (MEAM) potential fitted to reproduce the properties of both aluminum and silicon [133] together with their bonding at the interface. In the simulation, the system was subject to a uniaxial tensile strain normal to the interface until debonding occurred. The internal stress was monitored and plotted as a function of the strain (Figure 4.7). The extracted atomistic stress-strain curve showed that after an initial elastic stretching, the interface begins to break (at 15% strain), and the stress rapidly decreases and then starts to oscillate around zero due to elastic spring-back effects of the

layers after separation. Gall et al. [134] also studied interface debonding for pure aluminum and pure silicon (Figure 4.8) and found that the Al-Si interface is weaker than either the Al-Al or the Si-Si interface.

It is to be noted, as the authors discuss in their paper (Gall et al. [134]), that such atomistically-derived stress-strain relations are not yet applicable for direct extraction of CZM traction-displacement relationships. The atomistic stress-strain plots from these simulations represent the local debonding of an ideal flat interface with dimensions between 10 and 80 nm that does not include the many variables (e.g. voids, dislocations, etc) that affect the interface. For example, the predicted debonding stress level of ~20 GPa for an Al-Si interface (Figure 4.8) is highly elevated compared to the experimental ultimate tensile strength of ~200 MPa for a cast Al-Si alloy where fractured and debonded Si particles were observed [135,136].

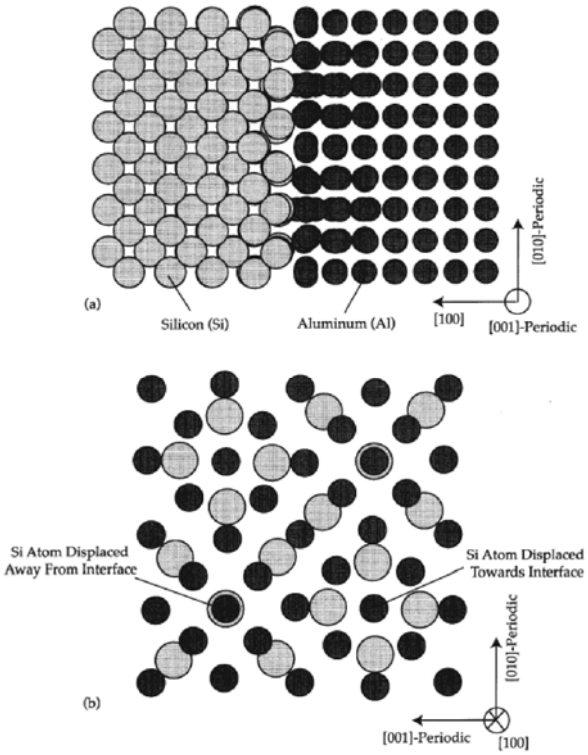

Figure 4.6. Atomic structure of Al-Si interface. (From Gall et al. [134]).

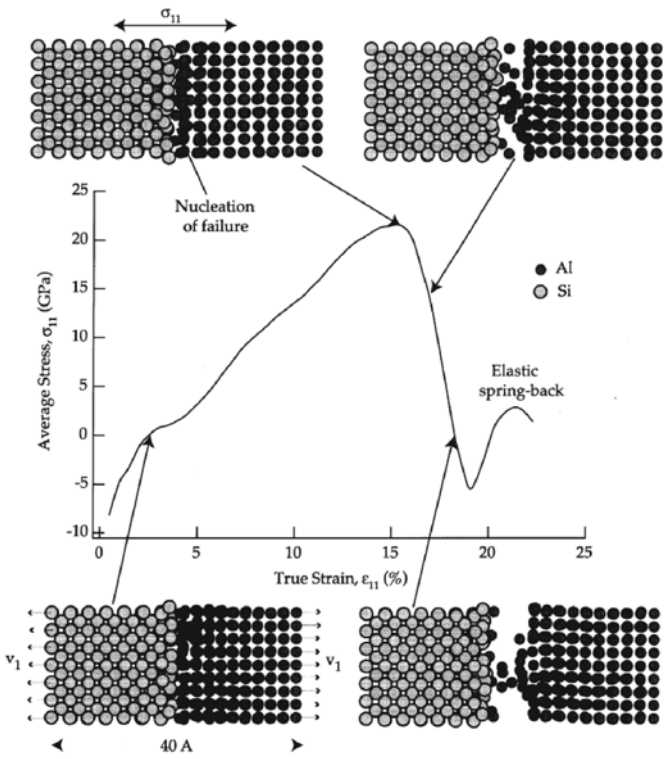

Figure 4.7. Atomistic derivation of a stress-strain relation during debonding of an Al-Si interface. The four snapshots above and below the plot show structural changes of the interface at different stages of debonding at the atomic level. (From Gall et al. [134]).

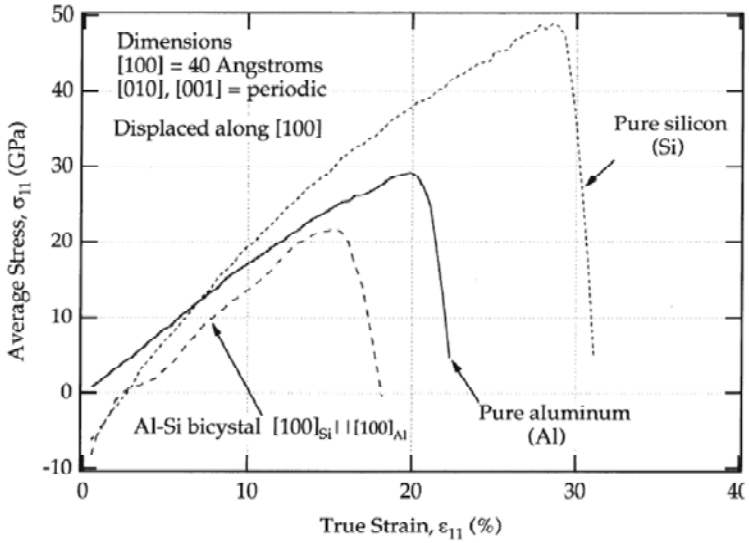

Figure 4.8. Atomistic stress-strain relations for Al-Si, Al-Al, and Si-Si interfaces. (From Gall et al. [134]).

Several other attempts to extract relevant parameters for CZM decohesion laws from molecular-dynamics or molecular-static simulations have been made by various groups in the last few years [137-139]]. In addition to classical MD simulations, first principles quantum-mechanics-based atomistic models [140] were also used to study adhesion in an NiAl-Cr interface by first principles calculations. All of those models showed highly elevated debonding stress ranging from 15 to 50 GPa, which was two orders of magnitude higher than the experimentally observed strength of the corresponding materials.

There are various reasons for this discrepancy between atomistic simulations and experimental characterizations. In addition to various idealizations related to interface structure, an important factor is the selection of the thermodynamic ensemble. The approach typically used is based on simulating the debonding of a perfect, flat interface under a constant tensile strain rate perpendicular to the interface using a canonical *NVP* ensemble in which the volume is maintained constant. In these references [137,138,140], the system size varied between 4 and 80 nm, and the dynamics of the atoms was severely constrained by the boundary conditions, which did not allow for Poisson lateral contraction and shear deformation. As a result, plastic processes, such as dislocation slip, interface sliding, and interface diffusion, were strongly suppressed. Consequently, the simulated mechanism for interface decohesion in these works reproduced an idealized process of atomic adhesion (strength) rather than that of fracture at the interface.

The goal of developing a sequential multiscale simulation capability in the current research is to derive accurate CZMs that can be used to characterize grain boundary failure in polycrystalline microstructures. For the present analysis, the Mode I fracture studies presented in Section 2.2 together with additional GB sliding analyses of the flat symmetric tilt Σ99 GB interface in an aluminum bicrystal are analyzed using the developed MD-FEM concurrent coupling method (ESCM, detailed in Chapter 3). The ESCM approach ensures that the atomistic simulation is performed under correct elastic far-field boundary and loading conditions.

For Mode I fracture and GB sliding, the simulation approach used in this research is based on a MD simulation model of crack propagation under time-independent, or steady-state, conditions through the selected GB orientation and topology in aluminum at low temperature (100 K). The purpose of the MD simulation is to reveal and analyze the atomistic processes taking place near the crack tip and to derive a traction-displacement relationship for a continuum CZM element.

4.3.1 Determination of atomistic traction-displacement laws using cohesive zone volume elements

A new generic methodology for extracting effective atomistically-based CZMs using a MD model is detailed next. The traction-displacement relationship of a CZM describes how the traction, τ, developed in the process zone near the crack, depends on the crack opening λ. In general, the traction-displacement relationship, $\tau(\lambda)$, considers both normal and tangential components of the traction. In the case of a normal opening (Mode I) crack under applied load, only the normal component of the traction is important for crack growth.

Obtaining σ^s_{yy} from MD simulation can be accomplished by dividing the computational box surrounding the region experiencing relative opening displacements into $2N_L+1$ slices of thickness δ, as shown in Figure 4.9, so that $(2N_L+1)\delta = L$. At the beginning of the simulation, before crack growth is initiated, a three-dimensional parallelepiped volume element (called a Cohesive Zone Volume Element, CZVE) is defined at each location where the slice crosses the GB plane at $y = 0$ (illustrated by the shaded regions along the midline and surrounding the lenticular crack opening in Figure 4.9). The CZVE has a length δ_x along x and extends to $y = \pm\delta_y$ on both sides of the GB interface. Its thickness equals the system thickness h. When the propagating crack passes through a CZVE during the simulation and the CZVE starts to open, its shape deforms. To be able to keep track of the CZVE volume, the atoms that have belonged initially to the CZVE are marked, i.e., their identification numbers are stored for each CZVE, and are further used to identify the CZVE. The virial stress defined in Equation (2.19), with

the "*i*"-index going over the marked atoms of a CZVE, and Ω equal to the volume of the CZVE, is used to calculate $\sigma^s_{yy}(x_p,t)$ as a function of the position x_n of the n^{th} CZVE along the GB interface at time t during the simulation. Here, $p \in [0, N_L]$ for the crack tip propagating in the $+x$ direction, and $p \in [0, -N_L]$ for the crack tip propagating in the $-x$ direction. At the same instant t, the crack opening $\lambda(x_p,t)$ at the same position x_p is also estimated. Thus, every estimate of $\sigma^s_{yy}(x_p,t)$ corresponds to one estimate for $\lambda(x_p,t)$, allowing the construction of the function $\sigma^s_{yy}(\lambda(x_p,t))$ for each CZVE.

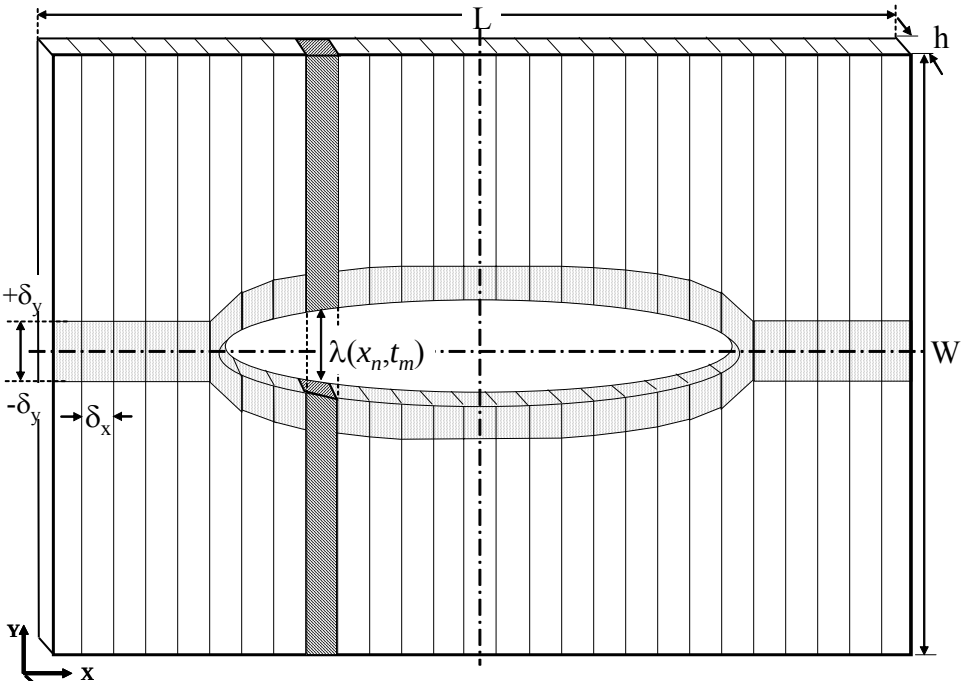

Figure 4.9. Schematic diagram of the slicing of the system volume in the MD simulation and defining the representative regions for extracting the parameters for the cohesive-zone interface elements in a continuum simulation.

Figure 4.10 shows the stress and opening profiles ($\sigma^s_{yy}(x)$ and $\lambda(x)$ curves, respectively) at time t = 123 ps for a growing crack along the Σ99 symmetric tilt GB prestressed at 4.25 GPa. A fit to the continuum expression for the stress at a crack tip

$$\sigma^s_{yy}(x) = \frac{K_I}{\sqrt{2\pi(x - x_o)}} + \sigma_o \qquad (4.4)$$

is superimposed on the stress profile ahead of the brittle tip, propagating in the $+x$ direction. The fit shows a $1/\sqrt{r}$ type dependence of the stress profile, and K_I is determined to be 0.36 MPa-m$^{1/2}$. Such dependence is not recovered for the ductile tip, propagating in the $-x$ direction in Figure 4.10, because the stress is continuously relieved by plastic dissipation mechanisms.

The opening of the crack, $\lambda(x,t)$, as a function of x can be estimated in various ways. A convenient method is to use the previously described slicing of the simulation system along the x-axis (Figure 4.9). The separation between atoms on either side of the GB interface increases as the crack passes through a slice, creating an opening of size λ in the middle of the slice (the dashed slice in Figure 4.9 is given as an example). The opening changes the slice's gyration radius R_g (or the angular momentum), and one can estimate the size of the opening by calculating R_g. Assuming a uniform mass distribution, the continuum expression of R_g as a function of λ is

$$R_g^2 = \frac{\int_{\lambda/2}^{W/2} y^2 dy}{\int_{\lambda/2}^{W/2} dy} = \frac{1}{12}\left(W^2 + W\lambda + \lambda^2\right) \tag{4.5}$$

Alternatively, expressed through the atomic coordinates, the discrete formula for R_g is:

$$R_g^2 = \frac{1}{N}\sum_{i=1}^{N}\left(y_i - y_C\right)^2 = \frac{1}{N}\sum_{i=1}^{N} y_i^2 - \left(\frac{1}{N}\sum_{i=1}^{N} y_i\right)^2 \tag{4.6}$$

where y_i is the y-coordinate of atom i, and the sum is over all N atoms in the slice. $y_C = \frac{1}{N}\sum_{i=1}^{N} y_i$ is the y-coordinate of the mass center of the slice. Calculating R_g from Equation (4.6) and substituting it in Equation (4.5), the crack opening at the slice is the positive root of λ from Equation (4.5).

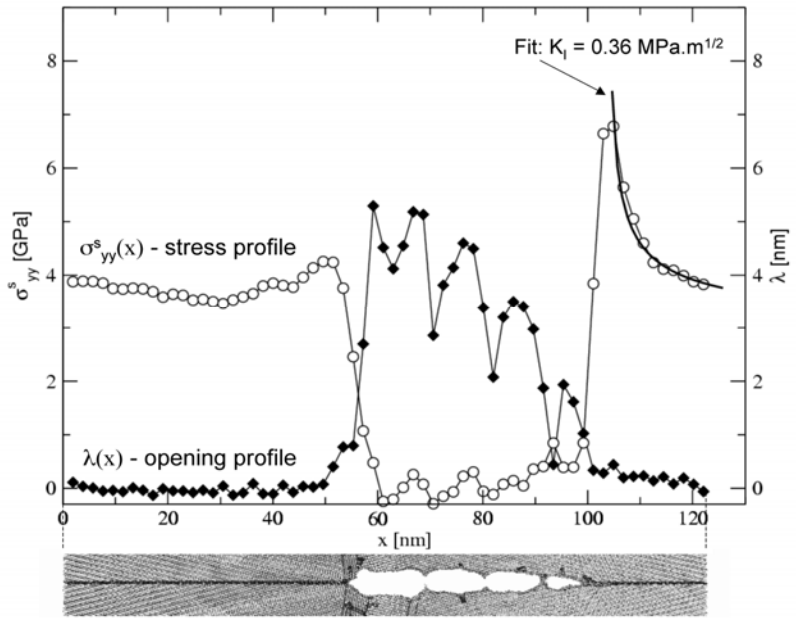

Figure 4.10. Stress and opening profiles extracted along the crack growing for 123 ps in a system prestressed at 4.25 GPa hydrostatic load. The corresponding snapshot of the crack is shown at the bottom.

The $\sigma^s_{yy}(x)$ and $\lambda(x)$ profiles in Figure 4.10 are for a single instant of time of the crack propagation (in this case, t = 123ps). If the whole simulation of the interface debonding is divided into N_t equal intervals of time t_q ($q \in [0, N_t]$), many such profiles can be taken of many CZVEs placed along the GB. When plotted in a σ^s_{yy} vs. λ plot, each ($\sigma^s_{yy}(x_p,t_q)$, $\lambda(x_p,t_q)$ pair represents a point $\sigma^s_{yy}(\lambda(x_p,t_q))$. After sorting these data points in an ascending order on λ, so that $\lambda_i < \lambda_{i+1}$, and taking a moving average (or a consecutive mean):

$$\tau(\lambda_i) = \frac{1}{(2M+1)} \sum_{j=-M}^{M} \sigma^s_{yy}(\lambda_{i+j}) \tag{4.7}$$

in which the results are averaged over M points backward and M points forward from λ_i, a construction of a statistically representative traction-displacement function $\tau(\lambda)$ can be made.

Though the introduced CZVE is used to extract the behavior for the decohesion element in the FE model, it should not be considered a MD equivalent of a decohesion element. While the decohesion elements are strictly *surface* elements in a 3D finite element model, the CZVE encompasses a *volume* at the surfaces on either side of the crack, large enough to allow for the convergence in the stress estimate in Equation (2.19). Each CZVE along the GB interface in the MD simulation has a unique response, depending on the local structural irregularities at the atomic level, while in a FE simulation, the decohesion elements for one type of interface are all identical. The relation between the CZVE and the CZM is made through statistical averaging (Equation (4.7)). The assumption is made that under the steady-state conditions of crack propagation, the statistical average over many CZVEs scanned at different instants of time will produce a statistically unique traction-displacement curve. Assuming a Gaussian distribution of $\sigma^s_{yy}(\lambda(x,t))$ from each individual measurement of each CZVE, the dispersion around the average traction-displacement curve will decrease proportionally to the square root of the number of atoms belonging to the CZVE. Thus, a larger volume of the CZVE would better average out the statistical fluctuations. In MD simulations, this volume is limited by the small size of the damage zone around the crack tip and by the large stress gradients inside it. This makes the dispersion large, and a sufficient number of measurements is required to produce a reliable traction-displacement function.

For the CZM generated using the purely atomistic model (shown in Figure 2.10), the size of the CZVE is defined by $\delta_x = \delta_y = \delta = 1/3[7\ 7\ 10]a_o \approx 1.9$ nm (see Figure 4.9) for this simulation, which gives a volume of $2h\delta^2 = 20.7$ nm^3 containing 1245 atoms that contribute to the stress-displacement response of one CZVE. For the simulated system in Figure 2.10, $2N_L + 1 = 63$ CZVEs fit along the 120 nm GB interface. During the simulation, the $\sigma^s_{yy}(\lambda)$ state for each CZVE is scanned every 4 ps for a period of 200 ps crack propagation time. This gives 3150 points for $\sigma^s_{yy}(\lambda)$ dependence from each simulation run. These points provide adequate statistics to extract the traction-displacement curve through suitable averaging. Because the two crack tips propagate in a

very different manner, as discussed in Chapter 2, the statistical averaging (Equation (4.7)) must be performed separately for these two directions.

The values of $\sigma^s_{yy}(\lambda)$ for the brittle tip of the pure MD simulation prestressed at 4.25 GPa are given in Figure 4.11(a). In the figure, the dots are the individual measurements for 4.25 GPa hydrostatic load simulation, from which an average was taken to produce the corresponding $\sigma^s_{yy}(\lambda)$ curve. The curves for a 3.75 and 4.0 GPa prestress are produced in a similar way.

At 52 nm of propagation (Figure 2.13(d)), 25 CZVEs have experienced a complete transition from a fully closed to a fully opened state. The averaging interval is set to M = 100, which is empirically found to give a sufficiently smooth curve. The curve for the brittle tip closely reproduces a bilinear type of constitutive relation for the CZM element and is similar to the one suggested by Camacho and Oritz [107] for brittle materials. The bilinear types of CZM models were used in several recent FE simulations of brittle fracture during multi-axial dynamic loading of ceramic microstructures [128,129]. The traction-displacement curves for 3.75 and 4.00 GPa, obtained in the same way, also given in Figure 4.11(a) (the data points, over which the traction-displacement curves are averaged are omitted for clarity), show that varying the prestress of the system in this range does not change the essential character of the averaged $\sigma^s_{yy}(\lambda)$ dependence. The peak stress σ_p shows a slight systematic decrease with decreasing load, and is probably an effect of the propagation speed decrease but remains approximately $\sigma_p \approx 5.0$ GPa at $\lambda_p \approx 0.4$ nm. It should be noted that the value for λ_p is taken relative to the initial state at an applied hydrostatic loading of 3.75 to 4.25 GPa. In reality, $\sigma^s_{yy}(\lambda)$ for $\lambda < \lambda_p$ should follow the elastic response of the GB before debonding. The full opening, or full debonding, of the interface happens at $\lambda_o \approx 2.5$ nm, when σ^s_{yy} becomes zero.

The corresponding data $\sigma^s_{yy}(\lambda)$ for the ductile tip, propagating in the $-x$ direction, where dissipative mechanisms including twinning dominate the deformation, is presented in Figure 4.11(b). Again, only the data points for 4.25 GPa prestress are given for clarity, while the averaged traction-displacement curves are shown for the three loads of 3.75,

4.0, and 4.25 GPa, as in Figure 4.11(a). In contrast with the behavior in the +*x* direction, a strong influence of the prestress on the traction-displacement curves is observed for the –*x* direction. This influence is most pronounced on λ_o, which changes from $\lambda_o^{(1)} = 2.7$ nm to $\lambda_o^{(3)} = 4.3$ nm as the prestress is increased from 3.75 to 4.25 GPa. The peak stress σ_p again shows the slight systematic decrease with decreasing load, which was observed in Figure 4.11(a), accompanied by a shift in λ_p.

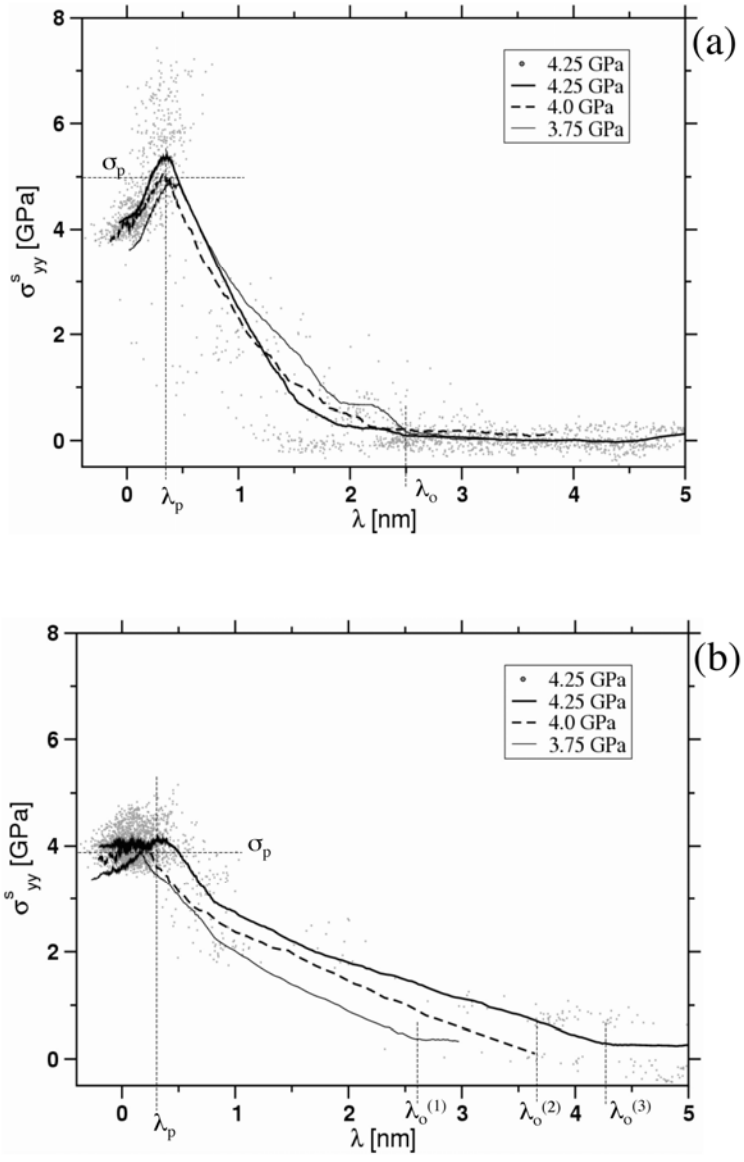

Figure 4.11. Surface stress vs. crack opening curves $\sigma^s_{yy}(\lambda)$ characterizing the propagation of the cleavage tip in the +*x* direction (a) and in the –*x* direction (b) for three preloads.

The extracted traction-displacement relationships for the ductile and the brittle crack tips are presented for comparison in Figure 4.12. The case of 4.25 GPa prestress is chosen because there, the crack has achieved its largest growth in both directions (Figure 2.13(d)) and has produced the most data points for calculating the moving average statistics using the CZVEs. Figure 4.10 reveals how the different atomistic processes, taking place at the two crack tips, are affecting the decohesion law of the interface debonding. This comparison is also very informative on the significance of the form of

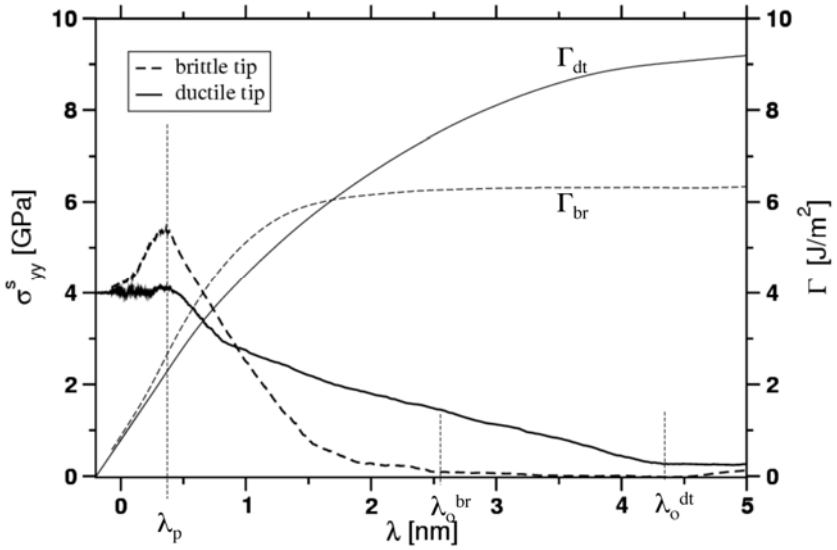

Figure 4.12. Traction-displacement relationship $\sigma^s_{yy}(\lambda)$ and the corresponding work of separation $\Gamma(\lambda)$ for the case of 4.25 GPa prestress compared for the brittle (+*x*) and the twinning (-*x*) tip.

the traction-displacement curve and how this form reflects the underlying physical processes as revealed by atomistic MD simulations. The ductile traction-displacement curve demonstrates a substantially larger debonding deformation λ_o, compared to the case of almost brittle debonding ($\lambda_o^{dt} > \lambda_o^{br}$, see Figure 4.10). The corresponding peak stress σ_p is lower for the ductile case, which is possibly a result of the emission of twinning dislocations relieving the stress at the crack tip. The lower σ_p and the larger λ_o exhibited by the twinning tip produces a more extended debonding region for the ductile traction-

displacement curve, compared to the steeper curve in the case of brittle fracture. This difference substantiates the use of a trapezoidal type of curve with a plastic straining region and reduced peak stress for the case of elasto-plastic fracture [141] and a bilinear curve for brittle fracture [107]. Despite a lower peak stress, the traction-displacement curve with twinning has about 50% larger area, meaning a larger work of separation. The larger work of separation also explains the smaller propagation distance in the ductile ($-x$) direction, compared to the brittle ($+x$) direction in the MD simulation (see Figure 2.13(d) discussed in Chapter 2). These traction-displacement relationships are depicted in Figure 4.12.

When using the coupled MD-FEM ESCM approach (presented in Chapter 3), the finite geometry distortion using a pure MD simulation is avoided. The recomputed 'brittle' Mode I CZM is compared with the initial pure MD results in Figure 4.13. As shown, the peak stress is increased slightly, but the overall energy and functional form of the CZM is closely reproduced. The 'ductile' Mode I CZM was not recomputed.

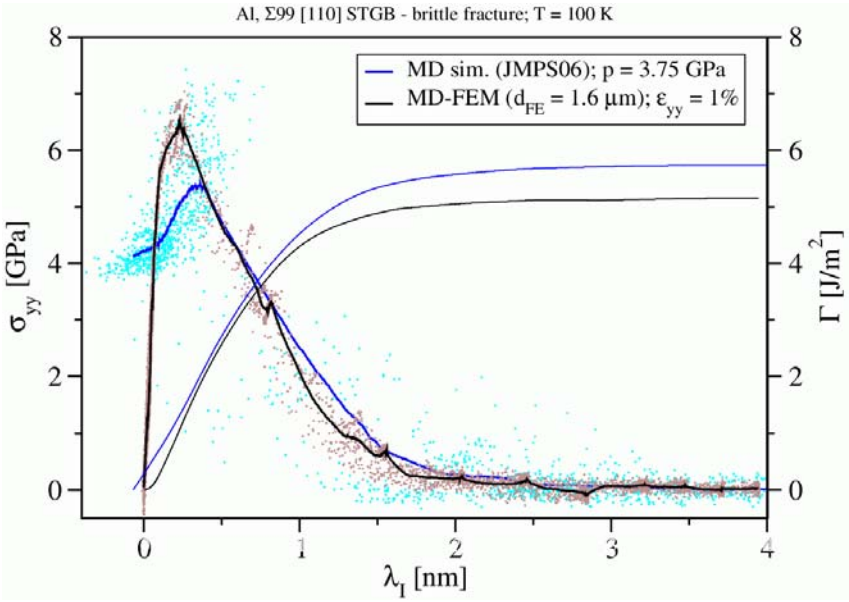

Figure 4.13. Comparison between the brittle CZM derived using pure MD and coupled MD-FEM models.

4.3.2 CZM models for interfacial sliding

Cohesive zone models have been used to simulate shear resistance and friction during interfacial sliding, such as grain boundary sliding, in a material. While the process of sliding may look very similar to Mode II or Mode III fracture (as shown in Figure 4.1), there are several differences between fracture and interfacial sliding, making sliding a fundamentally different deformation mode.

First, by definition, fracture is always related to the creation of a free surface, while in pure sliding (at the atomic scale) there is no free surface creation. For example, during GB sliding, which is a common deformation mechanism in creep deformation [75,142] and governs superplasticity in metals [143], displacement takes place internally between atomic planes and does not involve free surface creation.

Second, while fracture is a localized process taking place at a crack tip, sliding is a delocalized process along the entire interface. The associated CZM curve for fracture has a finite displacement jump, and its integration (Equation (4.1)) always gives a finite energy of decohesion. In contrast, the relative tangential displacement between the two sliding surfaces (i.e. sliding distance) of an interface can be as large as the size of the interface. The tractions (both normal and tangential) do not depend on the displacement but only on the properties of the interface and the applied load. The associated work of friction is proportional to the sliding distance. The interface dependent property is the friction coefficient, usually defined as the ratio between the tangential and normal tractions $\mu = \tau / \sigma_n$ [129].

Third, fracture creates strong stress gradients due to the stress intensity at the crack tip, while interfacial sliding between smooth surfaces preserves a uniform stress along the sliding planes.

Recently, several CZM models for interfacial sliding have been developed. Wei and Anand [130] modeled the strength of nanocrystalline nickel using CZM models based on

experimental data from electrodeposited nanocrystalline Ni with grain sizes between 15 and 40 nm. In their model, the Mode I and Mode II cohesive zone curves were very similar, the only difference being that the Mode II curve was extended to twice as large of an opening displacement as Mode I while keeping a relatively small constant stiffness in the plastic region. This resulted in prediction of a certain amount of sliding with some hardening of the Ni grain boundaries before debonding. Warner et al. [143] parameterized CZMs for grain boundary sliding in copper using atomistic simulation data. Two major assumptions were made in the parameterization: (1) the shear strength τ^{max} of the CZM was assumed to be constant with shear displacement, and (2) the shear and tensile strengths were assumed to be uncoupled because the authors were not able to extract any data that could quantify their coupling. Parameterization of CZMs for sliding between contact surfaces that accounts for surface roughness and friction was performed by Zavattieri and Espinosa [129] for the case of ceramics subjected to pressure-shear loading. The grain-level micromechanical model employed by the authors was successfully used to identify specific failure mechanisms in brittle materials.

Other deformation effects can be generated during MD simulation that are difficult to include in a standard CZM constitutive relationship. One effect is GB migration under an

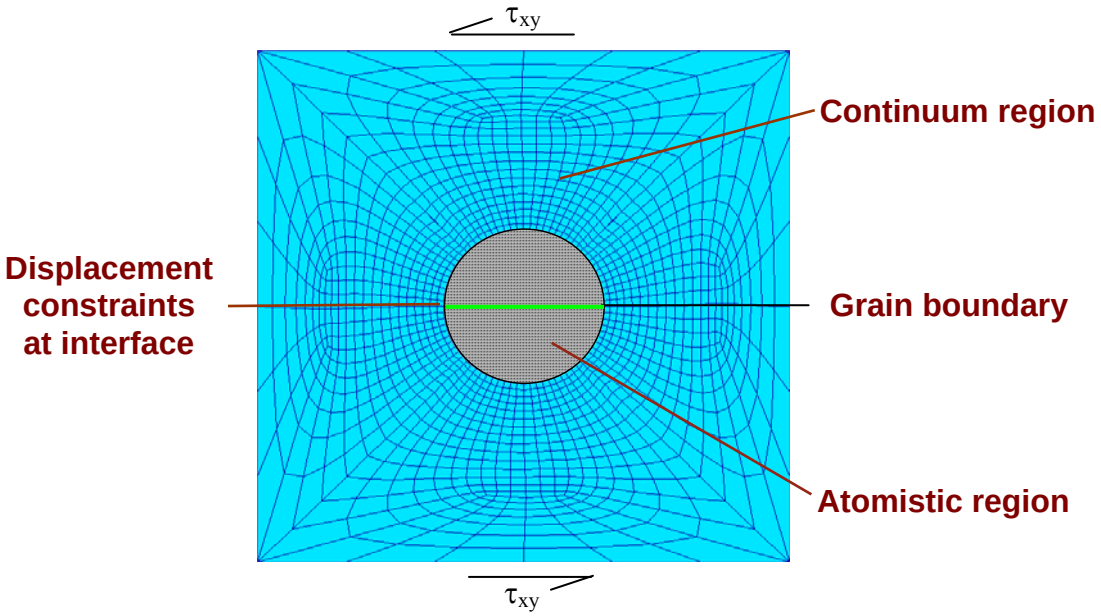

Figure 4.14. ESCM model under pure shear loading.

applied shearing stress [144]. For example, Figure 4.14 depicts the coupled MD-FEM model using ESCM (Chapter 3) under pure shear loading. Figure 4.15 shows the initial location of the GB situated along the line $y = 0$ in the coupled MD-FEM model subjected to applied shear in the [7 7 10] direction. A vertical reference line along x = 0 has been added to clearly show the relative motion of the upper and lower crystal due to sliding. Apparent in Figure 4.16, after 258.7 ps of simulation, is the undesirable migration of the GB that adds to the complexity of the sliding motion and presents a difficulty in developing a constitutive relationship for CZM representation. This difficulty involves the change in the GB structure and the presence of lattice distortions in the form of sessile dislocations and twinning in the wake of the repositioned GB.

The resulting CZM computed is shown in Figure 4.17. The initial portion of the traction-displacement curve shows the response of the GB structure shown in Figure 4.15 which yields a peak traction of approximately 1 GPa. As sliding progresses with an accompanying vertical migration of the GB leading to the atomic structure shown in Figure 4.16, the traction required to maintain sliding decreases. This decrease is attributable to possible restructuring of the GB and surrounding grain due to lattice

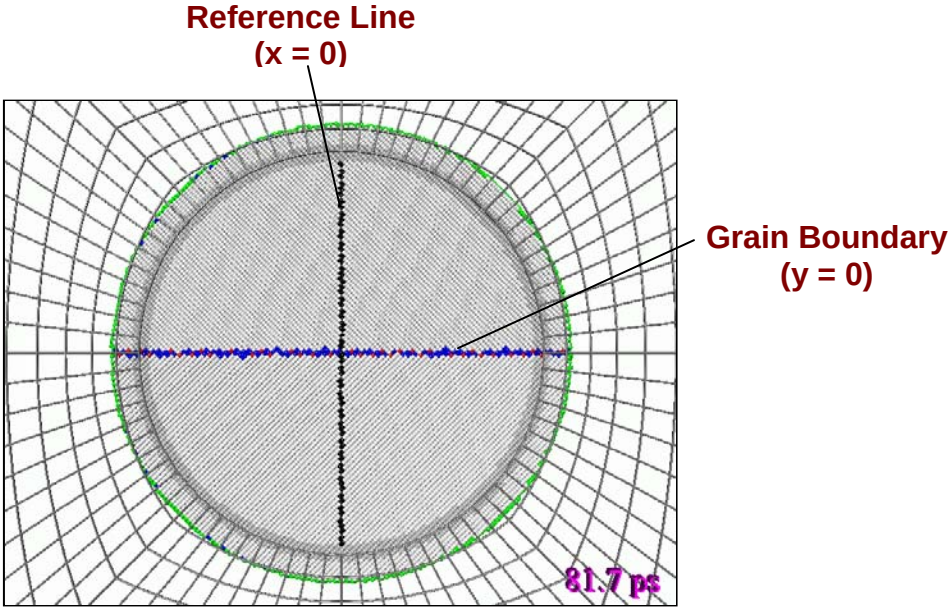

Figure 4.15. Initial configuration of GB subjected to shearing forces to induce sliding in the [7 7 10] direction.

defects – dislocations and twinning – in the wake region. Details of the mechanisms involved are presented in Cahn et al. [144]. This complex damage profile suggests the difficulty of describing this process with a simple CZM formalism.

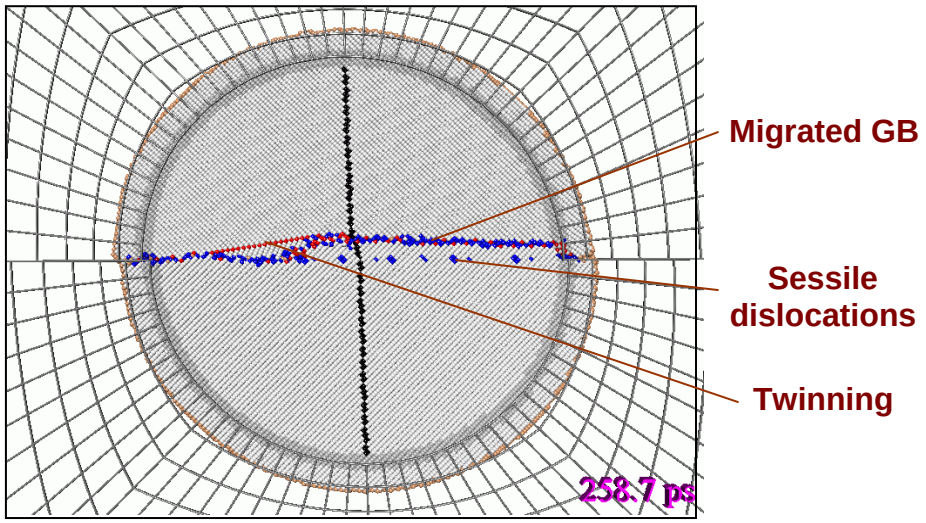

Figure 4.16. Migration of GB and resulting lattice defects due to applied shear.

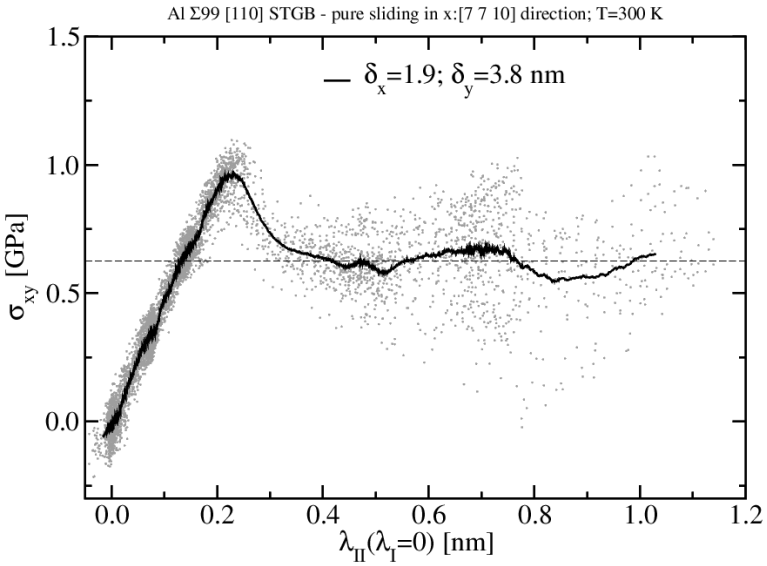

Figure 4.17. Resulting MD-derived CZM for Mode II sliding in the [7 7 10] direction.

For Mode II sliding in the [1 1 0] direction, when the atomic system is rotated through 90^{o}, the initial configuration is similar to that shown in Figure 4.15 for sliding in the [7 7 10] direction. This orientation provides a lower energy barrier to sliding and does not invoke energy transfer to cause GB migration. The configuration after 216 ps is shown in Figure 4.18. The resulting CZM curve is presented in Figure 4.19.

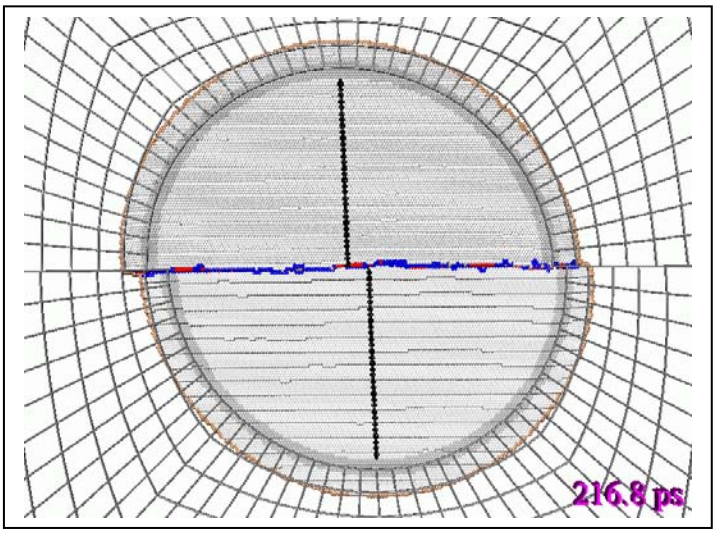

Figure 4.18. Final configuration of GB under Mode II sliding in the [1 1 0] direction.

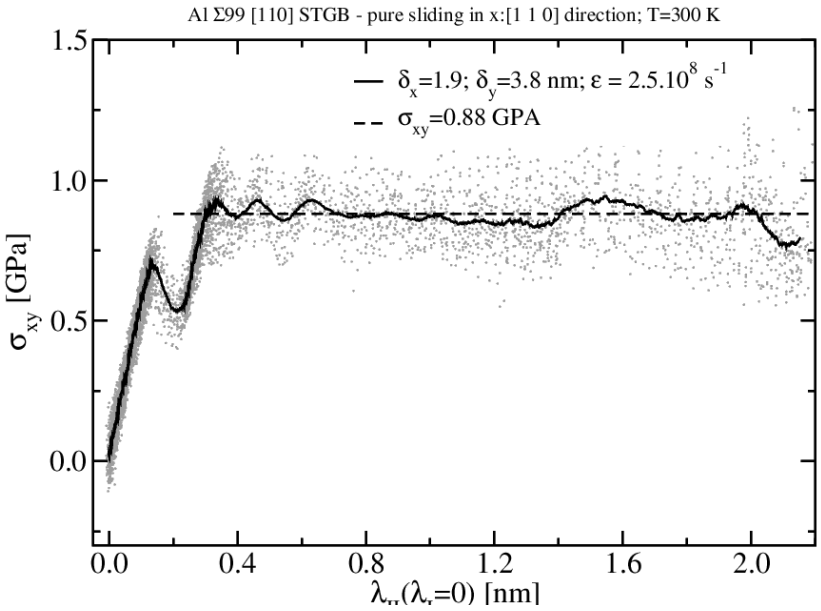

Figure 4.19. MD-derived CZM for pure Mode II sliding in the [1 1 0] direction.

From Figure 4.19, it is apparent that the [1 1 0] direction possesses a smaller energy barrier to be overcome and does not excite mechanisms resulting in GB migration. The resulting CZM shows an increase in traction to approximately 0.85 GPa to initiate sliding, after which the traction to maintain sliding is constant and unchanged from the onset value.

The traction-displacement curves for the two sliding configurations considered show the expected behavior of requiring a constant traction to maintain sliding after an initial maximum traction is reached. The distinction between the analytical treatment of sliding and fracture, and the coupling of sliding with other deformation modes such as grain boundary migration will need to be addressed in future work.

4.4 Generalized representation of cohesive zone models

In the present research the atomistically-derived CZM laws can present a potentially complex profile. If the shape of the constitutive law on decohesion behavior is assumed, it is important to describe CZMs in a general manner to provide a more accurate representation of the traction-displacement relation by avoiding fixed functional forms that could constrain the mathematical description of the constitutive law. Figure 4.20

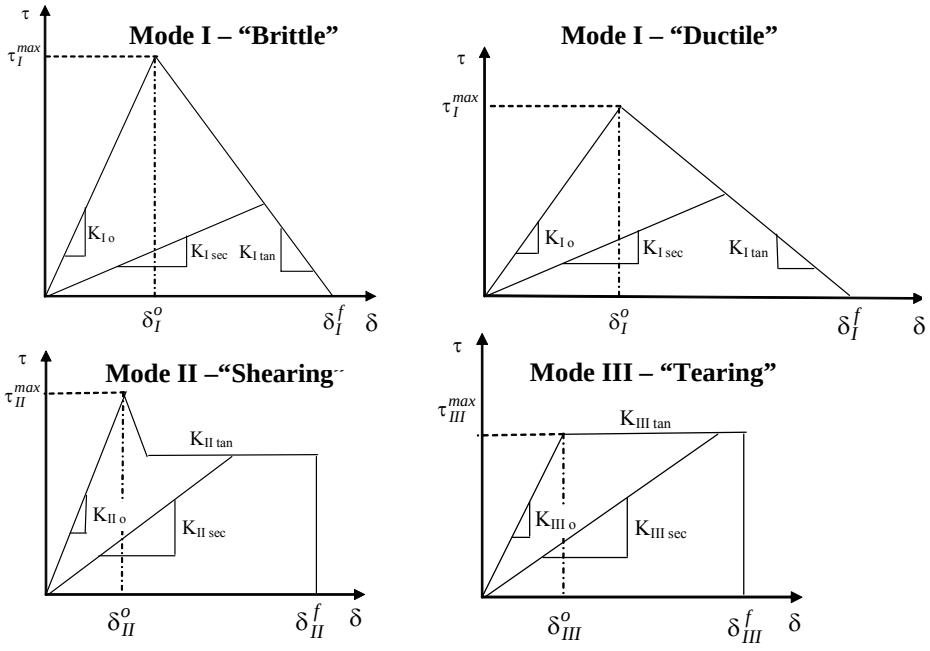

Figure 4.20. Hypothetical CZMs associated with fundamental fracture modes.

presents hypothetical CZMs derived from MD simulation under pure mode loading. Towards this aim and expanding upon the representation presented by Cocchetti et al. [145], explicit functional forms of the CZM traction-displacement laws can be replaced with general tabular input of piece-wise linear descriptions of the CZM associated with different opening modes as depicted in Figure 4.21. In this development, individual atomistically-based CZMs are combined by interpolation utilizing the same assumptions used for the phenomenological coupling of independent fracture modes. More precise coupling methods will require additional research into mixed-mode fracture-sliding deformation involving atomistic mechanisms that is beyond the scope of the current research.

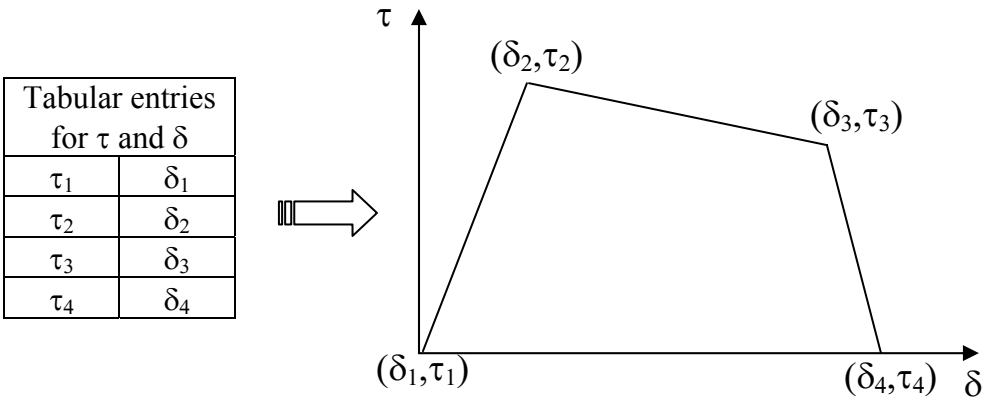

Figure 4.21. Tabular description of a general piece-wise linear CZM shape.

The resulting effective interpolated CZM may assume a form suggested by Figure 4.22. This hypothetical CZM for mixed-mode loading demonstrates softening behavior before the maximum traction is reached. Better convergence has generally been associated with a smooth representation of the constitutive law. Although the standard bilinear or trapezoidal CZM forms contain abrupt transitions, leading many investigators to select a smooth exponential law, the resulting constitutive relationship based on a piecewise linear combination can be smoothed to minimize abrupt changes in stiffness as a function of displacement jumps.

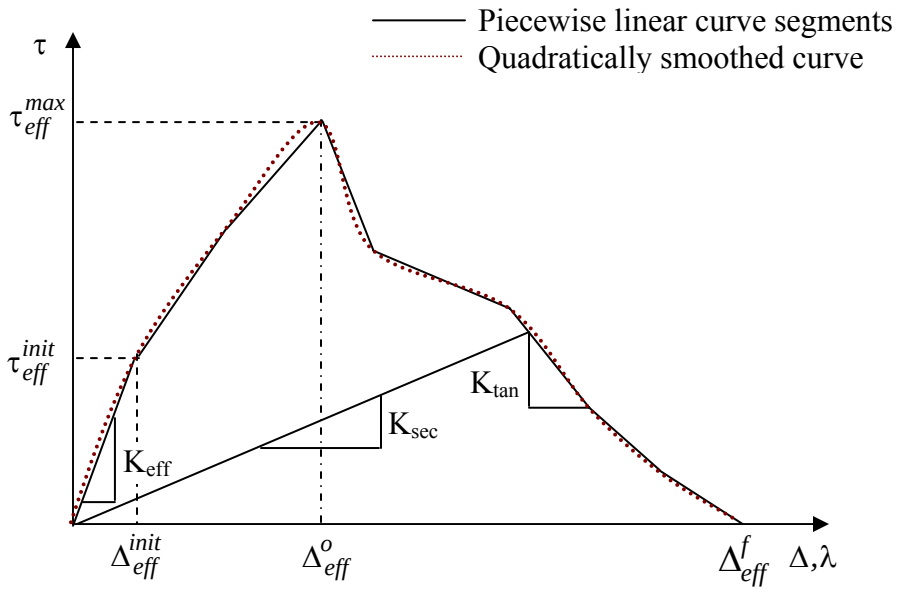

Figure 4.22. Stiffness definitions in an effective interpolated piecewise linear mixed-mode CZM curve.

For arbitrary CZM functional forms, Appendix 4.A presents a development based on a general piecewise linear description of the traction-displacement relationship. For mixed-mode applications, an interpolation procedure presented in Turon et al. [118] is adapted for developing effective CZMs based on 3-D fracture modes.

A rigorous analysis of determining sliding versus transverse fracture modes is an important topic in developing a nanoscale CZM framework. Further research directed towards developing CZM relationships for transverse sliding/fracture modes is suggested for future work. At atomistic length scales, calculations are possible to determine quantitative relationships between the energy consumed by different damage modes. This theoretically obviates the need to develop phenomenological CZM relations based on combined energy measures with experimental tuning to combine independent CZMs corresponding to different failure modes. Coupling approaches can be developed based on more physical considerations such as the effect on interatomic force interactions due to the kinematics of different failure modes. For example, obvious interactions such as the effect of resistance to transverse sliding deformation modes in the presence of

increasing separation of atomic planes due to Mode I opening can be formulated. Specifically, CZMs governing Mode I opening fracture and sliding under Mode II loading can be coupled by relating the maximum sliding traction to the normal opening through the relationship

$$\bar{\tau}_S^{max} = \left(1 - \frac{min\left(\delta_I, \delta_I^f\right)}{\delta_I^f}\right)\tau_S^{max} \tag{4.31}$$

which assumes a linear decrease in the maximum sliding traction as a function of opening in Mode I opening fracture. The effect of this coupling is shown in Figure 4.23.

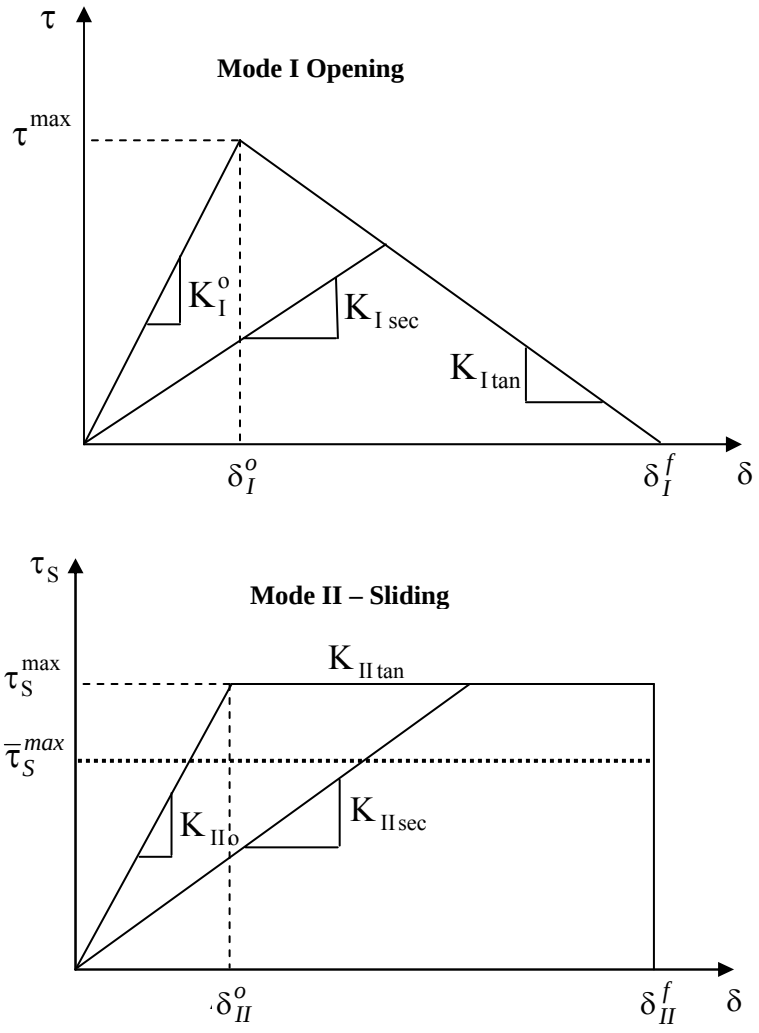

Figure 4.23. Coupling of Mode II sliding CZM with Mode I fracture.

4.5 Remarks on the general characterization of GB CZM parameters

Grain boundaries in polycrystalline metals present a variety of configurational differences that require characterization to predict intergranular fracture/sliding in general polycrystals [130]. Foremost is the size of the orientation space that, for 3-D microstructures, requires five parameters to describe the geometric orientation of a flat grain boundary. In contrast, transgranular fracture/sliding characterizations are expected to not present the same difficult due to the restricted progression of damage along well-defined slip planes.

In general, the quantification of GB strength requires the determination of various energy components. The energy balance of an isolated elastically strained system of an intergranular crack may be expressed as

$$\Delta E_{el} = E_s - \Delta E_{GB} + E_{pl} + \Delta Q \tag{4.32}$$

where ΔE_{el} is the decrease of the stored elastic energy as the crack grows; $E_s = 2l\gamma_s$ is the energy of the newly formed free surface of the crack; $\Delta E_{GB} = l\gamma_{GB}$ is the excess (i.e., above the perfect crystal) energy of the destroyed GB interface; E_{pl} is the energy related to all plastic processes taking place in the plastic zone around the crack tips; and ΔQ is the heat released in the process.

The parameters γ_s and γ_{GB} are relatively easy to obtain from the atomistic models of GBs or from the literature. However, the plastic energy E_{pl} depends strongly on the GB structure, orientation, and the direction and speed of crack propagation. MD energetic analysis on a [110] Σ99 symmetric tilt GB in aluminum (Yamakov, Saether, Phillips, and Glaessgen [131]) showed the contribution of different plastic processes, such as dislocation nucleation and twin or stacking-fault formation, to E_{pl} and their dependence on the speed of crack propagation. Further simulations on a selected set of GBs can give estimates for E_{pl} based on how many slip planes on both sides of the GB were activated.

However, the role of plasticity in the bounding material is clearly unique and cannot be assigned to the CZM.

Estimates of the free energy of a GB has been presented by Lusk and Beale [146], Esling [147], and Wynblatt and Chatain [148]. However, the free energy predictions concern the excess energy required to form a unit area of interface in the crystal and not the energy of separation in fracture. In the general energy equation, Equation (4.32), E_{GB}, may be calculated a number of ways. The classical analytical approach for calculating the energy and motions of small angle GBs was formulated by Read and Shockley [149]. An extension to high angle GBs has been developed [150,151]. For low angle boundaries, the GB energy may be expressed as

$$E_{GB} = \theta\left(E_c - E_s \ln\theta\right)/b \qquad \theta \le \theta_o \tag{4.33}$$

where E_c is the energy per unit length due to the dislocation cores, and E_s is the surface energy per unit length, and θ_o is usually taken as 15^o. From linear elasticity, the surface energy per unit length can be estimated for twist boundaries as $E_s = Gb/2\pi$ with G and b denoting the shear modulus and the Burgers vector, respectively, while for tilt boundaries, $E_s = Gb/[4\pi(1-\nu)]$, where ν is Poisson's ratio. An extension to the Read-Shockley equation, valid for the entire range of $\theta\,(0 \le \theta \le 180^o)$ is presented by Wolf et al. [151]. Other calculations of GB energy are given by Shih et al. [175] and Shenderova et al. [176].

Grain boundary energy as a function of the misorientation angle is shown in Figure 4.24. This figure shows the energy of both disordered and ordered GBs. The ordered GB preserves the crystal lattice between grains, such as a twin boundary, and is represented by cusps where the energy falls to a low state. These cusps correspond to misorientation angles related to low Σ CSL measures. These GB structures may be excluded as a small

subset of special orientations while the predominant GB interfaces correspond to generally disordered atomic states.

Additional complexity includes characterizing the topology of the grain boundary surface, which can be generally nonplanar, quantifying the characteristics of nucleation sites such as triple junctions and corners, the presence of defects along the boundary such as voids, the interaction with defects with long-range influence such as dislocations, and the existence of defect segregation clusters caused by impurity precipitates along the boundary. Grain boundary sliding under pure Mode II or Mode III loading can induce significant grain boundary migration due to assisted dislocation formation along the GB with low to intermediate angle slip planes in the adjacent crystals [144]. In addition, dynamic processes such as dislocation emission from GBs can alter the interface structure [139].

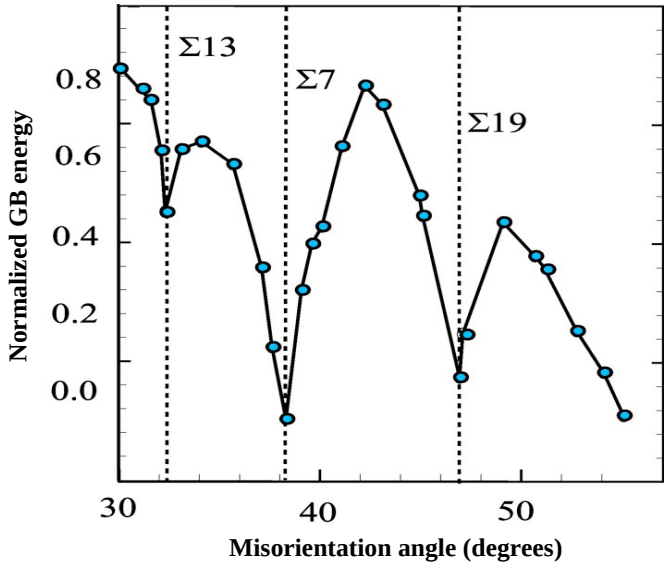

Figure 4.24. Normalized grain boundary energy as a function of misorientation angle. (From Luske and Beale [146]).

To attempt a characterization of the GB separation energies, future work may consider defining categories of GB structures that would exhibit similar behavior under

internal stress states. Detailed studies of specific microstructures would require full characterization of particular GB behavior while studies of representative microstructures to estimate larger ensembles of grains may permit a more generalized characterization of GB strength. Such a generalized or averaged characterization might be possible through a statistical parameterization of a 'general' or ‘universal’ GB response to internal loads [124]. One approach to determining equivalent classes of GBs has been attempted using a corollary between quasicrystals and interfaces [152]. In addition, some work on determining “universal” features of GB networks has been presented by Schuh et al. [153]. These characterization studies will be an ongoing effort in the area of multiscale methods development.

4.6 Concluding remarks for Chapter 4

Many issues involving the formulation and application of CZMs have been discussed. These issues include the development of a work potential, the effect of shape of the CZM relationship, the development of coupled CZM-based models for mixed-mode loading, and the different description of failure modes at microscopic/macroscopic and at nanoscopic length scales – namely fracture versus sliding deformations.

CZM methods at macroscopic length scales are well developed and are empirically based on experimentally determined peak tractions and measured displacement jumps. These constitutive relationships offer a comprehensive approach for representing brittle and ductile material failure in the form of discrete fundamental fracture modes. Interpolation approaches for mixed-mode loading involving CZMs describing individual fracture modes have been presented that have been generalized to piece-wise linear descriptions that avoid simplified functional relationships to better describe generic traction-displacement relationships.

At nanoscopic length scales, the complexity of atomistic mechanisms involved in material failure have been discussed. These failure modes require further investigation

into developing consistent descriptions and interactions of fracture and sliding deformation modes for the complete development of an atomistic CZM-based analysis framework.

In addition, it has been noted that a complete description of damage and failure at atomistic length scales using a CZM formalism is a daunting task. This description will require CZM characterizations that include the energetics of GBs as a function of crystallographic orientation for predicting intergranular failure, energy measures for inelastic transgranular fracture and slip along crystal glide planes, and the influence of surrounding crystal defects that include dislocations and voids. Within the current paradigm of using CZMs to simulated failure, an extensive database of constitutive relationships accounting for all variables that describe intergranular and intragranular failure will need to be determined. This endeavor will be an ongoing effort that will ultimately allow the simulation of damage progression in polycrystalline metallic microstructures.

Therefore, for the purpose of illustrating the developed multiscale methodology, the MD-derived CZM laws obtained in the current research using a Σ99 symmetric tilt GB will be parametrically scaled to qualitatively assess changes in peak tractions, maximum opening displacement, and total strain energy release rate on fracture development and propagation.

APPENDIX 4.A

Formulation of a general representation for mixed-mode cohesive zone models

A generic tabular description of the traction-displacement relationships is used to replace the common use of fixed mathematical representations such as trapazoidal, bilinear, or exponential forms. This representation is desirable for cases where the shape of the CZM law is important and exhibit a form that would introduce an unacceptable inaccuracy by being approximated by a simple mathematical representation. The tabular representation is based, with some modification, on an interpolation procedure to account for mode-mixity presented by Turon et al. [118]. The displacements are computed as the relative change of the displacements on either cohesive surface and, thus, represent discontinuities or 'displacement jumps.'

The computation of critical strain energy release rates is given by a linear integration of the discrete tabulated CZM laws for each mode

$$\begin{aligned} G_{Ic} &= \int_0^{\delta_I^f} \tau_{zz}(\delta_I)\,\mathrm{d}\delta_I = \frac{1}{2}\sum_{i=1}^{N_1}\left(\tau_{zz}^{i+1}+\tau_{zz}^{i}\right)\left(\delta_I^{i+1}-\delta_I^{i}\right) \\ G_{IIc} &= \int_0^{\delta_{II}^f} \tau_{zy}(\delta_{II})\,\mathrm{d}\delta_{II} = \frac{1}{2}\sum_{i=1}^{N_2}\left(\tau_{zy}^{i+1}+\tau_{zy}^{i}\right)\left(\delta_{II}^{i+1}-\delta_{II}^{i}\right) \\ G_{IIIc} &= \int_0^{\delta_{III}^f} \tau_{xz}(\delta_{III})\,\mathrm{d}\delta_{III} = \frac{1}{2}\sum_{i=1}^{N_3}\left(\tau_{xz}^{i+1}+\tau_{xz}^{i}\right)\left(\delta_{III}^{i+1}-\delta_{III}^{i}\right) \end{aligned} \tag{4.A1}$$

where the superscript, *i*, indicates the tabular entry record.

During solution increments, the current accumulated strain energy for each mode is calculated by summing the area under the traction-displacement curves similar to Equation 4.A1 but ending the integration at the current values of the predicted displacement jumps (δ_1, δ_2, and δ_3) for each mode

$$
\begin{aligned}
G_I &= \frac{1}{2}\sum_{i=1}^{M_1}\left(\tau_{zz}^{i+1}+\tau_{zz}^{i}\right)\left(\delta_1^{i+1}-\delta_1^{i}\right), \qquad \delta_1^{i+1} \le \left\langle \delta_1 \right\rangle \\
G_{II} &= \frac{1}{2}\sum_{i=1}^{M_2}\left(\tau_{zz}^{i+1}+\tau_{zz}^{i}\right)\left(\delta_2^{i+1}-\delta_2^{i}\right), \qquad \delta_2^{i+1} \le \left|\delta_2\right| \\
G_{III} &= \frac{1}{2}\sum_{i=1}^{M_3}\left(\tau_{zz}^{i+1}+\tau_{zz}^{i}\right)\left(\delta_3^{i+1}-\delta_3^{i}\right), \qquad \delta_3^{i+1} \le \left|\delta_3\right|
\end{aligned}
\tag{4.A2}
$$

where the Macaulay bracket is defined as $\langle x \rangle = 1/2\ (x + |x|)$ and is used to exclude negative values of δ_1 that would indicate interpenetration in Mode I. The absolute values of the transverse displacement jumps, $|\delta_2|$ and $|\delta_3|$, are used if the tables are based solely on the positive values of the shear traction-displacement relationships.

The total strain energy is given by the sum of normal and tangential fracture/sliding components

$$G_T = G_I + G_S \tag{4.A3}$$

where

$$G_S = G_{II} + G_{III} \tag{4.A4}$$

Mode mixity is defined by the ratio of accumulated strain energy measures or

$$\beta = \frac{G_S}{G_T} \tag{4.A5}$$

Critical strain energy release rate measures for mixed-mode loading are given by

$$G_{Sc} = G_{IIc} + G_{IIIc} \tag{4.A6}$$

$$G_{Tc} = G_{Ic} + G_{Sc} \tag{4.A7}$$

The opening criterion for fracture is based on a combined energy release rate criterion given by

$$G_c = (1-\beta)G_{Ic} + \beta G_{Sc} \tag{4.A8}$$

Equation (4.A8) corresponds to the empirical model of Benzeggagh and Kenane [154] used by Turon et al. ([118], Equation 35) with the fitting exponent set equal to unity.

Various quantities need to be extracted from the tables. The initial stiffnesses, corresponding to each deformation mode, are obtained directly from the individual CZMs using the initial slopes of the table entries as

$$\begin{aligned} K_{1o} &= \left(\tau_1^2 - \tau_1^1\right) / \left(\delta_1^2 - \delta_1^1\right) \\ K_{2o} &= \left(\tau_2^2 - \tau_2^1\right) / \left(\delta_2^2 - \delta_2^1\right) \\ K_{3o} &= \left(\tau_3^2 - \tau_3^1\right) / \left(\delta_3^2 - \delta_3^1\right) \end{aligned} \tag{4.A9}$$

The displacements corresponding to the onset of damage for each mode are obtained as by locating the displacement corresponding to the departure of the traction-displacement relationship from the initial stiffness indicating the onset of material softening. For the j^{th} deformation mode, the displacement corresponding to damage onset is determined by the first occurrence of the slope of the tabular traction-displacement relationship differing from the initial slope or

$$\frac{\tau_j^{i+1} - \tau_j^i}{\delta_j^{i+1} - \delta_j^i} \neq K_{jo} \;\Rightarrow \delta_j^o = \delta_j^i \;, \quad i = 1,2,3,... \tag{4.A10}$$

The displacements corresponding to damage propagation are simply the maximum input displacements corresponding to a zero traction, which may be assumed to be the last entry in the table.

$$\begin{aligned} \delta_1^f &= \delta_1^i \mid \tau_1^{M_1} = 0 \\ \delta_2^f &= \delta_2^i \mid \tau_2^{M_2} = 0 \\ \delta_3^f &= \delta_3^i \mid \tau_3^{M_3} = 0 \end{aligned} \tag{4.A11}$$

The effective displacement jump is given by

$$\lambda = \sqrt{\langle \delta_1 \rangle^2 + (\delta_S)^2} \tag{4.A12}$$

where

$$\delta_S = \sqrt{(\delta_2)^2 + (\delta_3)^2} \tag{4.A13}$$

Similarly, an effective measure of traction corresponding to the effective displacement jump is calculated by interpolating the input traction-displacement tables using the displacement jumps for each mode given by δ_1, δ_2, and δ_3 to obtain the tabulated shear tractions, τ_1, τ_2, and τ_3, and forming an effective value as

$$\tau_{eff} = \sqrt{\tau(\delta_1)^2 + \tau(\delta_2)^2 + \tau(\delta_3)^2} \tag{4.A14}$$

Effective initiation displacement is computed by Turon et al. [118] by considering the failure criterion of Ye [155] and is given by

$$\Delta^o = \sqrt{(1-\beta)(\delta_1^o)^2 + \beta\left[(\delta_2^o)^2 + (\delta_3^o)^2\right]} \tag{4.A15}$$

For the current development, lacking a fixed functional form for CZM relationships, a similar argument is used to approximate the effective propagation displacement as

$$\Delta^f = \sqrt{(1-\beta)(\delta_1^f)^2 + \beta\left[(\delta_2^f)^2 + (\delta_3^f)^2\right]} \tag{4.A16}$$

The effective initial stiffness, K_{eff}, is assumed to be a function of the initial stiffnesses of each CZM based on the relative participation of various loading modes

$$K_{eff} = \frac{G_I}{G_T} K_{1o} + \frac{G_{II}}{G_T} K_{2o} + \frac{G_{III}}{G_T} K_{3o} \tag{4.A17}$$

and the secant stiffness, K_{sec}, is estimated as

$$K_{sec} = \frac{\tau_{eff}}{\lambda} \tag{4.A18}$$

The critical state variable in the form of a damage parameter is defined as the change in secant stiffness with respect to the initial stiffness as

$$d = 1 - \frac{K_{sec}}{K_{eff}} \tag{4.A19}$$

This damage parameter represents the measure of material property degradation due to mixed-mode displacement jumps.

The definition of free energy follows Turon et al. [118], incorporating a damage parameter that accounts for mixed-mode loading such that

$$\Phi(\delta, d) = (1 - d)\Phi^o - d\Phi^o\left(\bar{\delta}_{i1}\langle -\delta_1 \rangle\right) \tag{4.A20}$$

where the second term on the right hand side accounts for interpenetration due to closure in Mode I, d is the continuum damage parameter, and $\bar{\delta}_{ij}$ is the Kroneker Delta function. The energy term for elastic reversible loading is given by

$$\Phi^o = \frac{1}{2}\delta_i D_{ij} \delta_j \tag{4.A21}$$

Generating the constitutive law follows for the initial portion of the traction-displacement curve.

$$\tau_i = \frac{\partial \Phi}{\partial \delta_i} = (1-d) D_{ij}^{sec} \delta_j - d D_{ij}^{sec} \bar{\delta}_{1i} \langle -\delta_1 \rangle \tag{4.A22}$$

where D_{ij}^{sec} represents the secant material stiffness, and it is assumed that each CZM for the various fracture modes may possess a different initial modulus or

$$D_{ij}^{sec} = \bar{\delta}_{ij} K_j \tag{4.A23}$$

This yields a traction-displacement law given by

$$\begin{Bmatrix} \tau_1 \\ \tau_2 \\ \tau_3 \end{Bmatrix} = \begin{bmatrix} (1-d)K_{1o} & & \\ & (1-d)K_{2o} & \\ & & (1-d)K_{3o} \end{bmatrix} \begin{Bmatrix} \delta_1 \\ \delta_2 \\ \delta_3 \end{Bmatrix} - dK_{1o} \begin{Bmatrix} \langle -\delta_1 \rangle \\ 0 \\ 0 \end{Bmatrix} \tag{4.A24}$$

where K_{io} are the initial stiffnesses of the individual CZMs.

The tangent constitutive relation is obtained by relating the derivatives of τ and δ.

$$\dot{\tau} = \bar{\delta}_{ij} K_j \left[1 - d \left(1 + \bar{\delta}_{1j} \frac{\langle -\delta_j \rangle}{\delta_j} \right) \right] - \bar{\delta}_{ij} K_j \left(1 + \bar{\delta}_{1j} \frac{\langle -\delta_j \rangle}{\delta_j} \right) \delta_j \dot{d} \tag{4.A25}$$

Differentiating Equation (4.A19) yields

$$\dot{d} = \frac{1}{K_{eff}} \dot{K}_{sec} = \frac{1}{K_{eff}} \left(\frac{\partial K_{sec}}{\partial \lambda} \dot{\lambda} \right) \tag{4.A26}$$

The flux of the displacement norm is given by

$$\dot{\lambda} = \frac{\partial \lambda}{\partial \delta_k} \dot{\delta}_k = \frac{\delta_k}{\lambda} \left(1 + \bar{\delta}_{1k} \frac{\langle -\delta_k \rangle}{\delta_k} \right) \dot{\delta}_k \tag{4.A27}$$

The change of the secant stiffness with the displacement norm, $\partial K_{sec}/\partial\lambda$, is evaluated numerically from the effective mixed-mode CZM relationship. Substituting Equations (4.A26) and (4.A27) into (4.A25) yields the rate equation

$$\dot{\tau} = D_{ij}^{tan}\,\dot{\delta} \tag{4.A28}$$

where the tangent constitutive matrix is given by

$$D_{ij}^{tan} = D_{ij} - K_i\left[1+\bar{\delta}_{1i}\frac{\langle -\delta_i\rangle}{\delta_i}\right]\left[1+\bar{\delta}_{1j}\frac{\langle -\delta_j\rangle}{\delta_j}\right]\frac{1}{\lambda}\left(\frac{\partial K_{sec}}{\partial\lambda}\right)\delta_i\delta_j \tag{4.A29}$$

Chapter 5
Decohesion Finite Element Formulations

5.1 Introduction

Decohesion finite elements (also referred to in the literature as “interface elements”, “cohesive elements,” or “CZM elements”) were initially introduced by Hilleborg et al. [156] to study fracture in concrete. Needleman [157,158] later formulated a decohsion element to study dynamic fracture in isotropic solids. The formulations of these elements presented here are based on the work of Beer [159]. The basic topology of decohesion elements is formed by separable surfaces that can open under constitutive relationships that relate tractions and displacements. These element formulations have found broad application to modeling brittle and ductile fracture whether or not crack paths are known a priori. Fundamental to decohesion elements are assumed cohesive zone models (CZMs) that govern the prediction of separation – fracture – of element surfaces [160]. Chapter 4 detailed the development of CZMs for continuum and atomistic applications under uniaxial and mixed-mode load conditions. Considerations involving the development of effective interpolated CZMs for macroscopic applications and the coupling of CZMs describing fracture and sliding modes for nanoscopic applications were addressed. Issues related to the form of the assumed CZMs were also discussed.

When the location of fracture is not known a priori, decohesion elements can be placed between all continuum elements within a finite element mesh. While decohesion elements can add artificial compliance to the model [161], more involved simulations involving adaptive meshing can limit the number of decohesion elements by placing these elements only in regions of high stress [127]. Figure 5.1 depicts a micromechanical simulation of intergranular fracture with decohesion elements placed along all grain boundaries.

For sequential multiscale analysis, decohesion elements can be used to simulate the evolution of failure of material across length scales. For a MD-based CZM, the methodology is very generic and can be used for any interface that is subjected to fracture provided that the atomistic simulation captures all relevant mechanisms. The sequential multiscale approach eliminates the computational constraints on the MD domain size in utilizing even the most efficient concurrent multiscale methods, and permits the simulation of microstructures with much larger characteristic dimensions. At the level of microns, important damage and failure behavior in polycrystalline metals can be simulated including fracture along grain boundaries in metals (intergranular fracture), fracture along weak slip planes (transgranular fracture), and fracture through interfaces between grains and small second phase particles.

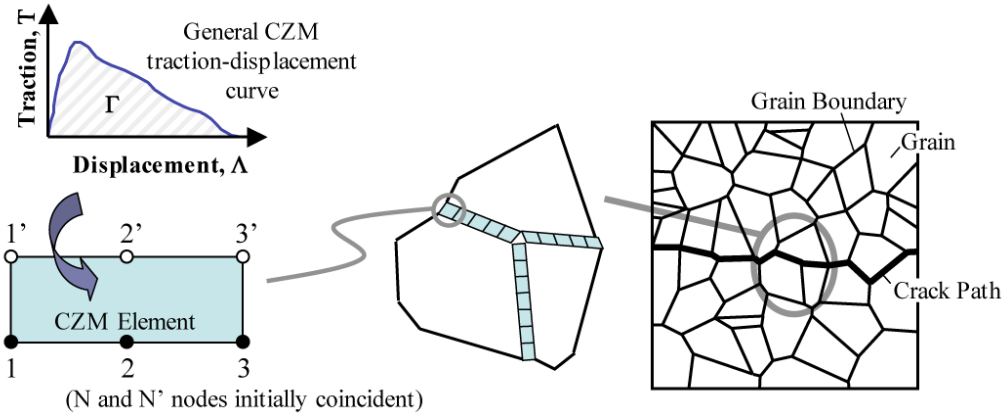

Figure 5.1. Embedding decohesion elements along GBs to study microstructural fracture.

The basic formulation of decohesion finite elements is outlined here. The difference between different formulations is typically a function of the dimensionality, order of element interpolants, and the particular choice of CZMs that are incorporated into the element formulation. Decohesion elements are formulated with two sets of initially coincident nodes defining two superposed surfaces forming a cohesive interface. This is depicted in Figure 5.2 by the surfaces denoted Ω^+ and Ω^- that have been separated for clarity. The particular configuration shown in Figure 5.2 represents an 8-node linear decohesion element used to simulate the cohesive behavior between connected solid continuum elements. Shape functions appropriate to the order of assumed variation over the element domain govern the interpolation of quantities over the superposed surfaces.

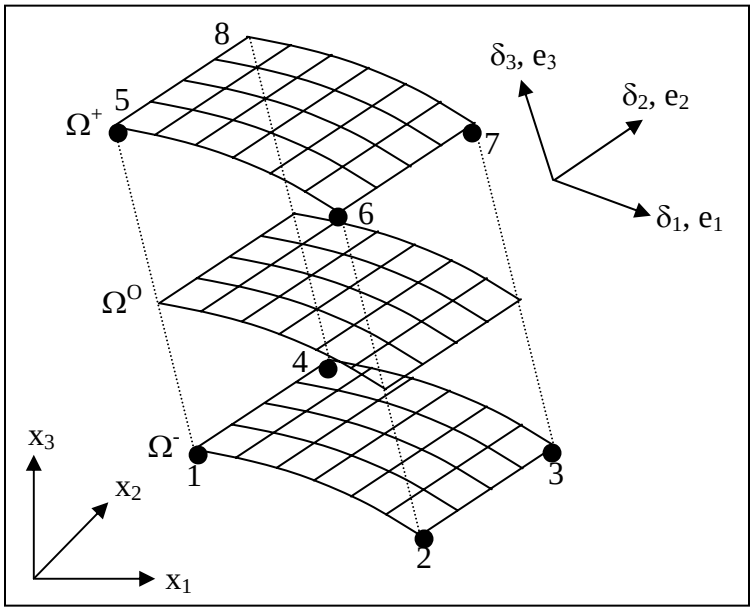

Figure 5.2. Decohesion element cohesive surfaces.

These elements incorporate CZMs to simulate failure modes and are placed between continuum finite elements to predict softening and failure of the interface.

The essential feature of decohesion elements is the incorporation of a CZM (discussed in Chapter 4) that is defined by displacement jumps, denoted by Δ_i, which measure the discontinuity of the i^{th} displacement components between initially coincident top (δ_i^+) and bottom surfaces (δ_i^-) (see Beer [159], Camanho et al. [162], and Cook, et al. [163]). Discretizing each surface into k finite element nodes and assuming the displacement field varies over the surface defined by standard Lagrangian shape functions N_k yields the relationship

$$\begin{Bmatrix} \Delta_1 \\ \Delta_2 \\ \Delta_3 \end{Bmatrix} = \begin{Bmatrix} \delta_1^+ - \delta_1^- \\ \delta_2^+ - \delta_2^- \\ \delta_3^+ - \delta_3^- \end{Bmatrix} = \begin{Bmatrix} N_k \delta_{1k} \\ N_k \delta_{2k} \\ N_k \delta_{3k} \end{Bmatrix} \tag{5.1}$$

where δ_{ik} is the i^{th} relative displacement at the k^{th} node referenced to the middle surface of the element Ω^O. Transforming between local (e_1,e_2,e_3) and global (x_1,x_2,x_3) coordinate systems using the transformation tensor T_{ij} yields

$$\{u\} = [T]\{\Delta\} = [T][N]\{\delta\} = [B]\{\delta\} \tag{5.2}$$

Relating the element tractions, τ_i, to the relative element displacements, u_i, is performed using the decohesion element constitutive operator, D_{ij}, as

$$\{\tau\} = [D]\{u\} \tag{5.3}$$

The governing equation can be obtained from the principle of virtual work

$$\int_{\Omega^o} d\{u\}^T \{\tau\} d\Omega^o - \{f\}^T d\{u\} = 0 \tag{5.4}$$

which yields, for a geometrically linear problem, the relationship

$$\int_{\Omega^o} [B]^T \{\tau\} d\Omega^o - \{f\}^T = 0 \tag{5.5}$$

where [*B*] is constant. Substituting Equations (5.2) and (5.3) into Equation (5.5) yields the standard governing equation for linear elastostatics

$$[K]\{\delta\} = \{f\} \tag{5.6}$$

where

$$[K] = \int_{\Omega^o} [B]^T [D][B] d\Omega^o \tag{5.7}$$

The constitutive matrix, [*D*], is formulated based on the assumed traction-displacement relationship together with other assumptions that have been assumed for the element. For example, Equation (4.30) was developed for a tangent constitutive relation based on a bilinear CZM and incorporates a damage parameter as a state variable for mixed-mode failure and a variable term that accounts for interpenetration due to possible closing in Mode I fracture [118].

Various additional details of decohesion element formulations can be found in Chen et al. [110], Foulk et al. [111], Alfano and Crisfield [112], Goyal et al. [116], Camanho et al. [162], Turon et al.[118], Segurado and Llorca [164], Gustafson et al. [165],

Hamitouche et al. [166], and Van den Bosch et al. [177]. However, most of the differences in these formulations pertain to specific definitions of the CZM relationships incorporated into the decohesion element.

An additional issue of CZMs regards the initial stiffness associated with the constitutive relationship for each fracture mode. For macroscopic analysis, this initial stiffness assumes the role of a penalty constraint. As a formal penalty parameter, this quantity is set to the highest value that will not cause ill-conditioning in the global element stiffness matrix. This constraint is used to prevent relative displacements between the top and bottom surfaces before the onset of softening. Using a value that is less than optimally large introduces a spurious compliance into the model that can alter results, particularly in models where decohesion elements are placed between many continuum elements when an a priori determination of where a dominant crack path will be generated cannot be made. However, at nanoscopic length scales, this initial stiffness typically is calculated based on the elastic properties of the grain boundary or between lattice planes because the thickness of the cohesive surface can no longer be generally regarded as infinitesimal. In this case, the initial stiffness of the CZM is no longer a mathematical penalty parameter but becomes reduced to represent the actual elasticity of a finite thickness cohesive zone. Under arbitrarily small loads, the displacement field is not homogeneous and the cohesive surface exhibits an elastic separation due to straining below the peak traction. To avoid adding spurious compliance to the model due to a numerically finite initial stiffness, the additional elasticity introduced by decohesion elements can be accounted for directly by assigning an initial thickness to the decohesion elements or by adjusting the elastic properties of adjacent continuum elements.

Convergence difficulties have been encountered and have been related to numerical problems caused by abrupt changes in slope of the CZM relationship – such as at the vertices of triangular and trapezoidal CZM relations - during loading and unloading cycles in which large variations can occur in computing the tangent stiffness matrix [167]. Another effect that can hinder convergence involves the type of numerical quadrature used to evaluate the element integrals. It has been found that Gaussian

quadrature tends to couple kinematic degrees of freedom across the element that can be seen in the eigenmodes of the element deformation states. Using Newton-Cotes quadrature methods act to uncouple the eigenmodes and have been associated with an improvement in convergence behavior [168]. Additional numerical aspects, such as bounds on element size, have been presented [169,170,132], and augmented solution schemes that include numerical relaxation to improve convergence characteristics have been advanced [167].

5.2 Directional decohesion element formulation

At atomistic length scales it has been shown that, for a common symmetric tilt GB (Chapter 2), Mode I fracture can vary between ductile and brittle propagation modes depending on direction, and relative in-plane sliding modes can exhibit significant variations in traction-displacement response (Chapter 4). This directional dependence of Mode I fracture motivated the development of a directional decohesion finite element formulation for simulating intergranular crack development. The unique feature of this element is the adaptive application of different CZMs depending on the grain orientation through the capability to automatically compute the magnitude of opening over the element surfaces and determine the direction of crack propagation. This element incorporates the direction-dependant CZMs for Mode I opening and permits different functional forms for Mode II and Mode III CZMs to be used in computing an effective mixed-mode CZM. The appropriate Mode I CZM is selected based on the orientation of the surrounding slip systems along the direction of propagation from which ductile or brittle opening behavior is imposed (see Figure 5.4). Several different element configurations are presented which incorporate Rice's criterion [64] to predict brittle or ductile fracture and apply the appropriate CZM during an incremental-iterative solution procedure. The distinct directional difference in crack propagation behavior was discussed in Chapter 2, and the atomistic determination of corresponding CZM parameters was presented in Chapter 4. A synopsis of these results is presented in Figure 5.3

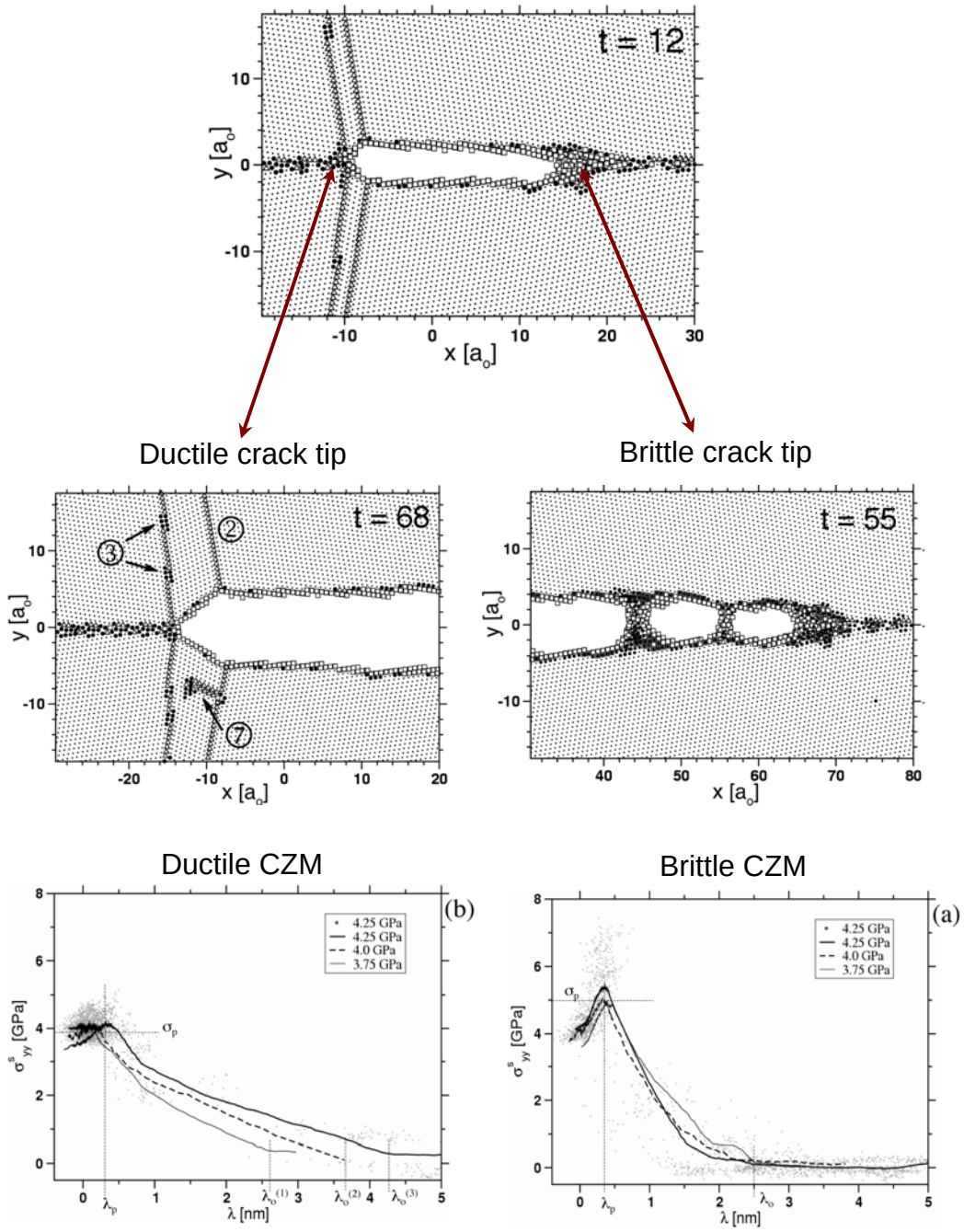

Figure 5.3. Direction-dependant crack growth behavior incorporated into decohesion finite element formulations.

The additional parameters needed in selecting the appropriate CZM, including surface, GB, stacking-fault, and twinning energy, are readily available from published experimental data. Others, such as the unstable stacking-fault energy and the unstable

twinning energy, need more precise estimates and may require the use of first-principal calculations. The directional decohesion element formulations have been encoded into user-defined (UEL) subroutines to enable simulations to be performed using the commercial finite element code ABAQUS [79].

Until the final effective opening displacement has been reached and the decohesion element stiffness terms are zero, calculations are performed using various relative nodal displacements to approximate the displacement gradients over the element surface and determine the direction of propagation. For cases in which various opening displacements are equal or zero, a default direction is assumed. The propagation vectors, $\vec{\boldsymbol{d}}$ and $\vec{\boldsymbol{s}}$, are used to specify the direction of Mode I fracture and the direction of sliding under Mode II loading, respectively. The fracture propagation direction determines the appropriate CZM to use and the relative mode mixity is used to interpolate an appropriate effective CZM as discussed in Section 4.3 for use in the decohesion element.

Figure 5.4 shows a configuration of a crack plane and slip plane with the angle between the two specified by θ. The orientation of the Burgers vector, $\boldsymbol{b}$, lying in the slip plane, showing the direction of slip is given by the angle ϕ.

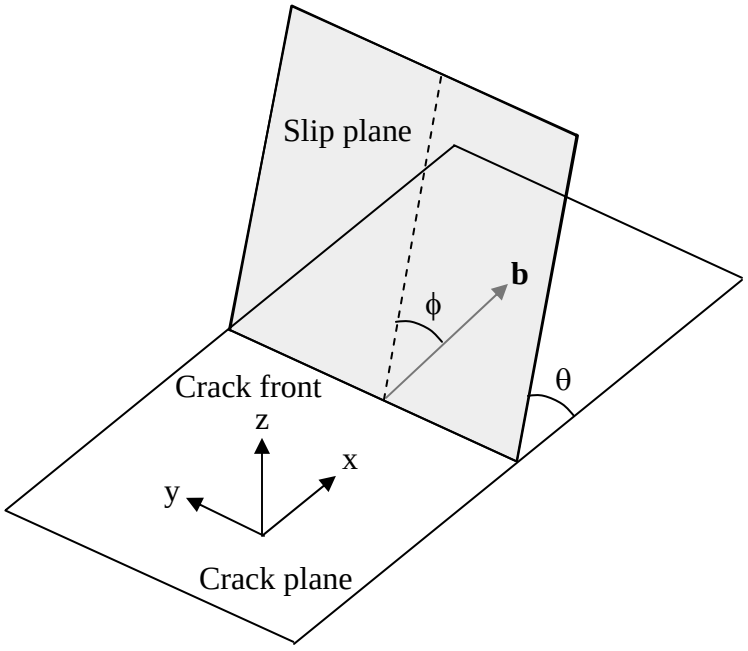

Figure 5.4. Geometric configuration of a crack with an intersecting slip plane.

For a slip direction aligned with the crack opening such that $\phi = 0$, the Rice criterion [64] for dislocation emission associated with Mode I opening along two propagation directions can be written as

$$\eta = \frac{\gamma_{us}}{2\gamma_s - \gamma_{GB}} - \frac{(1 \pm \cos\theta)\sin^2\theta}{8} \quad \text{where} \quad \begin{array}{l} \eta > 0 \text{ for brittle fracture} \\ \eta < 0 \text{ for ductile fracture} \end{array} \tag{5.8}$$

where $+\cos\theta$ is associated with the -*x* direction and $\cos(\pi - \theta) = -\cos\theta$ is associated with the +*x* direction. Rice's criterion gives the condition for predicting a brittle versus ductile crack propagation. For a Σ99 symmetric tilt GB in aluminum, an unstable stacking-fault energy of γ_{us} = 0.168 J/m^2, a surface energy of the GB as γ_s = 0.952 ± 0.010 J/m^2, and an excess GB energy given by γ_{GB} = 0.60 ± 0.05 J/m^2 is presented in Yamakov, Saether, Phillips, and Glaessgen [131]. For this system, the resulting Rice criterion can be expressed as

$$(1 \pm \cos\theta)\sin^2\theta > 1.0307 \pm 0.01 \tag{5.9}$$

The directional decohesion elements developed for the present research consist of a 1-D 6-node decohesion element for joining 2-D quadratic triangular continuum elements and a 2-D 12-node decohesion element to join 3-D quadratic tetrahedral elements. For both elements, the orientation of slip planes with respect to the cohesive surface is required input. To apply Rice's criterion, the direction of Mode I opening for each decohesion element must be determined. In mapped coordinates, the surface is defined by the local *x'* and *y'* coordinates corresponding to the node positions, and can be defined using a general scalar field representation as $\phi = F(x',y')$, where ϕ represents the variation of a relative displacement component over this region. The nodal displacement components of interest can be assigned at the node locations as a normal *z'* coordinate and a 3-D planar surface can be constructed. Using this surface, the elements of the outer normal vector give the *x'* and *y'* components of the change in magnitude of the relative displacements in the local *x'* and *y'* directions.

For a 1-D decohesion element, the direction of opening or sliding is simply given by the sign of the slope of the relative normal displacements or relative tangential displacements along the element. For a 2-D decohesion element, the interpolated relative nodal displacements are used to compute a normal to a plane surface from which the relative directions of opening are obtained as the in-plane components of the normal. The equation of a surface is given by

$$Ax' + By' + Cz' = D \tag{5.10}$$

where x' and y' are the mapped coordinate axes, and z' is the value of the scalar field at each (x',y') point over the domain. The normal to this surface is given by

$$\vec{n} = A\vec{e}_{x'} + B\vec{e}_{y'} + C\vec{e}_{z'} \tag{5.11}$$

where $\vec{e}_{\alpha}$ are unit basis vectors in the local element coordinate system, and the components of interest are calculated as

$$A = \begin{vmatrix} 1 & y_1' & \phi_1 \\ 1 & y_2' & \phi_2 \\ 1 & y_3' & \phi_3 \end{vmatrix} = y_1'(\phi_2 - \phi_3) + y_2'(\phi_3 - \phi_1) + y_3'(\phi_1 - \phi_2)$$

$$B = \begin{vmatrix} x_1' & 1 & \phi_1 \\ x_2' & 1 & \phi_2 \\ x_3' & 1 & \phi_3 \end{vmatrix} = \phi_1(x_2' - x_3') + \phi_2(x_3' - x_1') + \phi_3(x_1' - x_2') \tag{5.12}$$

All global displacement quantities are mapped to a local element coordinate system for the determination of opening behavior. Failure propagation vectors are computed in the local frame and mapped back to the global coordinate system to compare with grain orientation angles to select which appropriate directional CZM laws are to be applied. Figure 5.5 shows the 6-node decohesion element configuration. Although the element is

quadratic, the Mode I opening direction is determined by computing an approximate linear gradient of the relative opening displacements, Δv_i, over the element using only the end nodes. The degree of sliding in Mode II is computed by a summation of all relative *x*-displacements, Δu_i, over the element.

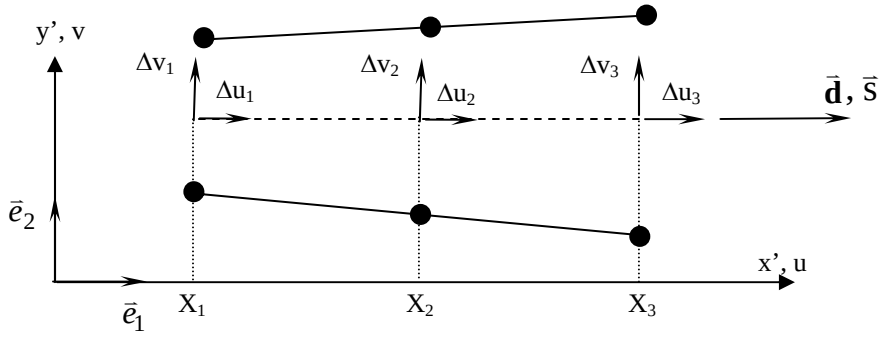

Figure 5.5. Relative opening displacements for Mode I and Mode II fracture in a 6-node quadratic decohesion element.

The kinematics and integration scheme used in the new 6-node 1-D directional decohesion element is similar to the element presented by Alfano and Crisfield [112]. The sign of the difference between relative displacements determines the directionality of Mode I opening and Mode II sliding across the element. In determining the sense of relative motion, only the end nodes of the upper or lower surface need to be considered. The propagation vectors are then computed as

$$\vec{d} = \text{Sgn}\left(\Delta v_3 - \Delta v_1\right)\vec{e}_1 \tag{5.13}$$

$$\vec{s} = \text{Sgn}\left(\Delta u_1 + \Delta u_3\right)\vec{e}_1 \tag{5.14}$$

where *Sgn* indicates the Sign function.

The 12-node decohesion element is shown in Figure 5.6. The element is defined with respect to a local (*x*',*y*',*z*') element coordinate system, and the kinematics are similar to an element presented by Segurado and Llorca [164].

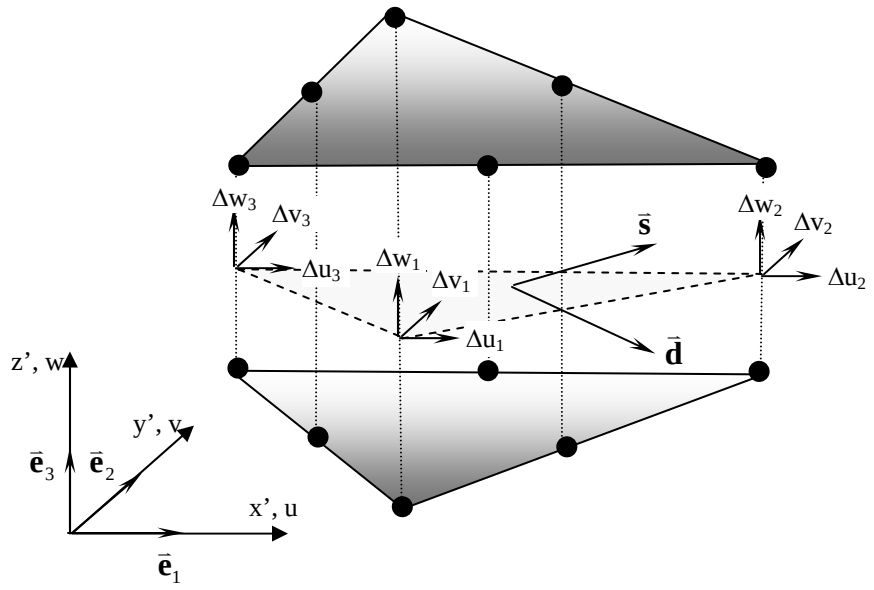

Figure 5.6. Estimated direction of GB opening and sliding in mixed-mode fracture.

The calculation of the direction of crack propagation will differ depending on the magnitude of traction on the GB. For Mode I, the expected opening direction is given by the propagation vector, $\vec{d}$, as

$$\vec{d}_{opening} = A_I \, \vec{e}_1 + B_I \, \vec{e}_2 \tag{5.15}$$

where the A_I and B_I are given in Equations (5.12) with $\phi_i = \Delta w_i$. Because the current development assumes a symmetric tilt GB, the orientation angle θ specifies the relative angle between a slip plane and the cohesive zone plane. The direction of opening in Mode I is given by $\beta = \tan^{-1} B_I / A_I$.

This element can be enhanced to include a full description of grain boundary orientation with respect to available slip planes. For the present analysis, it is assumed that the crack plane is offset from the nearest slip plane by a single tilt angle θ as shown in Figure 5.3. Thus, defining the local coordinate system to be in line with the GB, the

direction of opening is simply given by the sign of the A_I component of the propagation vector $\vec{d}$ or Sign(A_I).

The component directions of Mode II and Mode III failure are given by Equations (5.9) with $\phi_i = \Delta u_i$ and $\phi_i = \Delta v_i$, respectively. The propagation vectors for these two modes are given by

$$\begin{aligned} \vec{s}_{\Delta u} &= A_{II}\,\vec{e}_1 + B_{II}\,\vec{e}_2 \\ \vec{s}_{\Delta v} &= A_{III}\,\vec{e}_1 + B_{III}\,\vec{e}_2 \end{aligned} \tag{5.17}$$

The direction of the in-plane propagation vectors may then be used to quantitatively determine the degree of mode mixity for sliding or fracture tangential to the crack plane. However, quantitative rules and definitions for differentiating between Mode II and Mode III sliding or fracture at atomistic length scales have yet to be developed.

5.3 Concluding remarks in Chapter 5

The directional decohesion element developed herein adds an additional feature to decohesion element formulations applied to microstructural applications at the grain scale by automatically determining the direction of opening in the various fracture/sliding modes and selecting the appropriate CZMs that govern mixed failure modes. The prediction of intergranular fracture in arbitrary GB orientations will require additional rotation angles to be input to define the GB, and more involved calculation of the relative orientation of the cohesive plane and surrounding slip systems will need to be performed. Some additional derivations might be required to modify the opening criterion for the case when the crack plane does not lie along an atomic plane and intersects a slip plane in a skewed orientation.

For the present use, the assumption of a symmetric tilt GB only requires the input of a single angle to specify grain orientation on either side of the GB. This angle can then be

used in the Rice [64] and Tadmor-Hai [65] criteria (discussed in Section 2.3.4.2) to predict brittle or ductile crack propagation in Mode I fracture. In the present development, only Rice's criterion has been considered. In addition to automating the selection of appropriate CZMs for Mode I fracture, arbitrary functional forms for the CZMs describing the constitutive behavior for Mode I or Mode II/Mode III sliding or fracture can be used in the presented interpolation procedure to obtain an effective mixed-mode atomistically-based CZM. In addition, other treatments in the application of CZMs for coupled or uncoupled mixed-mode loading can be directly incorporated into the element formulation.

Chapter 6

Illustration of the Developed Multiscale Methodology

6.1 Introduction

The multiscale methodology developed in the current research involves both the novel concurrent multiscale Embedded Statistical Coupling Method (ESCM) detailed in Chapter 3 and a new sequential multiscale method based on cohesive zone volume elements (CZVEs) for extracting constitutive relationships in the form of CZMs as discussed in Chapter 4. This methodology permits tractable solutions to be obtained for MD simulations over material domains that would preclude fully atomistic simulation due to the resulting size of the atomic system. A first application of the developed methods for extracting MD-based CZM parameters and the formulation of directional decohesion elements presented in Chapter 5 has been to enhance the initial ESCM approach. This enhancement involves incorporating decohesion finite elements in the continuum FEM domain of the ESCM model to simulate fracture across both computational domains. A second application involves using the atomistic-based CZMs in sequential multiscale analysis to simulate material failure at the higher dimensional scales of microscopic polycrystalline material domains. Because the complete characterization of failure mechanisms at the atomic scale in the current bottom-up approach will require significant additional study of intergranular and intragranular failure using CZM representations, only selected illustrative demonstrations of the developed sequential multiscale methodology will be presented in the current chapter.

6.2 Enhancement to the ESCM concurrent multiscale approach

The procedure for extracting atomistically-based CZM parameters and the development of decohesion finite elements has led to an enhancement of the ESCM model. This new development involves the inclusion of decohesion elements and an

iterative nonlinear solution procedure in the continuum FEM domain that permit a nearly seamless propagation of fracture from the continuum domain into the MD region.

6.2.1 Crack Propagation through a Continuum-Atomistic Interface

A continuum-atomistic model for crack propagation along the Σ99 GB shown in Figure 6.1 and analyzed using the enhanced ESCM analysis is presented. The crack grows as an edge crack in the continuum environment subject to mode I loading conditions and penetrates into the atomistic environment (Figure 6.2). The continuity of the crack propagation process through the MD-FEM interface is achieved by using the CZM relation derived for interface debonding based on a pure MD simulation presented in Chapter 2. Note that the edge crack in Figure 6.2 is shown rotated to indicate that the simulation can be used for interfaces of arbitrary orientation.

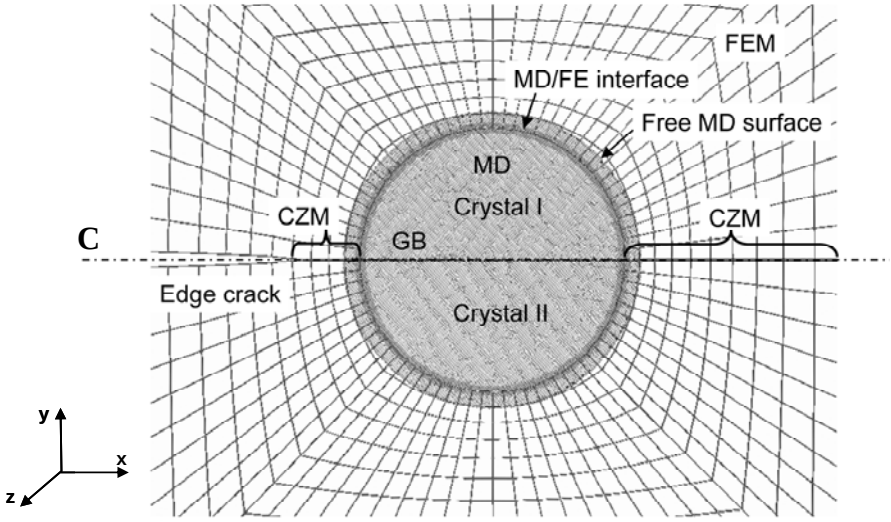

Figure 6.1**.** Configuration of the simulation model for edge-crack propagation along a grain boundary in aluminum.

The dimensions of the coupled MD-FEM model used for this simulation are d_{FE} = 900 nm in the *x*- and *y*- directions, with a circular MD domain in the *x*-*y* plane of diameter, d_{MD} = 45 nm. The system thickness in the *z*-direction is h = 2.9 nm with periodic boundary conditions to emulate a bulk atomic state in this direction. The

simulation was performed at a temperature T = 300 K and maintained by a Nose-Hoover thermostat (Nose [76]) applied locally across the MD region to better regulate 'hot spots' that can develop in highly distorted regions such as around crack tips.

An edge crack was inserted along the line of symmetry, *c*, in the FEM mesh which ended with four finite elements on the left side before reaching the MD-FEM interface (Figure 6.1). These four remaining finite elements were connected through decohesion elements placed along the crack direction (line ***c*** in Figure 6.1), which meet the atomistic GB at the MD-FEM interface. On the right side of the MD domain, the debonding interface is continued through another line of CZM elements, which extends to the opposite outer boundary of the FEM domain.

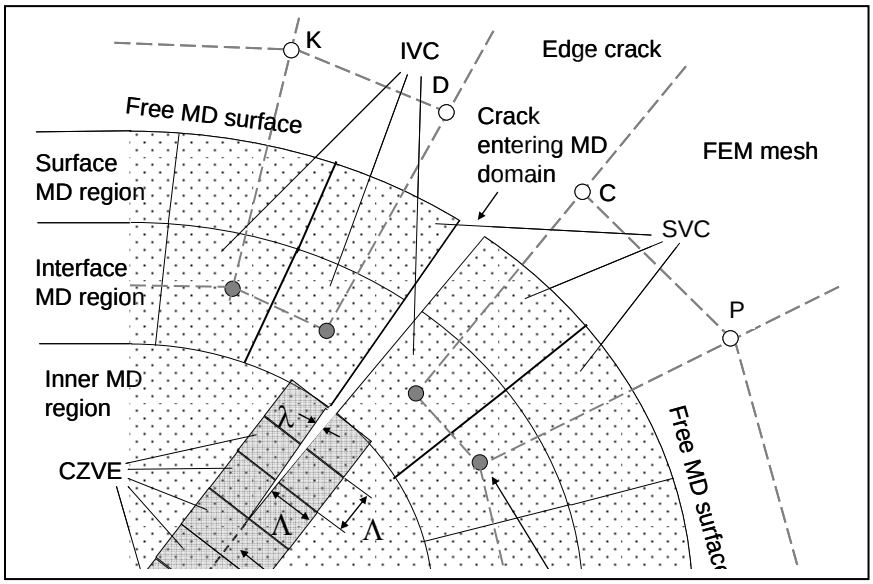

Figure 6.2**.** CZVE elements along the crack path inside the inner MD region within the ESCM.

The system was subject to uniaxial strain, ε_{yy}, applied as displacement boundary conditions at the outer boundary of the FEM domain. The strain was gradually increased from 0.4% to 2% in steps of 0.4% every 20 MD-FEM iterations (20 ps MD simulation time), allowing the MD system to more smoothly follow the stress increase in the surrounding FEM domain.

The process of crack propagation using the enhanced ESCM is depicted in Figure 6.3 through a set of snapshots, magnified to show the physical configuration of the MD domain in the center of the MD-FEM coupled model. The GB interface in the MD domain is visualized as a line of blue and red atoms, indicating atoms in a disordered or hcp surrounding, respectively, reflecting the non-crystalline structure of the GB interface. In Figures 6.3(a) and 6.3(b), the crack propagates through the FEM mesh, sequentially opening the decohesion elements placed on its path. In Figure 6.3(c), the crack tip enters the MD region. The snapshot has captured the instant when the debonding of the Surface and the Interface MD Regions of ESCM is accomplished in unison with the opening of the last decohesion element. The crack tip is about to enter the inner MD region and to continue its propagation in a fully atomistic way. In Figure 6.3(d), decohesion of the GB in the inner MD region has begun. Shortly afterward, in Figure 6.3(e), plastic processes start to develop in terms of nucleation of a pair of dislocations, seen as two short blue lines, marking the extended dislocation cores on both sides of the crack tip. Figure 6.3(f) presents the crack propagated well inside the MD domain. Active dislocation nucleation has already developed and accompanies the crack's propagation. An important result of this process, shown in Figures 6.3(a-f), is the preservation of the structural continuity between the atomistic and the continuum domains at the MD-FE interface through the entire process of crack propagation from the FEM domain to the MD region.

The stress continuity along the MD-FE interface is also well preserved during the entire process. Figure 6.4(a-f) shows the stress state corresponding to the configurational snapshots presented in Figure 6.3. The largest discrepancy between the stress of the MD system and the FEM mesh is seen in Figures 6.4(b) and 6.4(c) where the dynamics of the MD domain did not converge completely before the next stepwise increase of the strain in the static FEM domain was applied. The continuity is improved later in the simulation, in Figures 6.4(d-e), when the crack propagates further within the MD region.

The problem of coupling the dynamic response of the MD domain to the static response of the FEM system is discussed in detail in Saether et al. [87]. While the dynamic coupling in the ESCM approach cannot be fully achieved without the use of a

dynamic FEM simulation, the iterative scheme of coupling, in which the FEM state is continuously updated in accordance with the reported MD displacements, appears to be sufficient to reproduce the evolution of systems with relatively slow dynamics.

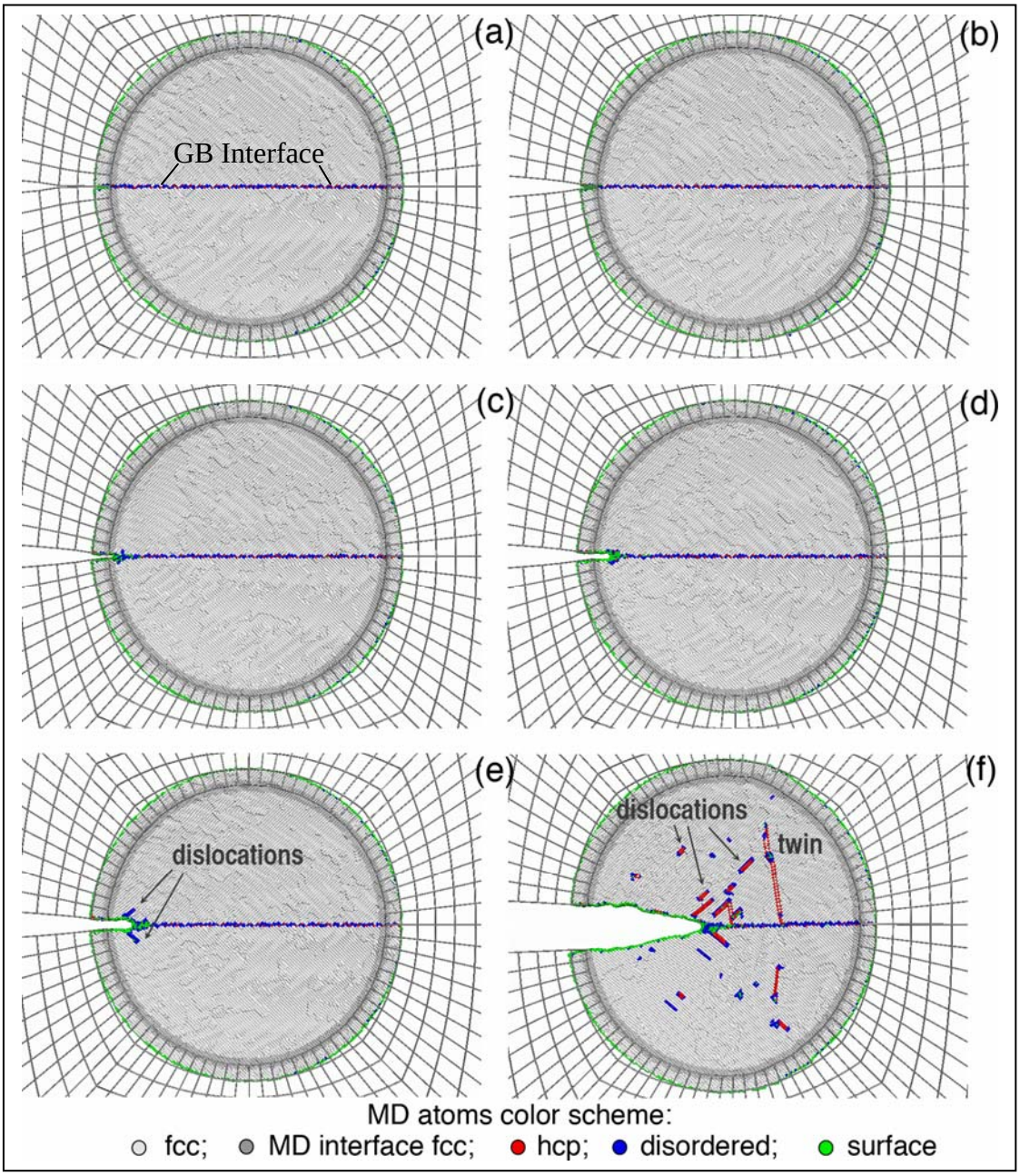

Figure 6.3**.** Snapshots of the ESCM model configurations simulating an edge crack propagating along a GB in a bicrystal of aluminum with CZM elements along the GB interface.

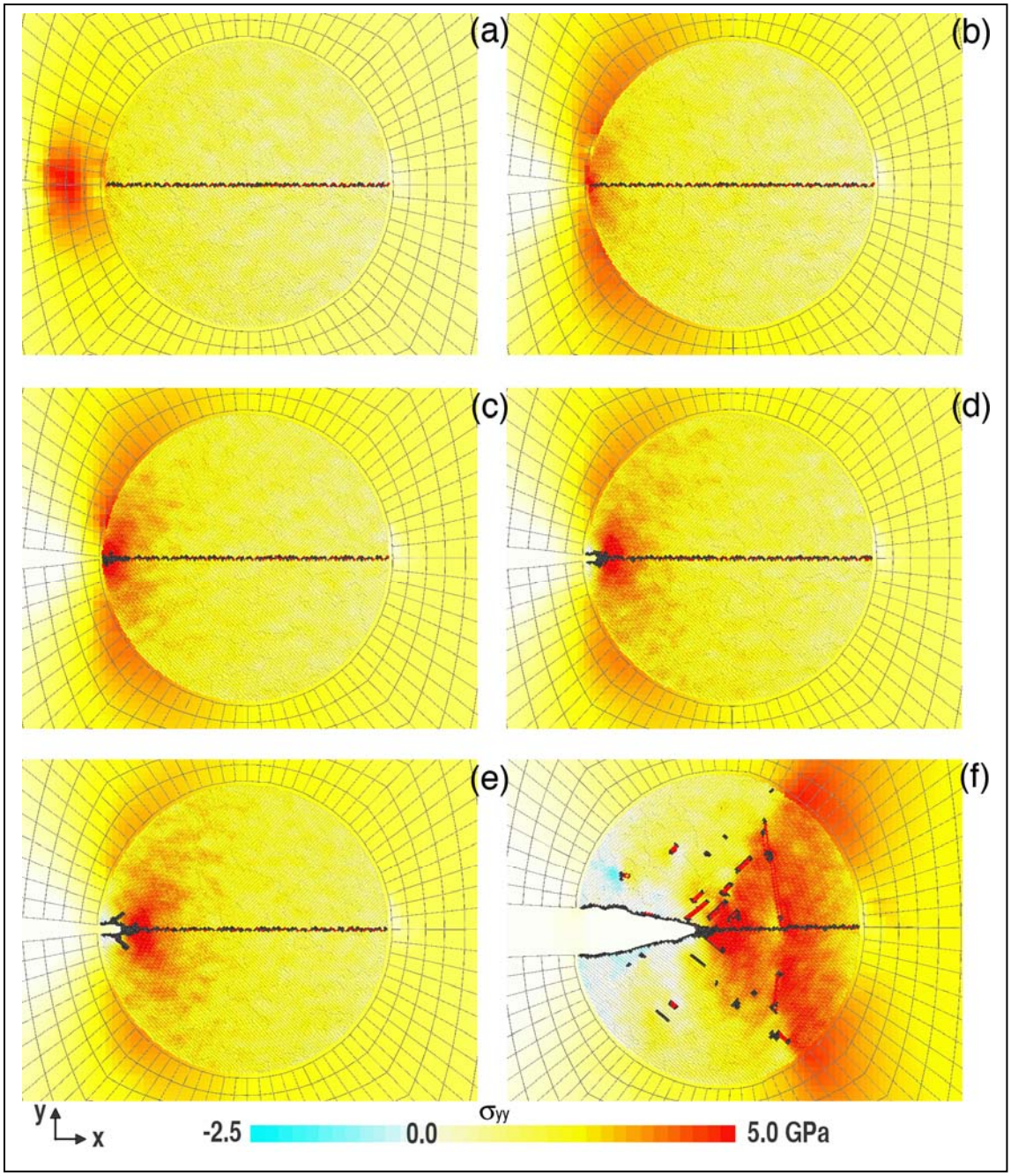

Figure 6.4. Stress map of σ_{yy} corresponding to the snapshots given in Figure 6.3.

6.3 Sequential multiscale simulation of intergranular failure in aluminum microstructures

In order to illustrate the developed multiscale methodology, the MD-based CZMs developed for a common GB are parametrically scaled to qualitatively demonstrate the

effect of different grain boundary properties on the resulting response of a bicrystal and polycrystalline metallic microstructures. The GB selected is a symmetric tilt Σ99 grain boundary with high energy (energy above the perfect crystal) and lower strength (compared to other GBs). Σ99 is representative of a common class of GBs and, because of it's lower strength, is more likely to participate in material failure involving intergranular fracture. The scaled values of CZM parameters are assumed to represent the presence of vacancies, interstitials, dislocations, and other defects in addition to differing elastic/plastic properties of other GB orientations compared to the baseline Σ99 configuration considered in the current MD simulations. The augmented CZMs are incorporated into 1-D and 2-D decohesion finite elements discussed in Chapter 5 to qualitatively analyze GB failure in aluminum.

6.3.1 Analysis of Mode I fracture in a 2-D bicrystal

A model containing an edge crack under tension is used to interrogate Mode I fracture along a GB in an aluminum bicrystal. The traction-displacement relationship is assumed to be bilinear such that the parametrically varied CZMs can assume the forms presented in Figure 6.5. The variations in the CZMs represent process zones that range from perfectly brittle to perfectly ductile. An intermediate model expressed as a general

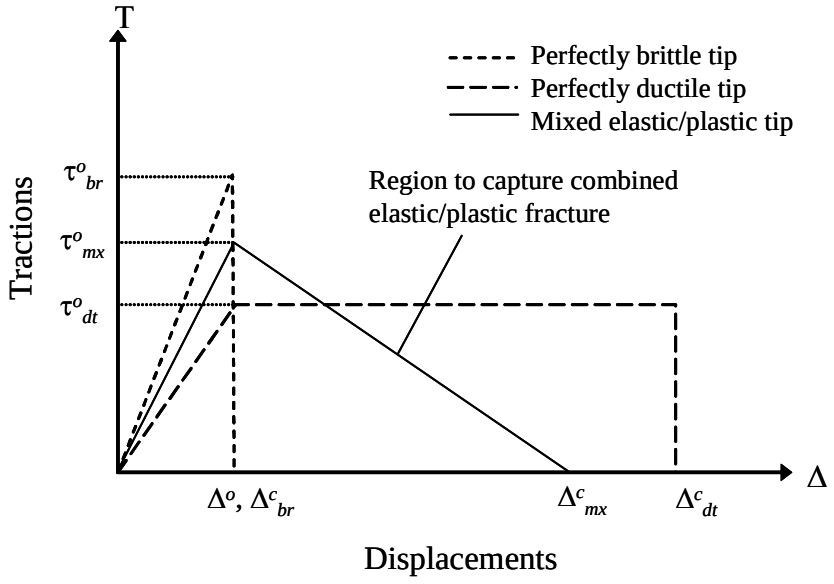

Figure 6.5. Possible bilinear traction-displacement relationships.

bilinear traction-displacement relationship is also shown in Figure 6.5 and represents the common situation in which a mixture of elastic and inelastic deformation mechanisms are present and characterize the propagation of fracture. Mixed traction-displacement relationships were determined in Chapter 5 and the designation “brittle” and “ductile” could be described perhaps more precisely as ‘more brittle’ and ‘more ductile’, respectively (see Figure 5.3). The parameters τ^o_{dt}, τ^o_{mx}, τ^o_{br} represent the peak tractions of the perfectly brittle, intermediate, and perfectly ductile CZM models, respectively. Similarly, Δ^c_{dt}, Δ^c_{mx}, and Δ^c_{br} represent the maximum displacements of the perfectly brittle, intermediate, and perfectly ductile CZM models, respectively.

To guide the parameterization of CZM parameters, the consideration of GB energy components from Section 4.5 is revisited. The area of the bilinear function represents the energy of decohesion per unit length, or the fracture toughness of the interface G. In the case of intergranular fracture, the energy of decohesion is given by a restatement of Equation (4.32) in terms of energy fluxes as

$$G = 2\gamma_s + \gamma_{pl} - \gamma_{GB} + \Delta q \tag{6.1}$$

where γ_s is the rate of free energy generated by the newly created surface, γ_{GB} is the energy change of the GB, Δq is the rate of unit heat production (which will be neglected in further developments), and γ_{pl} is the rate of plastic energy dissipated through various inelastic processes along the fracture zone, introduced for ductile materials by Orowan [173] and Irwin [174].

The area defined by the CZM can be expressed through the parameters τ^o and Δ^c in Figure 6.5 as

$$G = \frac{1}{2}\tau^o_{mx}\Delta^c_{mx} \tag{6.2}$$

In the case of perfectly brittle decohesion ($\Delta^c_{mx} = \Delta^o$ and $\gamma_{pl} = 0$)

$$\frac{1}{2}\tau^o \Delta^o = 2\gamma_s - \gamma_{GB} \tag{6.3}$$

which also applies for the initial linear-elastic part of the bilinear CZM law ($\Delta^c < \Delta^o$) assuming linear elastic response of the interface up to the point of debonding. In this region, the rate of increase of the traction τ with Δ is given by the stiffness C_{GB} of the GB interface, defined as

$$\tau^o = C_{GB}\Delta^o \tag{6.4}$$

C_{GB} can be estimated from the initial slope of the extracted MD traction-displacement law, as given in Figure 6.5. A number of recent MD simulations on nanocrystalline metals show that the GB stiffness is on average about 30% lower than the crystal stiffness, which can be used as a reasonable approximation for C_{GB} when no data is available [78].

Combining Equations (6.1) and (6.2) with Equations (6.3) and (6.4) gives the following expressions for the parameters in the bilinear CZM model

$$\begin{aligned} \tau^o &= \sqrt{2C_{GB}\left(2\gamma_s - \gamma_{GB}\right)} \\ \Delta^o &= \sqrt{\frac{2\left(2\gamma_s - \gamma_{GB}\right)}{C_{GB}}} \\ \Delta^c_{mx} &= \frac{2\left(2\gamma_s - \gamma_{GB} + \gamma_{pl}\right)}{\sqrt{2C_{GB}\left(2\gamma_s - \gamma_{GB}\right)}} \end{aligned} \tag{6.5}$$

The estimation of the energy parameters γ_s and γ_{GB} have been discussed in Section 5.2 and, for aluminum with a Σ99 symmetric tilt GB, the surface energy of the GB may be taken as γ_s = 0.952 ± 0.010 J/m^2, and the excess GB energy is given by γ_{GB} = 0.60 ± 0.05 J/m^2. The plastic energy γ_{pl} depends strongly on the GB structure and the direction

of crack propagation. An energy analysis using MD performed by Yamakov, Saether, Phillips, and Glaessgen [67] showed the contribution of different plastic processes, such as dislocation nucleation and twin or stacking-fault formation, to γ_{pl} and their dependence on the speed of crack propagation. Further simulations on a selected set of GBs can give estimates for γ_{pl} based on how many slip planes on both sides of the GB were activated (see Yamakov, Saether, Phillips, and Glaessgen [131]). An adaptive CZM using Rice type of criteria can be applied to a general GB to decide how many slip systems are possible to become active during decohesion and to choose the appropriate γ_{pl} for each case. For the present illustration, various degrees of plasticity are assumed in the scaled CZM parameters.

For macroscale applications in which the cohesive zone is considered as having zero thickness, the GB stiffness is assumed numerically infinite and is applied as a penalty constraint. For simulations at lower dimensional scales, the GB thickness increasingly contributes to the compliance of the physical model such that, at the nanoscale, a finite stiffness of the GB must be utilized to represent the local elasticity of the GB. At this scale, the GB elastic modulus cannot be neglected and is important to understanding the elastic behavior of nanocrystalline materials [171].

Figure 6.6 shows the configuration considered in the finite element analysis implementation of the parametrically varied cohesive zone models. Two hundred (200) decohesion elements were used to represent the GB. The size of the configuration is chosen to be $l_x = l_y = 380$ nm, so that the characteristic length of the decohesion element placed along the crack path is $l_x/200 = 1.9$ nm is equal to the size of the CZVE used in the MD simulations [131]. Six-node quadratic triangular finite elements are used to represent the elastic continuum having the elastic properties of aluminum (E=72 GPa, ν=0.34). The simple bicrystal configuration shown in Figure 6.6 has a single interface between the two crystals and an initial crack of length $a_o = 7.6$ nm. The model is loaded with a linearly increasing tensile displacement in the y-direction that increases from $U_y = 0$ at $l_x = 0$ to $U_y = 6\%$ strain at $l_x = 380$ nm.

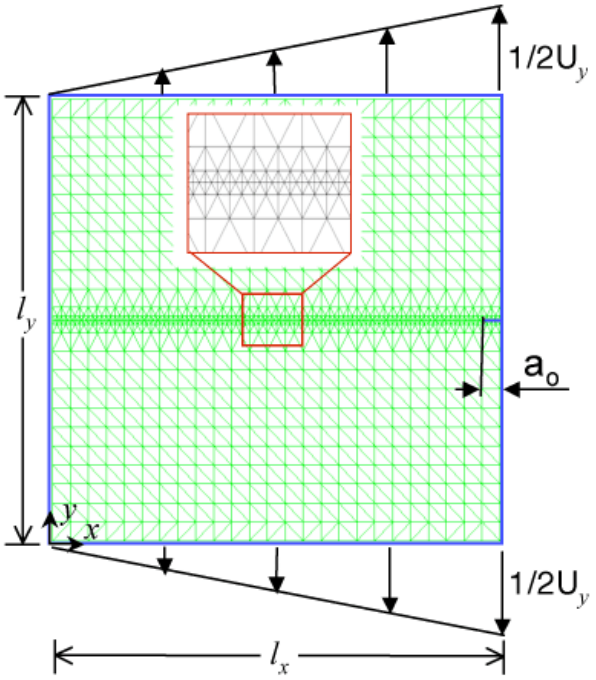

Figure 6.6. Edge cracked tension models for Mode I opening.

In a CZM, the length of the process zone corresponds to the softening region in which the relative displacements extend from Δ^o to Δ^c (see Figure 6.1). In Figure 6.7, a_1 indicates the beginning of material softening representing the beginning of the development of the process zone ahead of the crack tip, while a_2 indicates the crack tip at which the process zone has evolved into a free surface.

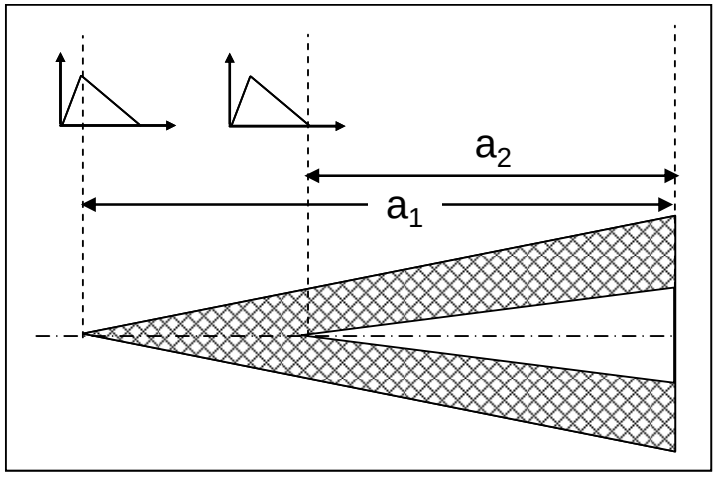

Figure 6.7. Assumed process zone in CZM representation.

Parametric studies were performed to assess the effect of the relative amount of elastic and plastic deformation at the crack tip on the fracture characteristics of the configuration shown in Figure 6.6. This was achieved by varying the shape of the CZMs using the MD extracted cohesive zone curves shown in Figure 4.5 as a baseline. Two sets of parameterized CZMs were generated as shown in Figure 6.8. Baseline values of the CZM

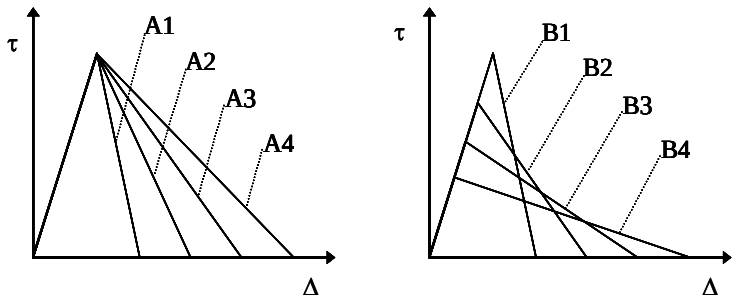

(a) Series A: equal peak traction (b) Series B: equal toughness

Figure 6.8. Cohesive zone models used in two series of parametric studies.

parameters were obtained from the MD-calculated CZMs shown in Figure 5.3. In the first set (Figure 6.8a), the effect of the relative amount of elastic and plastic deformation was varied, resulting in different values of the energy of crack face separation or toughness, G, while keeping τ_{mx} constant. In the second set (Figure 6.8b), the ratio of elastic to plastic deformation was varied by changing the maximum opening displacement, Δ_{mx}, for CZMs having the same toughness. Keeping G constant results in a varied maximum peak traction τ_{mx}. By considering these two cases, the effect of the shape and the area of the CZM curve on the fracture properties of the interface can be demonstrated. In Figure 6.8, CZMs A1 and B1 correspond to the MD-generated results shown in Figure 4.5. The parameters used to define the models shown in Figure 6.4a and Figure 6.8b are shown in Tables 6.1a and 6.1b, respectively.

Table 6.1. CZM parameters used to simulate different relative elastic and plastic behavior at the crack tip in a bicrystal. Fracture toughness is a function of the increase in plasticity.

(a) Peak traction held constant at τ^{o}_{mx} = 5.0 GPa.

CZM	Δ^{c}_{mx} (nm)	G (J/m^2)
A1	2.17	5.42
A2	2.89	7.22
A3	4.33	10.84
A4	6.50	16.25

(b) Fracture toughness held constant at G = 5.42 J/m^2.

CZM	τ^{o}_{mx} (GPa)	Δ^{o} (nm)	Δ^{c}_{mx} (nm)
B1	5.00	1.07	2.17
B2	3.75	0.80	2.89
B3	2.50	0.53	4.33
B4	1.75	0.37	6.19

Figures 6.9 and 6.10 show the results for the bicrystal configuration of Figure 6.6. The length of the crack was determined in two ways (see Figure 6.7). First, all CZM element integration points that exceeded the peak traction τ_{mx} were assessed to give the position a_1 of the front edge of the process zone at the crack tip where 'softening' starts. Second, only those CZMs that exhibited complete loss of stiffness were assessed to determine the position a_2 where the process zone ends and a free surface is formed. In this way, the fracture process zone is determined as the 'softening' region between a_1 and a_2.

Figure 6.9a shows the position a_1 and a_2 of the front and end of the crack process zone as a function of the linearly increasing far-field strain. Here, CZM Series A was considered. In all cases, a_1 is greater than a_2 as it indicates the beginning of the process zone. Note that the size of the process zone, estimated as the distance between the a_1 and a_2 lines for each G, increases with increasing G. In addition, the two sets of lines exhibit

a systematic trend towards shorter crack lengths as the fracture toughness G increases. The shortening of the effective crack length, taken as the mean of the two positions a_1 and a_2 with increasing G, is presented in Figure 6.9b. While keeping the peak traction τ_{mx}, corresponding to the onset of damage, constant, the increase of G leads to the crack opening at larger strains due to the greater energy that must be consumed to propagate the crack.

Figure 6.10a presents the analogous results for CZM Series B. As in Series A, the size of the process zone increases with increasing strain. However, in Series B, the effect is due to the increased size of the CZM plastic region by decreasing τ_{mx} while holding G constant. The effective crack length versus applied strain is shown in Figure 6.10b. Two different regions of crack growth can be seen. First, at the moment of opening, the crack is unstable, and the mean crack length exhibits an instantaneous growth until it reaches a stable equilibrium. The shaded region in Figure 6.10b indicates the zone of unstable growth. Second, after reaching the equilibrium state, the equilibrium crack lengths for all τ_{mx} follow the common equilibrium master curve. This result shows that when G is constant, the equilibrium crack length for a given strain remains the same and does not depend on the peak traction τ_{mx}. Thus, the peak traction in the CZM affects only the initial strain of crack opening.

The results presented in Figure 6.11 demonstrate that the process zone in both CZM Series A and B systematically increases when the CZM parametric curve extends towards larger crack opening displacements, either through increasing of the fracture toughness at constant peak traction, or through decreasing of the peak traction while keeping the fracture toughness constant. Note that the decrease of τ_{mx} has a more pronounced effect on the process zone than increasing G and indicates that lowering the traction barrier for debonding results in a larger increase of the process zone in front of the crack tip compared to the case when G is increased.

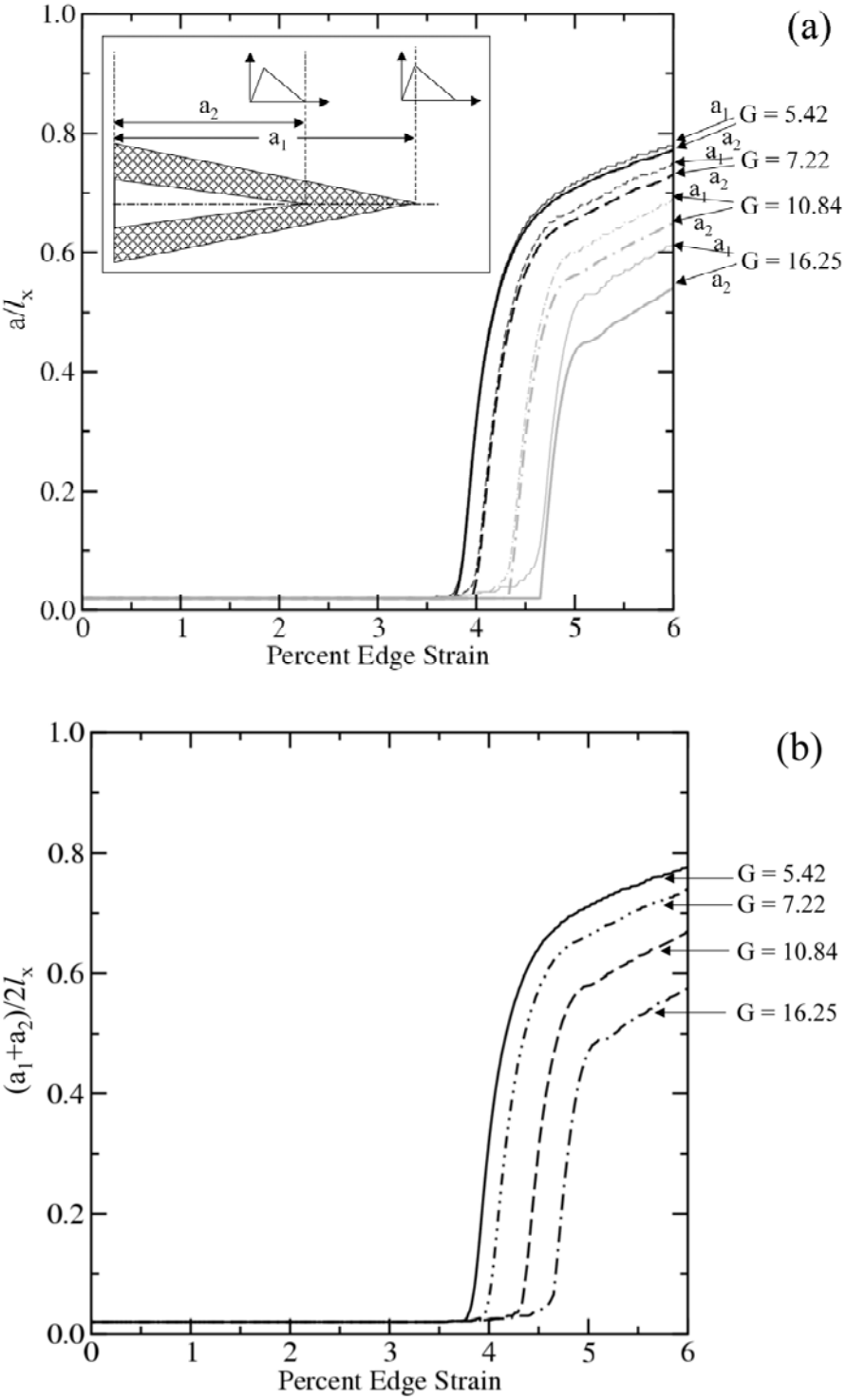

Figure 6.9. Relative crack length vs. percent edge strain for CZM Series A.

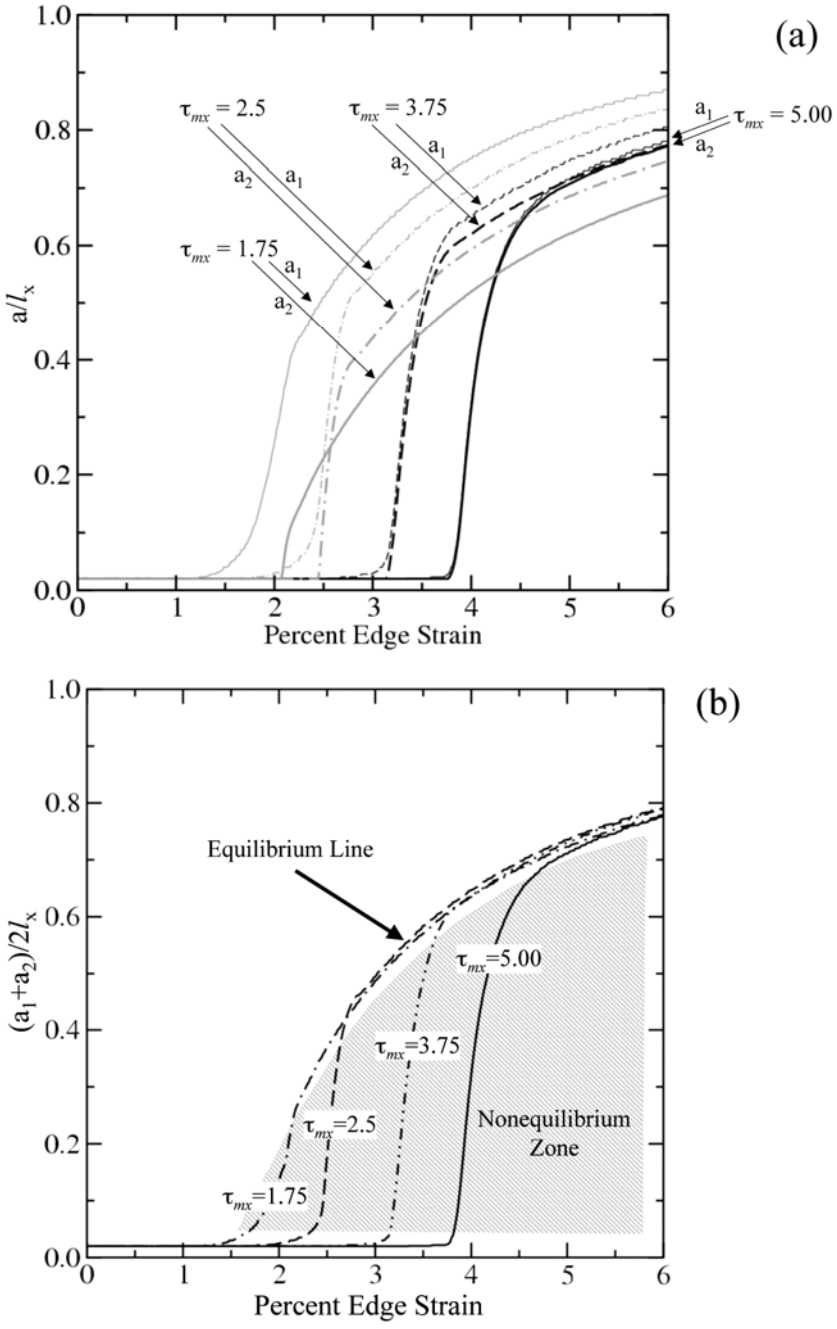

Figure 6.10. Relative crack length vs. percent edge strain for CZM Series B.

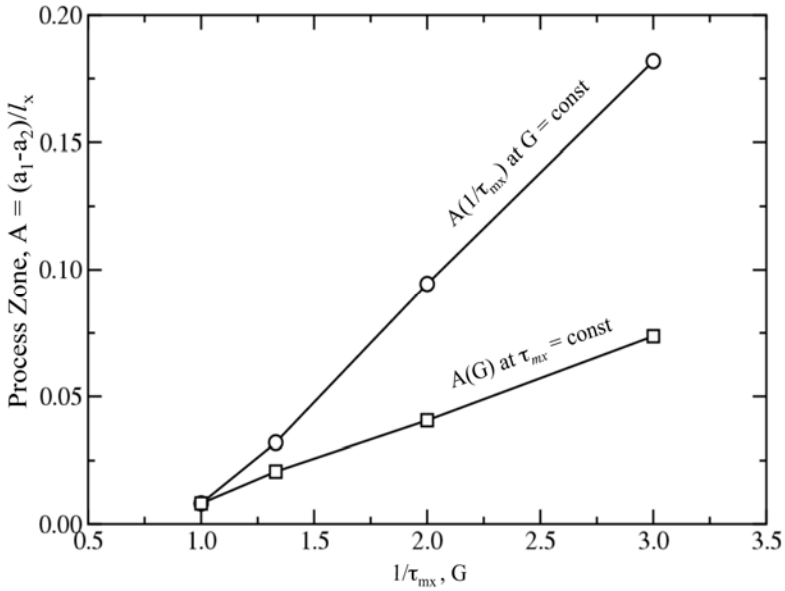

Figure 6.11. Process zone vs. $1/\tau_{mx}$ for Series B and Process zone versus G for Series A.

6.3.2 Analysis of mixed-mode fracture in a 2-D polycrystal

Figure 6.12 shows a more complex 2-D configuration consisting of a tessellated polycrystalline microstructure having many grain boundaries. The model has dimensions of $l_x = l_y = 47.5$ nm, and consists of 50 grains. Parametric studies were performed by

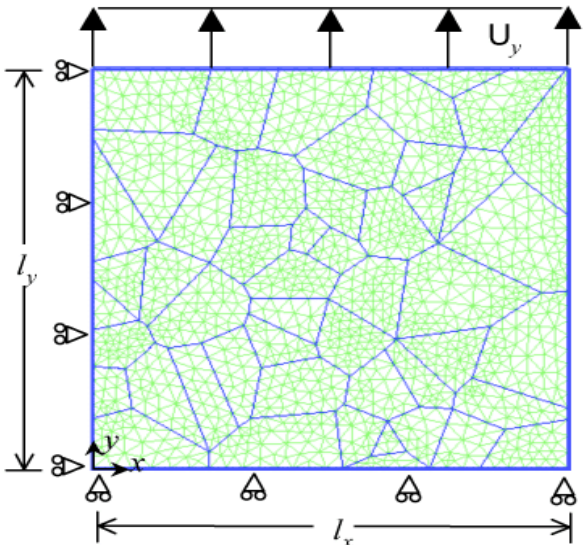

Figure 6.12. Random microstructural model.

linearly combining the CZM parameters using the MD extracted cohesive zone curves describing brittle and ductile Mode I fracture shown in Figure 4.11. CZM properties for shear sliding under Mode II loading were arbitrarily selected to simulate an elastic-perfectly plastic behavior. All parameters are shown in Table 6.2.

Using brittle Mode I CZM properties for all the GBs, Figure 6.13 shows the sequence of decohesion processes under normal applied displacements. The CZM parameters for Mode I opening obtained from MD analysis yielded an initial GB stiffness that is similar to the stiffness of the adjoining grains. Thus, these interfaces are shown to open at low levels of applied strain (Figure 6.13a). The opening of the cohesive zones along the GBs are exaggerated in the figure. At higher applied strains, the energetics of GB opening dictate the location at which a dominant crack begins to form (Figure 6.13b). At a critical applied strain, the local coalescence of GB opening forms a dominant microcrack as shown in Figure 6.13c. It is also seen that due to unloading after the dominant microcrack

Table 6.2. CZM parameters defining brittle Mode I behavior at the 2-D crack tip.

CZM	Brittle Mode I
τ^{o}_{mx} (GPa)	5.00
Δ^{o} (nm)	1.07
Δ^{c}_{mx} (nm)	2.17
G (J/m^2)	6.50

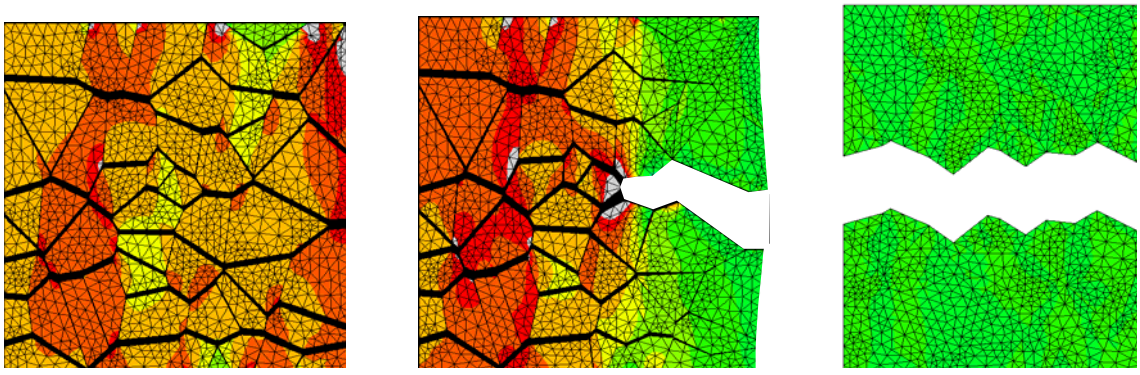

(a) Initial opening of GBs, ε_y = 16%

(b) Local crack formation, ε_y = 17%

(c) Dominant microcrack, ε_y = 22%

Figure 6.13. Process of dominant microcrack formation in a polycrystal model using cohesive zone models.

has fractured the model, the stiffness in other decohesion elements act to pull the opening cohesive zones back to an unloaded state (see Figure 4.2).

To illustrate the qualitative influence of CZM parameters, comparative simulations were performed with properties for Mode I fracture assigned as a parametric series of proportions of the Mode I brittle and ductile CZM parameters presented in Table 1. These parameters, ϕ, were obtained as

$$\phi_{combined} = \alpha\, \phi_{brittle} + (1 - \alpha)\, \phi_{ductile} \tag{6.6}$$

where α ranged from 1.0 to 0.0. The Mode II shear parameters (Table 6.2) were kept constant in each simulation.

Material properties for the grains were assumed linear isotropic with a Young's modulus of 100.0 GPa and Poisson's ratio of 0.34. The varied CZM parameters for Mode I decohesion are presented in Table 6.3.

Table 6.3. CZM parameters used to simulate different proportions of elastic and plastic Mode I opening behavior at the 2-D crack tip.

Mode I CZM parameters.

CZM	α	Δ^c_{mx} (nm)	G (J/m^2)
C1	1.00	2.17	5.43
C2	0.75	3.04	7.20
C3	0.50	3.91	8.75
C4	0.25	4.78	10.1
C5	0.00	5.65	11.2

Figure 6.14 shows the resulting stress-strain response of the polycrystal model using variations in the proportion of brittle and ductile Mode I cohesive zone behavior. The global stress versus strain results confirm the expected trend of decreasing maximum stress with increasing ductility in the CZM law however the yielding portion of the stress-

strain relationship is variable and shows only a slight increase in plasticity. A change in the predicted crack path is exhibited due to the changing load transfer due to the variations in the cohesive properties of the GBs.

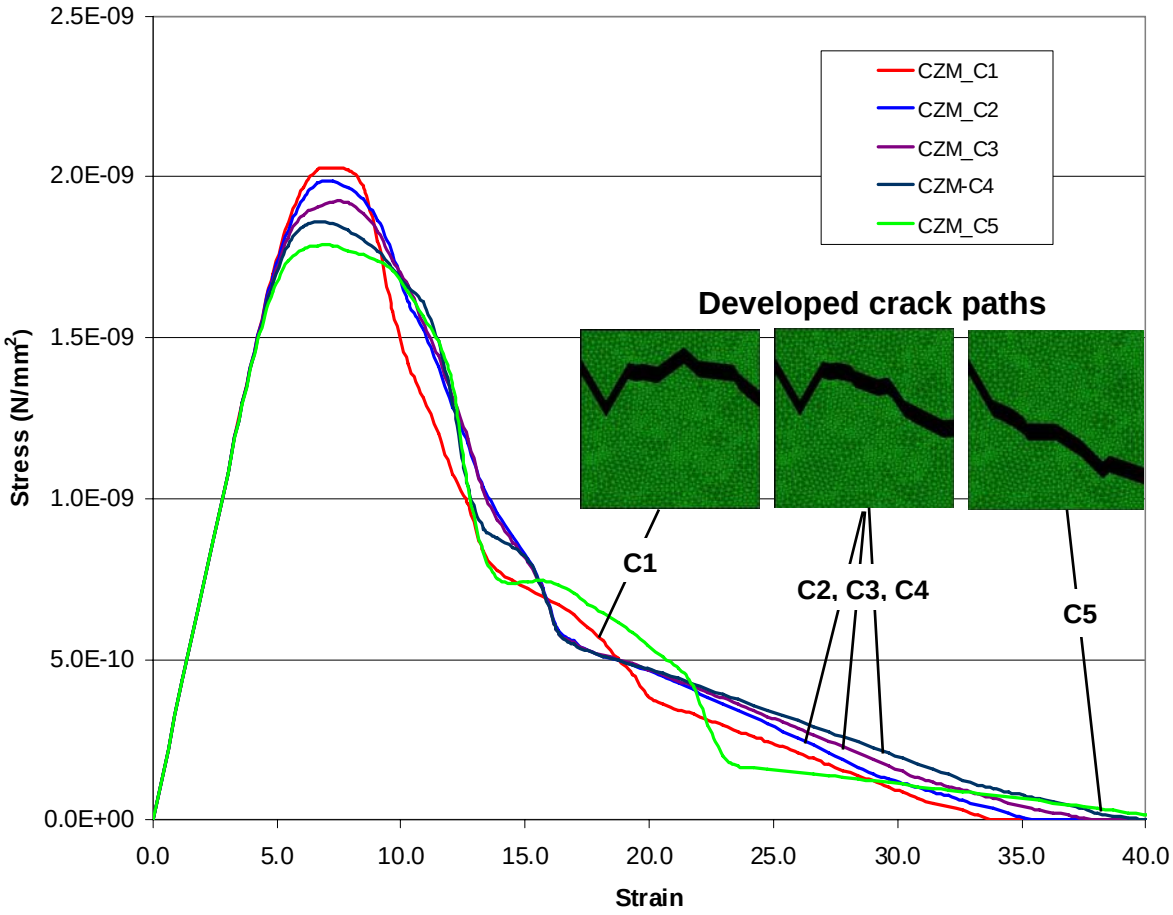

Figure 6.14. Parametric study of Mode I stress/strain response in a polycrystal with brittle vs ductile GBs.

6.3.3 Analysis of general mixed-mode fracture in 3-D polycrystalline models

Two 3-D polycrystal models were used to illustrate the functionality of directional decohesion elements based on grain orientation. The first model focuses on the behavior of the junction between grains. In a 3-D model, grain boundaries typically form triple lines and quadripole junctions, however, to best illustrate the directional behavior of

fracture propagation, the model is limited to 3-grains forming a triple junction. Modeling the cohesive surfaces placed along each GB using the 12-node directional decohesion element discussed in Section 5.2 will, in general, require five GB orientation parameters to be input to each element. However, for the current demonstration, each GB is assumed as a symmetric tilt GB that can be characterized by a single misorientation angle This symmetric tilt angle θ_i is specified for the i^{th} GB as shown in Figure 6.15. Future developments will involve a more detailed description of GB orientation. During simulation with the current assumptions, the local direction of opening must be computed to determine the angle θ between the opening direction and nearest slip plane in order to apply Rice's criterion.

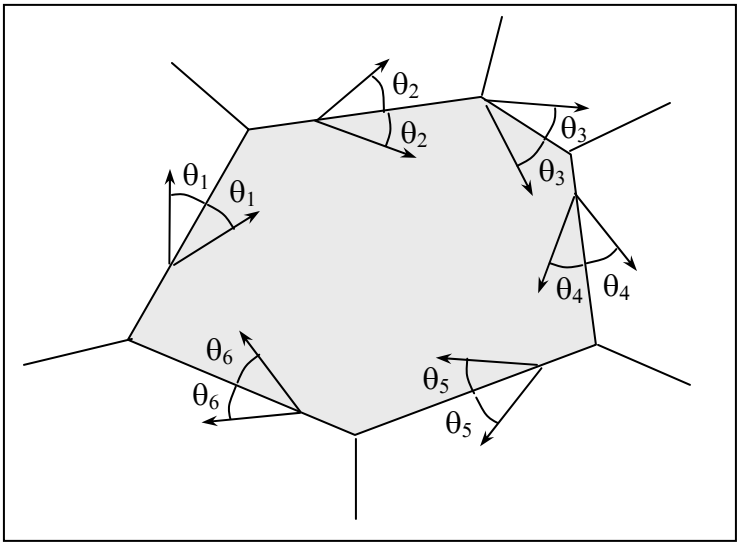

Figure 6.15. Assumed symmetric tilt angles for GBs.

The grains were assumed isotropic (E = 100 GPa, $\nu = 0.3$) and Table 6.4 presents the CZM parameters used in this simulation. The local direction of Mode I propagation is computed to determine the angle θ between the Mode I opening direction and the nearest slip plane in order to apply Rice's criterion. The directional decohesion element detailed in Section 5.2 was coded into a user-defined element for use in ABAQUS. This routine implemented Rice's criterion which was automatically applied during element processing to determine whether the brittle or ductile Mode I CZM parameters were to be applied.

Grain boundary parameters are presented in Table 6.4. The model geometry, loading, and results of changing the tilt angle for each GB is shown in Figure 6.16.

Table 6.4. CZM parameters defining GB properties in the triple junction model.

CZM	Brittle Mode I	Ductile Mode I	Shear
τ^{o}_{mx} (GPa)	5.00	8.00	0.80
Δ^{o} (nm)	1.07	1.71	0.40
Δ^{c}_{mx} (nm)	2.17	8.00	1.00

The principal result of the simulation presented in Figure 6.16 is the demonstration that the local crack path is a function of the direction of Mode I fracture propagation and the GB tilt angle. These effects are shown to be represented through the use of the formulated directional decohesion finite element.

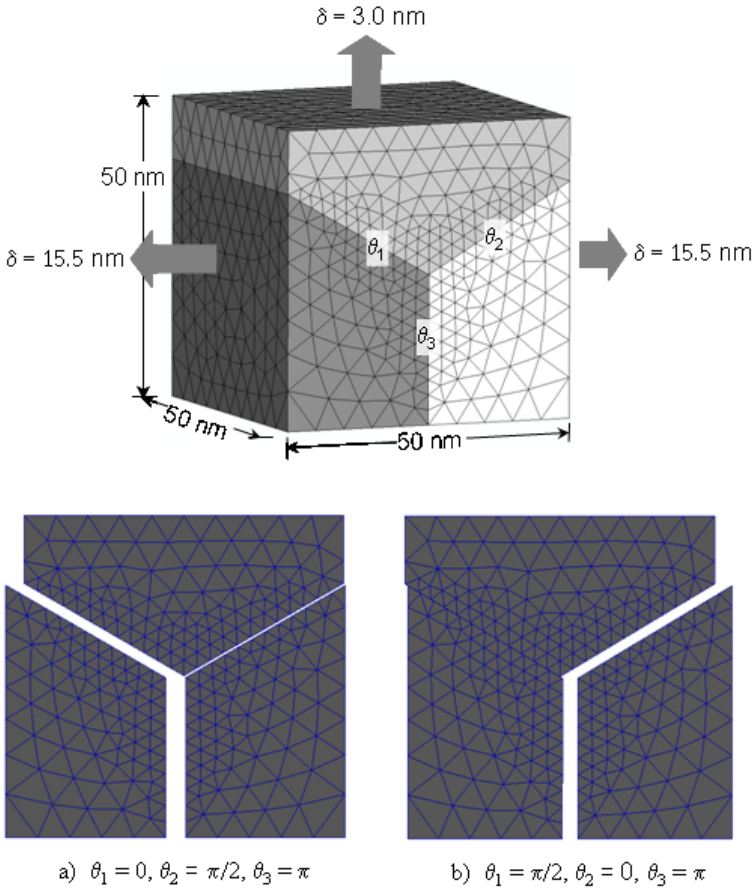

Figure 6.16. Simulation of a triple junction showing different opening behavior with different assumed GB tilt angles using directional decohesion elements.

The second model is a 3-D polycrystal model used to illustrate the effect of randomly changing CZM parameters along GBs on the global stress-strain response and fracture surface creation. This model was constructed by extruding in the 2-D model used in Section 6.3.2 in the thickness direction and is depicted in Figure 6.17. The same loading and support conditions shown in Figure 6.12 were used.

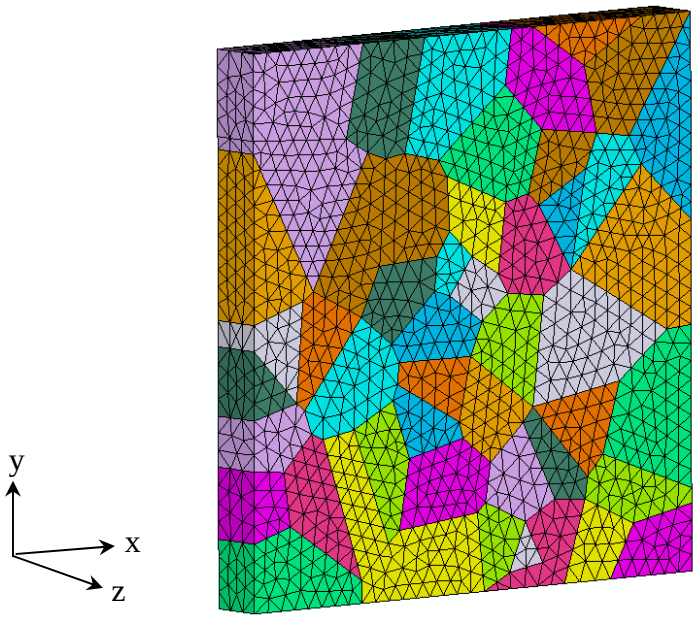

Figure 6.17. Model of a 3-D 50-grain microstructure.

The tilt orientation of each GB was assigned randomly with the misorientation angle ranging from $\theta = (-\pi, +\pi)$. It should be noted that this assignment is nonphysical; the tilt angles should follow from an initial assignment of grain orientations. However, because properties of arbitrarily oriented tilt GBs are not available, the selection of random angles for each GB serve equally well to illustrate the methodology and the effect of propagation direction along each GB. For convenience, Mode II sliding and Mode III sliding were assumed to be described by the same CZM parameters. The 3-D 25-grain microstructure model, shown in Figure 6.17, has side dimensions of 47.5 nm and a thickness of 4.75 nm.

The grain properties were modeled as linear isotropic with a modulus of 100 GPa and a Poisson's ratio of 0.34. The Mode I CZM parameters used t^o_{mx} = 5 GPa for brittle fracture and t^o_{mx} = 4 GPa for ductile fracture for the current simulation as determined by the MD-based analysis presented in Section 4.3.1. Both CZMs used an initial stiffness of 4.69GPa. Following the previous examples, parametrically varied CZM parameters to simulate other GB configurations with differing relative degrees of elastic and plastic processes are presented in Table 6.5.

Table 6.5. CZM parameters used to simulate different proportions of elastic and plastic Mode I opening behavior at the 3-D crack tip.

Brittle Mode I CZM. Peak traction held constant at τ^o_{mx} = 5.0 GPa.

CZM	Δ^c_{mx} (nm)	G (J/m^2)
D1	2.17	5.42
D2	2.89	7.22
D3	4.33	10.84
D4	6.50	16.25

Ductile Mode I CZM. Peak traction held constant at τ^o_{mx} = 4.0 GPa.

CZM	Δ^c_{mx} (nm)	G (J/m^2)
D1	3.75	7.50
D2	5.00	10.0
D3	6.25	12.5
D4	10.0	20.0

For Mode II and Mode III deformation fields, the maximum traction was selected as $\tau_{mx} = 0.8\,\text{GPa}$ based on GB sliding simulations presented in Section 4.3.2. The maximum displacement jump was set as Δ^c_{mx} = 2 nm to represent the interatomic force interaction between atoms associated with the upper and lower cohesive surfaces under pure sliding over an average side length of the grains in the model.

Figure 6.18 shows the evolution of a dominant crack in the 3-D polycrystal model. For each set of CZM parameters listed in Table 6.4, the random assignment of GB tilt angles and the relative similarity of different Mode I CZM relations for the same Σ99 GB, each model exhibited some difference in the fracture state at intermediate loading stages but all resulted in the same dominant crack path configuration as shown in Figure 6.18.

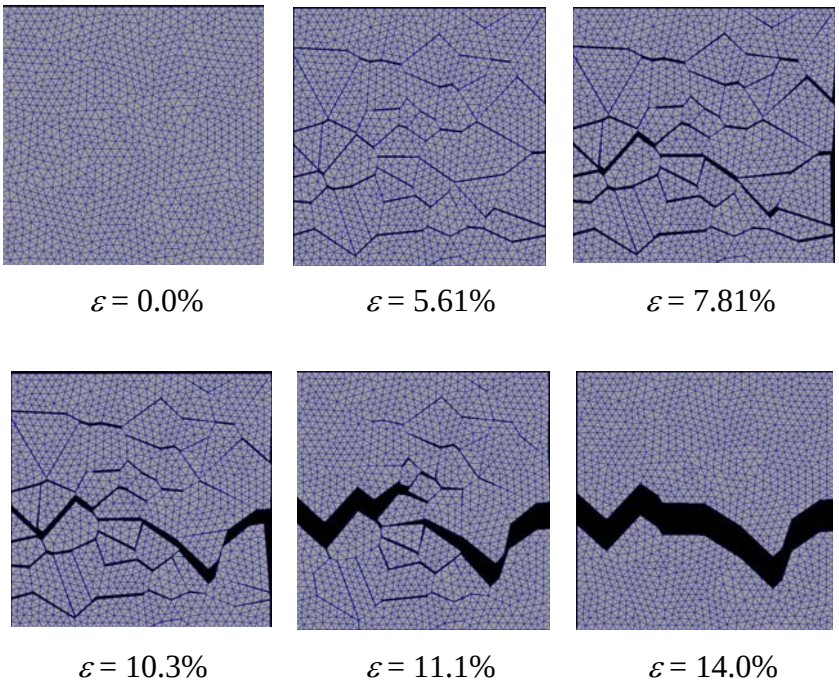

Figure 6.18. Failure sequence in the 3-D polycrystal model.

The stress-strain response is shown in Figure 6.19. The results show identical behavior up to the maximum stress of 1.8E-11 (N/nm^2) that corresponds to the maximum tractions that were held constant in all models. The variation in the maximum ultimate displacement for each model shows the expected increase in the degree of plasticity in the softening portion of the global stress-strain curves.

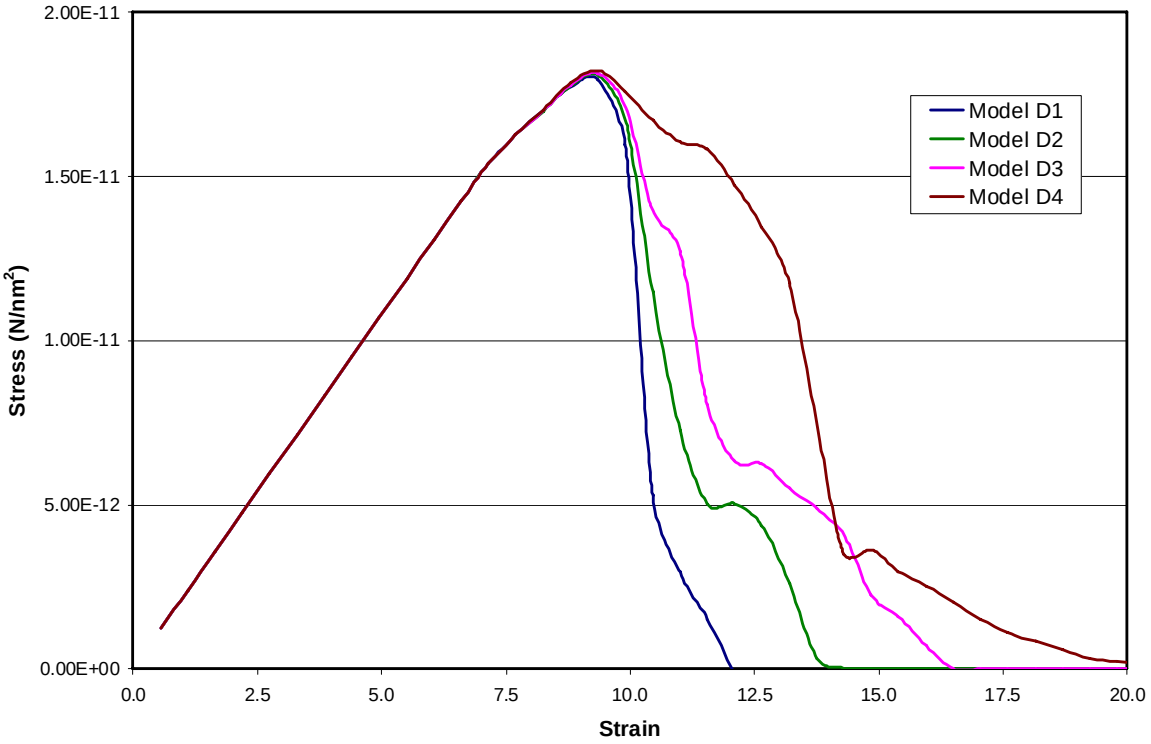

Figure 6.19. Stress-strain curves for the 3-D polycrystal model.

6.4 Concluding remarks for Chapter 6

For concurrent multiscale methods, an enhancement to ESCM was presented by showing the unique simulation of a crack propagating from a continuum domain into an atomistic region. This was accomplished by including nonlinear decohesion finite elements and solution procedures in the FEM component of the coupled MD-FEM approach. For illustrating sequential multiscale analysis using the developed methods, a 2-D bicrystal and 2-D and 3-D polycrystal models were analyzed using a parametric variation of the basic MD-derived CZM parameters determined for a high angle, high energy Σ99 symmetric tilt GB. These simulations illustrate the sensitivity of results based on the intrinsic separation energy of intergranular fracture. The parametric studies using the bicrystal model demonstrate that the process zone in both CZM Series A and B systematically increases with larger maximum crack opening displacements. This is due to either increasing the fracture toughness at constant peak traction or decreasing the peak

traction while keeping the fracture toughness constant. For a 2-D 50-grain polycrystalline model, the stress versus strain results confirm the expected trend of increasing softening due to increasing ductility in the CZM law. In addition, a change in the predicted crack path was observed due to the changing load transfer dictated by the change in cohesive properties of the GBs. For the 3-D 50-grain model, a random set of misorientation angles were assigned to each GB, and Rice's criterion was automatically applied using the directional decohesion element formulation to select a ductile or brittle CZM. A parameterized increase in ductility was applied to each CZM, and the illustration example demonstrated the expected softening behavior in the overall stress-strain response to applied displacements. In the range of values assumed and the random assignment of GB tilt angles, the crack path remained invariant, which is in contrast to the 2-D polycrystal simulation results that involved different assumptions for the variation of GB properties.

Future efforts will need to attempt a characterization of the complete range of GB CZMs to model actual polycrystalline microstructures. This characterization involves a potentially huge number of specific analyses using the methodology developed herein to assess the full 5-space of GB orientations together with the additional variables of the presence of defects such as voids, precipitates, and dislocations that interact with the GB to alter the energy of decohesion. To make this determination tractable, GB orientations might be categorized into classes of equal energy boundaries. The effect of interacting defects may also be found to fall into distinct configurations that might limit the number of configurations that need to be analyzed to determine separation energy. Capturing the complexity of interacting material processes become an immediate necessity in a bottom-up strategy to fully define and communicate this information up to higher length scales to predict failure.

Chapter 7

Summary and Significance of the Current Research

The present research contributes to an improved capability of representing atomistic damage processes for predicting failure in polycrystalline materials. An integrated multiscale methodology has been developed to form a rigorous procedure for uniting physics-based material models across length scales. In order to focus the current research, intergranular fracture along a selected grain boundary (GB) was emphasized. Molecular dynamic (MD) simulations considered crack propagation along a common Σ99 GB in aluminum and yielded significantly different traction-displacement relationships for the crack growing in different directions along the GB. While in one direction the crack progressed in a brittle manner, the propagation in the opposite direction was of a ductile type, characterized by the presence of plastic mechanisms including dislocation emission and deformation twinning at the crack tip. The difference in fracture mechanisms is due to the relative orientation of slip planes to the GB interface making different angles and energy barriers with respect to the two opposite propagation directions. The brittle vs. ductile propagation simulated in both directions along the GB interface has been found to agree well with predictive criteria of Rice [64] and Tadmor-Hai [65]. In addition to the main task of quantifying directional crack growth characteristics, two new developments to general MD methods have been developed. These developments involve an efficient phonon damping scheme that preserves the atomic temperature state which is commonly disrupted using standard velocity rescaling schemes, and the use of local thermostating over the atomistic region to better mitigate thermal ‘hot spots’, such as at crack tips.

The initial MD analysis exhibited constraint effects on the simulation of an embedded crack due to the computational limitation on simulating large atomic systems that necessitated the use of periodic boundary conditions. This limitation was eliminated by the development of a unique embedded statistical coupling method (ESCM) that permits a concurrent multiscale simulation involving the coupling of discrete MD and continuum

finite element methods (FEM) in which ensemble averages are used to link the disparate computational procedures. The present work provided a theoretical 'bridge' between FEM and MD methods and included the development of a standalone FEM program incorporating hybrid stress continuum elements, mixed-mode decohesion elements, and an iterative nonlinear solution algorithm. This new MD-FEM coupling strategy allows large material domains to be modeled with minimal computational cost and avoids the limitations of current methods that have difficulty in representing finite temperature states and typically require a direct atom-node linkage at the interface.

The research presented herein contributes the development of a new statistically-based procedure using cohesive zone volume elements (CZVEs) to extract atomistically-based parameters defining cohesive zone models (CZMs). This procedure improves on other approaches for determining atomistically-based CZM parameters by accounting for proper ensemble constraints (such as allowing volume fluctuation, thus avoiding the simulation of an incompressible material) and simulating energy consumption involved in fracture rather than simple adhesion between grains. Both pure MD analysis and simulations using ESCM methodology were used to determine effective cohesive zone parameters that were compared. A sequential multiscale scheme was developed to represent atomistic failure processes through a CZM paradigm to simulate failure at larger length scales. The CZM formalism provides a numerically efficient means of considering a broad range of GBs incorporating mechanisms and configurations from the atomistic modeling that contribute to the variations in GB properties. A generalized definition of CZMs using traction-displacement relationships expressed in general mathematical form as tabular entries was developed to allow the implementation of nonstandard atomistic-based functional forms.

The difficulty in fully characterizing CZMs to represent all possible GB configurations and their differing failure and intergranular fracture/sliding behavior has been discussed. The vast number of geometric parameters and damage processes involved in characterizing intergranular inelastic behavior is an important consideration in attempting a "bottom-up" approach for directly making accurate microscopic predictions of intergranular damage and failure. In contrast, transgranular fracture/sliding

characterizations are expected to not present the same difficult due to the restricted progression of damage along well-defined slip planes. The range of processes affecting nanoscale response to local stress states requires a statistical treatment. MD simulations provide valuable information of nanoscale processes such as transgranular dislocation formation and interactions, GB dynamics with variable topology and damage states such as nanovoids and precipitates, and the mutual interaction of GB systems and intergranular failure processes. All these effects contribute to the difficulty in obtaining complete characterizations of microstructural failure using CZMs.

A 6-node and 12-node directional decohesion finite element were formulated incorporating Rice's criterion to automatically select the appropriate CZM to simulate differing GB crack propagation characteristics (brittle or ductile) based on the direction of propagation and surrounding slip system orientation. Element input requires the crystallographic orientation of the adjacent grains in the microstructure and additional material parameters including surface, GB, stable and unstable stacking-fault, and unstable twinning energy in order to determine brittle or ductile Mode I fracture. This element formulation adds a significant new feature to decohesion element methods by modifying the element behavior based on the direction of crack propagation.

A series of 2-D and 3-D models were selected to illustrate the developed methodology. CZMs were parametrically varied about the values determined for a Σ99 symmetric tilt GB. For an aluminum bicrystal, using the atomistically-derived traction-displacement results as a basis, two different parameterizations for an atomistically-based CZM were considered where the relative amount of elastic and plastic deformation was varied either through varying the fracture toughness while keeping the peak traction constant or through varying the peak traction while maintaining constant fracture toughness. In both cases, the increase of plasticity results in an increase in the process zone size at the crack tip. Preserving the fracture toughness resulted in a constant equilibrium crack length at a fixed strain, independent of the peak traction. The peak traction affects the initial strain at which the crack opens. Additional parameterizations of CZMs were made to illustrate dominant crack formation in 2-D and 3-D aluminum

polycrystals. The specific modeling of a 3-D triple junction was used to clearly illustrate the effectiveness of directional decohesion finite elements.

The inclusion of a complete set of damage mechanisms is well beyond the scope of the current research effort. The goal of the present research has been to demonstrate new multiscale methods through the prediction of intergranular GB fracture processes from atomistic length scales to polycrystalline microstructures. The incorporation of additional failure mechanisms is left for future enhancements and applications of the developed multiscale methodology.

References

1. Liu, W.K., Karpov, E.G., Zhang, S., and Park, H.S., 2004, “An Introduction to Computational Nanomechanics and Materials,” *Comput. Meth. Appl. Mech. Engrg.*, **193**, pp. 1529-1578.
2. Park, H.S., and Liu, W.K., 2004, “An Introduction and Tutorial on Multiple-Scale Analysis in Solids,” *Comput. Methods Appl. Mech. Engrg.*, **193**, pp. 1733-1772.
3. Gravemeier, V., Lenz, S., and Wall, W.A., 2008, “Towards a Taxonomy for Multiscale Methods in Computational Mechanics: Building Blocks of Existing Methods,” *Comput. Mech.*, **41**, pp.279-291.
4. Oden, J.T., Vemaganti, K., and Moes, N., 1999, “Hierarchical Modeling of Heterogeneous Solids,” *Comput. Methods Appl. Mech. Engrg.*, **172**, pp. 3-25.
5. Tadmor, E.B., Phillips, R., and Ortiz, M., 2000, “Heirarchical Modeling in the Mechanics of Materials,” *Int. J. Solids & Struct.*, **37**, pp. 379-389.
6. Wagner, G.J. and Liu, W.K., 2001, “Hierarchical Enrichment for Bridging Scales and Meshfree Boundary Conditions,” *Int. J. Num. Meth. Engrg*., **50** , pp. 507–524.
7. Su, H., Liu, W.K., Moran, B., Vernerey, F., and Olson, G.B., 2004, “Multi-Scale Constitutive Model and Computational Framework for the Design of Ultra-Hight Strength, High Toughness Steels,” *Comput. Methods Appl. Mech. Engrg.*, **193**, pp. 1865-1908.
8. Clayton, J.D., and Chung, P.W., 2006, “An Atomistic-to-Continuum Framework for Nonlinear Crystal Mechanics Based on Asymptotic Homogenization,” *J. Mech. Phys. Solids*, **54**, pp. 1604-1639.
9. Oden, J.T., Prudhomme, S., Romkes, A., and Bauman, P. 2006, "Multi-scale Modeling of Physical Phenomena: Adaptive Control of Models," *SIAM Journal on Scientific Computing*, **28**, pp. 2359-2389.
10. Broughton, J. Q., Abraham, F. F., Bernstein, N., and Kaxiras, E., 1999, “Concurrent Coupling of Length Scales: Methodology and Application,” *Phys. Rev. B*, **60**, pp. 2391-2403.
11. Abraham, F.F., Brodbeck, D., Rafey, R.A., and Rudge, W.E., 1994, "Instability Dynamics of Fracture: A Computer Simulation Investigation." *Phys. Rev. Lett*., **73**, pp. 272-275.
12. Abraham FF, Broughton JQ, Bernstein N, and Kaxiras E, 1998, “Spanning the Continuum to Quantum Length Scales in a Dynamics Simulation of Brittle Fracture,” *Europhysics Letters*, **44**, p. 783.

13. Abraham, F.F., Bernstein, N., Broughton, J.Q., and Hess, D., 2000, "Dynamic Fracture of Silicon: Concurrent Simulation of Quantum Electrons, Classical Atoms, and the Continuum Solid," *Materials Research Society Bulletin*, **25**, pp. 27-32.
14. Abraham, F.F., 2001, "The Atomic Dynamics of Fracture," *J. Mech. Phys. Solids*, **49**, pp. 2095-2111.
15. Shen, S. and Atluri, S.N., 2004, "Computational Nano-Mechanics and Multi-Scale Simulation," *CMC: Computers, Materials, & Continua*, **1**, pp. 59-90.
16. Shen, S. and Atluri, S.N., 2004, "Multiscale Simulation based on the Meshless Local Petrov-Galerkin (MLPG) Method," *Computer Modeling in Engineering & Sciences*, **5**, pp. 235-255.
17. Buehler, M.J., 2006, "Concurrent Scale Coupling Techniques: From Nano to Macro," Lecture Series 3, CEE, IAP.
18. Kohlhoff, S., Gumbsch, P., and Fischmeister, H.F., 1991, "Crack Propagation in BCC Crystals Studied with a Combined Finite-Element and Atomistic Model," *Phil. Mag. A*, **64**, pp. 851-878.
19. Gumbsch, P. and Beltz, G.E., 1995, "On the Continuum Versus Atomistic Descriptions of Dislocation Nucleation and Cleavage in Nickel." *Mod. Sim. Mat. Sci. and Engrg.*, **3,** pp. 597-613.
20. Gumbsch, P., 1995, "An Atomistic Study of Brittle-Fracture - toward Explicit Failure Criteria from Atomistic Modeling." *J. Mat. Res.*, **10,** pp. 2897-2907.
21. Kroner, E., 1967, "Elasticity Theory of Materials with Long Range Cohesive Forces," *Int. J. Solids Struct.*, **3**, pp. 731-742.
22. Rudd R.E., and Broughton J.Q., 1998, "Coarse-Grained Molecular Dynamics and the Atomic Limit of Finite Elements," *Phys. Rev. B*, **58**, p. R5893.
23. Rudd R.E., and Broughton J.Q., 2005, "Coarse-Grained Molecular Dynamics: Nonlinear Finite Elements and Finite Temperature," *Phys. Rev. B*, **72**, p.144104.
24. Tadmor, E. B., Ortiz, M., and Phillips, R., 1996, "Quasi-Continuum Analysis of Defects in Solids," *Phil. Mag. A*, **73**, pp. 1529-1563.
25. Knap, J. and Ortiz, M., 2001, "An Analysis of the Quasicontinuum Method," *J. Mech. Phys. Solids*, **49**, pp. 1899-1923.
26. Miller, R.E., and Tadmor, E.B., 2002, "The Quasi-continuum Method: Overview, Applications, and Current Direction," *J. Computer-Aided Materials Design*, **9**, pp. 203-239.
27. Sansoz, F., and Molinari, J.F., 2007, "Size and Microstructure Effects on the Mechanical Behavior of FCC Bicyrstals by Quasicontinuum Method," *Thin Solid Films*, **515**, pp.3158-3163.

28. Born, M., and Huang, K., 1954, *Dynamical Theory of Crystal Lattices*, Oxford University Press,
29. Shenoy, V., Shenoy, V., and Phillips, R., 1999, "Finite temperature quasicontinuum methods," Materials Research Society Symposium Proceedings, 538, PP. 465-471.
30. Xiao, S.P., and Belytschko, T., 2004, "A bridging Domain Method for Coupling Continua with Molecular Dynamics," *Comp. Meth. Appld. Mech. Engrg.*, **193**, p.1645.
31. Shilkrot, L.E., Curtin, W.A. and Miller, R.E., 2002, "A Coupled Atomistic/Continuum Model of Defects in Solids." *J. Mech. and Phys. Solids*, **50**, pp. 2085-2106.
32. Shilkrot, L.E., Miller, R.E. and Curtin, W.A., 2002, "Coupled Atomistic and Discrete Dislocation Plasticity." *Phys. Rev. Lett.*, **89**, p. 025501-1.
33. Curtin, W.A. and Miller, R.E., 2003, "Atomistic/Continuum Coupling in Computational Materials Science." *Mod. Sim. Mat. Sci. and Engrg.*, **11,** pp. R33-R68.
34. Shilkrot, L.E., Miller, R.E., and Curtin, W.A., 2004, "Multiscale Plasticity Modeling: Coupled Atomistics and Discrete Dislocation Mechanics," *J. Mech. and Phys. Solids* **52**, pp. 755-787.
35. Shiari, B., Miller, R.E., and Curtin, W.A., 2005, "Coupled Atomistic/Discrete Dislocation Simulations of Nanoindentation at Finite Temperature." *J. Engrg. Mat. and Tech. Transactions of the ASME,* **127,** pp. 358-368.
36. Van der Giessen, E., and Needleman, A., 1995, "Discrete Dislocation Plasticity: A Simple Planar Model," *Mod. Sim. Mat. Sci. Eng.* **3**, pp. 689-735.
37. Hao, S., Liu, W.K., Moran, B., Vernerey, F., and Olson, G.B., 2004, "Multi-Scale Constitutive Model and Computational Framework for the Design of Ultra-High Strength, High Toughness Steels," *Comput. Methods Appl. Mech. Engrg.*, **193**, pp. 1865-1908.
38. Haile, J.M., 1991, *Introduction to Molecular Dynamics: Elementary Methods*, John Wiley & Sons, Inc.
39. Allen, M.P. and Tildesley, D.J., 1987, *Computer Simulation of Liquids,* Oxford University Press, Oxford.
40. Richon, A.B., 1994, "An Introduction to Molecular Modeling," *Mathematech*, **1**, p 83.
41. Swope, W.C., Andersen, H.C., Berens, P.H., and Wilson, K.R., 1982, "The Velocity Verlet Algorithm," *J. Chem. Phys.* **76**, p. 637.
42. Lennard-Jones, J.E., 1925, "On the Forces between Atoms and Ions," *Proceedings of the Royal Society of London. Series A*, **109**, pp. 584-597.
43. Daw, M.S., and Baskes, M.I., 1984, "Embedded-Atom Method: Derivation and Application to Impurities, Surfaces, and Other Defects in Metals," *Phys. Rev. B*, **29**, p. 6443.

44. Daw, M.S., Foiles, S.M., and Baskes, M.I., 1992, "The Embedded-Atom Method: A Review of Theory and Applications," *Mat. Sci. Reports*, **9**, pp. 251-310.
45. Rice, O.K., 1967, *Statistical Mechanics, Thermodynamics and Kinetics*, W.H. Freeman and Co.
46. Saether, E., Frankland, S.J.V, and Pipes, R.B., 2003, "Transverse Mechanical Properties of Single Walled Carbon Nanotube Crystals. Part I: Determination of Elastic Moduli," *Comp. Sci. and Tech.*, **63**, pp. 1543-1550.
47. Saether, E., 2003, "Transverse Mechanical Properties of Carbon Nanotube Crystals. Part II: Sensitivity to Lattice Distortion," *Comp. Sci. and Tech.*, **63**, pp. 1551-1559.
48. Parrinello, M. and Rahman, A., 1981, "Polymorphic Transitions in Single Crystals: A New Molecular Dynamics Method," *J. Appl. Phys.*, **52**, pp.7182-7190.
49. Zimmerman, J.A., Jones, R.E., Klein, P.A., Bammann, D.J., Webb, E.B., and Hoyt, J.J., 2002, "Continuum Definitions for Stress in Atomistic Simulation," SAND Report, Sandia National Laboratory, SAND2002-8608.
50. Malvern, L.E., 1969, *Introduction to the Mechanics of a Continuous Medium*, Prentise-Hall, Inc., New Jersey.
51. Marsden, J.E. and Hughes, T.J.R., 1983, *Mathematical Foundations of Elasticity*, Dover Publications, Inc., New York.
52. Clausius, R.J.E, 1870, "On a Mechanical Theorem Applicable to Heat," *Phil. Mag.*, **40**, pp. 122-127.
53. Maxwell, J.C, 1870, "On Reciprocal Figures, Frames and Diagrams of Forces," *Trans. R. Soc. Edinb.*, **XXVI**, pp. 1 – 43.
54. Maxwell, J.C., 1874, "Van der Waals on the Continuity of the Gaseus and Liquid States," *Nature*, pp. 477-480.
55. Zhou, M., 2003, "A New Look at the Atomic Level Virial Stress: On a Continuum-Molecular System Equivalence," *Proc. R. Soc. Lond. A.* **459**, pp. 2347-2392.
56. Zimmerman, J.A., Webb III, E.B., Hoyt, J.J., Jones, R.E., Klein, P.A. and Bammann, D.J., 2004, "Calculation of Stress in Atomistic Simulation," *Mod. Sim. Mat. Sci. and Eng.*, **12**, pp. S319-S332.
57. Basinski, Z.S., Duesbery, M.S., and Taylor, R., 1971, *Can. J. Phys.*, **49**, p. 2160.
58. Cheung, K.S. and Yip, S., 1991, "Atomic-Level Stress in an Inhomogeneous System," *J. Appl. Phys.*, **70**, pp. 5688-5690.
59. Cormier, J., Rickman, J.M., and Delph, T.J., 2001, "Stress Calculation in Atomistic Simulations of Perfect and Imperfect Solids," *J. Appl. Phys.*, **89**, pp. 99-104.

60. Gumbsch, P., Zhou, S.J., and Holian, B.L., 1997, “Molecular Dynamics Investigation of Dynamic Crack Stability,” *Phys. Rev. B*, **55**, pp. 3445 – 3455.
61. Phillips, S.C, Essex, J.W., and Edge, C.M., 2000, “Digitally Filtered Molecular Dynamics: The Frequency Specific Control of Molecular Dynamics Simulations,” *J. Chem. Phys.*, **112**, pp. 2586 – 2597.
62. Hull, D., and Bacon, D.J., 2001, *Introduction to Dislocations*, Fourth Edition, Butterworth, Heinemann.
63. Lee, B.J., and Choi, S.H., 2004, “Computation of Grain Boundary Energies,” *Mod. Sim. Mater. Sci. Eng.*, **12**, pp. 621-632.
64. Rice, J.R., 1992, “Dislocation Nucleation from a Crack Tip: An Analysis Based on the Peierls Concept,” *J. Mech. Phys. Solids*, **40**, pp. 239-271.
65. Tadmor, E.B., and Hai, S., 2003, "A Peierls Criterion for the Onset of Deformation Twinning at a Crack Tip," *J. Mech. Phys. Solids*, **51**, pp. 765-793.
66. Yamakov, V., Saether, E., Phillips, D.R., and Glaessgen, E.H., 2005, “Dynamic Instability in Intergranular Fracture,” *Phys. Rev. Lett.*, **95**, pp. 015502-1-4.
67. Yamakov, V., Saether, E., Phillips, D.R., and Glaessgen, E.H., 2007, “Dynamics of Nanoscale Grain-Boundary Decohesion in Aluminum by Molecular-Dynamics Simulation,” *J. Mat. Sci.*, **42**, p.1466.
68. Honeycutt, J.D., and Andersen, H.C., 1987, “Molecular Dynamics Study of Melting and Freezing of Small Lennard-Jones Clusters,” *J. Phys. Chem.*, **91**, pp. 4950-4963.
69. Clarke, A. S., and Jonsson, H., 1993, “Structural Changes Accompanying Densification of Random Hard-Sphere Packings,” *Phys. Rev. E*, **47**, pp. 3975-3984.
70. Dahmen, U., Hetherington, J.D., O’Keefe, M.A., Westmacott, K.H., Mills, M.J., Daw, M.S., and Vitek, V., 1990, "Atomic Structure of a Σ99 Grain Boundary in Al: A Comparison Between Atomic-Resolution Observation and Pair-Potential and Embedded-Atom Simulations," *Phil. Mag. Lett.*, **62**, pp. 327-335.
71. Wolf, D., 1990, “Correlation between Structure, Energy, and Ideal Cleavage Fracture for Symmetrical Grain Boundaries in FCC Metals,” *J. Mater. Res.*, **5**, pp. 1708-1730.
72. Mishin, Y., Farkas, D., Mehl, M.J., and Papaconstantopoulos, D.A., 1999, “Interatomic Potentials for Monoatomic Metals from Experimental Data and Ab Initio Calculations,” *Phys. Rev. B*, **59**, pp. 3393-3407.
73. Yamakov, V., Wolf, D., Salazar, M., Phillpot, S.R., and Gleiter, H., 2001, “Length-Scale Effects in the Nucleation of Extended Lattice Dislocations in Nanocrystalline Al by Molecular-Dynamics Simulation,” *Acta Mater.*, **49**, pp. 2713-2722.

74. Yamakov, V., Wolf, D., Phillpot, S.R., and Gleiter, H., 2003, "Dislocation-Dislocation and Dislocation-Twin Reactions in Nanocrystalline Al by Molecular-Dynamics Simulation," *Acta Mater.*, **51**, pp. 4135-4147.

75. Yamakov, V., Wolf, D., Phillpot, S.R., Mukherjee, A.K, and Gleiter, H., 2002, "Dislocation Processes in the Deformation of Nanocrystalline Al by Molecular-Dynamics Simulation," *Nature Mater.*,**1**, pp. 45-48.

76. Nose, S., 1984, "A Unified Formulation of the Constant Temperature Molecular Dynamics Method," *J. Chem. Phys*. **81**, pp. 511-519.

77. Weertman, J., and Weertman, J. R., 1992, *Elementary dislocation theory*. Oxford University Press, New York.

78. Schiotz, J., Vegge, T., Di Tolla, F.D., and Jacobsen, K.W., 1999, "Atomic-Scale Simulations of the Mechanical Deformation of Nanocrystalline Metals," *Phys. Rev. B,* **60**, pp. 11971-11983.

79. ABAQUS/Standard User's Manual, Hibbitt, Karlsson, and Sorensen, Inc., 2004.

80. Cleri, F., Phillpot, S.R., Wolf, D., 1999, "Atomistic Simulations of Intergranular Fracture in Symmetric-Tilt Grain Boundaries," *Interface Sci.*, **7**, pp. 45-55.

81. Barber, M., Donley, J., and Langer, J. S., 1989, "Steady-State Propagation of a Crack in a Viscoelastic Strip," *Phys. Rev. A*, **40**, pp. 366-376.

82. Ching, E.S.C., 1994, "Dynamic Stresses at a Moving Crack Tip in a Model of Fracture Propagation," *Phys. Rev. E*, **49**, pp. 3382-3388.

83. Lutsko, J. F., 1988, "Stress and Elastic Constants in Anisotropic Solids: Molecular Dynamics Techniques," *J. Appl. Phys.*, **64**, pp. 1152-1154.

84. Wolf, D., and Jaszczak, J. A., 1993, "Tailored Elastic Behavior of Multilayers through Controlled Interface Structure," *J. Comp. Aided Mater. Design*, **1**, pp. 111-148.

85. Saether, E., Yamakov, V., and Glaessgen, E.H., 2007 "A Statistical Approach for the Concurrent Coupling of Molecular Dynamics and Finite Element Methods," *48th AIAA SDM Conference*, Honolulu, HI, Report No. AIAA-2007-2169.

86. Saether, E., Yamakov, V., and Glaessgen, E.H., 2008, "An Embedded Statistical Method for Coupling Molecular Dynamics and Finite Element Analyses," *Int. J. Num. Meth. Engrg.*, (In review).

87. Saether, E., Yamakov, V., and Glaessgen, E.H., 2008 "New Developments in the Embedded Statistical Coupling Method: Atomistic/Continuum Crack Propagation," *49th AIAA SDM Conference*, Schuamburg, IL, Report No. AIAA-2008.

88. O'Rourke J, 2001, *Computational Geometry in C*, 2nd Edition, Cambridge University Press.

89. Holian, B.L, Ravelo, R., 1995, "Fracture Simulations using Large-Scale Molecular Dynamics," *Phys. Rev. B*, **51**, p. 11275.
90. Schäfer, C., Urbassek, H.M., Zhigilei, L.V., and Garrison, B.J., 2002, "Pressure-Transmitting Boundary Conditions for Molecular-Dynamics Simulations," *Comp. Mat. Sci.*, **24**, p. 421.
91. Moseler, M., Nordiek, J., and Haberland, H., 1997, "Reduction of the Reflected Pressure Wave in the Molecular-Dynamics Simulation of Energetic Particle-Solid Collisions," *Phys. Rev. B*, **56**, p.15439.
92. Cai, W., Koning, M., Bulatov, V.V. and Yip, S., 2000, "Minimizing Boundary Reflections in Coupled-Domain Simulations," *Phys. Rev. Lett.*, **85**, p. 3213.
93. Park, H.S., Karpov, E.G., and Liu, W.K., 2005, "Non-Reflecting Boundary Conditions for Atomistic, Continuum and Coupled Atomistic/Continuum Simulations," *Int. J. Num. Meth. Engrg.*, **64**, p. 237.
94. Pian, T.H.H., and Tong, P., 1986, "Relations between Incompatible Displacement Model and Hybrid Stress Model," *Int. J. Num. Meth. Engrg.*, **22**, p.173.
95. Saether E., 1995, "Explicit Determination of Element Stiffness Matrices in the Hybrid Stress Method," *Int. J. Num. Meth. Engrg.*, **38**, p. 2547.
96. Hirth, J.P., and Lothe, J., 1982, *Theory of Dislocations*, Wiley, New York.
97. Lekhnitskii, S.G., 1987, *Anisotropic Plates*, Gordon and Breach Science Publishers, USA.
98. Tsuru T., and Shibutani Y., 2006, "Atomisitc Simulations of Elastic Deformation and Dislocation Nucleation in Al under Indentation-Induced Stress Distribution," *Mod. Sim. Mat. Sci. Engrg.*, **14**, p. S55.
99. Huang, Z., Thomson, P., and Shenglin D., 2007, "Lattice Contractions of a Nanoparticle due to the Surface Tension: A Model of Elasticity," *J. Phys. Chem. Solids*, **68**, p. 530.
100. Qu, S., Shastry, V., Curtin, W.A., and Miller, R.E., 2005, "A Finite-Temperature Dynamic Coupled Atomistic/Discrete Dislocation Method," *Mod. Sim. Mat.. Sci. Eng*. **13**, pp. 1101-1118.
101. Dugdale, D.S., 1960, "Yielding of Steel Sheets containing Slits," *J. Mech. Phys. Solids*, **8**, pp. 100-108.
102. Barenblatt, G.I., 1962, "The Mathematical Theory of Equilibrium Cracks in Brittle Fracture," *Adv. Appl. Mech.*, **7**, pp. 55-129.
103. Maugis, E., 1992, "Adhesion of Spheres – the JKR-DMT Transition using a Dugdale Model," *J. Colloid Interface Sci.*, **150**, pp. 243-269.
104. Kem, K.S., McMeeking, R.M., and Johnson, K.I., 1998, "Adhesion, Slip, Cohesive Zones and Energy Fluxes for Elastic Spheres in Contact," *J. Mech. Phys. Solids*, **46**, pp. 243-266.

105. Tvergaard, V. and Hutchinson, J.W., 1992, "The Relation Between Crack Growth Resistance and Fracture Process Parameters in Elastic-Plastic Solids," *J. Mech. and Phys. Solids*, **40**, pp. 1377-1397.
106. Costanzo, F. and Allen, D. H., 1995, "A Continuum Thermodynamic Analysis of Cohesive Zone Models," *Int. J. Engrg. Sci.*, **33**, pp. 2197-2219.
107. Camacho, G. T. and Ortiz, M., 1996, "Computational Modeling of Impact Damage in Brittle Materials," *Int. J. Solids Struct.*, **33**, pp. 2899-2938.
108. Klein, P. and Gao, H., 1998, "Crack Nucleation and Growth as Strain Localization in a Virtual-Bond Continuum," *Engr. Fract. Mech*, **61**, pp. 21-48.
109. Ortiz, M., and Pandolfi, A., 1999, "Finite-Deformation Irreversible Cohesive Elements for Three-Dimensional Crack-Propagation Analysis," *Int. J. Num. Meth. Engrg.*, **44**, pp. 1267-1282.
110. Chen, J., Crisfield, M., Kinloch, A.J., Busso, E.P., Matthews, F.L., and Qui, Y., 1999, "Predicting Progressive Delamination of Composite Material Specimens via Interface Elements," *Mech. Comp. Mat. Struct.*, **6**, pp. 301-317.
111. Foulk, J.W., Allen, D.H., and Helms, K.L.E., 2000, "Formulation of a Three-Dimensional Cohesive Zone Model for Application to a Finite Element Algorithm," *Comput. Methods Appl. Mech. Engrg.*, **183**, pp. 51-66.
112. Alfano, G., and Crisfield, M.A., 2001, "Finite Element Interface Models for the Delamination Analysis of Laminated Composites: Mechanical and Computational Issues," *Int. J. Num. Meth. Engrg.*, **50**, pp. 1701-1736.
113. Dávila, C.G., 2001, "Mixed-Mode Decohesion Elements for Analysis of Progressive Delamination," *42nd AIAA SDM Conference*, Seattle, WA, Paper No. AIAA-01-1486.
114. Iesulauro, E., 2002, "Decohesion of Grain Boundaries in Statistical Representations of Aluminum Polycrystals," Cornell University Report 02-01.
115. Iesulauro, E., Ingraffea, A.R., Arwade, S., and Wawrzynek, P.A., 2002, "Simulation of Grain Boundary Decohesion and Crack Initiation in Aluminum Microstructure Models," in Fatigue and Fracture Mechanics: 33rd Volume, ASTM STP 1417, (W.G. Reuter and R.S. Piascik, Eds., American Society for Testing and Materials, West Conshohocken, PA, 2002).
116. Goyal, V.K., Johnson, E.R., Davila, C.G., and Jaunky, N., 2002, "An Irreversible Constitutive Law for Modeling the Delamination Process Using Interface Elements," NASA/CR-2002-211758.

117. Cleri, F., 2001, "Representation of Mechanical Loads in Molecular Dynamics Simulations," *Phys. Rev. B*, **65**, p. 014107.
118. Turon, A., Camanho, P., Costa, J., and Davila, C., 2004, "An Interface Damage Model for the Simulation of Delamination Under Variable-Mode Ratio in Composite Materials," NASA/TM-2004-213277.
119. Alfano, G., and Sacco, E., 2006, "Combining Interface Damage and Friction in a Cohesive-Zone Model," *Int. J. Num. Meth. Engrg.*, **68**, pp. 542-582.
120. Hong, S., and Kim, K.S., 2003, "Extraction of Cohesive-Zone Laws from Elastic Far-Fields of a Cohesive Crack Tip: A Field Projection Method," *J. Mech. Phys. Solids*, **51**, pp. 1267-1286.
121. Li, W. and Siegmund, T., 2004, "Numerical Study of Indentation Delamination of Strongly Bonded Films by use of a Cohesive Zone Model," *Computer Modeling in Engineering & Sciences*, **5**, pp. 81-90.
122. Li, H. and Chandra, N., 2003, "Analysis of Crack Growth and Crack-Tip Plasticity in Ductile Materials Using Cohesive Zone Models," *Int. J. Plast.*, **19**, pp. 849-882.
123. Chandra, N., and Shet, C., 2004, "A Micromechanistic Perspective of Cohesive Zone Approach in Modeling Fracture," *Computer Modeling in Engineering & Sciences*, **5**, pp. 21-33.
124. Rose, J.H, Smith, J.R. and Ferrante, J., 1983, "Universal Feature of Bonding in Metals," *Phys. Rev. B.*, **28**, pp.1835-1845.
125. Nguyen, O., and Ortiz, M., 2002, "Coarse-Graining and Renormalization of Atomistic Binding Relations and Universal Macroscopic Cohesive Behavior," *J. Mech. Phys. Solids*, **50**, pp. 1727-1741.
126. Volokh, K.Y., 2004, "Comparison Between Cohesive Zone Models," *Commun. Num. Meth. Engrg.*, **20**, pp. 845-856.
127. Zhang, Z., Paulino, G.H., and Celes, W., 2007, "Extrinsic Cohesive Modelling of Dynamic Fracture and Microbranching Instability in Brittle Materials," *Int. J. Num. Meth. Engrg.*, **72**, pp. 893-923.
128. Zavattieri, P.D., Raghuram, P.V., and Espinosa, H.D., 2001, "A Computational Model of Ceramic Microstructures Subjected to Multi-Axial Dynamic Loading," *J. Mech. Phys. Solids*, **49**, pp. 27-68.
129. Zavattieri, P.D., and Espinosa, H.D., 2003, "An Examination of the Competition Between Bulk Behavior and Interfacial Behavior of Ceramics Subjected to Dynamic Pressure-Shear Loading," *J. Mech. Phys. Solids*, **51**, pp. 607-635.

130. Wei, Y.J., and Anand, L., 2004, “Grain Boundary Sliding and Separation in Polycrystalline Metals: Application to Nanocrystalline FCC Metals,” *J. Mech. Phys. Solids.*, **52**, pp. 2587-2616.

131. Yamakov, V., Saether, E., Phillips, D.R., and Glaessgen, E.H., 2006, “Molecular-Dynamics Simulation-Based Cohesive Zone Representation of Intergranular Fracture Processes in Aluminum,” *J. Mech. and Phys. Solids*, **54**, p.1899.

132. Turon, A., Davila, C.G., Camanho, P.P., and Costa, J., 2007, “An Engineering Solution for Mesh Size Effects in the Simulation of Delamination using Cohesive Zone Models,” *Eng. Fract. Mech*., **74**, pp. 1665-1682.

133. Baskes, M.I., 1992, “Modified Embedded-Atom Potentials for Cubic Materials and Impurities,” *Phys. Rev. B*, **46**, pp. 2727-2742.

134. Gall, K., Horstemeyer, M.F., Van Schilfgaarde, M., and Baskes, M.I., 2000, “Atomistic Simulations on the Tensile Debonding of an Aluminum-Silicon Interface,” *J. Mech. Phys. Solids*, **48**, pp. 2183-2212.

135. Dighe, M.D. and Gokhale, A.M., 1997, “Relationship Between Microstructural Extremum and Fracture Path in a Cast Al-Si-Mg Alloy,” *Scripta Mater*., **37**, pp. 1435-1440.

136. Samuel, A. M. and Samuel, F. H., 1995, “A Metallographic Study of Porosity and Fracture Behavior in Relation to the Tensile Properties in 319.2 End Chill Castings,” *Metall. Mater. Trans.*, **26A**, pp. 2359-2372.

137. Komanduri, R., Chandrasekaran, N., and Raff, L. M., 2001, “Molecular Dynamics (MD) Simulation of Uniaxial Tension of Some Single-Crystal Cubic Metals at Nanolevel,” *Int. J. Mech. Sci.*, **43**, pp. 2237-2260.

138. Spearot, D., Jacob, K.I., and McDowell, D.L., 2004, “Non-Local Separation Constitutive Laws for Interfaces and Their Relation to Nanoscale Simulations,” *Mech. Mater*., **36**, pp. 825-847.

139. Spearot, D.E., Jacob, K.I., and McDowell, D.C., 2005, “Nucleation of Dislocations from [001] Bicrystal Interfaces in Aluminum, “ *Acta Materialia*, **53**, pp. 3579-3589.

140. Raynolds, J.E., Smith, J.R., Zhao, G.L., and Srolovitz, D.J., 1996, “Adhesion in NiAl-Cr from First Principles,” *Phys. Rev. B*, **53**, pp. 13883-13890.

141. Tvergaard, V., and Hutchinson, J.W., 1996, “Effect of Strain-Dependent Cohesive Zone Model on Predictions of Crack Growth Resistance,” *Int. J. Solids Struct.*, **33**, pp. 3297-3308.

142. Raj, R. and Ashby, M.F., 1971, “On Grain Boundary Sliding and Diffusion Creep,” *Metall. Trans.*, **2**, p. 1113.

143. Ashby, M.F. and Verrall, R.A., 1973, "Diffusion-Accommodated Flow and Superplasticity," *Acta Mater.*, **21**, pp. 149-163.
144. Cahn, J.W., Mishin, Y., and Suzuki, A., 2006, "Coupling Grain Boundary Motion to Shear Deformation," *Acta Mat.*, **54**, pp. 4953-4975.
145. Cocchetti, G., Maier, G., and Shen, X.P., 2002, "Piecewise Linear Models for Interfaces and Mixed Mode Cohesive Cracks," *Computer Modeling in Engineering & Sciences*, **3**., pp. 279-298.
146. Lusk, M.T. and Beale, P.D., 2004, "Grain-Boundary Free Energy in an Assembly of Elastic Disks," *Phys. Rev. B*, **69**, p 026117.
147. Esling, C., Zuo, L., and Wang, G., 2005, "Some Theoretical and Computational Aspects in Grain Boundaries and Triple Lines," *J. Mat. Sci*., **40**, pp. 841-845.
148. Wynblatt, P., and Chatain, D., 2006, "Anisotropy of Segregation at Grain Boundaries and Surfaces," *Met. Mat. Trans. A*, **37A**, pp. 2595-2620.
149. Read, W.T., and Shockley, W., 1950, "Dislocation Models of Crystal Grain Boundaries," *Phys. Rev.* **78**, p. 275.
150. Wang, G-J., and Vitek, V., 1986, "Relationships Between Grain Boundary Structure and Energy," *Acta. Metall*, **34**, pp. 951-960.
151. Wolf, D., Merkle, K.L., In: Wolf, D., and Yip, S., 1992, Eds. Materials Interfaces: Atomic Structure and Properties. London: Chapman and Hall, Ch. 3.
152. Romeu, D., 2003, "Interfaces and Quasicrystals as Competing Crystal Lattices: Towards a Crystallographic Theory of Interfaces," *Phys. Rev. B.*, **67**, p. 024202.
153. Schuh, C.A., Kumar, M., and King, W.E. 2005, "Universal features of grain boundary networks in FCC materials," *J. Mat. Sci.*, **40**, pp. 847-852.
154. Benzeggagh, M. L. and Kenane, M., 1996, "Measurement of Mixed-Mode Delamination Fracture Toughnesss of Unidirectional Glass/Epoxy Composites With Mixed-Mode Bending Apparatus," *Comp. Sci. and Tech.*, **49**, pp. 439-439.
155. Ye, L., 1988, "Role of Matrix Resin in Delamination Onset and Growth in Composite Laminates," *Comp. Sci. Tech.*, **33**, pp. 257-277.
156. Hilleborg, A., Modeer, M., and I.E., P., 1976, "Analysis of Crack Formation and Crack Growth in Concrete my Means of Fracture Mechanics and Finite Elements," *Cement & Concrete Res*., **6**, pp. 773-792.
157. Needleman, A., 1987, "A Continuum Model for Void Nucleation by Inclusion Debonding," *J. Appld. Mech*., **54**, pp. 525-531.

158. Needleman, A., 1990, "An Analysis of Decohesion Along an Imperfect Interface," *Int. J. Fract*., **42**, pp. 21-40.
159. Beer, G., 1985, "An Isoparametric Joint/Interface Element for the Finite Element Analysis," *Int. J. Numer. Meth. Engrg*., **21**, pp. 585-600.
160. Rabinovitch, O., 2008, "Debonding Analysis of Fiber-Reinforced-Polymer Strengthened Beams: Cohesive Zone Modeling versus a Linear Elastic Fracture Mechanics Approach," *Eng. Fract. Mech.*, **75**, pp.2842-2859.
161. Diehl, T., 2008, "On Using a Penalty-Based Cohesive-Zone Finite Element Approach, Part I: Elastic Solution Benchmarks," *Int. J. Adhesion & Adhesives*, **28**, pp.237-255.
162. Camanho, P.P., Davila, C.G., and De Moura, M.F., 2003, "Numerical Simulation of Mixed-Mode progressive Delamination in Composite Materials," *J. Comp. Mat*., **37**, pp. 1415-1438.
163. Cook R.D, Malkus D.S, and Plesha M.E, 2001, *Concepts and Applications of Finite Element Analysis*, Third Edition, John Wiley & Sons.
164. Segurado, J., and LLorca, J., 2004, "A New Three-Dimensional Interface Finite Element to Simulate Fracture in Composites," *Int. J. Solids Struct.*, **41**, pp. 2977-2993.
165. Gustafson, P.A., and Waas, A.M., 2008, "Efficient and Robust Traction Laws for the Modeling of Adhesively Bonded Joints," *49th AIAA SDM Conference*, Schaumburg, IL, Paper No. AIAA 2008-1847.
166. Hamitouche, L., Tarfaoui, M., and Vautrin, A., 2008, "An Interface Debonding Law Subject to Viscous Regularization for Avoiding Instability: Application to the Delamination Problems," *Eng. Fract. Mech.*, **75**, pp. 3084-3100.
167. Gao, Y.F., and Bower, A.F., 2004, "A Simple Technique for Avoiding Convergence Problems in Finite Element Simulations of Crack Nucleation and Growth on Cohesive Interfaces," *Mod. Sim. Mater. Sci. Engrg.*, **12**, pp. 453-463.
168. Schellekens, J.C.J., and de Borst, R., 1993, "On the Numerical Integration of Interface Elements," *Int. J. Num. Meth. Engrg.*, **36**, pp. 43-66.
169. Allen, D.H., and Searcy, C.R., 2000, "Numerical Aspects of a Micromechanical Model of a Cohesive Zone," *J. Reinforced Plastics and Composites*, **19**, pp. 240-248.
170. Tomar, V., Zhai, J., and Zhou, M., 2004, "Bounds for Element Size in a Variable Stiffness Coihesive Finite Element Model," *Int. J. Num. Meth. Engrg*., **61**, pp. 1894-1920.
171. Zheng, L., and Xu, T.D., 2004, "Method for Determining the Elastic Modulus at Grain Boundaries for Polycrystalline Materials," *Mat. Sci. and Tech.*, **20**, pp. 605-609.

172. Chandra, N., and Shet, C., 2004, "A Micromechanistic Perspective of Cohesive Zone Approach in Modeling Fracture," *Computer Modeling in Engineering & Sciences*, **5**, pp. 21-33.
173. Orowan, E., 1945, *Transactions of the Institute of Engineers and Shipbuilders Scotland* **89,** p. 165.
174. Irwin, G.R., 1949, In: Jonassen, F., Roop, W.P., and Bayless, R.T., (Eds.), *American Society of Metals, Cleveland*, p. 147.
175. Shih, K.K., and Li, J.C.M., 1975, "Energy of Grain Boundaries Between Cusp Misorientations," *Surf. Sci.*, **50**, pp. 109-124.
176. Shenderova, O.A., Brenner, D.W., Nazarov, A.A., Romanov, A.E., and Yang, L.H., 1998, "Multiscale Modeling Approach for Calculating Grain-Boundary Energies from First Pinciples," *Phys. Rev. B.*, **57**, p. R3181.
177. Van den Bosch, M.J., Schreurs, P.J.G., and Geers, M.G.D, 2007, "A Cohesive Zone Model with a Large Displacement Formulation Accounting for Interfacial Fibrilation," *European J. Mech. A/Solids*, **26**, pp.1-19.